

PHD THESIS

---

# Quantum simulation with an optical kagome lattice

---

MAX MELCHNER VON DYDIOWA

ST CATHARINE'S COLLEGE

MARCH 2022



UNIVERSITY OF  
CAMBRIDGE

Cavendish Laboratory

This thesis is submitted for the degree of Doctor of Philosophy



# Declaration

This thesis is the result of my own work and includes nothing which is the outcome of work done in collaboration except as specified in the text.

I further state that no substantial part of my thesis has already been submitted, or, is being concurrently submitted for any such degree, diploma or other qualification at the University of Cambridge or any other university or similar institution.

This thesis does not exceed the limit of 60,000 words, including abstract, tables, footnotes and appendices, as set out by the Faculty of Physics and Chemistry.



## Abstract

This thesis reports on the construction and operation of an ultracold atom-based quantum simulator for studying the kagome lattice and the associated flat band. Despite a copious amount of theoretical effort to elucidate the physics of the kagome lattice, experimental kagome physics is still in its infancy. In the case of ultracold atoms, this is mainly due to considerable technical challenges involved in creating an optical kagome lattice, such as the need for active phase stabilization for bichromatic superlattices. We show that we have overcome these challenges and give a thorough account of our machine's technical details. Furthermore, we present calculations and measurements that fully characterise the kagome quantum simulator.

Much of the theoretical work on the kagome lattice has focussed on its flat band. Populating flat bands with ultracold atoms has proven to be difficult and it has so far not been possible to prepare flat bands in thermodynamic equilibrium. We show a route towards studying quantum manybody physics in the flat band of the kagome lattice using negative temperatures. In addition we report, for the first time, on the creation of a negative temperature state in a triangular lattice.

This thesis additionally serves to collect and consolidate theoretical research that we can directly study with our machine. In particular, we will discuss the properties of bosons in flat bands and their experimental signatures, with the aim of guiding and accelerating the near-term developments and experiments.

Finally, we detail our progress towards realizing a quantum gas microscope for the kagome lattice. In this context, we present a new method for super-resolution microscopy of ultracold atoms in optical lattices.



# Contents

<b>1</b>	<b>Introduction</b>	<b>1</b>
1.1	Quantum simulation . . . . .	1
1.2	Ultracold atoms & optical lattices . . . . .	1
1.3	The kagome lattice & flat bands . . . . .	3
1.4	Quantum simulation with an optical kagome lattice . . . . .	12
1.5	Thesis outline . . . . .	12
<b>2</b>	<b>The optical kagome lattice</b>	<b>15</b>
2.1	Optical triangular lattice . . . . .	15
2.1.1	Interfering lattice . . . . .	15
2.1.2	Phase degrees of freedom . . . . .	19
2.1.3	Lattice potential . . . . .	20
2.2	Optical kagome lattice . . . . .	21
2.3	Kagome band structure . . . . .	23
2.4	Wannier states . . . . .	31
2.5	Tunnelling rates (Hubbard $t$ ) . . . . .	39
2.6	Interactions (Hubbard $U$ ) . . . . .	42
<b>3</b>	<b>Negative temperatures &amp; bosons in flat bands</b>	<b>45</b>
3.1	Negative temperatures . . . . .	45
3.1.1	Classical negative temperatures . . . . .	45
3.1.2	Negative temperatures in optical lattices . . . . .	47
3.2	Kagome flat band signatures . . . . .	52
3.3	Flat band BEC (high density) . . . . .	55
3.3.1	Mean-field approach . . . . .	58
3.4	CDW & supersolid (low density) . . . . .	65
<b>4</b>	<b>Machine design</b>	<b>71</b>
4.1	Vacuum system . . . . .	71
4.1.1	Baking & vacuum maintenance . . . . .	79
4.2	Red & high power table lasers . . . . .	80
4.2.1	Cooling and imaging lasers . . . . .	80
4.2.2	Dipole and lattice lasers . . . . .	83
4.3	Experiment table optics . . . . .	86
4.3.1	MOT . . . . .	86
4.3.2	Optical transport . . . . .	89
4.3.3	Dipole trap . . . . .	91
4.3.4	Kagome lattice . . . . .	92
4.3.5	Phase stabilization . . . . .	94
4.3.6	Imaging breadboard . . . . .	97
4.4	Experiment coils . . . . .	98
4.5	RF and MW setup . . . . .	102

<b>5</b>	<b>Experimental sequence</b>	<b>105</b>
5.1	MOT . . . . .	105
5.2	Molasses . . . . .	106
5.3	Magnetic trap & MW evaporation . . . . .	108
5.4	Hybrid trap . . . . .	109
5.5	Transport . . . . .	112
5.5.1	RF transfer . . . . .	114
5.6	Dipole trap . . . . .	114
5.7	Lattice . . . . .	116
5.8	Negative temperature protocol . . . . .	119
<b>6</b>	<b>Alignment and calibration</b>	<b>121</b>
6.1	Lattice beam alignment . . . . .	121
6.2	Lattice depth & phase (Kapitza-Dirac) . . . . .	122
6.3	Calibration of Feshbach coil current . . . . .	130
6.4	Trap frequency measurements . . . . .	131
<b>7</b>	<b>Kagome Mott insulators and triangular lattice negative temperatures</b>	<b>133</b>
7.1	Triangular lattice . . . . .	133
7.1.1	Superfluid to Mott insulator transition . . . . .	134
7.1.2	Preparation of negative temperature states . . . . .	137
7.2	Kagome lattice . . . . .	142
7.2.1	Superfluid to Mott insulator transition . . . . .	145
<b>8</b>	<b>Towards quantum gas microscopy for the kagome lattice</b>	<b>147</b>
8.1	Imaging transition . . . . .	148
8.2	Blue vs red-detuned lattices . . . . .	151
8.3	Imaging lattice . . . . .	151
8.4	Single-layer selection . . . . .	156
8.5	Microscope objective . . . . .	159
<b>9</b>	<b>Conclusion &amp; outlook</b>	<b>163</b>
<b>A</b>	<b>Optics glossary and red table optics layout</b>	<b>167</b>
<b>B</b>	<b>Guide star lattice</b>	<b>169</b>
<b>C</b>	<b>Lattice curvature</b>	<b>173</b>
C.1	Square lattice . . . . .	173
C.2	Triangular lattice . . . . .	175
C.3	Honeycomb lattice . . . . .	176
C.4	Kagome lattice . . . . .	177
<b>D</b>	<b>Wilson lines in the kagome lattice</b>	<b>181</b>
D.1	Honeycomb lattice . . . . .	181
D.2	Kagome lattice . . . . .	182
	<b>References</b>	<b>185</b>

---

# 1 Introduction

## 1.1 Quantum simulation

Quantum computers hold the promise of efficiently solving computational problems that would take state-of-the-art supercomputers billions of years to solve [1]. In fact, they have already been used to crack such problems [1–3] and could one day be used to help shed light onto open problems in e.g. proteomics [4], quantum chemistry [5], material development [6], and unresolved questions in the field of quantum matter [7]. In addition, quantum computers can be used to efficiently solve a variety of optimization problems [8].

In contrast to quantum computers, quantum simulators are designed with a specific model in mind and can only be used effectively for a limited and hardware-specific set of problems. Nevertheless, quantum simulation has seen enormous growth in the last 20 years owing to considerable technical advances. Quantum simulators are already capable of reaching computationally intractable regimes in a variety of different fields, including spin models [9–11] and Fermi-Hubbard physics [12] and have been used extensively to benchmark classical algorithms [13–16]. The interplay between theory and experiment has led to significant advances in both directions, such as new algorithms for classical computers [17] and the implementation of various theoretical models, such as the SSH [18], Haldane [19], Heisenberg [20], and Hofstadter [21] models.

Another factor that has contributed to the rise of quantum simulation is the continuing intractability of building a powerful quantum computer. Current gate-based quantum computers are limited to  $\sim 50$  qubits and have so far only shown quantum advantage for relatively obscure and ad hoc problems [1–3]. For powerful, universal, and error-corrected quantum computation, a fully-connected architecture of several hundreds or thousands of logical qubits is required. To implement full error-correction with currently achievable gate fidelities and coherence times, each logical qubit would have to be encoded in thousands of physical qubits [22], which increases the necessary qubit numbers to well beyond what is currently possible. It will likely take several years, if not decades, until a universal quantum computer with thousands of qubits becomes operational. However, with increasing gate fidelities, more sophisticated architectures and improved coherence times, it should only be a matter of time until powerful quantum computers are ubiquitous and analogue, model-specific, quantum simulators become obsolete.

For the foreseeable future, quantum simulators will have the upper hand in extracting useful information from complex quantum systems [16].

## 1.2 Ultracold atoms & optical lattices

With the ability to cool atomic clouds to quantum degeneracy it becomes possible to prepare ground states of model Hamiltonians and measure system properties in both real- and momentum space. A large variety of Hamiltonians have been engineered using cold atoms in optical and magnetic potentials.

Several achievements have paved the way for ultracold atoms to be at the forefront of contemporary quantum simulation. Among these are the realization of Bose-Einstein condensates (BECs) [23, 24] and quantum-degenerate Fermi gases [25]. These states of matter, in which particles obey Bose-Einstein statistics or Fermi-Dirac statistics are a crucial resource for ultracold atom-based quantum simulation. Shortly after the creation

of BECs, Feshbach resonances were observed [26, 27]. Feshbach resonances are routinely targeted to vary the inter-particle interaction strength and thus constitute another key ingredient for any versatile quantum simulator. The field of ultracold atoms has since branched out in several different directions, including the creation of molecules that host large electric dipole moments [28], quantum degenerate gases of elements with large magnetic dipole moments such as Er and Dy [29, 30] and alkaline-earth (and alkaline-earth like) atoms such as Sr and Yb that host ultra-narrow transitions that are routinely used for optical clocks [31, 32].

Optical Lattices are commonly formed by interfering at least two laser beams in such a way that the resulting intensity pattern is stationary. Ultracold atoms are influenced by this static intensity distribution via the AC Stark shift, which causes them to experience a spatially varying potential (see Fig. 1.1). In this way it is possible to implement both periodic [18, 33–37] and non-periodic [38, 39] lattices.

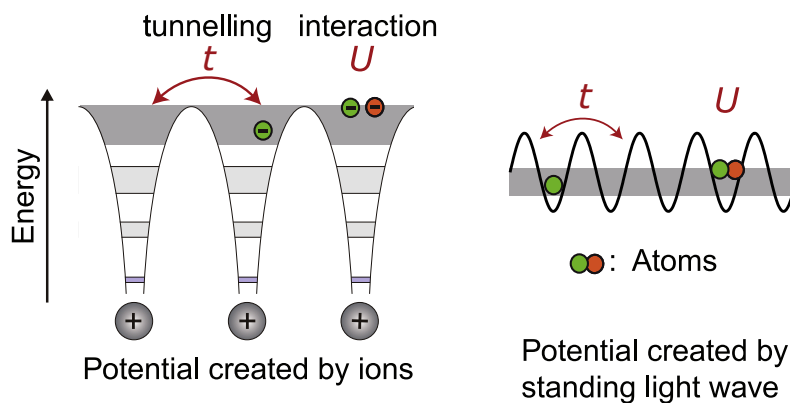


**Figure 1.1** – Analogy between solid-state ionic lattices (left) and optical lattices (right). The Hubbard parameters  $t$  and  $U$  determine the tunnelling rate and interaction strength, respectively. Figure adapted from [40].

The realization of the Mott insulator to superfluid transition with ultracold atoms in an optical lattice is often considered the paradigmatic example of quantum simulation with ultracold atoms [41]. In this experiment the tunability of the lattice potential made it possible to prepare different phases of the Bose-Hubbard model and probe the associated quantum phase transition. This experiment set the stage for the rapid development of novel, more tunable, and more complex quantum simulators [42, 43]. Among the most important developments in optical lattice-based quantum simulators for our research are the realization of bichromatic superlattices [18, 36, 44], topological Bloch bands [18, 19, 45], Floquet engineering [46, 47], negative temperatures [48], and quantum gas microscopy of bosonic [49–54] and fermionic [55–60] atoms.

In addition, a multitude of technical improvements, such as the incorporation of evolutionary algorithms and machine learning [61–64], all-optical production of BECs [65–67], and optical transport [68–70] have made quantum simulators simpler, more robust, and increased their repetition rate.

**Properties of optical lattices** The kinetic energy of quantum particles subjected to a periodic potential is governed by a band structure, which determines single-particle

behaviour. This is analogous to bands found in solid-state systems, where the location of the Fermi energy determines whether a material is conducting, semi-conducting or insulating. Thus, an optical lattice quantum simulator can be used to simulate electrons in solid-state systems. Upon introducing interactions between particles, the single-particle band structure description is insufficient and more complex models are required to describe particle dynamics. Interacting particles in a periodic potential are often described by either the Bose-Hubbard or Fermi-Hubbard models and various extensions thereof. There are a number of key differences between solid-state-based and optical lattice-based implementations of the Hubbard model.

One of the strengths of ultracold atoms in optical lattices is tunability. While the lattice geometry and lattice spacing is generally fixed for each apparatus, the lattice depth can be controlled via the lattice beam power. In addition, the dimensionality of the lattice can be changed easily by freezing out motion in unwanted directions. The tunability of the optical lattice depth along with the tunability inherent to ultracold atoms, such as the control over interactions and the ability to use both bosonic and fermionic particles, can be combined to create extremely versatile quantum simulators.

In addition, ultracold atoms are easily scalable to many tens to hundreds of thousands of particles, making it possible to access regimes that are difficult or impossible for classical algorithms to simulate. This scalability is in stark contrast to other quantum simulation platforms such as ions in ion traps, photons, and superconducting circuits [71].

Optical lattices are also inherently defect-free. Solid-state materials often suffer from imperfections and defects which can obscure signatures of effects that only occur in very pure samples, such as the fractional quantum Hall effect [72].

In the case of fermions, optical lattice quantum simulators allow us to easily change the Fermi level over a wide range by simply changing the number of atoms in a degenerate Fermi gas [73]. In solid-state systems the Fermi level can be changed in a narrow range by e.g. doping the compound [74]. However each sample has a fixed Fermi level, so changing the Fermi level in solid-state systems usually requires growing a new compound [75].

One of the most severe limitations to quantum simulation with ultracold atoms in optical lattices has been, perhaps paradoxically, that it is currently not possible to reach the low temperatures required to observe certain strongly correlated phases of matter such as spin-liquids and long-range antiferromagnetic order. In solid-state systems the temperature can be reduced to about  $1/10,000$  of the Fermi temperature ( $T_F$ ) [76], whereas for ultracold, fermionic atoms temperatures are typically on the order of  $1/10 T_F$  [77–79]. This means that ground states with small energy gaps to excited states (e.g. spin liquids) cannot be currently explored straightforwardly with optical lattice quantum simulators.

### 1.3 The kagome lattice & flat bands

The kagome lattice is a periodic lattice of corner-sharing triangles and is closely related to the triangular and honeycomb lattices (see Fig. 1.2). It occurs naturally in certain minerals such as Herbertsmithite, pyrochlores and in recently discovered vanadium-based compounds [74, 80–82]. The kagome lattice is highly geometrically frustrated and, as a result, hosts a flat motional band. These properties are expected to give rise to a number of interesting phases for both fermions and bosons. We will summarize the most relevant physics in what follows.

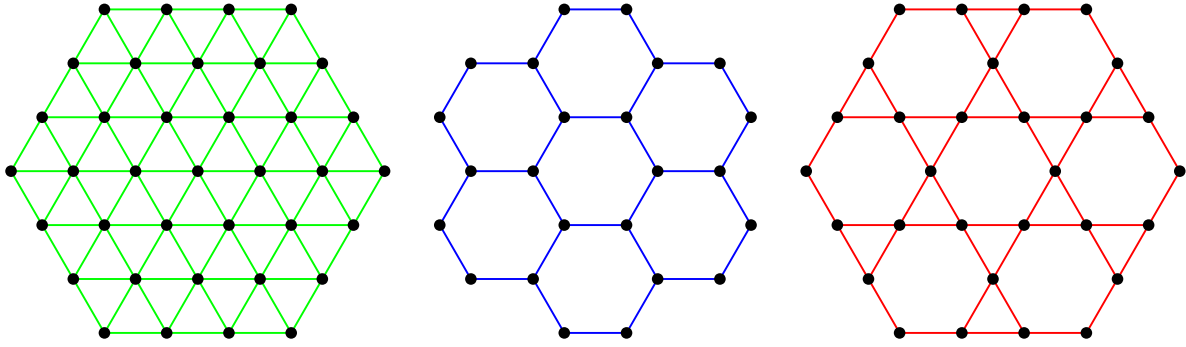


**Figure 1.2** – Left: triangular lattice, centre: honeycomb lattice, right: kagome lattice. The black points indicate lattice sites and the coloured links connect the nearest neighbours.

**Single-particle properties of flat bands** A band is called flat when all associated Bloch states have the same energy. They can arise due to geometric frustration such as in the pyrochlore lattice in 3D [83], the kagome lattice in 2D [84], and the sawtooth chain in 1D [85]. Frustration is typically associated with models of antiferromagnetically interacting spins on a lattice such as the XY model on the triangular lattice or the classical Heisenberg model on the pyrochlore lattice. In these models the ground state is degenerate since many different spin configurations minimize total magnetic energy. For antiferromagnetically interacting spins on the kagome and pyrochlore lattice, the number of degenerate ground states scales as the number of lattice sites, which causes a macroscopically degenerate, flat band to emerge.

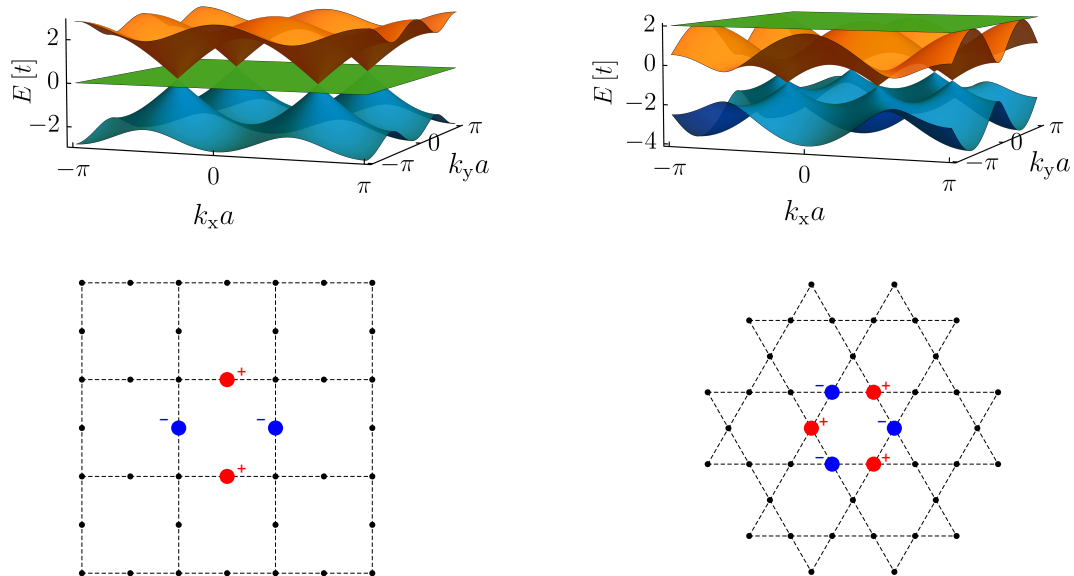


**Figure 1.3** – Top left (right): tight-binding band structure of the Lieb (kagome) lattice. The flat band in the Lieb (kagome) lattice is the second (third) of three bands. Bottom left (right): localized state of the Lieb (kagome) lattice. Red & blue signify the amplitude of the localized wave function. Localized states on the kagome lattice form hexagons.

Frustration is not limited to antiferromagnetically interacting spin systems but, as we will outline below, also affects bosonic and fermionic particles.

A unique property of flat bands is that they can be expressed in a basis of localized eigenstates. These states can be thought of as the Fourier transform of a flat (i.e. constant) band in momentum space. Fig. 1.3 shows the tight-binding dispersion relations, i.e. energy ( $E$ ) as a function of momentum ( $k_x a$  &  $k_y a$ ), and the localized states for the Lieb and kagome lattices. The localized states are constructed such that tunnelling of the wave function to neighbouring sites is cancelled due to destructive interference of the wave function with itself. As a consequence, localized states have zero group velocity ( $\mathbf{v}_g$ ) and infinite effective mass ( $m_{\text{eff}}$ ),

$$\mathbf{v}_g = \frac{1}{\hbar} \frac{\partial E(\mathbf{k})}{\partial \mathbf{k}} \rightarrow 0 \Rightarrow m_{\text{eff}} = \hbar^2 \left( \frac{\partial^2 E(\mathbf{k})}{\partial \mathbf{k}^2} \right)^{-1} \rightarrow \infty. \quad (1.1)$$

The infinite effective mass of particles in flat bands make flat band systems promising candidates for studying heavy-fermion materials, which are expected to host superconductors with high critical temperatures [86, 87].

In real systems a band will never be perfectly flat; disorder and interactions will generally cause some flat band states to have lower energy than others.

### Bosons in flat bands

**High density** A BEC forms when the phase-space density of bosons surpasses a critical value. At this critical phase-space density all available energy states are occupied and any additional atoms will occupy the ground state. The critical density can be calculated by noting that

$$\int_0^\infty f(\varepsilon) g(\varepsilon) d\varepsilon = N_{\text{therm}}, \quad (1.2)$$

where  $N_{\text{therm}}$  is the thermal atom number,  $g(\varepsilon)$  is the density of states, which is specific to each potential, and  $f(\varepsilon)$  is the thermal distribution function. The exact shape of  $g(\varepsilon)$  determines whether a BEC forms or not. If the integral diverges, which is the case for 1D and 2D free-space systems, then the critical density diverges and no BEC can form. On the other hand, in dimensions higher than two in free space or harmonic potentials in 2D, the integral is finite and BECs can form.

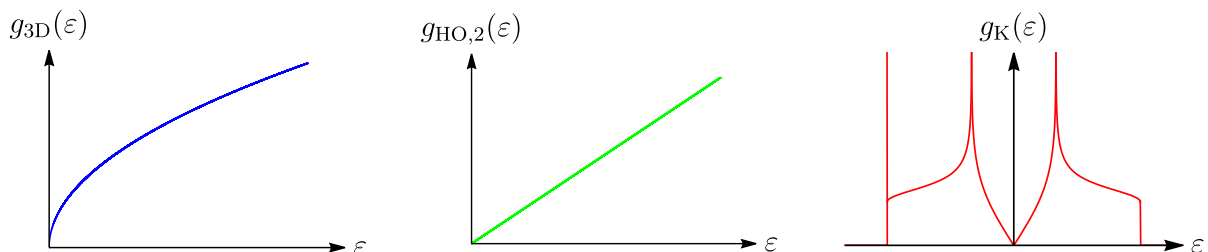


**Figure 1.4** – In free space in 3D (left) and in a 2D harmonic oscillator (centre) the integral over the product of density of states and Bose-Einstein distribution is finite. This is not the case for bosons in the flat band of the (inverted) kagome band structure (right). Note the divergence in density of states due to the flat band at the lower band edge.

In the case of a flat band, the density of states is effectively a delta-function; there are infinitely many states with the same energy, i.e. this state is macroscopically degenerate (see Fig. 1.4). If we use the single-particle dispersion relation we would therefore not expect a BEC to form in the flat band of the kagome lattice. It was however shown that bosons can condense in flat bands in the presence of interactions [88, 89]. Interactions lift the single-particle degeneracy and determine into which momentum state bosons ultimately condense. This constitutes an interaction-driven formation of a BEC, which is in stark contrast to normal BEC formation where condensation can be understood entirely from the single-particle picture.

In the mean-field approximation and for strong repulsive interactions, the Bose-Hubbard (BH) model,

$$\hat{H}_{\text{BH}} = -t \sum_{\langle i,j \rangle} (\hat{a}_i^\dagger \hat{a}_j + \text{h.c.}) + \frac{U}{2} \sum_i \hat{n}_i (\hat{n}_i - 1), \quad (1.3)$$

where  $t$  and  $U > 0$  are the tunnelling energy and interaction energy, respectively, maps onto the classical XY model,

$$\hat{H}_{\text{BH, MF}} \approx -tn \sum_{\langle i,j \rangle} \cos(\phi_i - \phi_j). \quad (1.4)$$

Here,  $n$  is the mean particle number per site and  $\phi_i$  is the mean-field wave function's phase on site  $i$ . In the classical XY model, the phase  $\phi_i$  encodes the orientation of a 2D spin on site  $i$  (see Fig. 1.5).

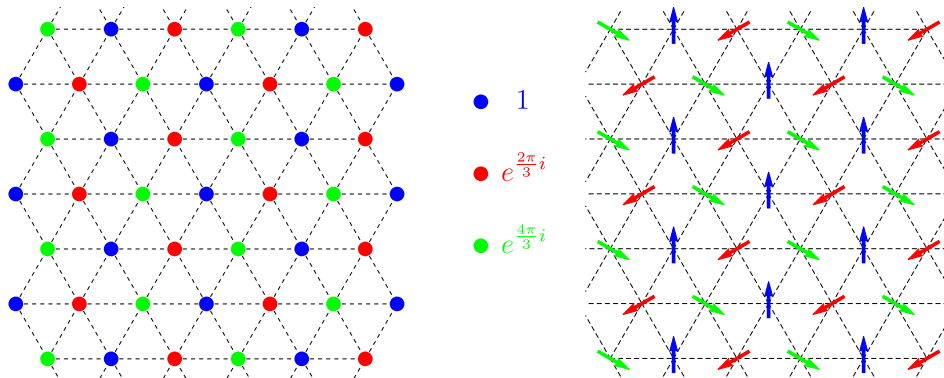


**Figure 1.5** – Equivalence of frustrated, mean-field BH model with repulsive interactions (left) and classical XY model (right) on the triangular lattice. The in-plane vector orientation in the XY model is mapped onto the phase of the superfluid wave function.

For  $t > 0$ , the BH model is therefore equivalent to a ferromagnetic XY model and the lowest energy state has equal phase (spin orientation) on each site. This in turn corresponds to the  $\mathbf{q} = 0$  Bloch state. For  $t < 0$ , the mean-field BH model is equivalent to the antiferromagnetic XY model. In this case the phases (spins) on each site are not equal and the lowest energy state is at some point other than  $\mathbf{q} = 0$ . This mapping between mean-field BH model and classical XY model can be used to simulate the classical XY model on frustrated lattices, such as the triangular [90] and kagome [88, 91] lattices, with ultracold atoms.

Studying the antiferromagnetic XY model with bosons requires inverting the tunnelling term of the BH model. This can be done by e.g. Floquet shaking [46, 47, 92] or negative temperatures [48, 93]. In our experiment we aim to create negative temperatures to study frustrated bosonic phases in the triangular and kagome lattices. The distinctive phase pattern of frustrated superfluids manifests itself in the momentum distribution of the wave function, which can be directly probed with our machine.

**Low density** Below a certain density, localized hexagon states (see Fig. 1.3) constitute an exact ground state of repulsively interacting particles (or atoms) in a flat band. As the density is increased, atoms fill up more and more hexagon states until a critical atom number of  $N_c = \frac{1}{9}N$  is reached, where  $N$  is the number of lattice sites. At the critical density, the atoms are closely packed and form a charge-density wave (CDW), but the system does not contain any interaction energy since the atomic wave functions do not overlap (see Fig. 1.6) [83]. Any increase in density above the critical density will invariably come at the cost of some kinetic or interaction energy. In [84] it was shown that an increase in density will not immediately destroy the CDW, but rather cause condensation into interstitial sites of the CDW, i.e. superfluid order emerges. A system that displays both superfluid and CDW order is commonly referred to as being supersolid [94–96]. Superfluid order breaks the continuous U(1) symmetry associated with the condensate phase, and CDW order breaks a discrete or continuous translational symmetry. In the case of the kagome lattice supersolid, the CDW is imposed by the lattice and a discrete translational symmetry (in this case  $\mathbb{Z}_3$ ) is broken. This is in contrast to supersolid formation in the bulk where a continuous translational symmetry is broken [96].

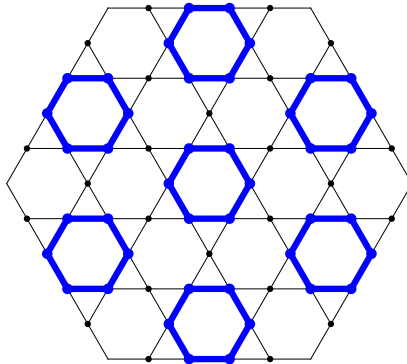


**Figure 1.6** – Close packing of repulsively interacting bosons in the flat band of the kagome lattice. Each hexagon state (shown in blue) contains one boson with a phase pattern as shown in Fig. 1.3. The CDW state breaks  $\mathbb{Z}_3$  symmetry since two other tight-packing configurations can be constructed. It can thus be seen as the bosonic analogue of a Wigner crystal [97].

**Fermions in flat bands** Fermionic physics in the kagome lattice has received considerable attention for a variety of reasons. Flat bands give rise to high-temperature superconductivity [98] and are integral to the fractional quantum Hall effect [99, 100]. Furthermore, the Fermi-Hubbard model maps onto the antiferromagnetic Heisenberg model at half-filling and strong repulsive interactions [83, 101]. The ground state of the HAFM on the kagome lattice is predicted to be a quantum spin-liquid [102, 103].

**BCS theory** Fermions in flat bands can be treated with BCS theory, which predicts that the superconducting pairing gap should scale linearly with the interaction strength in systems with a diverging density of states [104–106]. This behaviour is in stark contrast to conventional superconductors for which the pairing gap and, consequently, the critical temperature, only scales as  $e^{-\frac{1}{U\rho(E_F)}}$ , where  $U$  is the inter-particle interaction strength and  $\rho(E_F)$  is the density of states at the Fermi level [105, 107]. Thus, flat band materials hold the promise of displaying high- $T_c$  superconductivity. Recently, it was shown that magic-angle bilayer graphene can host a flat band and indeed becomes superconducting at a remarkably high temperature<sup>1</sup> when the Fermi energy is tuned to lie within the flat band [76]. Open questions include the exact pairing mechanism and what the limits are to the pairing gap’s scaling with density of states and interaction strength [108, 109].

**Fractional Chern insulators** In the years since the discovery of the fractional quantum Hall effect (FQHE) many theoretical proposals suggested that FQH physics and Laughlin states could emerge in systems other than the 2D electron gas [110–113]. FQH states are highly entangled many-body wave functions and are extremely hard to simulate classically [114], making it desirable to have a dedicated quantum simulator for FQH physics. A recent experimental highlight was the creation of Laughlin states made of light [100]. While this was the first implementation of Laughlin states beyond 2D electron gases, the number of involved particles was limited to two, whereas in 2D electron gases the Laughlin state is composed of several million electrons [115]. Cold atom-based quantum simulators could act as an intermediate platform that could host Laughlin states composed of several hundreds or thousands of particles. To this end, fractional Chern insulators (FCIs) have been proposed as a way to observe Laughlin states in optical lattice quantum simulators [110, 116].

FQH physics requires four basic ingredients.

Firstly, a FQH system needs to display macroscopic degeneracy. For a 2D electron gas in a strong magnetic field this condition is naturally fulfilled by Landau levels. In FCIs this condition can be met by invoking flat-band models [111] such as the Lieb [116] and kagome [110] lattice.

Second, the flat band needs to be topologically non-trivial. An external magnetic field, such as that needed to create degenerate Landau levels, additionally breaks time-reversal symmetry (TRS) and leads to Landau levels acquiring a non-trivial topological invariant and, consequently, a quantized Hall conductance. Optical lattice quantum simulators use neutral atoms, which, in contrast to electrons, do not pick up an Aharonov-Bohm phase in the presence of an external magnetic field. Fortunately, it is still possible to break TRS and thus create topologically non-trivial bands by inducing complex next-to-nearest neighbour (NNN) tunnelling [110, 116, 117] (see Fig. 1.7). Experimentally, complex NNN tunnelling can be induced in optical lattices via Floquet shaking [19, 64], resulting in dispersive bands with non-zero Chern number. The same technique could be used to create topological flat bands [118].

---

<sup>1</sup>High when expressed in units of  $T_F$ , but still only on the order of a few kelvin.

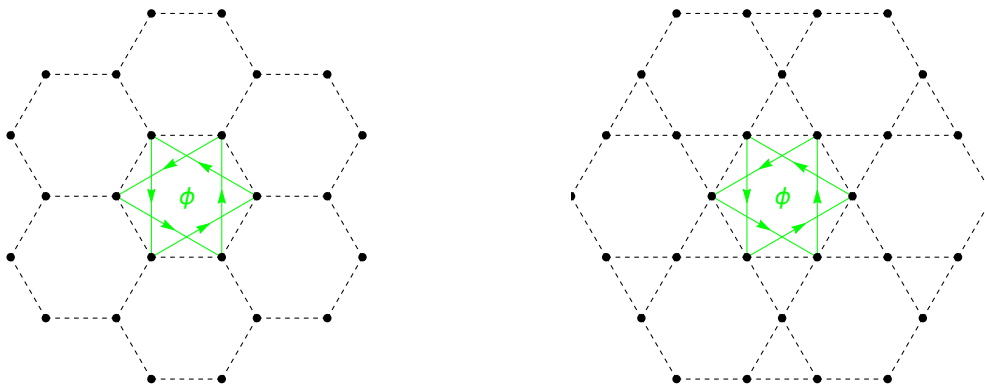


**Figure 1.7** – In the Haldane model [117] (left), complex next-to-nearest neighbour tunnelling (green arrows) breaks time-reversal symmetry. Nearest-neighbour tunnelling is real and is indicated by dashed lines between lattice sites (black dots). A particle moving counterclockwise around a hexagon picks up a phase  $\phi$ . Right: creating a nearly flat topological band on the kagome lattice. Dashed lines, dots and green arrows are equivalent to the left plot.

Third, the inter-particle interaction has to be much larger than the band width while simultaneously being much smaller than the band gap to higher bands. In the 2D electron gas, this can be achieved by increasing the external magnetic field which increases the gap between the lowest Landau level and higher Landau levels. For cold atoms in optical lattices both the interaction strength as well as the band gap can be controlled independently making it possible to find regimes in which  $\Delta \gg U \gg \text{BW}$  [99].

Finally, it is necessary to be able to fine-tune the particle number or the degeneracy of the topological flat band. This is easily achieved in 2D electron gases since the lowest Landau level degeneracy is proportional to the external magnetic field which can be easily and accurately tuned. For cold atoms the total atom number can be tuned but it is difficult to accurately prepare a precise atom number. However, recent technical innovations, such as potential shaping with digital micromirror devices might make it possible to overcome this limitation.

**Kagome Heisenberg antiferromagnet** To finish the introduction to kagome lattice physics we will briefly outline perhaps the most studied aspect of the kagome lattice: frustrated quantum magnetism. We briefly discussed previously how the repulsively interacting Bose-Hubbard model can be mapped onto the classical XY model. In a similar manner, the Fermi-Hubbard model can be mapped onto the antiferromagnetic Heisenberg model (HAFM). In the regime of a balanced two-component Fermi mixture and strong repulsive interactions, the site-occupation of individual fermions maps directly onto spin in the Heisenberg model [101]. The Fermi-Hubbard model is commonly written as

$$\hat{H}_{\text{FH}} = -t \sum_{\langle i,j \rangle, \alpha} (\hat{c}_{i,\alpha}^\dagger \hat{c}_{j,\alpha} + \text{h.c.}) + \frac{U}{2} \sum_i \hat{n}_{i,\uparrow} \hat{n}_{i,\downarrow}, \quad (1.5)$$

where  $\alpha \in \{\uparrow, \downarrow\}$  labels the fermion flavour. In ultracold atom quantum simulators, different spins are commonly encoded in different hyperfine states [20, 119, 120]. For

strong repulsive interactions double occupancies are suppressed and the system will turn into a  $n=1$  Mott insulator. The Fermi-Hubbard model can then be rewritten as

$$\hat{H}_{\text{HB}} = J \sum_{\langle i,j \rangle} \hat{\mathbf{S}}_i \cdot \hat{\mathbf{S}}_j, \quad (1.6)$$

where  $J = \frac{4t^2}{U}$ ,  $\hat{\mathbf{S}}_i = \sum_{\alpha,\beta} \hat{c}_{i,\alpha}^\dagger \boldsymbol{\sigma}_{\alpha,\beta} \hat{c}_{i,\beta}$ , and  $\boldsymbol{\sigma} = (\sigma_x, \sigma_y, \sigma_z)^T$  is the Pauli vector [101]. Note that the prefactor to Eq. 1.6 is positive, i.e. the spin-exchange interactions are antiferromagnetic.

The Heisenberg model was recently realized with ultracold fermions in a square optical lattice [20], but has so far not been realized on frustrated lattices such as the triangular or kagome lattices.

The Heisenberg Hamiltonian (Eq. 1.6) on the triangular and kagome lattices can be rewritten as a sum over triangular plaquettes ( $\Delta$ ) [121],

$$\begin{aligned} \hat{H}_{\text{HB}} &= \frac{J}{2} \sum_{\Delta} \hat{\mathbf{S}}_{\Delta,1} \cdot \hat{\mathbf{S}}_{\Delta,2} + \hat{\mathbf{S}}_{\Delta,2} \cdot \hat{\mathbf{S}}_{\Delta,3} + \hat{\mathbf{S}}_{\Delta,3} \cdot \hat{\mathbf{S}}_{\Delta,1} \\ &= \frac{J}{4} \sum_{\Delta} \left( \hat{\mathbf{S}}_{\Delta,1} + \hat{\mathbf{S}}_{\Delta,2} + \hat{\mathbf{S}}_{\Delta,3} \right)^2 + \text{const.} \end{aligned} \quad (1.7)$$

It is easy to see from this expression that the ground state must satisfy

$$\hat{\mathbf{S}}_{\Delta,1} + \hat{\mathbf{S}}_{\Delta,2} + \hat{\mathbf{S}}_{\Delta,3} = 0. \quad (1.8)$$

In the triangular lattice case, this equation imposes three constraints on six degrees of freedom (two for each spin), meaning that the ground state has  $\text{SO}(3)$  symmetry. Intuitively this can be thought of as the freedom to simultaneously rotate all spins along the three principal axes in 3D (Eq. 1.8 remains fulfilled if the three spins are rotated simultaneously) [121].

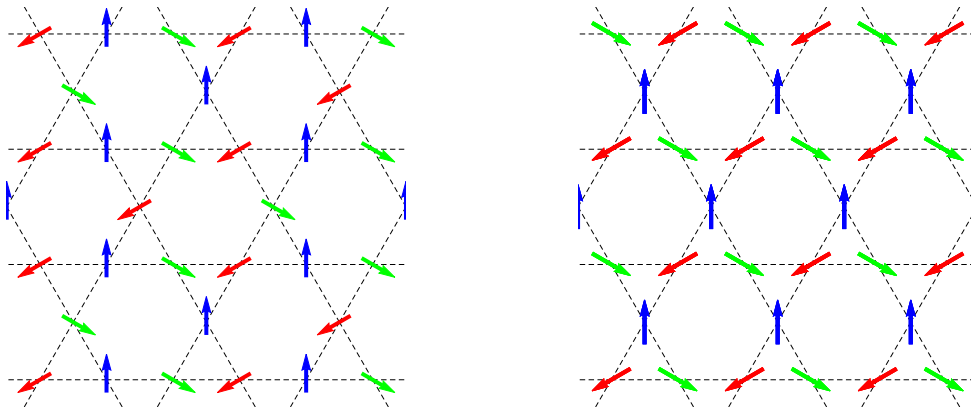


**Figure 1.8** – Two different spin configurations on the kagome lattice that obey Eq. 1.8. Left:  $\sqrt{3} \times \sqrt{3}$  spin configuration that is allowed also on the triangular lattice [122, 123]. Right:  $\mathbf{q} = 0$  spin configuration that is forbidden on the triangular lattice (hexagons cannot be filled with appropriate spin.) [122, 123].

Since each triangle in the triangular lattice shares two sites with a neighbouring triangle, any increase in the lattice size will not increase the degrees of freedom of the ground state. The spins on a single triangle determine the spins on the entire lattice (see Fig. 1.5). The kagome lattice is composed of corner-sharing triangles instead of edge-sharing triangles. This means that the spin distribution is not fixed by a single triangle and that the ground state degeneracy increases as the system size increases. The number of degrees of freedom in the ground state of the kagome lattice is thus comparable to the total number of degrees of freedom.

The Heisenberg model allows for the formation of spin singlets which is classically forbidden. It can be shown that the formation of spin singlets in the HAFM can lower the ground state energy with respect to the classical Néel order [124]. Spin singlets also lead to an overall reduction of the staggered magnetization.[20, 123, 125, 126].

The HAFM on the triangular and kagome lattices has been extensively studied [102, 123, 124, 127–129], the main focus being the calculation of ground state energies and staggered magnetization and the gap between ground state and first excited state. Numerical simulations have revealed that the triangular lattice displays a finite (non-zero) staggered magnetization in its ground state [127]. The ground state of the kagome lattice HAFM however has proven to be a hard problem to crack. No consensus has emerged on whether the ground state of the kagome lattice HAFM displays magnetic order, or whether it is gapped or gapless. Numerical and experimental observations indicate that the ground state staggered magnetization is strongly suppressed and that the energy gap between ground and first excited state (if there is one) is much smaller than the spin-exchange energy [129].

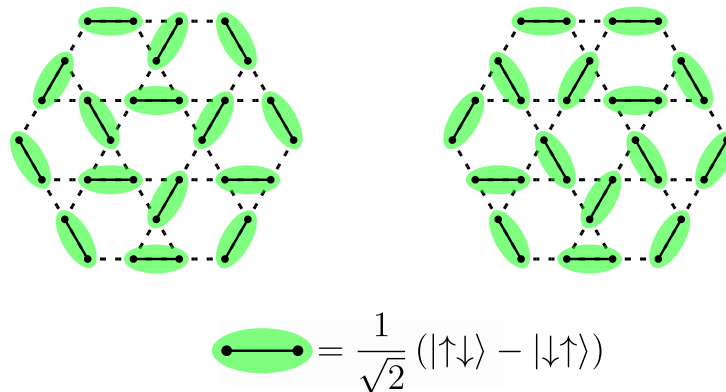


**Figure 1.9** – Two distinct valence bond tilings on the kagome lattice. The ground state of the kagome HAFM is predicted to be a superposition of many different configurations of singlet-tilings [130].

P. W. Anderson argued in 1972 that a resonating valence bond (RVB) state should have a lower energy than a classical Néel ordered state on a triangular lattice [124]. The RVB state is a macroscopic superposition of different singlet tilings (see Fig. 1.9) and has a number of fascinating properties. Firstly, since each spin forms a singlet state with another spin, the net staggered magnetization is zero, i.e. there is no spontaneous symmetry breaking at  $T=0$  and no long-range order even in the ground state. This property matches quite well with what is observed numerically in the kagome lattice [131]. Furthermore, the RVB state is a quantum liquid, often referred to as a spin liquid,

since singlet states can propagate freely in the lattice. The RVB state, just as the Laughlin and BCS states, thus presents us with another example of a quantum fluid of fermions. RVB states were shown to have non-local topological order [132, 133] and present a promising platform for topological quantum computing [134]. Very recently, experiments with optical tweezer arrays have explored the RVB state on the kagome lattice [11].

## 1.4 Quantum simulation with an optical kagome lattice

Having outlined various kagome and flat-band specific physics, it is worth mentioning existing quantum simulators for the kagome lattice. The optical kagome lattice is technically very demanding as it requires a minimum of six lattice beams and active lattice phase stabilization [36]<sup>2</sup>. An optical kagome lattice was first implemented in Berkeley in 2012 [36]. Many fascinating experiments have been conducted with <sup>87</sup>Rb on this machine to date, including the realization of the Mott insulator to superfluid transition in a kagome lattice [137], trimerized kagome lattice physics [138], and population of the flat band via transport in momentum space [139]. However, several regimes of kagome physics have so far not been explored. First and foremost is the exploration of flat-band physics in thermodynamic equilibrium. Secondly, <sup>87</sup>Rb lacks broad Feshbach resonances preventing complete control of interaction strength. Finally, the Berkeley machine is restricted to bosonic physics only. Any of the aforementioned fermionic flat band physics is thus currently out of reach. The machine that was built in the course of my PhD is the second optical kagome lattice machine. We incorporated a number of features that we think will allow us to explore physics beyond what the Berkeley machine can do. This includes the possibility of loading both bosonic <sup>39</sup>K and fermionic <sup>40</sup>K into the lattice which both have broad Feshbach resonances. Tunable interactions allow for negative temperatures, which in turn give us access to flat band physics in thermal equilibrium. In addition, we are working towards implementing a quantum gas microscope. With a quantum gas microscope, we can measure local observables, such as density and spin correlations, and directly measure CDW order in a bosonic Wigner crystal and magnetic properties of fermions in the kagome lattice at low temperatures.

As of writing, our machine is reliably creating superfluids and Mott insulators of <sup>87</sup>Rb and <sup>39</sup>K in the optical kagome lattice and can create robust population inversion via negative temperatures in the optical triangular lattice. Negative temperatures in triangular lattices have not been achieved before and are interesting in their own right. However, our immediate aim is to use negative temperatures to populate the flat band of the kagome lattice with <sup>39</sup>K. This will open up the world of bosonic flat band physics.

## 1.5 Thesis outline

This thesis gives a detailed account of machine design and operation, and our progress towards simulating bosonic flat band physics.

Chapter 2 covers various kagome-related theory, including how to create optical triangular, honeycomb, and kagome lattices and the numerical calculation of their band structures. Furthermore, we discuss using a band-projected position operator approach to

---

<sup>2</sup>Other proposals for creating an optical kagome lattice exist but are even more demanding from a technical point of view [135, 136].

calculate maximally localized Wannier states on the triangular, honeycomb, and kagome lattices, which we use to calculate Hubbard parameters.

We move on to discuss the theory of negative temperatures and of bosons in the flat band of the kagome lattice in chapter 3. The focus will be primarily on the mean-field properties at high densities and the transition from charge-density wave to supersolid at low densities.

Chapter 4 gives an in-depth, technical description of the kagome machine. We introduce our vacuum system and describe the various optical setups for cooling and trapping  $^{39}\text{K}$ ,  $^{40}\text{K}$  and  $^{87}\text{Rb}$ , and to create the optical lattices.

In chapters 5 and 6 we detail the experimental sequence and give details on machine calibration and operation.

Chapter 7 summarizes preliminary data taken with our machine. We will focus on the analysis of the superfluid to Mott insulator transition in the triangular and kagome lattices, and present data showing negative temperatures in the triangular lattice.

In chapter 8 we discuss our progress towards implementing a quantum gas microscope for the kagome lattice. We will outline several design choices we made and introduce a novel super-resolution technique that should allow for single-site resolved fluorescence imaging.

Finally, chapter 9 gives a brief summary and discusses ongoing and future developments in the kagome lab.

This thesis as well as Dan Reed's thesis [140] are the first PhD theses to come out of this experiment. A lot of the experimental details, such as the machine design and experimental sequence, are similar between our theses, reflecting the fact that we both contributed extensively and worked together closely. Though our work overlapped significantly, we cover different aspects of the kagome experiment in our theses. While Dan's thesis contains a detailed description of our phase detection and locking scheme, and shows detailed measurements of the phase stabilization performance, my thesis is more geared towards calculating properties of the kagome lattice and unravelling the physics of bosons in flat bands with the aim of guiding near-term experiments. We made an effort to reference the other thesis if a more in-depth description is provided.

**Acknowledgements** To begin, I want to thank Dan Reed for his dedication, hard work and consummate professionalism. Over the last four and half years, I have not seen any other person as much as I have Dan and I am grateful that we became good friends. His can-do attitude and readiness to fix broken equipment, with no regard for whether we are technically qualified to do so, has saved us countless weeks of down-time. His understanding of electronics, mechanical engineering and optics far exceeds mine and I consider myself fortunate to have had a partner with his set of skills. We began as humble Master's students and together embarked on a journey into the unknown. We set out on a path of glory, assembled our army (of optics), forged our weapons of steel (the vacuum chamber), created the one ring (the monolithic mount) and laid siege to the gates of knowledge (the kagome lattice). Neither sloth nor plague could stop us in our divine quest. When at last we broke through (via active phase stabilization), we found a land of plenty (of physics to do). Though we must now leave this veritable paradise of new discoveries, we shall have given our comrades a golden opportunity to flourish. It is through them that our hopes and dreams (papers) may be redeemed.

I would also like to thank Tiffany Harte for her many contributions to the kagome machine, including the extremely reliable TAs, the microscope objective and her help in designing and running the machine. Thanks also to Luca Donini, who contributed greatly to machine development, such as with the complicated lattice optics and the interferometric measurements of the objective, as well as applying his exceptional programming and IT skills to sequence writing, debugging and machine operation. Many thanks also to Pob Shanokprasith for his dedication and diligence, for working long hours with me (even over Christmas!) and who, to my delight, fixed numerous small and annoying bugs that we became accustomed to ignoring. We leave our machine in the capable hands of Luca, Pob, Dan Braund and Mehedi Hasan, who have proven their dedication and skill. While the machine is already running smoothly, I have no doubt that they will take the machine's capabilities to another level. A big thank you also to Ulrich Schneider, who has been a steadfast and capable team leader and I am grateful to him for trusting us to build a machine as ambitious as the kagome machine.

Thanks to the early members of the QC team (Konrad Viebahn, Matteo Sbroscia & Ed Carter) for their willingness to answer questions when we designed our machine, and the current members (Jr-Chiun Yu, Bo Song, Shaurya Bhawe & Lee Reeve) for discussions about getting our sequences to work. I would also like to thank members of Zoran's group, including Lena Dogra, Nishant Dogra, Chris Eigen and Panos Christodoulou for fruitful discussions and for sharing their equipment with us.

We received a lot of help from Cavendish facilities and the Cavendish mechanical and electronics workshops. I thank Alan Turner for putting up with our nagging and getting our lab infrastructure up to shape and Gary Large for efficiently organizing the manufacture of the several hundred components we received from the mechanical workshop over the years. I would also like to thank Kevin Mott in the student workshop for his guidance and patience whenever we were using the machines. I am also grateful to Dr. Stephen Topliss for providing us with the bulk of our electronics.

We also had significant contributions from several Master's students, including Damien Bloch, who designed our exceptionally robust optical transport, Vanessa Koh, who helped design our (also exceptionally robust) phase stabilization, and Xintong Su, who helped optimize our transport sequences.

A special thanks to Pob, Tiffany, Matteo, Luca, Mehedi, Nishant, Dan (B.) and Ulrich for proof-reading chapters of my thesis.

Finally I would also like to thank my family and friends for their unwavering support and love.

## 2 The optical kagome lattice

The interference of two or more laser beams creates an optical lattice, a stationary pattern of peaks and troughs in light intensity. Depending on the wavelength of the lasers forming the optical lattice, neutral atoms will feel, via the AC Stark shift, either an attractive force towards, or a repulsive force away from regions of high intensity. Typical lattice depths are on the order of  $1 \mu\text{K}$ - $100 \mu\text{K}$ . Thus, in order for optical lattices to have any appreciable effect, neutral atoms need to be cooled to ultracold temperatures via e.g. a magneto-optical trap and subsequent evaporative cooling. The theory of the AC Stark shift is well-established [141]. We will therefore forgo a detailed theoretical derivation and instead focus on the implementation of the optical kagome lattice instead. We will start by discussing how to implement an optical triangular lattice.

### 2.1 Optical triangular lattice

There are two basic ways to implement a triangular lattice with three beams. In the following section both schemes are introduced and their differences in various lattice parameters are discussed.

#### 2.1.1 Interfering lattice

In the interfering lattice implementation, three beams are polarized in-plane and enclose an angle of  $120^\circ$  with respect to each other (see Fig. 2.1).

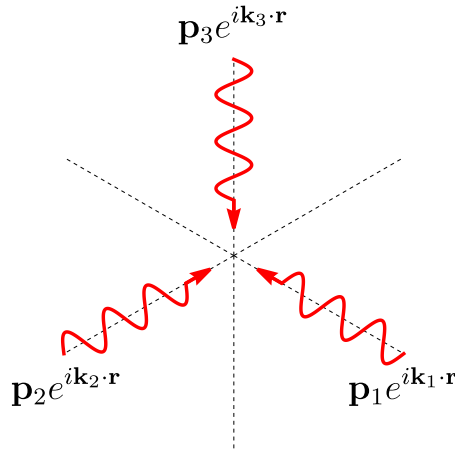


**Figure 2.1** – Layout of the lattice beams for an interfering triangular lattice.

The time-averaged intensity distribution can be written as

$$I(\mathbf{r}) = \frac{c\epsilon_0}{2} |\mathbf{E}_{\text{tot}}(\mathbf{r})|^2 = I_0 \left| \sum_{j=1}^3 \mathbf{p}_j e^{i\mathbf{k}_j \cdot \mathbf{r}} \right|^2, \quad (2.1)$$

where  $I_0$  is the intensity of each lattice beam and

$$\mathbf{k}_1 = \frac{k}{2} \begin{pmatrix} -\sqrt{3} \\ 1 \end{pmatrix}, \quad \mathbf{k}_2 = \frac{k}{2} \begin{pmatrix} \sqrt{3} \\ 1 \end{pmatrix}, \quad \mathbf{k}_3 = k \begin{pmatrix} 0 \\ -1 \end{pmatrix}, \quad (2.2)$$

$$k = |\mathbf{k}_1| = |\mathbf{k}_2| = |\mathbf{k}_3|$$

are the corresponding wavevectors<sup>3</sup>.  $\mathbf{p}_j$  are the lattice beam polarizations. They are normalized and obey  $\mathbf{p}_j \cdot \mathbf{k}_j = 0$ . Eq. 2.1 can be rewritten as

$$\begin{aligned} I(\mathbf{r}) &= I_0 \left\{ 3 - \cos(-\sqrt{3}kx) - \cos\left(\frac{k}{2}(\sqrt{3}x - 3y)\right) - \cos\left(\frac{k}{2}(\sqrt{3}x + 3y)\right) \right\} \\ &= 2I_0 \sum_{j=1}^3 \cos^2(\boldsymbol{\kappa}_j \cdot \mathbf{r} - \frac{\pi}{2}), \end{aligned} \quad (2.3)$$

where

$$\begin{pmatrix} \boldsymbol{\kappa}_1 \\ \boldsymbol{\kappa}_2 \\ \boldsymbol{\kappa}_3 \end{pmatrix} = \frac{1}{2} \begin{pmatrix} 1 & -1 & 0 \\ -1 & 0 & 1 \\ 0 & 1 & -1 \end{pmatrix} \begin{pmatrix} \mathbf{k}_1 \\ \mathbf{k}_2 \\ \mathbf{k}_3 \end{pmatrix}. \quad (2.4)$$

The second line of Eq. 2.3 gives an explicit link to the retro-reflected implementation of a triangular lattice, which is discussed later in this chapter. Note that the intensity minima form a triangular lattice, while the intensity maxima form a honeycomb lattice.

We now introduce individual phases for each lattice beam,

$$\begin{aligned} I(\mathbf{r}) &= I_0 \left| \sum_{j=1}^3 \mathbf{p}_j e^{i\mathbf{k}_j \cdot \mathbf{r} + i\phi_j} \right|^2 \\ &= I_0 \left\{ 3 - \cos(-\sqrt{3}kx + \phi_1 - \phi_2) - \cos\left(\frac{k}{2}(\sqrt{3}x - 3y) + \phi_3 - \phi_1\right) \right. \\ &\quad \left. - \cos\left(\frac{k}{2}(\sqrt{3}x + 3y) + \phi_2 - \phi_3\right) \right\} \\ &= 2I_0 \sum_{j=1}^3 \cos^2(\boldsymbol{\kappa}_j \cdot \mathbf{r} + \Phi_j - \frac{\pi}{2}), \end{aligned} \quad (2.5)$$

where

$$\begin{pmatrix} \Phi_1 \\ \Phi_2 \\ \Phi_3 \end{pmatrix} = \frac{1}{2} \begin{pmatrix} 1 & -1 & 0 \\ -1 & 0 & 1 \\ 0 & 1 & -1 \end{pmatrix} \begin{pmatrix} \phi_1 \\ \phi_2 \\ \phi_3 \end{pmatrix}. \quad (2.6)$$

---

<sup>3</sup>Note that we chose these particular lattice vectors because they correspond to the orientation of our experimental images. The lattice beam labels are also how we label the lattices in our machine hardware and software.

The above equation shows that there are two phase degrees of freedom. In particular, if  $\phi_1 - \phi_2$  and  $\phi_3 - \phi_1$  are fixed, then  $\phi_2 - \phi_3 = -(\phi_3 - \phi_1) - (\phi_1 - \phi_2)$  is fixed as well. We can rewrite the phase degrees of freedom as positional degrees of freedom by solving the following equation for  $x_0$  and  $y_0$  in terms of  $\phi_1$ ,  $\phi_2$  &  $\phi_3$ ,

$$\begin{aligned}
& I_0 \left\{ 3 - \cos \left( -\sqrt{3}kx + \phi_1 - \phi_2 \right) - \cos \left( \frac{k}{2} \left( \sqrt{3}x - 3y \right) + \phi_3 - \phi_1 \right) \right. \\
& \quad \left. - \cos \left( \frac{k}{2} \left( \sqrt{3}x + 3y \right) + \phi_2 - \phi_3 \right) \right\} \\
& \stackrel{!}{=} I_0 \left\{ 3 - \cos \left( -\sqrt{3}k(x - x_0) \right) - \cos \left( \frac{k}{2} \left( \sqrt{3}(x - x_0) - 3(y - y_0) \right) \right) \right. \\
& \quad \left. - \cos \left( \frac{k}{2} \left( \sqrt{3}(x - x_0) + 3(y - y_0) \right) \right) \right\}.
\end{aligned} \tag{2.7}$$

This results in  $x_0 = \frac{1}{\sqrt{3}k}(\phi_1 - \phi_2)$  and  $y_0 = \frac{1}{3k}(-\phi_1 - \phi_2 + 2\phi_3)$ .

Any change in one of the three lattice beam phases thus results in a translation of the lattice. The shape of the lattice potential stays the same regardless of the lattice beam phases.

In general we will assume that the intensities of all three beams are equal so that we get an undistorted triangular lattice. For completeness, we want to briefly discuss the case in which the three lattice intensities are not equal, which is the most general case. The total potential of an interfering lattice with beam-specific phases and intensities can be written as

$$\begin{aligned}
I(\mathbf{r}) &= \left| \sum_{j=1}^3 \sqrt{I_j} \mathbf{p}_j e^{i\mathbf{k}_j \cdot \mathbf{r} + i\phi_j} \right|^2 \\
&= \left( I_1 + I_2 + I_3 - \sqrt{I_1 I_2} \cos \left( -\sqrt{3}kx + \phi_1 - \phi_2 \right) \right. \\
& \quad \left. - \sqrt{I_1 I_3} \cos \left( \frac{k}{2} \left( \sqrt{3}x - 3y \right) + \phi_3 - \phi_1 \right) \right. \\
& \quad \left. - \sqrt{I_2 I_3} \cos \left( \frac{k}{2} \left( \sqrt{3}x + 3y \right) + \phi_2 - \phi_3 \right) \right) \\
&= I_{\text{off}} + 2 \sum_{j=1}^3 \mathcal{I}_j \cos^2 \left( \mathbf{k}_j \cdot \mathbf{r} + \Phi_j - \frac{\pi}{2} \right),
\end{aligned} \tag{2.8}$$

where

$$\begin{aligned}
\mathcal{I}_1 &= \sqrt{I_1 I_2}, & \mathcal{I}_2 &= \sqrt{I_1 I_3}, & \mathcal{I}_3 &= \sqrt{I_2 I_3}, \\
I_{\text{off}} &= \sum_j (I_j - \mathcal{I}_j).
\end{aligned} \tag{2.9}$$

Note that  $I_{\text{off}}$  is constant and thus can be omitted when calculating the potential energy.

A second way to implement a triangular lattice with three beams is by overlapping three 1D-lattices in a  $120^\circ$  configuration (see Fig. 2.2).

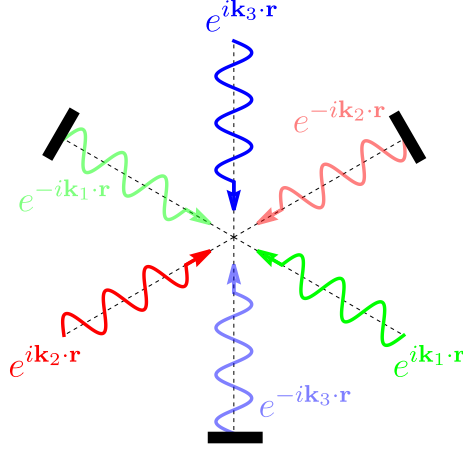


**Figure 2.2** – Layout of the lattice beams for a retro-reflected triangular lattice. Note that each beam only interferes with its retro-reflected counterpart. Thus the polarization of each beam is irrelevant as long as it is linear. To avoid interference between different lattice beams, the frequencies can be shifted by a small amount with respect to each other. Here, different colours correspond to different frequencies<sup>4</sup>.

1D lattices are commonly implemented by retro-reflecting a laser beam,

$$I_{1D}(x) = I_0 |e^{ikx} + e^{-ikx+i\phi}|^2 = 4I_0 \cos^2 \left( kx - \frac{\phi}{2} \right). \quad (2.10)$$

The potential for a 1D retro-reflected lattice thus reduces to a  $\cos^2$  function. The phase  $\phi$  can be controlled via the laser frequency or via the position of the retro-reflecting mirror. The retro-reflected triangular lattice can be written as

$$I(\mathbf{r}) = 4I_0 \sum_{j=1}^3 \cos^2 \left( \mathbf{k}_j \cdot \mathbf{r} - \frac{\pi}{2} \right). \quad (2.11)$$

Comparing this expression to Eq. 2.3 reveals that the retro-reflected lattice is rotated by  $90^\circ$  with respect to the interfering lattice and has a smaller lattice spacing. Additionally, the lattice depth is twice as large in the retro-reflected case for the same lattice beam intensity. Practically speaking, a triangular lattice formed of three interfering (retro-reflected) 532 nm lattice beams will have a lattice spacing of 354.7 nm (307.2 nm)<sup>5</sup>. This mapping between retro-reflected and interfering implementations of the triangular lattice allows us to calculate lattice-specific quantities such as band widths, tunnelling rates, and on-site interaction strengths, for e.g. only the retro-reflected lattice. If we want to calculate the lattice-specific quantities for an interfering lattice, we then just have to use the results obtained for the retro-reflected implementation and redefine the recoil

<sup>4</sup>In practice, the fractional frequency difference between lattice beams is on the order of  $4 \times 10^{-7}$ .

<sup>5</sup>Note that interfering three 1064 nm beams at  $120^\circ$  will form a honeycomb lattice for <sup>39</sup>K, <sup>40</sup>K and <sup>87</sup>Rb, which can be thought of as an inverted, ‘repulsive’ triangular lattice. This is due to the fact that 1064 nm is red-detuned with respect to the D1 and D2 transitions of these isotopes.

energy. While we currently implement our triangular lattices using interfering lattice beams, we will potentially move to the retro-reflected implementation in the future, see [appendix B](#), making it desirable that we be able to calculate lattice quantities for both implementations.

### 2.1.2 Phase degrees of freedom

We will now look at the phase degrees of freedom of the retro-reflected triangular lattice. Each 1D-lattice can have its own phase, resulting in three independent phase degrees of freedom,

$$\begin{aligned}
 I(\mathbf{r}) &= 4I_0 \sum_{j=1}^3 \cos^2 \left( \mathbf{k}_j \cdot \mathbf{r} + \frac{\psi_j}{2} \right) \\
 &= 2I_0 \left\{ 3 + \cos \left( k \left( y - \sqrt{3}x \right) + \psi_1 \right) + \cos \left( k \left( y + \sqrt{3}x \right) + \psi_2 \right) \right. \\
 &\quad \left. + \cos \left( -2ky + \psi_3 \right) \right\}.
 \end{aligned} \tag{2.12}$$

We saw above that two phases can be absorbed by lattice translation. From this we can deduce that the lattice structure keeps its shape when

$$\psi_3 = -\psi_2 - \psi_1. \tag{2.13}$$

By comparing [Eq. 2.12](#) with [Eq. 2.3](#) we can see that the triangular lattice is formed in the retro-reflected case if  $\psi_1 = \psi_2 = \psi_3 = \pi$ . Using [Eq. 2.13](#) we can make the broader statement that the retro-reflected lattice will be a triangular lattice if

$$\sum_j \psi_j \equiv \pi \pmod{2\pi}. \tag{2.14}$$

The sum of the three phases modulo  $2\pi$  defines a lattice structure. The set of lattice structures spans a 1-dimensional space. Furthermore, in a retro-reflected lattice, it is always possible to turn intensity maxima into intensity minima through a phase change. With

$$I_1(\mathbf{r}) = 4I_0 \sum_{j=1}^3 \cos^2(\mathbf{k}_j \cdot \mathbf{r}), \tag{2.15}$$

we find that the intensity pattern is inverted (apart from a global intensity offset) upon shifting the phase of each 1D lattice by  $\pi/2$ ,

$$\begin{aligned}
I_2(\mathbf{r}) &= 4I_0 \sum_{j=1}^3 \cos^2(\mathbf{k}_j \cdot \mathbf{r} - \frac{\pi}{2}) \\
&= 4I_0 \sum_{j=1}^3 \sin^2(\mathbf{k}_j \cdot \mathbf{r}) \\
&= 4I_0(3 - \sum_{j=1}^3 \cos^2(\mathbf{k}_j \cdot \mathbf{r})) \\
&= 12I_0 - I_1(\mathbf{r}).
\end{aligned} \tag{2.16}$$

Being able to invert the lattice intensity is a major advantage of retro-reflected lattices as it allows for effects arising due to the red- and blue detuning of the lattice beams to be corrected by changing the lattice beam phases<sup>6</sup>. This broader tunability comes at the cost of having to stabilize an additional phase.

### 2.1.3 Lattice potential

Having derived the intensity distribution of interfering and retro-reflected triangular lattices, we can move on to calculate the potential. Due to the AC Stark shift ultracold atoms feel a potential proportional to laser intensity [141],

$$V(\mathbf{r}) = UI(\mathbf{r}). \tag{2.17}$$

The sign and magnitude of  $U$  depends on the detuning of the lattice light with respect to the electronic transition of the atomic species<sup>7</sup>.

Triangular lattices can be either ‘attractive’ or ‘repulsive’, meaning that either the potential minima or maxima form a triangular lattice. A repulsive triangular lattice is equivalent to an attractive honeycomb lattice and vice versa. Table 2.1 and Fig. 2.3 show the different cases. The lattice beams of red (blue) detuned lattices have frequencies that are smaller (larger) than the principal atomic transition.

Detuning	Polarization	Lattice
Red	In plane	repulsive triangular
Red	Out of plane	attractive triangular
Blue	In plane	attractive triangular
Blue	Out of plane	repulsive triangular

**Table 2.1** – Different combinations of detuning and polarization of three interfering lasers and the resulting lattice geometry. The geometry of the beams is shown in Fig. 2.3.

<sup>6</sup>This does not apply to the confinement of the overall lattice potential, which still depends directly on the detuning of the lattice beams and is independent of phase.

<sup>7</sup>For rubidium and potassium in the ground state the principal transitions are the D1 and D2 lines, which lie between 766.7 nm and 795 nm for both species.

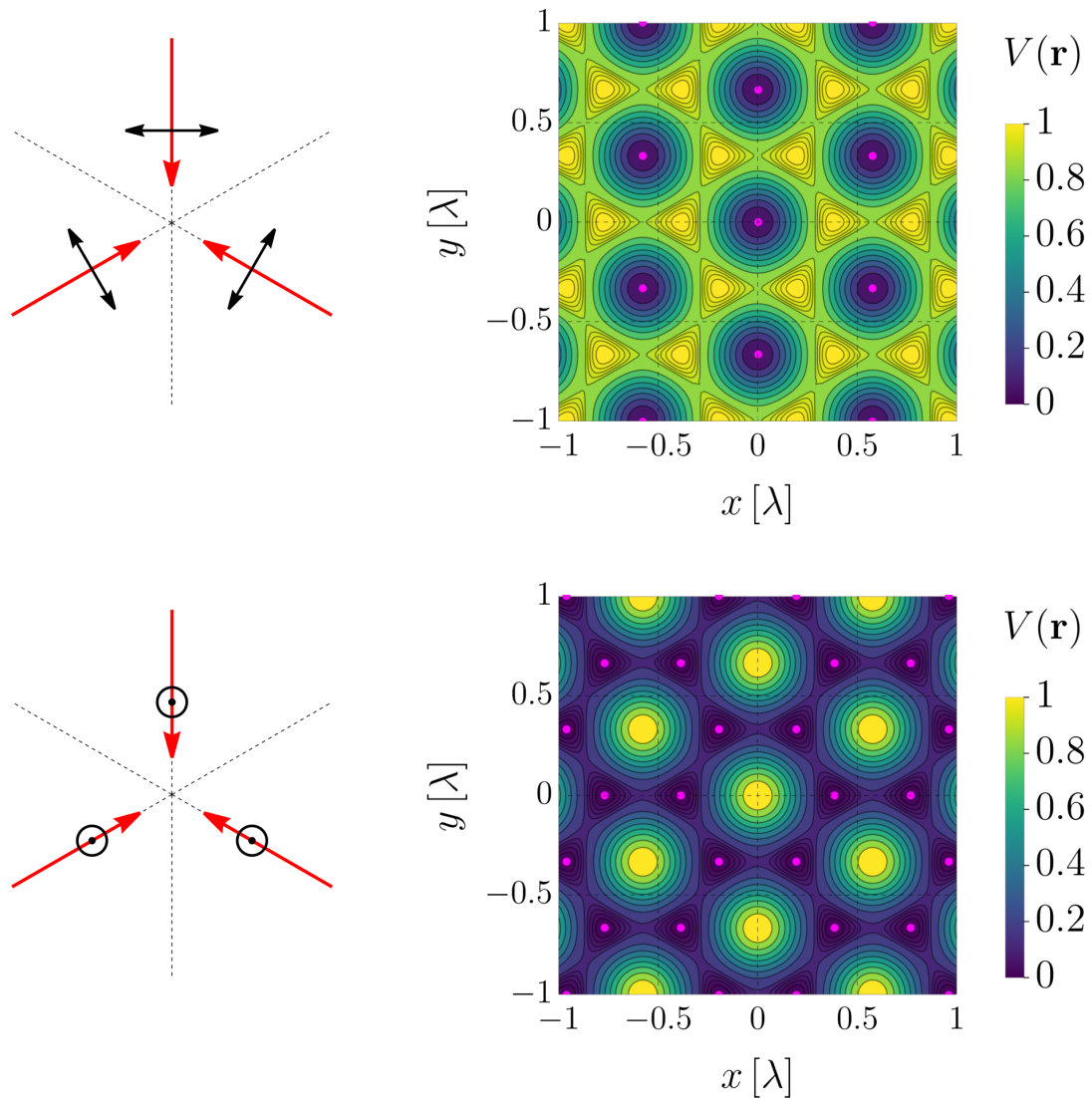


**Figure 2.3** – Lattice beam configurations (left) and corresponding potentials (right). The potentials are created by three blue-detuned beams with wavelength  $\lambda$ . In the left plots, the red arrows represent lattice beams and the black arrows represent their polarizations. In the bottom left plot, the black dots surrounded by black rings indicate that the polarization is in the plane perpendicular to the page. Magenta dots in the lattice potentials on the right signify points of minimum energy.

## 2.2 Optical kagome lattice

The kagome lattice can be implemented by superimposing two triangular lattices with a 2:1 ratio of lattice constants. An attractive ‘short’ lattice (with smaller lattice constant), creates a triangular lattice and a repulsive ‘long’ lattice (with larger lattice constant) lifts the energy of every fourth site of the short lattice, effectively creating the kagome pattern shown in Fig. 2.4.

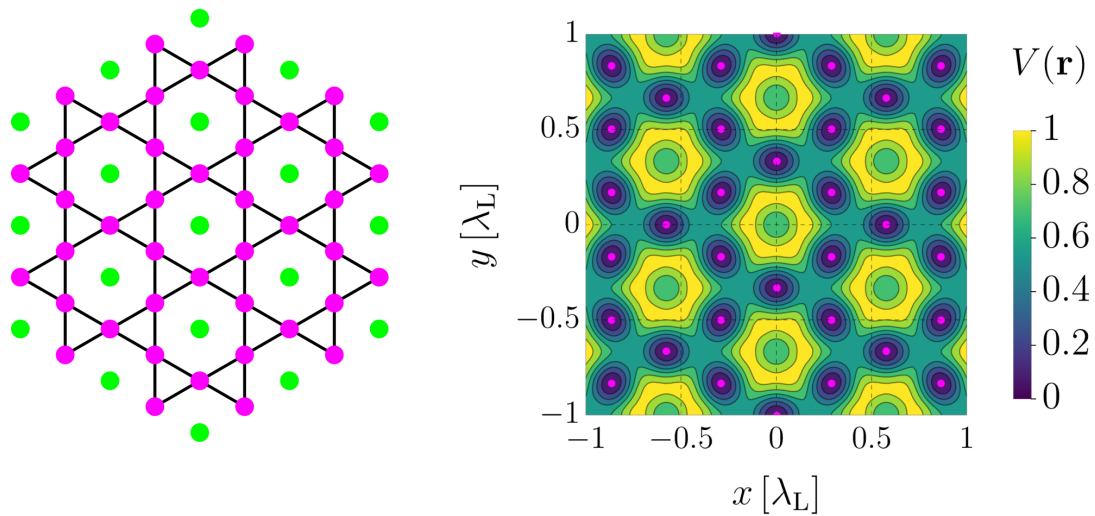


**Figure 2.4** – Left: overlaying a short, attractive triangular lattice (magenta) with a long, repulsive triangular lattice (green) results in a kagome lattice. Right: optical potential of the interfering kagome lattice. The wavelength of the long lattice is given by  $\lambda_L$ .

Depending on whether the kagome lattice is implemented with two interfering or two retro-reflected triangular lattices there are 4 or 6 phase degrees of freedom, respectively. Only two of these phases can be translated into lattice displacements while preserving the lattice structure. The other phase degrees of freedom cause changes in the lattice structure. Due to the two additional phases in the retro-reflected kagome lattice, the space of different lattices that can be implemented is correspondingly larger. In [section 4.3.5](#) we discuss how we actively stabilize the lattice beam phases in our experiment.

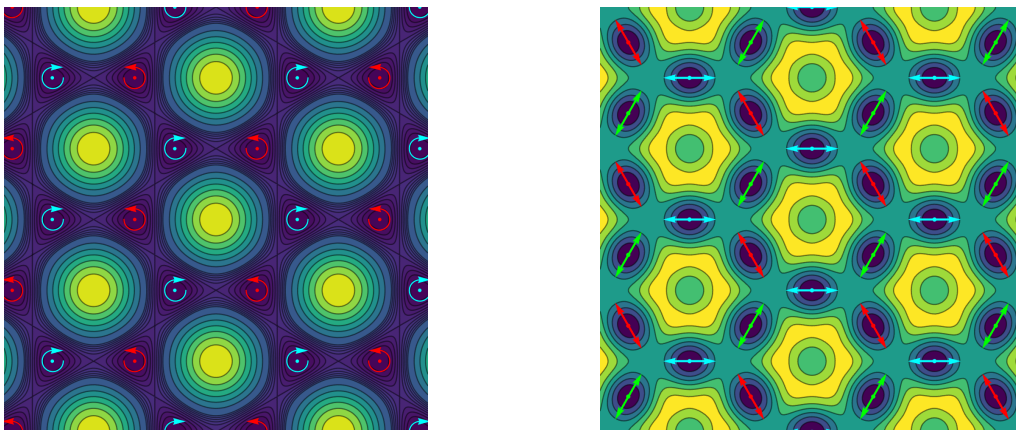


**Figure 2.5** – Left: polarization at honeycomb lattice sites. Alternating sites have opposite circular polarizations which causes  $m_F \neq 0$  to have a different energy on the two sites. Right: polarization at kagome lattice sites. At the kagome sites the optical lattice light is linearly polarized.

We initially planned to implement the kagome lattice with retro-reflected beams but eventually opted for the interfering implementation due to better compatibility with the

quantum gas microscope. We are planning to replace our current lattice with a retro-reflected lattice in the future however, see [appendix B](#).

**Lattice site polarization** The polarization of lattice light at the lattice sites can lead to extra inhomogeneous energy shifts if the light at the lattice sites is circularly polarized and atoms are prepared in Zeeman states with non-zero  $m_F$ <sup>8</sup>. In this case, circularly polarized light will lead to an additional vector Stark shift, which depends on the handedness of the lattice light at the lattice sites (see [Fig. 2.5](#)). This effect was observed in Kapitza-Dirac measurements with an optical honeycomb lattice [142]. For the kagome lattice, however, the lattice light is linearly polarized at the lattice sites and the atoms do not see a vector Stark shift. Since the scalar AC Stark shift is independent of the orientation of linearly polarized light, the energy at all lattice sites is equal in the optical kagome lattice.

## 2.3 Kagome band structure

We will now turn to the band structure of the kagome lattice, show that a flat band emerges in the tight-binding limit, and calculate the Bloch states.

We start by deriving the tight-binding band structure on a general bipartite lattice before discussing the tripartite, kagome lattice. In the tight-binding limit only tunnelling processes between adjacent sites are allowed. The Hamiltonian is thus

$$H = -t \sum_{\langle n,m \rangle} (\hat{c}_n^\dagger \hat{c}_m + \hat{c}_m^\dagger \hat{c}_n). \quad (2.18)$$

The brackets indicate nearest-neighbour tunnelling,  $\hat{c}_n$  and  $\hat{c}_n^\dagger$  are the annihilation and creation operator for a particle on site  $n$ , respectively, and  $t$  is the tunnelling energy. The sites of a bipartite lattice can be labelled such that any site A only connects to sites B and vice versa. The lattice constructed by all A sites and that composed of all B sites form the two sublattices of the bipartite lattice. Since tunnelling is restricted to nearest neighbours, any tunnelling process between two sites will be from an A site to a B site or vice versa, never between A and A or B and B.

The number of B sites that any site A is connected to depends on the lattice structure. The square lattice and the honeycomb lattice are bipartite lattices. However, sites of the square lattice connect to four other sites, while it is only three for the honeycomb lattice. We can rewrite the tight-binding Hamiltonian in terms of creation and annihilation operators on the A and B sites,

$$H = -t \sum_n \sum_{\{j\}(n)} (\hat{a}_n^\dagger \hat{b}_j + \hat{b}_j^\dagger \hat{a}_n) \quad (2.19)$$

where  $\hat{a}_n$  and  $\hat{b}_n$  are the annihilation operators for the  $n^{\text{th}}$  A and B site, respectively. The second sum indicates that for each site A a particle can only tunnel to the respective nearest-neighbour B sites. To obtain the tight-binding Hamiltonian in momentum space, we want to express [Eq. 2.19](#) in momentum space coordinates. We can write

---

<sup>8</sup>In our machine all atoms are prepared in Zeeman states with non-zero  $m_F$ .

$$\hat{a}_n = \frac{1}{\sqrt{N}} \sum_{\mathbf{k}} e^{i\mathbf{k} \cdot \mathbf{r}_{A,n}} \hat{a}_{\mathbf{k}}, \quad \hat{b}_n = \frac{1}{\sqrt{N}} \sum_{\mathbf{k}} e^{i\mathbf{k} \cdot \mathbf{r}_{B,n}} \hat{b}_{\mathbf{k}}, \quad (2.20)$$

where  $\mathbf{r}_{A,n}$  and  $\mathbf{r}_{B,n}$  are the positions of the  $n^{\text{th}}$  A and B site, respectively. The tight-binding Hamiltonian finally takes the form

$$\begin{aligned} H &= -\frac{t}{N} \sum_n \sum_{\{j\}(n)} \sum_{\mathbf{k}, \mathbf{k}'} (e^{-i\mathbf{k} \cdot \mathbf{r}_{A,n}} e^{i\mathbf{k}' \cdot \mathbf{r}_{B,j}} \hat{a}_{\mathbf{k}}^\dagger \hat{b}_{\mathbf{k}'} + \text{h.c.}) \\ &= -\frac{t}{N} \sum_n \sum_j \sum_{\mathbf{k}, \mathbf{k}'} (e^{i\mathbf{k}' \cdot \mathbf{r}_{NN}^j} e^{i(\mathbf{k}' - \mathbf{k}) \cdot \mathbf{r}_{A,n}} \hat{a}_{\mathbf{k}}^\dagger \hat{b}_{\mathbf{k}'} + \text{h.c.}) \\ &= -t \sum_{\mathbf{k}} \sum_j (e^{i\mathbf{k} \cdot \mathbf{r}_{NN}^j} \hat{a}_{\mathbf{k}}^\dagger \hat{b}_{\mathbf{k}} + \text{h.c.}) \\ &= \sum_{\mathbf{k}} \begin{pmatrix} \hat{a}_{\mathbf{k}} & \hat{b}_{\mathbf{k}} \end{pmatrix}^\dagger \underbrace{\begin{pmatrix} 0 & -t \sum_j e^{i\mathbf{k} \cdot \mathbf{r}_{NN}^j} \\ -t \sum_j e^{-i\mathbf{k} \cdot \mathbf{r}_{NN}^j} & 0 \end{pmatrix}}_{H(\mathbf{k})} \begin{pmatrix} \hat{a}_{\mathbf{k}} \\ \hat{b}_{\mathbf{k}} \end{pmatrix} \\ &= \sum_{\mathbf{k}} \varepsilon_{\mathbf{k}} \hat{\gamma}_{\mathbf{k}}^\dagger \hat{\gamma}_{\mathbf{k}}. \end{aligned} \quad (2.21)$$

Here we used the identity  $\sum_n e^{i(\mathbf{k}' - \mathbf{k}) \cdot \mathbf{r}_{A,n}} = N\delta(\mathbf{k}' - \mathbf{k})$  and set  $\mathbf{r}_{B,j} = \mathbf{r}_{A,n} + \mathbf{r}_{NN}^j$ , where  $\{\mathbf{r}_{NN}^j\}$  are the vectors connecting an A site to its nearest-neighbour B sites. The eigenvalues of  $H(\mathbf{k})$ ,  $\varepsilon_{\mathbf{k}}$ , are typically referred to as the tight-binding bands. The operator  $\hat{\gamma}_{\mathbf{k}}$  is the annihilation operator for a quasiparticle with energy  $\varepsilon_{\mathbf{k}}$ . The weights of  $\hat{a}_{\mathbf{k}}$  and  $\hat{b}_{\mathbf{k}}$  in  $\hat{\gamma}_{\mathbf{k}}$  are given by the eigenvectors of  $H(\mathbf{k})$  and we can find the band structure of a bipartite lattice by diagonalizing  $H(\mathbf{k})$ . The derivation above is equally applicable to lattices that are tripartite or more. Thus, the tight-binding Hamiltonian on the kagome lattice can be written as a sum over  $H_{\text{kag}}(\mathbf{k})$  with

$$H_{\text{kag}}(\mathbf{k}) = -2t \begin{pmatrix} 0 & \cos(\mathbf{k} \cdot \boldsymbol{\delta}_{AB}) & \cos(\mathbf{k} \cdot \boldsymbol{\delta}_{CA}) \\ \cos(\mathbf{k} \cdot \boldsymbol{\delta}_{AB}) & 0 & \cos(\mathbf{k} \cdot \boldsymbol{\delta}_{BC}) \\ \cos(\mathbf{k} \cdot \boldsymbol{\delta}_{CA}) & \cos(\mathbf{k} \cdot \boldsymbol{\delta}_{BC}) & 0 \end{pmatrix}. \quad (2.22)$$

Here,  $\boldsymbol{\delta}_{AB}$ ,  $\boldsymbol{\delta}_{BC}$ ,  $\boldsymbol{\delta}_{CA}$  are the differences in position between nearest-neighbour A & B, B & C, and C & A sites, respectively (see Fig. 2.7). The eigenvalues of  $H_{\text{kag}}(\mathbf{k})$  are the three bands of the tight-binding band structure and are given by

$$\begin{aligned} E_1(\mathbf{k}) &= t \left( -1 - \sqrt{3 + 2 \sum_j \cos(2\mathbf{k} \cdot \boldsymbol{\delta}_j)} \right), \\ E_2(\mathbf{k}) &= t \left( -1 + \sqrt{3 + 2 \sum_j \cos(2\mathbf{k} \cdot \boldsymbol{\delta}_j)} \right), \\ E_3(\mathbf{k}) &= 2t. \end{aligned} \quad (2.23)$$

The lowest two bands ( $E_1$  &  $E_2$ ) are equivalent to the tight-binding bands of the honeycomb lattice, i.e. they have the same shape and display Dirac cones. The third band ( $E_3$ ) is not a function of momentum and is thus flat (see Fig. 2.6).

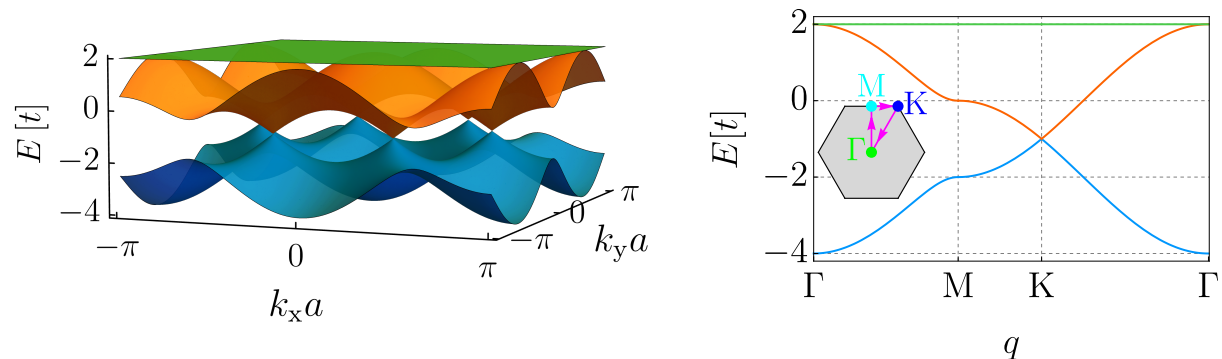


**Figure 2.6** – Kagome lattice tight-binding band structure. Left: band structure in 2D. Right: band structure along a one-dimensional path through points of high symmetry ( $\Gamma$ , M, K). Inset: one-dimensional path in reciprocal space.

The band width of the tight-binding bands is

$$\text{BW} = 6t, \quad (2.24)$$

where  $t$  is the nearest-neighbour tunnelling energy. With this relation we can calculate the tunnelling rate from the band width for deep lattices.

**Optical kagome lattice** We will now derive the band structure for an optical kagome lattice. We will see that for deep lattices the band structure approaches what we derived in tight-binding. For conceptual simplicity, we derive the band structure for the retro-reflected kagome lattice. The band structure of the interfering case is equivalent, apart from the orientation of the real-space lattice and the Brillouin zone<sup>9</sup>. The Bloch theorem states that the wave function of a particle with momentum  $\hbar\mathbf{q}$  in a periodic potential is the product of a plane wave and a function that has the same periodicity as the lattice,

$$\begin{aligned} \psi_{\mathbf{q}}(\mathbf{r}) &= u_{\mathbf{q}}(\mathbf{r})e^{i\mathbf{q}\cdot\mathbf{r}}, \\ u_{\mathbf{q}}(\mathbf{r}) &= u_{\mathbf{q}}(\mathbf{r} + \mathbf{R}_{n,m}), \end{aligned} \quad (2.25)$$

where  $\mathbf{R}_{n,m} = n\mathbf{a}_1 + m\mathbf{a}_2$  is a vector connecting two unit cells of the lattice (see Fig. 2.7). This allows us to write  $u_{\mathbf{q}}(\mathbf{r})$  as

$$u_{\mathbf{q}}(\mathbf{r}) = \sum_{n,m} c_{\mathbf{q},n,m} e^{i(n\mathbf{g}_1 + m\mathbf{g}_2)\cdot\mathbf{r}}. \quad (2.26)$$

<sup>9</sup>We chose to fix the orientation of our  $\mathbf{k}$ -vectors such that they are the same in the interfering and retro-reflected case, instead of fixing the orientation of the lattice itself. For the rest of this chapter, and in chapter 3 and appendix D all the real- and momentum space images have an orientation corresponding to the retro-reflected case. For the experimental sections (chapter 5, chapter 6, chapter 7 & chapter 8) we use the orientation of the interfering implementation.

The vectors  $\mathbf{g}_1$  and  $\mathbf{g}_2$  span the reciprocal lattice (see Fig. 2.7). The reciprocal lattice vectors can be calculated using the periodicity condition given in Eq. 2.25, which reduces to

$$\mathbf{g}_i \cdot \mathbf{a}_j = 2\pi\delta_{ij}. \quad (2.27)$$

The lattice is fully described by the real-space and reciprocal lattice vectors

$$\mathbf{a}_1 = a \begin{pmatrix} 1 \\ 0 \end{pmatrix}, \quad \mathbf{a}_2 = \frac{a}{2} \begin{pmatrix} 1 \\ \sqrt{3} \end{pmatrix}, \quad \mathbf{g}_1 = \frac{2\pi}{\sqrt{3}a} \begin{pmatrix} \sqrt{3} \\ -1 \end{pmatrix}, \quad \mathbf{g}_2 = \frac{4\pi}{\sqrt{3}a} \begin{pmatrix} 0 \\ 1 \end{pmatrix}, \quad (2.28)$$

where  $a = |\mathbf{a}_1| = |\mathbf{a}_2|$ . Fig. 2.7 shows the kagome lattice, its unit cell and the various vectors that are used to describe it. The kagome lattice can be thought of as a triangular lattice with equilateral triangles at the lattice sites. The unit cell contains three sites and the lattice can be obtained by translating the unit cell along linear combinations of the vectors  $\mathbf{a}_1$  and  $\mathbf{a}_2$ .

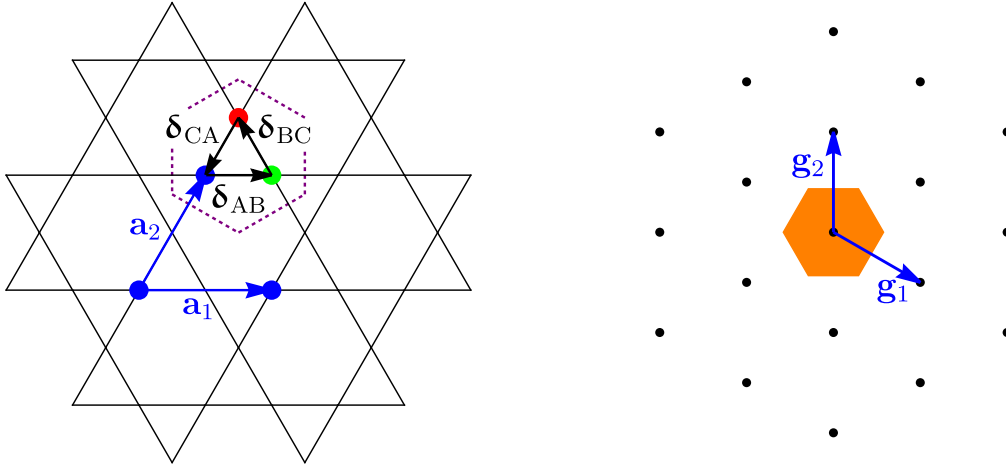


**Figure 2.7** – Left: kagome lattice in real space. The vertices are the lattice sites, whose position is described by linear combinations of  $\mathbf{a}_1$ ,  $\mathbf{a}_2$ ,  $\delta_{AB}$ ,  $\delta_{BC}$ , and  $\delta_{CA}$ . The dashed purple line encloses the unit cell. A (blue), B (green) and C (red) label the three sites of the unit cell. Right: corresponding reciprocal lattice in momentum space. The first Brillouin zone is shown in orange.

The energy of a Bloch wave is a function of its momentum and can be calculated by putting the ansatz in Eq. 2.25 into the time-independent Schrödinger equation:

$$\left( -\frac{\hbar^2}{2m} \nabla^2 + V(\mathbf{r}) \right) \psi_{\mathbf{q}}(\mathbf{r}) = E_{\mathbf{q}} \psi_{\mathbf{q}}(\mathbf{r}). \quad (2.29)$$

The potential of the retro-reflected implementation of the kagome lattice can be written as

$$V(\mathbf{r}) = V_S \sum_{j=1}^3 \cos^2 \left( 2\mathbf{k}_j \cdot \mathbf{r} + \frac{\pi}{2} \right) + V_L \sum_{j=1}^3 \cos^2(\mathbf{k}_j \cdot \mathbf{r}), \quad (2.30)$$

where  $V_S > 0$  and  $V_L > 0$  are the lattice depths of the short and long triangular lattice, respectively, and  $\mathbf{k}_1$ ,  $\mathbf{k}_2$ ,  $\mathbf{k}_3$ , and  $k$  are as in Eq. 2.2. We can express the magnitude of the wavevectors in terms of the lattice spacing,  $k = \frac{2\pi}{\sqrt{3}a}$ , which results in

$$\begin{aligned}\mathbf{k}_1 &= \frac{\pi}{\sqrt{3}a} \begin{pmatrix} -\sqrt{3} \\ 1 \end{pmatrix} = -\frac{\mathbf{g}_1}{2}, \quad \mathbf{k}_2 = \frac{\pi}{\sqrt{3}a} \begin{pmatrix} \sqrt{3} \\ 1 \end{pmatrix} = \frac{\mathbf{g}_1 + \mathbf{g}_2}{2}, \\ \mathbf{k}_3 &= \frac{2\pi}{\sqrt{3}a} \begin{pmatrix} 0 \\ -1 \end{pmatrix} = -\frac{\mathbf{g}_2}{2}.\end{aligned}\tag{2.31}$$

After inserting Eq. 2.30, Eq. 2.26 and the relations of Eq. 2.31 into Eq. 2.29, we obtain

$$\begin{aligned}& \left( \frac{\hbar^2}{2m} |\mathbf{q} + m\mathbf{g}_1 + n\mathbf{g}_2|^2 - \frac{3}{2}V_S + \frac{3}{2}V_L \right) c_{\mathbf{q},m,n} \\ & - \frac{V_S}{4} (c_{\mathbf{q},m-2,n} + c_{\mathbf{q},m+2,n} + c_{\mathbf{q},m-2,n-2} + c_{\mathbf{q},m+2,n+2} + c_{\mathbf{q},m,n-2} + c_{\mathbf{q},m,n+2}) \\ & + \frac{V_L}{4} (c_{\mathbf{q},m-1,n} + c_{\mathbf{q},m+1,n} + c_{\mathbf{q},m-1,n-1} + c_{\mathbf{q},m+1,n+1} + c_{\mathbf{q},m,n-1} + c_{\mathbf{q},m,n+1}) \\ & = E_{\mathbf{q}} c_{\mathbf{q},m,n}.\end{aligned}\tag{2.32}$$

We can reexpress this equation in terms of the long lattice recoil energy,  $E_R = \frac{\hbar^2 k^2}{2m}$ ,

$$\begin{aligned}& \frac{1}{k^2} |\mathbf{q} + m\mathbf{g}_1 + n\mathbf{g}_2|^2 c_{\mathbf{q},m,n} \\ & - \frac{s_S}{4} (c_{\mathbf{q},m-2,n} + c_{\mathbf{q},m+2,n} + c_{\mathbf{q},m-2,n-2} + c_{\mathbf{q},m+2,n+2} + c_{\mathbf{q},m,n-2} + c_{\mathbf{q},m,n+2}) \\ & + \frac{s_L}{4} (c_{\mathbf{q},m-1,n} + c_{\mathbf{q},m+1,n} + c_{\mathbf{q},m-1,n-1} + c_{\mathbf{q},m+1,n+1} + c_{\mathbf{q},m,n-1} + c_{\mathbf{q},m,n+1}) \\ & = \varepsilon_{\mathbf{q}}^{\text{ret}}(s_S, s_L) c_{\mathbf{q},m,n},\end{aligned}\tag{2.33}$$

where  $s_S$  and  $s_L$  are the lattice depth of the short- and long-wavelength lattices, respectively, in units of  $E_R$  and  $\varepsilon_{\mathbf{q}}^{\text{ret}}(s_S, s_L)$  is the energy of the Bloch wave with momentum  $\mathbf{q}$  in units of  $E_R$ . We have also omitted the constant energy shift  $\frac{3}{2}s_S + \frac{3}{2}s_L$ <sup>10</sup>.

By solving Eq. 2.33 numerically, we can find values for  $c_{\mathbf{q},m,n}$  and  $\varepsilon_{\mathbf{q}}^{\text{ret}}$ , from which we can reconstruct the Bloch waves and energies.

**Interfering lattice** Keeping the definition of  $E_R$  fixed (single photon recoil energy of the long lattice wavelength), the Bloch state energy in the interfering implementation is given by

$$\varepsilon_{\mathbf{q}}^{\text{int}}(s_S, s_L) = \frac{3}{4} \varepsilon_{\mathbf{q}}^{\text{ret}} \left( \frac{4}{3}s_S, \frac{4}{3}s_L \right).\tag{2.34}$$

The factor  $\frac{4}{3}$  arises since the effective lattice recoil energy in the interfering case is a factor of  $\left( \frac{a_{\text{int}}}{a_{\text{ret}}} \right)^2 = \left( \frac{2}{\sqrt{3}} \right)^2 = \frac{4}{3}$  lower than that of the retro-reflected implementation. Thus, for

<sup>10</sup>This is allowed because it only causes a constant shift to all energy levels. Any physical quantities only involve energy differences, which means that the constant offset can be omitted.

the same lattice depth in units of  $E_R$ , the lattice depth of the interfering case is a factor  $\frac{4}{3}$  larger in terms of its lattice recoil energy than in the retro-reflected case. Since the lattice recoil energy in the interfering case is only  $\frac{3}{4}$  of that of the retro case, the energy in terms of  $E_R$  must also be a factor  $\frac{3}{4}$  lower in the interfering case.

Fig. 2.8 shows the dispersion relation of the lowest four bands of the interfering kagome lattice for different lattice depths.

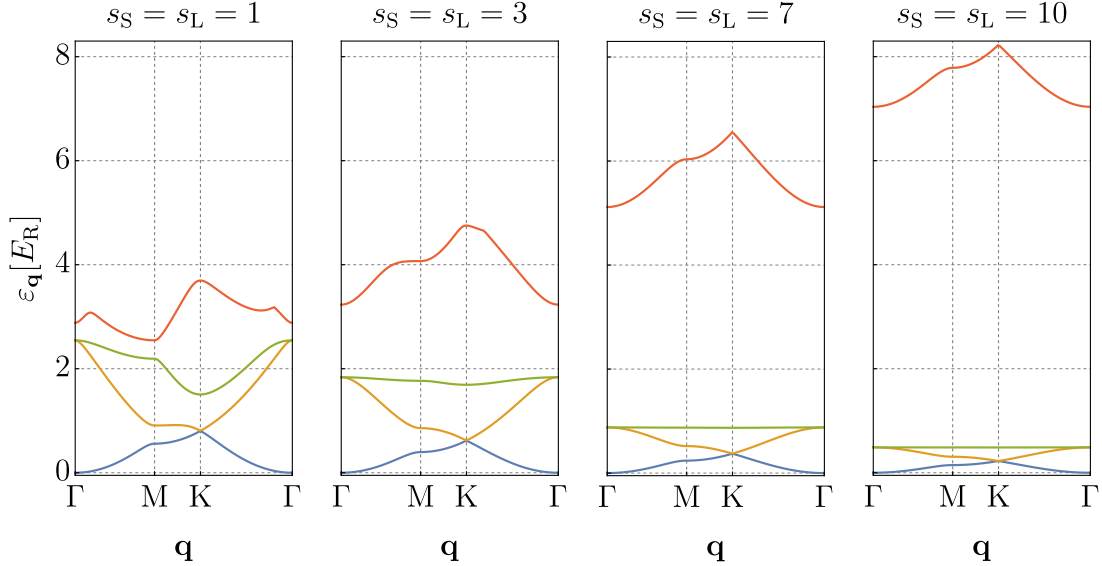


**Figure 2.8** – Band structure of the interfering kagome lattice along a path through points of high symmetry in the Brillouin zone.  $s_S$  and  $s_L$  refer to the lattice depth of the short- and long-wavelength lattices, respectively. Only the lowest four bands are shown.

The third band of the kagome lattice only becomes visibly flat for sufficiently deep lattices. From the tight-binding model, one expects the third band to be analytically flat. The discrepancy between the above and the tight-binding calculation is due to the fact that the tight-binding model is only a good approximation for sufficiently deep lattices. For shallow lattices higher-order tunnelling processes cause the third band to be dispersive.

Fig. 2.8 shows that we will have to perform experiments at lattice depths above  $s_S = s_L = 3$  to see effects of the flat band.

**Including lattice beam phases and intensities** For completeness we will also briefly derive the Bloch state equation when each lattice beam has an individual phase and intensity. The potential in this case is

$$V(\mathbf{r}) = \sum_{j=1}^3 V_{S,j} \cos^2(2\mathbf{k}_j \cdot \mathbf{r} + \frac{\psi_{S,j}}{2}) + \sum_{j=1}^3 V_{L,j} \cos^2(\mathbf{k}_j \cdot \mathbf{r} + \frac{\psi_{L,j}}{2}), \quad (2.35)$$

Here,  $\{\psi_{S,j}\}$  and  $\{\psi_{L,j}\}$  label the phases of the short and long lattice beams, respectively. The Bloch states can be calculated by solving

$$\begin{aligned}
& \frac{1}{k^2} |\mathbf{q} + m\mathbf{g}_1 + n\mathbf{g}_2|^2 c_{\mathbf{q},m,n} \\
& + s_{S,1} e^{-i\psi_{S,1}} c_{\mathbf{q},m-2,n} + s_{S,1} e^{i\psi_{S,1}} c_{\mathbf{q},m+2,n} \\
& + s_{S,2} e^{i\psi_{S,2}} c_{\mathbf{q},m-2,n-2} + s_{S,2} e^{-i\psi_{S,2}} c_{\mathbf{q},m+2,n+2} \\
& + s_{S,3} e^{-i\psi_{S,3}} c_{\mathbf{q},m,n-2} + s_{S,3} e^{i\psi_{S,3}} c_{\mathbf{q},m,n+2} \\
& + s_{L,1} e^{-i\psi_{L,1}} c_{\mathbf{q},m-1,n} + s_{L,1} e^{i\psi_{L,1}} c_{\mathbf{q},m+1,n} \\
& + s_{L,2} e^{i\psi_{L,2}} c_{\mathbf{q},m-1,n-1} + s_{L,2} e^{-i\psi_{L,2}} c_{\mathbf{q},m+1,n+1} \\
& + s_{L,3} e^{-i\psi_{L,3}} c_{\mathbf{q},m,n-1} + s_{L,3} e^{i\psi_{L,3}} c_{\mathbf{q},m,n+1} \\
& = \varepsilon_{\mathbf{q}}^{\text{ret}}(s_S, s_L) c_{\mathbf{q},m,n}.
\end{aligned} \tag{2.36}$$

The Bloch state equation for the interfering lattice can be straightforwardly derived from this by using Eq. 2.14 and Eq. 2.34.

**Lattice beam power** The lattice depth is determined by the intensity of the lattice beams at the position of the atoms. The intensity of a Gaussian beam at its focus is given by

$$I_{\text{max}} = \frac{2P}{\pi w_h w_v}, \tag{2.37}$$

where  $w_h$ ,  $w_v$  are the horizontal and vertical beam waist at the focus, respectively, and  $P$  is the beam power. Comparing Eq. 2.11 with Eq. 2.30 we find for the retro-reflected lattice that

$$V_i(P) = 4 |U_i| I_{\text{max}} = \frac{8P |U_i|}{\pi w_h w_v} \Leftrightarrow s_i(P) = \frac{8P |U_i|}{\pi w_h w_v} \left( \frac{\hbar^2 k^2}{2m} \right)^{-1}, \tag{2.38}$$

where  $i \in \{S, L\}$  and  $U_i$  is the AC Stark shift per unit intensity at  $\lambda_i$ , the wavelength of lattice  $i$ . Similarly, we find by comparing Eq. 2.3 and Eq. 2.30 that

$$V_i(P) = 2 |U_i| I \Leftrightarrow s_i(P) = \frac{4P |U_i|}{\pi w_h w_v} \left( \frac{\hbar^2 k^2}{2m} \right)^{-1} \tag{2.39}$$

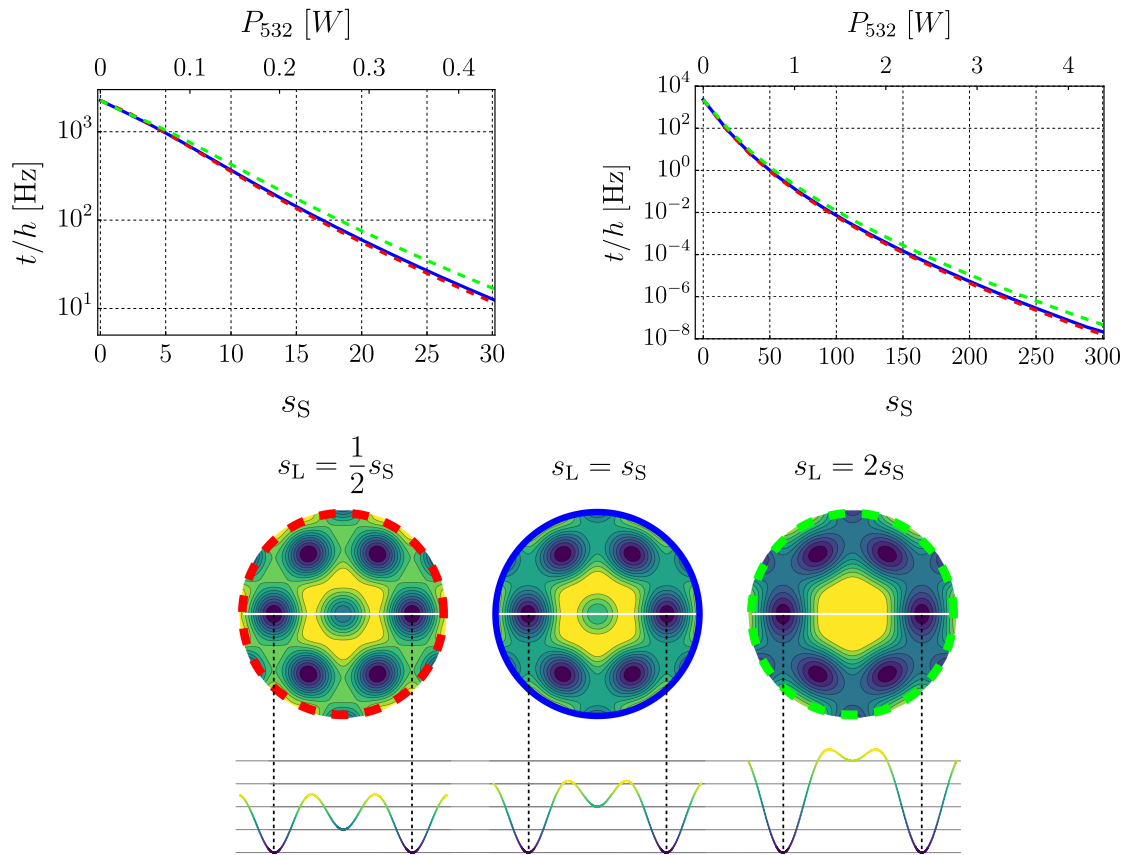
for the interfering lattice.

**Tunnelling rate and band gap** We now have all the necessary tools to calculate the tunnelling rate, band gap and flat band width in the kagome lattice as a function of lattice depth and lattice power. For the rest of this chapter, we restrict our discussion to  $^{39}\text{K}$  in the interfering kagome lattice<sup>11</sup> and assume beam waists of  $100 \mu\text{m} \times 50 \mu\text{m}$  (horizontal  $\times$  vertical)<sup>12</sup>. Furthermore, the lattice wavelengths are set to be  $\lambda_S = 532 \text{ nm}$  and  $\lambda_L = 1064 \text{ nm}$ . To calculate the tunnelling rate, we calculate the band width of the three lowest energy bands (s-bands) and apply Eq. 2.24. The band gap is given by the difference of the lowest energy of the fourth band and the highest energy of the third band.

<sup>11</sup>appendix B contains calculations done with the retro-reflected kagome lattice.

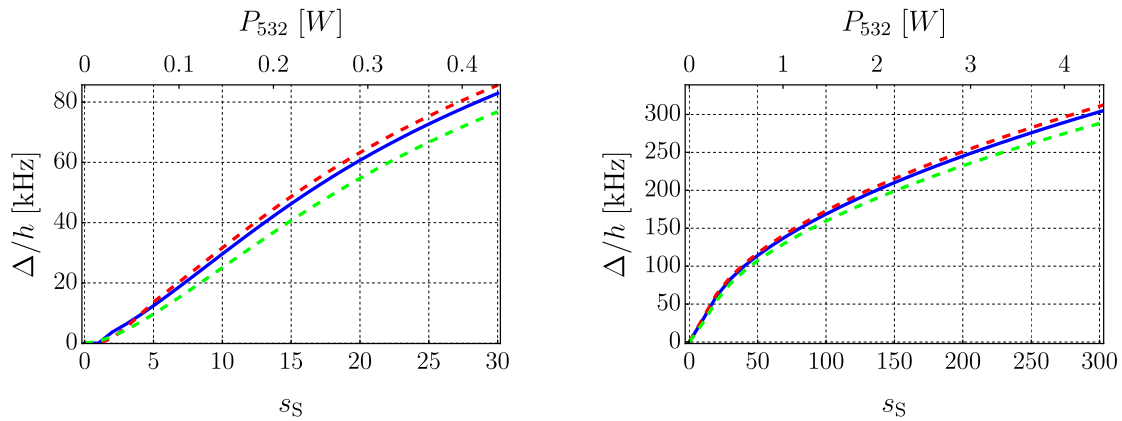
<sup>12</sup>These are our design beam waists.

The numerically determined tunnelling rate and band gap as functions of the lattice depth are shown in Fig. 2.9 and Fig. 2.10, respectively.



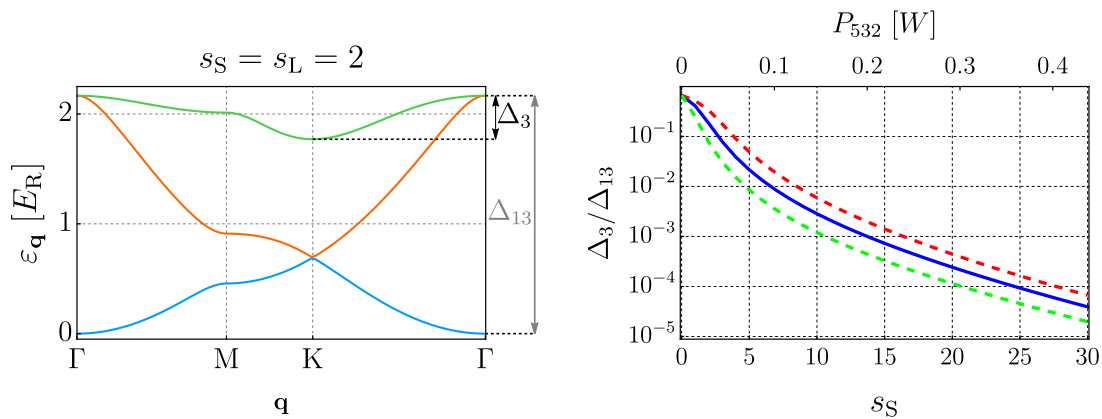
**Figure 2.9** – Top: tunnelling rate  $t$  in the s-band of the interfering kagome lattice as a function of lattice depth. The power per 532 nm beam required to create a short-wavelength lattice depth of  $s_S$  ( $P_{532}$ ) is specified on the top of both plots. Red dashed line:  $s_L = \frac{1}{2}s_S$ . Blue line:  $s_L = s_S$ . Green dashed line:  $s_L = 2s_S$ . Bottom: potential of the kagome lattice with different power ratios. The white line in the 2D potentials indicates the trajectory along which the 1D potentials are plotted.

Fig. 2.9 shows that the short-wavelength lattice almost completely determines the tunnelling rate and that the long-wavelength lattice only causes a small perturbation to the tunnelling rate. This behaviour applies to the band gap, the flat band width and the on-site interaction as well. The band gap between the third and fourth energy level approaches the on-site trap frequency as the lattice depth goes to infinity. Note that for deep lattices the band gap increases as the square root of the lattice depth. This is the behaviour expected from calculating the trap frequency directly. The band gap at 3 W per 532 nm beam is about 250 kHz, which is comparable to values reported for fluorescence imaging in other quantum gas microscope experiments [52, 56, 57, 59].



**Figure 2.10** – Band gap between s and p bands for the interfering kagome lattice as a function of lattice depth. Red dashed line:  $s_L = \frac{1}{2}s_S$ . Blue line:  $s_L = s_S$ . Green dashed line:  $s_L = 2s_S$ .

**Flat band width as a function of lattice depth** Fig. 2.11 shows the ratio of the band widths of the third (flat) band and the s-band of the kagome lattice. The flat band width decreases exponentially with lattice power. Strikingly, the flat band also becomes exponentially flat relative to the s-bands, whose band width also decreases exponentially with lattice beam power. Thus, it is possible to have a large tunnelling rate in the kagome lattice and still have a small flat-band width. For example, for  $^{39}\text{K}$  in a lattice with  $s_S = s_L = 15$ , the tunnelling rate is roughly 140 Hz and the flat band width is 0.1 Hz.



**Figure 2.11** – Left: optical kagome lattice band structure.  $\Delta_3$  and  $\Delta_{13}$  are the band widths of the flat band and full s-band, respectively. Right:  $\Delta_3/\Delta_{13}$  as a function of lattice depth for  $s_L = \frac{1}{2}s_S$  (red dashed),  $s_L = s_S$  (blue), and  $s_L = 2s_S$  (green dashed).

## 2.4 Wannier states

In this section we will calculate Wannier states for the kagome lattice and use them to determine the Hubbard parameters  $t$  and  $U$ . Knowing the prefactors to the terms in the Hubbard model and how they scale with lattice beam power is crucial for benchmarking our quantum simulator and for targeting specific phases of matter. It is worth noting that

knowledge of the Wannier states allows us to precisely tune the Hamiltonian to the exact parameters we want to conduct an experiment at.

Knowing beyond nearest-neighbour tunnelling rates is also useful to determine regimes in which these can be neglected, i.e. when only nearest-neighbour tunnelling has to be taken into account, and can be used to find parameter regimes to engineer complex NNN-tunnelling for e.g. creating topological bands [19, 110]. Calculating higher band tunnelling rates can also be used to determine the total tunnelling rate during fluorescence imaging where higher band occupation is unavoidable.

**Band-projected position operator** There are two standard methods to calculate multi-dimensional Wannier states and, in particular, Wannier states in non-separable lattice potentials. The first method was introduced by Marzari and Vanderbilt [143]. The idea is to numerically minimize the spatial spread of the Wannier function so as to get a maximally localized Wannier state. This method is known to occasionally converge to a local minimum that is not the maximally localized Wannier function [143–146]. It is also computationally intensive [146].

The second approach is to use band projected position operators [147–149]. The procedure here is to calculate the Wannier state directly by finding the eigenstates of the projected position operator. By projecting the position operator onto a suitably chosen subset of bands it is possible to numerically determine the maximally localized Wannier states for any site and any orbital (band) to arbitrary precision. While this method has been used to calculate Wannier states on simple cubic [148] and skewed honeycomb lattices [148, 149], it has so far not been used to calculate Wannier states on the triangular, symmetric honeycomb, and kagome lattices. Our adaptation of the band-projected position operator approach to the kagome lattice will be the subject of this chapter.

**Setting up the equation** Our calculation of the Wannier states closely follows [148]. We first want to express the position operator in the Bloch state basis. The real-space representation of a Bloch state,  $|\mathbf{k}, \alpha\rangle$ , is given by

$$\langle \mathbf{r} | \mathbf{k}, \alpha \rangle = \sum_{n_1, n_2} c_{n_1, n_2}^{\mathbf{k}, \alpha} e^{i(n_1 \mathbf{g}_1 + n_2 \mathbf{g}_2 + \mathbf{k}) \cdot \mathbf{r}}. \quad (2.40)$$

Here  $\mathbf{k}$  is the Bloch state momentum and  $\alpha$  labels the Bloch band. We discretize the position operator  $\hat{r}$  by calculating overlap integrals of the form  $\langle \mathbf{k}, \alpha | \hat{r} | \mathbf{k}', \alpha' \rangle$  for a discrete set of Bloch states in the Brillouin zone. The discretized position operator takes the form of a matrix, whose eigenvalues are the positions of lattice sites and eigenvectors are the Wannier states in the Bloch state basis.

For a two-dimensional lattice, we need to determine the discretized, band-projected position operator along two directions. These two directions are ideally orthogonal (this simplifies the math), but in a non-separable lattice this is not possible. For lattices with triangular geometry (i.e. triangular, honeycomb, and kagome lattices), we define

$$\hat{r}_1 = \frac{1}{2\pi} \mathbf{g}_1 \cdot \begin{pmatrix} \hat{x} \\ \hat{y} \end{pmatrix} = \kappa \left( \sqrt{3}\hat{x} - \hat{y} \right), \quad \hat{r}_2 = \frac{1}{2\pi} \mathbf{g}_2 \cdot \begin{pmatrix} \hat{x} \\ \hat{y} \end{pmatrix} = 2\kappa\hat{y}, \quad (2.41)$$

$$R_j = \sum_{\mathbf{k}, \mathbf{k}'} \sum_{\alpha, \alpha'} \langle \mathbf{k}, \alpha | \hat{r}_j | \mathbf{k}', \alpha' \rangle | \mathbf{k}, \alpha \rangle \langle \mathbf{k}', \alpha' |$$

where  $\kappa = \frac{1}{\sqrt{3}a}$  and  $R_j$  is the discretized and band-projected version of the position operator  $\hat{r}_j$ .<sup>13</sup> The reciprocal lattice vectors,  $\mathbf{g}_1$  and  $\mathbf{g}_2$ , are defined in Eq. 2.28. To ensure that  $R_j$  is a matrix, we introduce the indexing function  $\mathcal{I}(\mathbf{k}, \alpha)$ , which assigns a unique index to all combinations of  $\mathbf{k}$  and  $\alpha$ .<sup>14</sup> The elements of  $R_1$  and  $R_2$  are given by

$$\begin{aligned} R_{\mathcal{I}(\mathbf{k}, \alpha), \mathcal{I}(\mathbf{k}', \alpha')}^{(1)} &:= \langle \mathbf{k}, \alpha | \hat{r}_1 | \mathbf{k}', \alpha' \rangle \\ &= \kappa \int dx dy \sum_{n_1, n_2} \sum_{n'_1, n'_2} (c_{n_1, n_2}^{\mathbf{k}, \alpha})^* c_{n'_1, n'_2}^{\mathbf{k}', \alpha'} \\ &\quad \times e^{-i(n_1 \mathbf{g}_1 + n_2 \mathbf{g}_2 + \mathbf{k}) \cdot \mathbf{r}} e^{i(n'_1 \mathbf{g}_1 + n'_2 \mathbf{g}_2 + \mathbf{k}') \cdot \mathbf{r}} \left( \sqrt{3}x - y \right), \end{aligned} \quad (2.42)$$

$$\begin{aligned} R_{\mathcal{I}(\mathbf{k}, \alpha), \mathcal{I}(\mathbf{k}', \alpha')}^{(2)} &:= \langle \mathbf{k}, \alpha | \hat{r}_2 | \mathbf{k}', \alpha' \rangle \\ &= 2\kappa \int dx dy \sum_{n_1, n_2} \sum_{n'_1, n'_2} (c_{n_1, n_2}^{\mathbf{k}, \alpha})^* c_{n'_1, n'_2}^{\mathbf{k}', \alpha'} \\ &\quad \times e^{-i(n_1 \mathbf{g}_1 + n_2 \mathbf{g}_2 + \mathbf{k}) \cdot \mathbf{r}} e^{i(n'_1 \mathbf{g}_1 + n'_2 \mathbf{g}_2 + \mathbf{k}') \cdot \mathbf{r}} y. \end{aligned}$$

The expression to calculate  $R_{\mathcal{I}(\mathbf{k}, \alpha), \mathcal{I}(\mathbf{k}', \alpha')}^{(2)}$  can be rewritten as

$$\begin{aligned} R_{\mathcal{I}(\mathbf{k}, \alpha), \mathcal{I}(\mathbf{k}', \alpha')}^{(2)} &= 2\kappa \sum_{n_1, n_2} \sum_{n'_1, n'_2} (c_{n_1, n_2}^{\mathbf{k}, \alpha})^* c_{n'_1, n'_2}^{\mathbf{k}', \alpha'} \\ &\quad \times \underbrace{\left( \int dx dy e^{-i(n_1 \mathbf{g}_1 + n_2 \mathbf{g}_2 + \mathbf{k}) \cdot \mathbf{r}} e^{i(n'_1 \mathbf{g}_1 + n'_2 \mathbf{g}_2 + \mathbf{k}') \cdot \mathbf{r}} y \right)}_{\mathcal{K}_2(\mathbf{k}, \mathbf{k}')}. \end{aligned} \quad (2.43)$$

The integral can be evaluated analytically,

$$\begin{aligned} \mathcal{K}_2(\mathbf{k}, \mathbf{k}') &= \int dx dy e^{-i(n_1 \mathbf{g}_1 + n_2 \mathbf{g}_2 + \mathbf{k}) \cdot \mathbf{r}} e^{i(n'_1 \mathbf{g}_1 + n'_2 \mathbf{g}_2 + \mathbf{k}') \cdot \mathbf{r}} y \\ &= \int dx dy e^{i\left(\frac{2\pi}{a}(n'_1 - n_1) + (k'_x - k_x)\right)x} e^{i\left(\frac{4\pi}{\sqrt{3}a}(n'_2 - n_2) - \frac{2\pi}{\sqrt{3}a}(n'_1 - n_1) + (k'_y - k_y)\right)y} y \\ &= \int dx e^{i\lambda(\mathbf{k}, \mathbf{k}')x} \int dy e^{i\mu(\mathbf{k}, \mathbf{k}')y} y. \end{aligned} \quad (2.44)$$

<sup>13</sup>We introduced the extra factor of  $\frac{1}{2\pi}$  to ensure that the eigenvalues of the position operators are multiples of 1, not  $2\pi$ .

<sup>14</sup>This allows us to calculate eigenvalues of  $R_j$ .

Similarly,

$$\mathcal{K}_1(\mathbf{k}, \mathbf{k}') = \int dx e^{i\lambda(\mathbf{k}, \mathbf{k}')x} \int dy e^{i\mu(\mathbf{k}, \mathbf{k}')y} (\sqrt{3}x - y). \quad (2.45)$$

We call  $\mathcal{K}_i(\mathbf{k}, \mathbf{k}')$  the geometric tensors<sup>15</sup>. To evaluate these integrals we need to set sensible real-space integration bounds. We use the integration bounds shown in Fig. 2.12

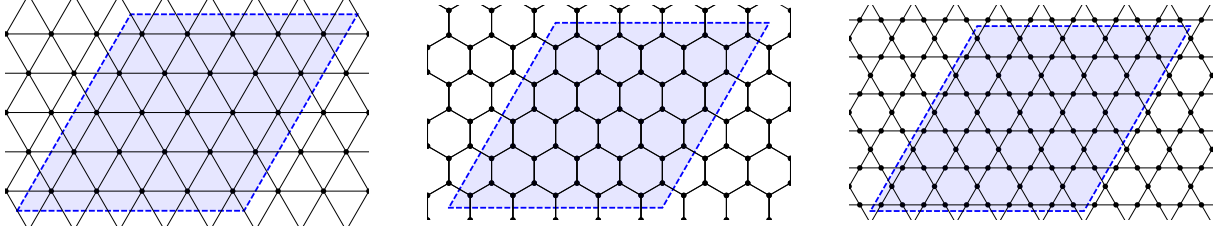


**Figure 2.12** – Triangular, honeycomb, and kagome lattices with the real-space integration region (blue, dashed line). Here,  $L=5$ .

The real-space integration is separated into three parts, as shown in figure Fig. 2.13.

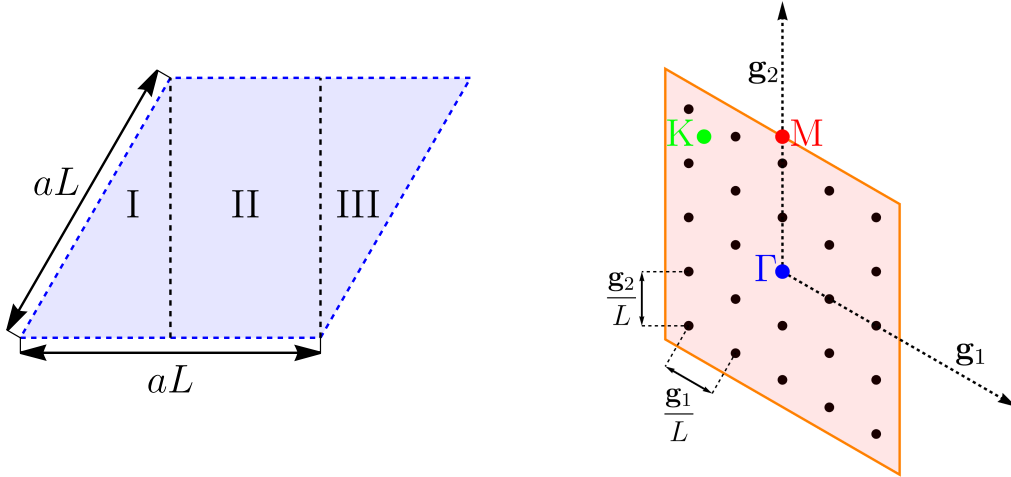


**Figure 2.13** – Left: the integration over a parallelogram in real space is split into three integrals (labelled I, II & III). Right: discretization of the Brillouin zone. Here,  $L=5$ . The orange line is the boundary of the BZ, the black points are the points at which  $\mathcal{K}_1$  &  $\mathcal{K}_2$  are evaluated.

Eq. 2.44 can thus be rewritten as the sum of three integrals,

$$\begin{aligned} \mathcal{K}_2(\mathbf{k}, \mathbf{k}') &= \int dx e^{i\lambda(\mathbf{k}, \mathbf{k}')x} \int dy e^{i\mu(\mathbf{k}, \mathbf{k}')y} y \\ &= \left( \int_{x=0}^{\frac{1}{2}aL} \int_{y=0}^{\sqrt{3}x} + \int_{x=\frac{1}{2}aL}^{aL} \int_{y=0}^{\frac{\sqrt{3}}{2}aL} + \int_{x=aL}^{\frac{3}{2}aL} \int_{y=\sqrt{3}(x-aL)}^{\frac{\sqrt{3}}{2}aL} \right) dx dy e^{i\lambda(\mathbf{k}, \mathbf{k}')x} e^{i\mu(\mathbf{k}, \mathbf{k}')y} y. \end{aligned} \quad (2.46)$$

<sup>15</sup>Not to be confused with the metric tensor or the quantum geometric tensor.

The geometric tensors,  $\mathcal{K}_1(\mathbf{k}, \mathbf{k}')$  and  $\mathcal{K}_2(\mathbf{k}, \mathbf{k}')$ , can be calculated analytically which significantly speeds up calculating the Wannier states.

**Discretizing a non-separable Brillouin zone** Fig. 2.13 shows a possible discretization of the Brillouin zone. We choose

$$\mathbf{k}_{ij} = - \left( 1 - \frac{1}{L} \right) \left( \frac{\mathbf{g}_1}{2} + \frac{\mathbf{g}_2}{2} \right) + \frac{1}{L} (i\mathbf{g}_1 + j\mathbf{g}_2) \quad i, j \in \{0, \dots, L-1\}. \quad (2.47)$$

The geometric tensors,  $\mathcal{K}_1$  &  $\mathcal{K}_2$ , are square matrices of dimension  $L^2 \times L^2$ . Each entry is a matrix of dimension  $N^2 \times N^2$ , where  $N$  is the number of orders of  $\mathbf{g}_1$  and  $\mathbf{g}_2$  used to determine the Bloch states.

**Eigenvalues of  $R_1$  and  $R_2$**  The eigenvalues of  $R_1$  and  $R_2$  are equal to the positions of the lattice sites along  $\mathbf{g}_1$  and  $\mathbf{g}_2$ , respectively. Each eigenvalue of  $R_1$  and  $R_2$  is  $L$ -fold degenerate, since all lattice sites get projected to a line spanned by  $\mathbf{g}_1$  or  $\mathbf{g}_2$ . For example, if there are two lattice sites that have the same coordinate in units of  $\mathbf{g}_1 \cdot \mathbf{r}$ ,  $R_1$  will have two degenerate eigenvalues corresponding to that coordinate. To determine a Wannier state on some site in the 2-dimensional lattice, we first find the eigenvalues of  $R_1$ , choose a degenerate subspace belonging to one of these eigenvalues, project  $R_2$  onto this degenerate subspace and then diagonalize  $R_2$ . The eigenvalues of  $R_1$  and  $R_2$  will have a structure as shown in Fig. 2.14.

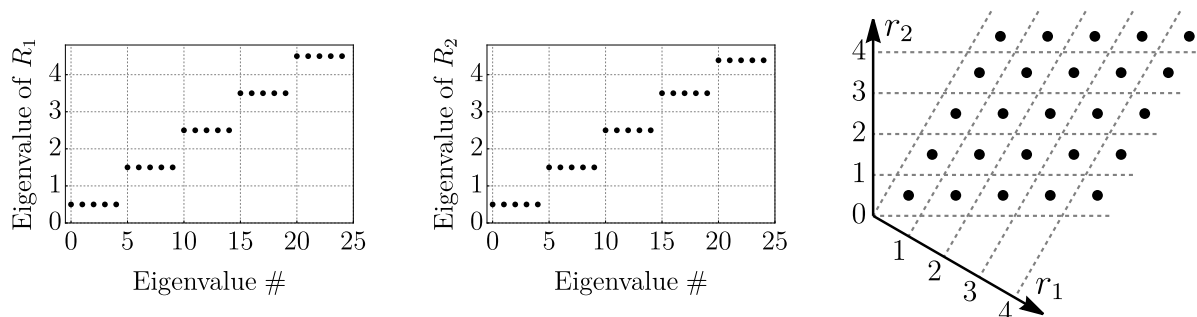


**Figure 2.14** – Left (centre): eigenvalues of  $R_1$  ( $R_2$ ) for the optical kagome lattice. Right: lattice sites reconstructed from eigenvalues of position operators  $R_1$  &  $R_2$ .  $L=5$ .

By choosing an uneven  $L$ , we ensure that there is only one site in the centre of the lattice. To determine this central site's Wannier state, we project  $R_2$  onto the subset of eigenstates of  $R_1$  with eigenvalue  $L/2$ . The eigenvalues of projected  $R_2$  are equal to the coordinates along  $g_2$  of those sites whose coordinate along  $R_1$  is  $L/2$ . We can now choose the unique, non-degenerate eigenvalue  $L/2$  of projected  $R_2$  to give us the lattice site at the centre of the lattice.

The associated eigenvector, with coefficients  $w_{\mathbf{k},\alpha}$ , is the Wannier state expressed in a Bloch-state basis ( $\mathbf{k}$ -state basis). To obtain a real-space representation of the Wannier state, we need to multiply the eigenvector of the (band-projected) position operator with the real-space representation of the Bloch states,

$$\begin{aligned}
w(\mathbf{r}) &= \sum_{\mathbf{k}, \alpha} w_{\mathbf{k}, \alpha} \langle \mathbf{r} | \mathbf{k}, \alpha \rangle \\
&= \sum_{n_1, n_2} \sum_{\mathbf{k}, \alpha} w_{\mathbf{k}, \alpha} c_{n_1, n_2}^{\mathbf{k}, \alpha} e^{i(n_1 \mathbf{g}_1 + n_2 \mathbf{g}_2 + \mathbf{k}) \cdot \mathbf{r}}.
\end{aligned} \tag{2.48}$$

Note that the geometric tensor and the real-space integration bounds can be applied to the triangular, honeycomb, and kagome lattices interchangeably. Only the Bloch states and energies change between the lattice types; the geometry of the Brillouin zone and unit cell are unchanged. To find the maximally localized Wannier states in the s-band of the triangular, honeycomb, and kagome lattices it is necessary to include the first, first two, and first three bands, respectively, when constructing the position operators. The lattice depth and type is encoded in the Bloch states. Bloch states are calculated by solving the Schrödinger equation as we did previously for the kagome lattice (Eq. 2.33).

**Making use of translational symmetry** We find that the numerical accuracy of the calculated Wannier states is higher for central sites. Therefore, we calculate the Wannier state at the central site of the lattice<sup>16</sup> and make use of translational symmetry to determine Wannier states on other lattice sites,

$$\begin{aligned}
w(\mathbf{r} - (p\mathbf{a}_1 + q\mathbf{a}_2)) &= \sum_{n_1, n_2} \sum_{\mathbf{k}, \alpha} w_{\mathbf{k}, \alpha} c_{n_1, n_2}^{\mathbf{k}, \alpha} e^{i(n_1 \mathbf{g}_1 + n_2 \mathbf{g}_2 + \mathbf{k}) \cdot (\mathbf{r} - (p\mathbf{a}_1 + q\mathbf{a}_2))} \\
&= \sum_{n_1, n_2} \sum_{\mathbf{k}, \alpha} w_{\mathbf{k}, \alpha} c_{n_1, n_2}^{\mathbf{k}, \alpha} e^{i(n_1 \mathbf{g}_1 + n_2 \mathbf{g}_2 + \mathbf{k}) \cdot \mathbf{r}} e^{-i\mathbf{k} \cdot (p\mathbf{a}_1 + q\mathbf{a}_2)} \\
&= \sum_{\mathbf{k}, \alpha} w_{\mathbf{k}, \alpha} e^{-i\mathbf{k} \cdot (p\mathbf{a}_1 + q\mathbf{a}_2)} \langle \mathbf{r} | \mathbf{k}, \alpha \rangle,
\end{aligned} \tag{2.49}$$

where  $\mathbf{a}_1$  and  $\mathbf{a}_2$  are the lattice vectors (defined in Eq. 2.28),  $p$  and  $q$  are integers, and we have made use of the relations in Eq. 2.27. The vector  $w_{\mathbf{k}, \alpha}$  is the eigenstate of the band-projected position operators on the central site. For lattices with multiple sites per unit cell, such as the honeycomb and kagome lattices, we first determine the Wannier state of each site in a unit cell at the centre of the lattice. Wannier states on sites outside the central unit cell can then be calculated by using Eq. 2.49.

**Wannier state phase** A Wannier function calculated with Eq. 2.48 is generally complex, but can be made to be real by multiplying it with a phase factor  $e^{-i\phi}$  where

$$\phi = \arg \left( \sum_{n_1, n_2} \sum_{\mathbf{k}, \alpha} w_{\mathbf{k}, \alpha} c_{n_1, n_2}^{\mathbf{k}, \alpha} \right). \tag{2.50}$$

In practice, the magnitude of the calculated Wannier states' imaginary part is negligible (on the order of machine precision) when incorporating this phase factor.

<sup>16</sup>Or central unit cell for lattices with multiple sites per unit cell.

**Triangular lattice** The triangular lattice only contains one site per unit cell, which causes the lowest band to split from higher bands. The maximally localized, s-wave Wannier states are thus the eigenstates of the position operator projected onto the lowest band. We determine the Bloch states by solving

$$\begin{aligned} & \frac{1}{k^2} |\mathbf{q} + m\mathbf{g}_1 + n\mathbf{g}_2|^2 c_{\mathbf{q},m,n} \\ & - \frac{s}{4} (c_{\mathbf{q},m-1,n} + c_{\mathbf{q},m+1,n} + c_{\mathbf{q},m-1,n-1} + c_{\mathbf{q},m+1,n+1} + c_{\mathbf{q},m,n-1} + c_{\mathbf{q},m,n+1}) \\ & = \varepsilon_{\mathbf{q}}^{\text{ret}}(s) c_{\mathbf{q},m,n}, \end{aligned} \quad (2.51)$$

where  $s$  is the depth of the triangular lattice in units of  $\frac{\hbar^2 k^2}{2m}$ .

Fig. 2.15 shows the numerically calculated, maximally localized, s-wave Wannier state in the optical triangular lattice.

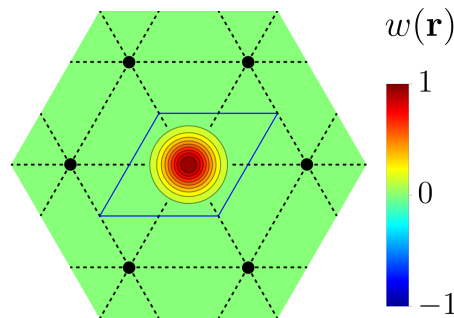


**Figure 2.15** – s-wave Wannier state in the triangular lattice with  $s=10$ . The region bounded by the blue line is a unit cell.

**Honeycomb lattice** As shown previously, the optical honeycomb lattice can be implemented by inverting the optical triangular lattice. The Bloch state equation is thus

$$\begin{aligned} & \frac{1}{k^2} |\mathbf{q} + m\mathbf{g}_1 + n\mathbf{g}_2|^2 c_{\mathbf{q},m,n} \\ & + \frac{s}{4} (c_{\mathbf{q},m-1,n} + c_{\mathbf{q},m+1,n} + c_{\mathbf{q},m-1,n-1} + c_{\mathbf{q},m+1,n+1} + c_{\mathbf{q},m,n-1} + c_{\mathbf{q},m,n+1}) \\ & = \varepsilon_{\mathbf{q}}^{\text{ret}}(s) c_{\mathbf{q},m,n}. \end{aligned} \quad (2.52)$$

Note the sign change of  $s$  compared to Eq. 2.51. To determine the maximally localized Wannier state in the honeycomb lattice, the position operators are projected onto the two lowest bands. This is necessary since the honeycomb lattice contains two sites per unit cell. Fig. 2.16 shows the eigenvalues of the position operators and the calculated Wannier functions for both sites in the unit cell.

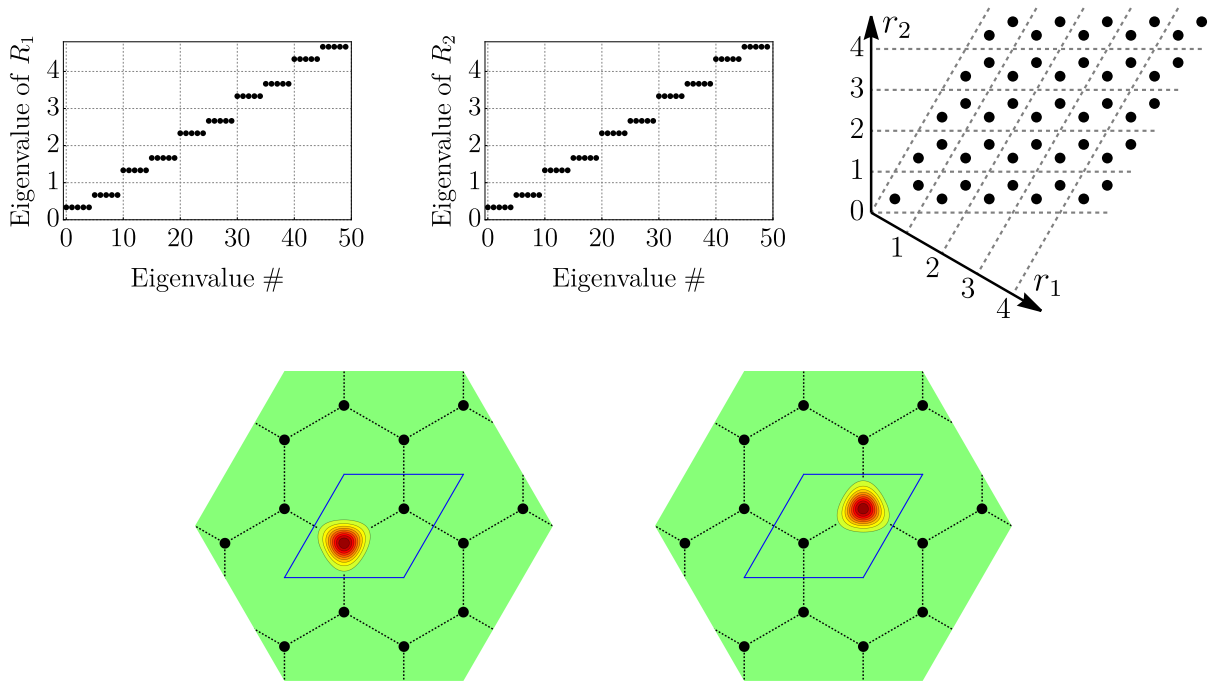


**Figure 2.16** – Top left (centre): eigenvalues of  $R_1$  ( $R_2$ ) for the honeycomb lattice potential. Top right: lattice sites reconstructed from eigenvalues of position operators  $R_1$  &  $R_2$ .  $L=5$ . Bottom: s-wave Wannier states on the honeycomb lattice for  $s=100$ . Colour function is as in Fig. 2.15.

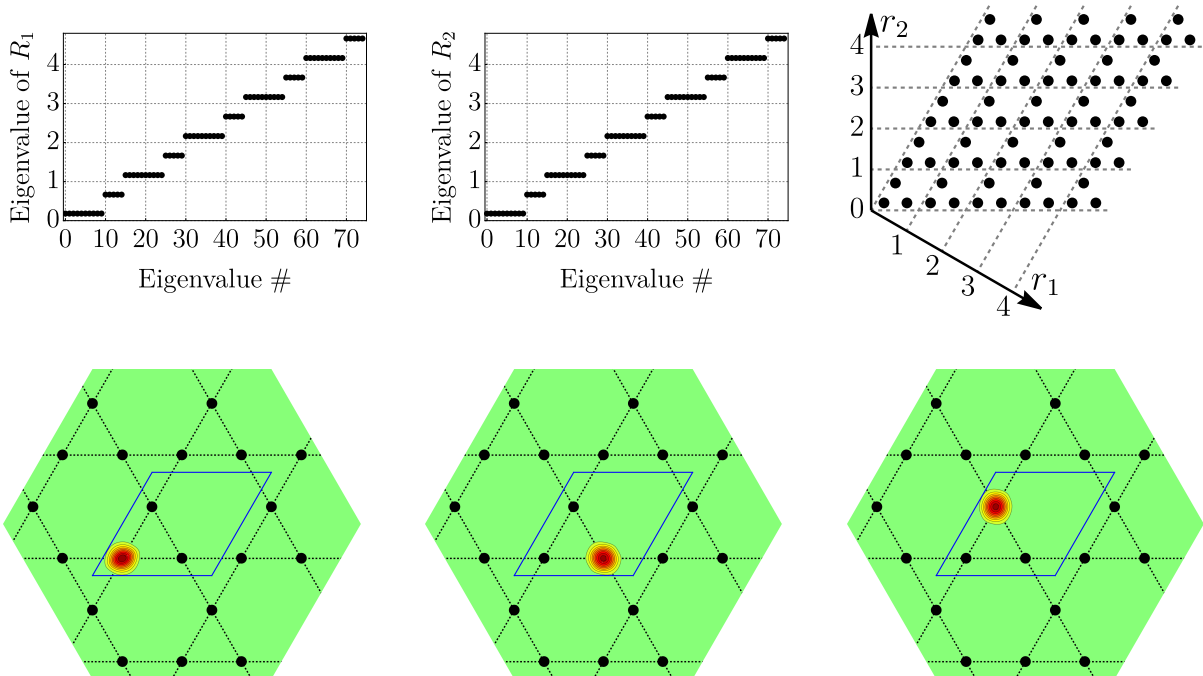


**Figure 2.17** – Left (centre): eigenvalues of  $R_1$  ( $R_2$ ). Right: lattice sites reconstructed from eigenvalues of position operators  $R_1$  &  $R_2$ .  $L=5$ . Bottom: s-wave Wannier states on the kagome lattice for  $s_S=s_L=15$ . Colour function is as in Fig. 2.15.

**Kagome lattice** To determine the Bloch states of the kagome lattice we solve Eq. 2.33. The kagome lattice contains three sites per unit cell so we project the position operators onto the three lowest bands to determine the maximally localized s-wave Wannier states. The energy spectra of the projected position operators and the resulting real-space representations of the Wannier functions on the kagome lattice are shown in Fig. 2.17.

**Kagome flat band** One of the kagome lattice's unique features is that it has a flat band. As discussed in chapter 1, it is possible to construct flat band eigenstates that are localized in real space. These can also be thought of as eigenstates of the position operator projected onto the flat band. By employing the same method used to construct the maximally localized, s-wave Wannier functions, we can also determine the shape of the flat band's localized eigenstates (Fig. 2.18)

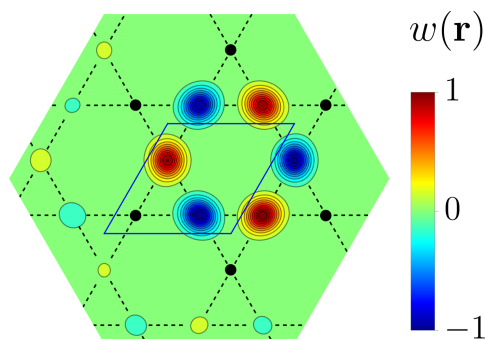


**Figure 2.18** – Maximally localized eigenstate of the position operator projected onto the third band of the kagome lattice with a lattice depth of  $s_S=s_L=5$ . Note the hexagonal structure and the alternating sign of the wave function's amplitude.

We can determine Wannier states on the flat band individually since any superposition of flat band Bloch states is again a flat band eigenstate. Projecting the position operators onto one of the dispersive sub-bands does not result in a physically relevant Wannier state.

## 2.5 Tunnelling rates (Hubbard $t$ )

We saw previously that the lowest bands of an optical lattice approach the tight-binding limit for deep lattices ( $s > 5$ ) and that we can calculate the nearest-neighbour tunnelling rate by numerically calculating the band width. However, this approach does not allow us to calculate further than nearest-neighbour tunnelling or tunnelling in higher motional bands (e.g. p-wave and d-wave bands). Wannier states can be used to determine tunnelling rates beyond nearest-neighbour, which could prove useful for future experiments involving Floquet shaking [19] and creating topological bands [110, 150]. We can express the single-particle optical lattice Hamiltonian ( $H$ ) in the lattice site basis,

$$\begin{aligned}
t_{ij} = H_{ij} &= \langle i | H | j \rangle = \sum_{\mathbf{k}, \mathbf{k}'} \sum_{\alpha, \alpha'} \langle i | \mathbf{k}, \alpha \rangle \underbrace{\langle \mathbf{k}, \alpha | H | \mathbf{k}', \alpha' \rangle}_{E_{\mathbf{k}, \alpha} \delta_{\mathbf{k}, \mathbf{k}'} \delta_{\alpha, \alpha'}} \langle \mathbf{k}, \alpha' | j \rangle \\
&= \sum_{\mathbf{k}} \sum_{\alpha} E_{\mathbf{k}, \alpha} (w_{\mathbf{k}, \alpha}^i)^* w_{\mathbf{k}, \alpha}^j,
\end{aligned} \tag{2.53}$$

where  $E_{\mathbf{k}, \alpha}$  is the energy of the Bloch state in band  $\alpha$  at momentum  $\mathbf{k}$ . We made use of the fact that  $H$  is diagonal in the Bloch state basis. In [Eq. 2.48](#) we showed that two Wannier vectors on the same sublattice but in different unit cells are related by

$$w_{\mathbf{k}, \alpha}^j = w_{\mathbf{k}, \alpha}^i e^{i\mathbf{k} \cdot (\mathbf{r}_i - \mathbf{r}_j)}. \tag{2.54}$$

Thus, for two sites  $i, j$  on a lattice with only one site per unit cell, [Eq. 2.53](#) simplifies to

$$t_{ij} = \sum_{\mathbf{k}} E_{\mathbf{k}} |w_{\mathbf{k}}^i|^2 e^{i\mathbf{k} \cdot (\mathbf{r}_i - \mathbf{r}_j)} = \frac{1}{L^2} \sum_{\mathbf{k}} E_{\mathbf{k}} e^{i\mathbf{k} \cdot (\mathbf{r}_i - \mathbf{r}_j)}, \tag{2.55}$$

where  $L^2$  is the number of  $\mathbf{k}$  points we use to discretize the two-dimensional Brillouin zone. Calculating the tunnelling rate on a lattice with a single site per unit cell, such as the triangular lattice, does not require us to calculate the Wannier state. However, for the honeycomb and kagome lattices [Eq. 2.54](#) does not hold and the Wannier states in general have to be calculated to determine the tunnelling rate.

In [Fig. 2.19](#) we show various tunnelling rates in the triangular, honeycomb, and kagome lattices calculated using [Eq. 2.53](#). Note that for deep kagome lattices, the nearest-neighbour tunnelling rate obtained via the Wannier state approach is identical to the tunnelling rate calculated using the band structure (see [Fig. 2.9](#)). For small lattice depths in the honeycomb and kagome lattices the calculated higher-order tunnelling rates deviate from the monotonic behaviour seen for deeper lattices. This is likely due to the fact that we only take into account the lowest two (three) bands when determining the Wannier states in the honeycomb (kagome) lattice. For shallow lattices the band gap is small and neglecting higher bands leads to inaccurate Wannier states.

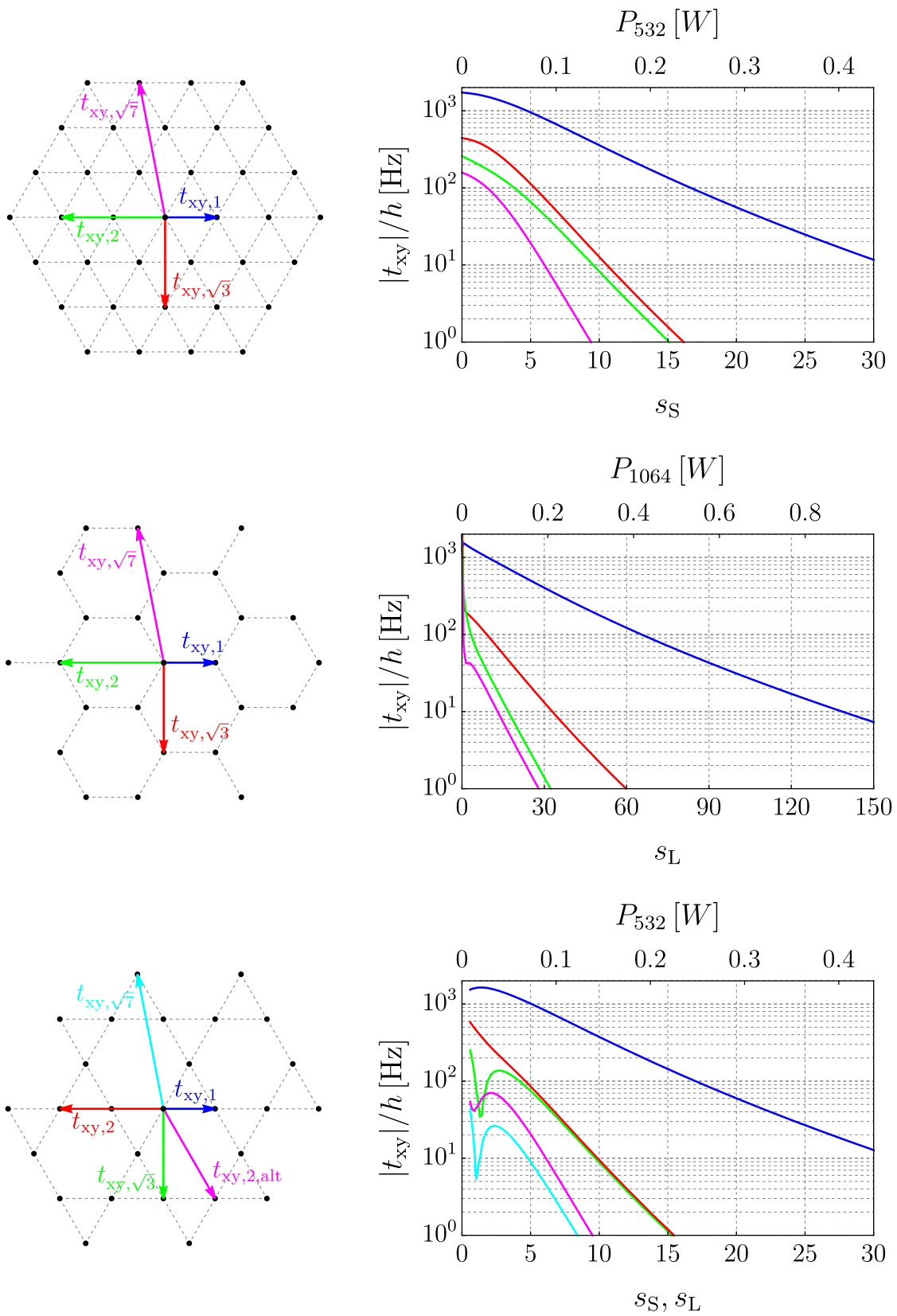


**Figure 2.19** – Tunnelling rates for  $^{39}\text{K}$  in the interfering triangular (top), honeycomb (centre), and kagome (bottom) lattices. The colours on the right correspond to the tunnelling term shown on the left.

## 2.6 Interactions (Hubbard $U$ )

The Wannier states allow us to calculate the on-site interaction (Hubbard  $U$ ) via

$$U = \frac{4\pi\hbar^2 a_s}{m} \int d^3r |w(\mathbf{r})|^4. \quad (2.56)$$

In terms of  $E_R$ ,  $U$  can be written as

$$\frac{U}{E_R} = \frac{2m}{\hbar^2 k^2} \frac{4\pi\hbar^2 a_s}{m} \int d^3r |w(\mathbf{r})|^4. \quad (2.57)$$

We can simplify the calculation of the integral by going to dimensionless units, i.e. by substituting  $\mathbf{r}$  with  $a\mathbf{x}$ <sup>17</sup>,

$$\int d^3r |w(\mathbf{r})|^4 = \frac{1}{a^3} \int d^3x |w(\mathbf{x})|^4, \quad (2.58)$$

where  $a$  is the spacing between unit cells. This dimensionless integral depends only on the lattice depth (in units of  $E_R$ ) and can be numerically calculated for Wannier states of the form Eq. 2.48. The interaction energy in terms of  $E_R$  is thus

$$\frac{U}{E_R} = \frac{8\pi a_s}{k^2 a^3} \int d^3x |w(\mathbf{x})|^4. \quad (2.59)$$

Note that the interaction energy scales as  $\frac{1}{\lambda}$  for a constant lattice depth  $s$ . The interaction energy for the triangular, honeycomb, and kagome lattices can be separated into a vertical ( $z$ ) and horizontal ( $xy$ ) component,

$$U = \frac{4\pi\hbar^2 a_s}{m} \int d^3r |w(\mathbf{r})|^4 = \frac{4\pi\hbar^2 a_s}{m} \int dx dy |w_{xy}(x, y)|^4 \int dz |w_z(z)|^4. \quad (2.60)$$

The spatial extent of a Wannier function along the vertical direction is affected by the vertical lattice depth. Deeper lattices cause the Wannier function to be more localized and thus lead to an increase in interaction energy. In contrast to the tunnelling rate, the interaction energy depends on the depth of the vertical lattice and must be taken into account when calculating  $U$ . Generally we are interested in knowing the interaction strength as a function of the depth of the horizontal lattice, since this is what is varied in a typical experiment.

Therefore, to visualize how the interaction strength varies as a function of horizontal lattice depth, we fix the vertical lattice depth to  $s_V = 30$ . The vertical component of the Wannier integral will just factor out as a constant. We calculate the vertical component of the Wannier state in the same way as we do the horizontal components, i.e. by finding the eigenstates of the band-projected position operator. Fig. 2.20 shows the interaction strength, nearest-neighbour tunnelling rate, and  $U/t$  for <sup>39</sup>K in the triangular, honeycomb, and kagome lattices. We find that the nearest-neighbour tunnelling rate in the kagome lattice is virtually identical to that of the triangular lattice.

<sup>17</sup>The additional factor of  $\frac{1}{a^3}$  can be derived by ensuring normalization of the Wannier function. For a more detailed discussion, see [148].

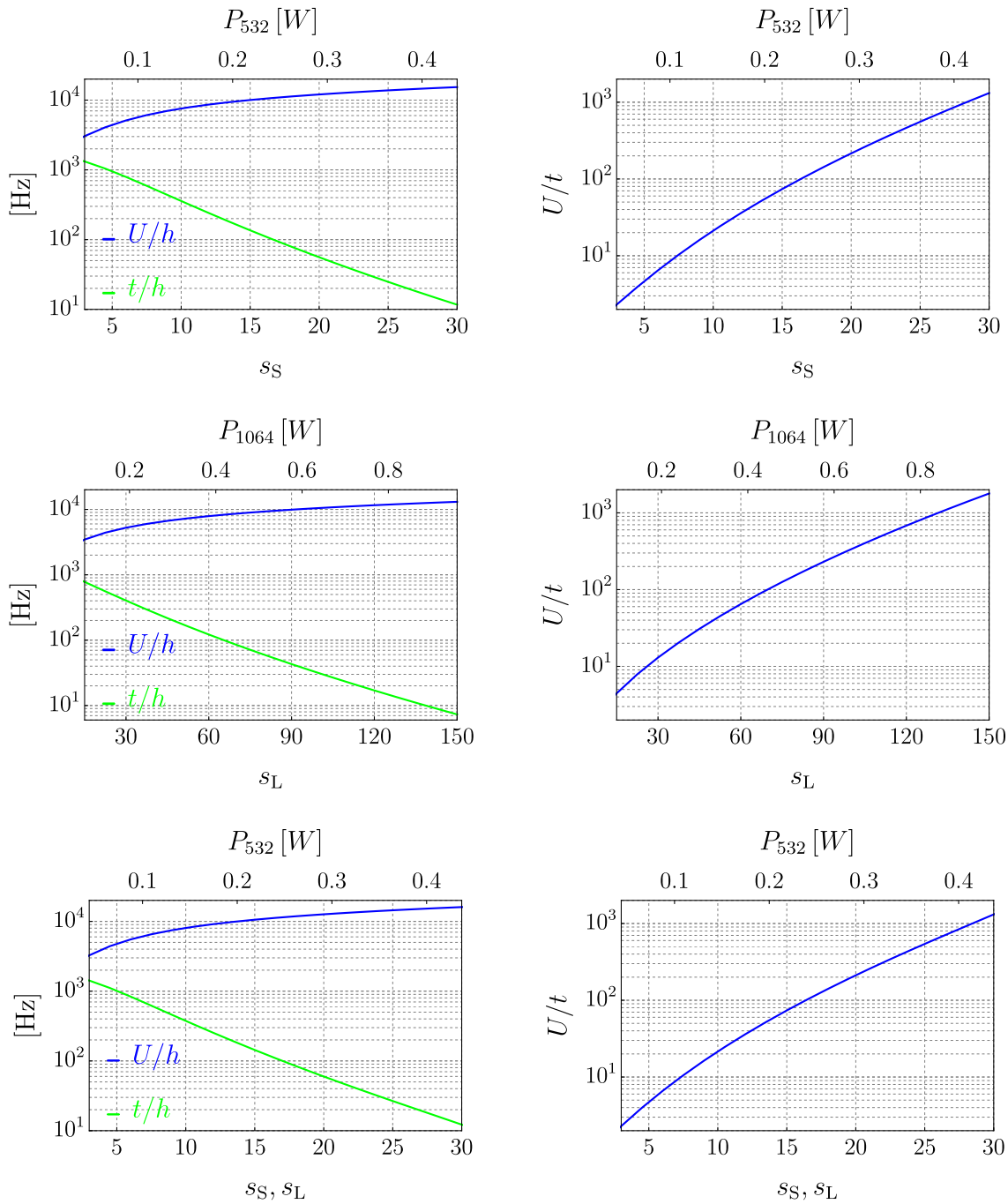


**Figure 2.20** – Hubbard  $U$  &  $t$  (left) and  $U/t$  (right) for  $^{39}\text{K}$  in the interfering triangular (top), honeycomb (centre), and kagome (bottom) lattices as a function lattice depth. We assume  $a_S=300a_0$  and a vertical lattice depth of  $30E_R$ . We also assume that the horizontal lattice beams have waists of  $100\ \mu\text{m} \times 50\ \mu\text{m}$ . Note that for the kagome lattice plots (bottom row),  $s_L = s_S$ . The wavelengths of the short-wavelength, long-wavelength, and vertical lattices are 532 nm, 1064 nm, and 1064 nm, respectively. The power per beam required to reach lattice depths  $s_S$  or  $s_L$  ( $P_{532}$  or  $P_{1064}$ , respectively) are specified on top of each plot.

This shows that the Hubbard parameters in the kagome lattice are dominated by the

short-wavelength lattice. Fig. 2.20 also shows that the honeycomb lattice requires much larger lattice depths than the triangular lattice to suppress the tunnelling rate to a given value. In practice this means that we need about twice the amount of 1064 nm power forming a honeycomb lattice to reach the same tunnelling rate as a triangular lattice formed of 532 nm lasers<sup>18</sup>.

The tunnelling rates and interaction strengths our code produces agree with those cited in [20, 41, 137, 145, 148, 151].

---

<sup>18</sup>The polarizability of <sup>87</sup>Rb and <sup>39</sup>K at 1064 nm is about -2.2 times the polarizability at 532 nm.

### 3 Negative temperatures & bosons in flat bands

In this chapter we show how to prepare a negative temperature state in an optical lattice system and we discuss expected signatures of bosons in the flat band of the kagome lattice. Our intention is to reconcile the various different points of view that have emerged in the study of bosonic phases of the kagome lattice. Since there are still many unknowns with regard to how closely our machine implements various established theoretical models for the kagome flat band, we will first discuss the expected single-particle behaviour and expected signatures before moving on to the interacting case. For interacting bosons we will summarize the effects expected in the high density [88, 152] and low density [84] regimes.

#### 3.1 Negative temperatures

Temperature is a property of a system in equilibrium. A classical system in thermodynamic equilibrium is described by Boltzmann statistics and quantum systems are generally described by either fermionic or bosonic statistics (Fermi-Dirac or Bose-Einstein, respectively). We will begin by taking a quick look at negative temperatures in a classical spin system [153].

##### 3.1.1 Classical negative temperatures

Already in the mid 1950s, Ramsey derived various quantities at negative temperatures and discussed some of the consequences of negative temperature Carnot machines [153]. A simple model system for understanding the consequences of negative temperatures is a classical Ising spin system in an external magnetic field. Defining the magnetic moment per spin to be  $\mu$  and the external magnetic field strength to be  $B$ , the partition function for a system of  $N$  spins is

$$\begin{aligned}
 Z &= \sum_i e^{-\beta E_i} = \sum_{n=-N/2}^{N/2} e^{-2\beta\mu B n} \\
 &= e^{\beta\mu B N} \sum_{n=0}^N e^{-2\beta\mu B n} = e^{\beta\mu B N} \left( \frac{1 - e^{-2\beta\mu B(N+1)}}{1 - e^{-2\beta\mu B}} \right) \\
 &= \frac{e^{\beta\mu B(N+1)} - e^{-\beta\mu B(N+1)}}{e^{\beta\mu B} - e^{-\beta\mu B}} = \frac{\sinh(\beta\mu B(N+1))}{\sinh(\beta\mu B)},
 \end{aligned} \tag{3.1}$$

where  $\beta = 1/k_B T$  and  $k_B$  and  $T$  are the Boltzmann constant and the temperature, respectively. From the partition function we can calculate various thermodynamic quantities, such as internal energy  $U$  and entropy  $S$ ,

$$\begin{aligned}
A &= -\frac{1}{\beta} \log(Z), \\
U &= \frac{\partial(\beta A)}{\partial \beta} = \mu B \left\{ \coth(\beta \mu B) - (N+1) \coth(\beta \mu B (N+1)) \right\}, \\
S &= k_B \beta^2 \frac{\partial A}{\partial \beta} = k_B \log \left( \frac{\sinh(\beta \mu B (N+1))}{\sinh(\beta \mu B)} \right) \\
&\quad + k_B \beta \mu B \left\{ (\coth(\beta \mu B) - (N+1) \coth(\beta \mu B (N+1))) \right\}.
\end{aligned} \tag{3.2}$$

Fig. 3.1 shows how the total internal energy and the entropy change as a function of  $-\beta \mu B$ .

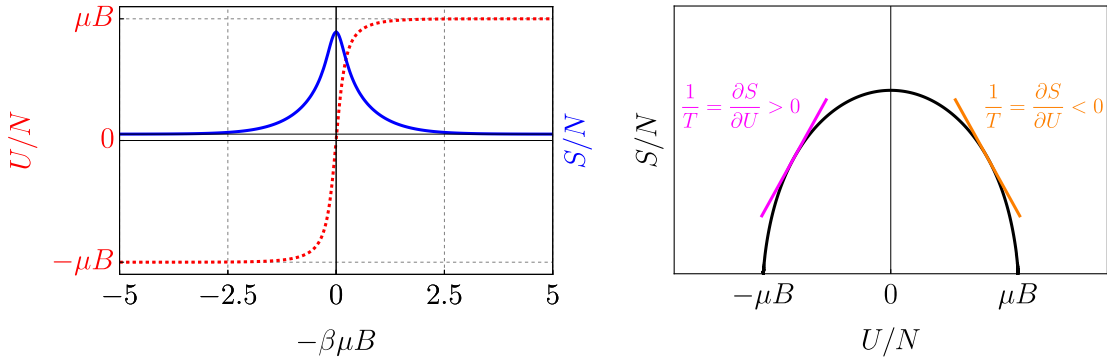


**Figure 3.1** – Left: internal energy (red) and entropy (blue) of an Ising spin system as a function of inverse temperature. As  $-\beta$  goes to  $-\infty$  ( $+\infty$ ),  $T$  goes to  $0^+$  ( $0^-$ ). At  $-\beta = 0$ ,  $T = \pm\infty$ . Right:  $S$  vs  $U$ . The spin system has zero entropy at maximum or minimum energy.

We use  $-\beta$  as a measure for temperature rather than  $T$ , since the thermodynamic quantities are continuous as we vary  $\beta$  from  $-\infty$  to  $\infty$ . This is not the case for  $T$ . Intuitively this makes sense since at  $T = -\infty$  and  $T = +\infty$  the system has the same statistical mixture of spin distributions, whereas for  $T = +0$  ( $T = -0$ ) all spins are parallel (anti-parallel) to the magnetic field.

We can see from these considerations that if we define temperature as the inverse of the derivative of entropy with internal energy,

$$\frac{1}{T} = \frac{\partial S}{\partial U}, \tag{3.3}$$

and the internal energy is bounded, then there are situations in which the entropy decreases as the internal energy is increased<sup>19</sup>. This is shown schematically in Fig. 3.1 for the spin system. Note that negative temperatures can also be stable in the thermodynamic limit, for which the energy and the particle number diverge. For the infinite system, negative temperatures are stable if the energy density, or per-particle energy is bounded. Without an upper bound on per-particle energy, the Boltzmann distribution at negative

<sup>19</sup>If the spectrum is bounded and the energy is increased, then eventually the system will only occupy the highest energy state and entropy is zero.

temperature is not normalizable and hence will not be stable. Note also that pumping entropy into a system at negative temperature will cause the internal energy to decrease, which is the opposite of what happens in the positive temperature case.

At this point we may ask ourselves what keeps a system at negative temperature from simply decaying to lower energy states like an out-of-equilibrium system might do. The answer is that a system with negative temperature has ‘too much’ energy. If the system is closed, there is no way of depositing energy that would be freed from a decay process. Since the excess energy that would be acquired through decay to lower energy states cannot be deposited, the decay process is suppressed and the negative temperature state remains intact. This is the same argument to why repulsively bound pairs are stable [154].

How can we create a negative temperature state? Negative temperatures manifest themselves by population inversion, i.e. states with high energy are populated more than those at low energy. Starting from a positive temperature state, pumping infinite heat into the system will only lead to an infinite temperature state at which all energies are equally occupied, not however to a state with population inversion. Pumping heat into the system also creates entropy, which drives it further away from population inversion, since negative temperatures very close to zero are also states with very low entropy. Thus, starting from a positive temperature state, it is not possible to create a negative temperature state via a purely thermodynamic process.

It is possible to overcome this limitation however. Rather than act upon the particles or spins, one can suddenly change the Hamiltonian itself so that some initial configuration is mapped onto the highest energy state of the new Hamiltonian. For example, we can prepare a low entropy state in the spin system discussed above, e.g. by increasing the magnetic field strength or lowering the temperature. At low entropies and positive temperatures, all spins are aligned with the external magnetic field. To create a low-entropy negative temperature state we only need to flip the magnetic field quickly so that the magnetic field and the spins are anti-aligned. This needs to be done quickly to avoid spins changing their orientation. By flipping the magnetic field we have now prepared the highest energy state at low entropy, i.e. the system is in a negative temperature state. Purcell and Pound used this protocol to create negative temperatures in nuclear spin systems [155]. We will use the same ideas developed here to show how we can create a negative temperature state in an optical lattice system.

### 3.1.2 Negative temperatures in optical lattices

**Bose-Hubbard energy terms** Negative temperatures are intuitive for spin systems as there is both an obvious lower bound on energy (all spins aligned with an external magnetic field) as well as an upper bound (all spins anti-aligned with an external magnetic field). In optical lattices it is not obvious, and indeed not always the case, that there is an upper bound on per-particle energy. If one were able to engineer an optical lattice system with an upper bound on per-particle energy then a negative temperature state would be stable. We will discuss the relevant energy scales in an optical lattice system independently and will show how an upper bound can be engineered provided that certain parameters in the Hamiltonian can be changed. Using the (Bose-)Hubbard Hamiltonian to describe the optical lattice system,

$$\hat{H} = \underbrace{-t \sum_{\langle i,j \rangle} \hat{a}_i^\dagger \hat{a}_j}_{\hat{H}_{\text{kin}}} + \underbrace{\frac{U}{2} \sum_i \hat{n}_i (\hat{n}_i - 1)}_{\hat{H}_{\text{int}}} + \underbrace{V \sum_i \hat{n}_i i^2}_{\hat{H}_{\text{conf}}}, \quad (3.4)$$

we can identify three independent energy scales:

**Kinetic energy** ( $\hat{H}_{\text{kin}}$ ) The kinetic energy describes tunnelling of bosons between nearest-neighbour lattice sites. For deep optical lattices, the per-particle kinetic energy is always bounded from below and above. In tight-binding (see [section 2.3](#)) this is obviously true since the allowed single-particle energies are restricted to lie within the tight-binding bands. It is however not as obvious why the per-particle energy should be bounded for a finite-depth lattice, where higher bands are separated by a finite band gap.

The solution to the presence of higher bands is to work at deep enough lattices so that we can restrict the kinetic energy to the s-bands. A closed, ergodic system in thermodynamic equilibrium will explore all states that have a certain energy. Ultracold atoms exchange momentum and thermalize via collisions. If the energy gap between the s-bands and the next band is large enough, the higher-lying states will be decoupled and any ensemble prepared in the s-bands will not be able to explore states beyond the energy gap.

Since ultracold atoms are usually prepared in the lowest band of an optical lattice, there is nothing further one needs to do to impose an upper bound on kinetic energy. Note that this is in stark contrast to a particle in free space, whose energy is bounded below but unbounded above<sup>20</sup>.

**Interaction energy** ( $\hat{H}_{\text{int}}$ ) The interaction energy is given by the second term of [Eq. 3.4](#). Only contact interactions are considered, so that interactions are purely on-site. We can distinguish between two cases.

For repulsively interacting particles, there is only a lower bound on per-particle energy but no upper bound (in the thermodynamic limit). In a  $n=1$  Mott-Insulator, each lattice site is populated by one particle. As a consequence, the interaction energy is zero. This is the lowest energy state the system can be in and thus there is a lower bound on energy. In contrast, in the thermodynamic limit, there is no upper bound on per-particle interaction energy, since an infinite number of particles on the same site will result in each particle having infinite energy. It is thus not possible to prepare a stable negative temperature state in a repulsively interacting cloud.

In the case of attractive interactions, the highest energy state is that in which all sites are occupied by at most one particle. In this case the interaction energy again vanishes. Thus there is an upper bound on per-particle interaction energy, permitting the construction of a negative temperature state. On the other hand, there is no lower bound on interaction energy in the thermodynamic limit since an infinite amount of particles sitting on the same site leads to a per-particle energy of negative infinity.

---

<sup>20</sup>The kinetic energy of a free particle is given by  $\hat{H}_{\text{kin}} = \frac{\mathbf{p}^2}{2m}$ , where  $\mathbf{p}^2$  is the particle momentum and can be arbitrarily large.

**Confinement/potential energy ( $\hat{H}_{\text{conf}}$ )** The third term of Eq. 3.4, which we call the confinement term, is caused by the ‘curvature’ of the optical lattice potential<sup>21</sup> (see appendix C for more details). Lattice curvature is an artefact of the Gaussian intensity profile of the lattice beams. We can distinguish between positive confinement and negative confinement (or anti-confinement).

In a confining (i.e. positive confinement) optical lattice, sites at the centre of the lattice, i.e. the point at which all lattice beams have maximum intensity, have lowest energy and the lattice site offset energy increases quadratically<sup>22</sup> with distance from the centre. This situation corresponds to  $V > 0$  in Eq. 3.4. In general, all optical lattices created with red-detuned wavelengths, such as 1064 nm for <sup>87</sup>Rb, <sup>39</sup>K, and <sup>40</sup>K, are confining. Confining lattices have a lower bound on per-particle energy, but no upper bound.

In an anti-confining (i.e. negative confinement) optical lattice the situation is reversed and the lattice site offset energy decreases quadratically as a function of distance from the lattice centre (i.e.  $V < 0$  in Eq. 3.4). Anti-confining potentials display an upper bound on per-particle energy but no lower bound, making them suitable for the preparation of a negative temperature state. Blue-detuned optical lattices are always anti-confining.

Note that the overall confinement does not only depend on the lattices themselves, but is also affected by any additional optical or magnetic potentials.

In summary, the Hubbard model has an upper bound on per-particle energy when the lattice is sufficiently deep, such that the first band gap is large,  $U$  is negative, i.e. atoms interact attractively, and  $V$  is negative.

**How to prepare a negative temperature state** Now that we know how to engineer an upper bound on per-particle energy in an optical lattice system, it is time to discuss how to actually prepare a negative temperature state. One fundamental issue arises immediately: we are faced with a positive-temperature world. How does one prepare a negative temperature state starting from a positive temperature state? It is much like creating anti-matter in a universe composed of ordinary matter, as soon as a positive temperature and negative-temperature system meet, they form a system with a temperature closer to infinity. Just like preserving anti-matter in a universe full of matter, we need to isolate the negative-temperature state from its detrimental positive-temperature surroundings. Luckily, cold-atom systems are some of the most isolated systems available and are decoupled from their surroundings, making them exquisitely suited for negative temperatures.

The question remains how to turn an isolated positive-temperature system into a negative-temperature system. Much like the classical spin system we discussed previously, we need to find some intermediate state that is simultaneously the lowest energy state of some initial Hamiltonian and the highest energy state of the target Hamiltonian. In the classical spin system we found that such a state is given by a spin configuration in which all spins are aligned with an external magnetic field. In the Hubbard model the intermediate state can be chosen to be the  $n=1$  Mott insulating state. When  $|U| \gg t, V$  and  $V > 0, U > 0$ , the  $n=1$  Mott insulator is the lowest energy state. Simultaneously,

<sup>21</sup>We will always use the term ‘lattice curvature’ to describe the global, slow variation of the lattice potential, not the curvature on length-scales of single lattice sites.

<sup>22</sup>The curvature is quadratic close to the centre of the lattice. Anharmonicities in the confining potential become more relevant as the distance to the centre increases.

it is the highest energy state when the energy terms are flipped, i.e.  $|U| \gg t, V$  and  $V < 0, U < 0$ .

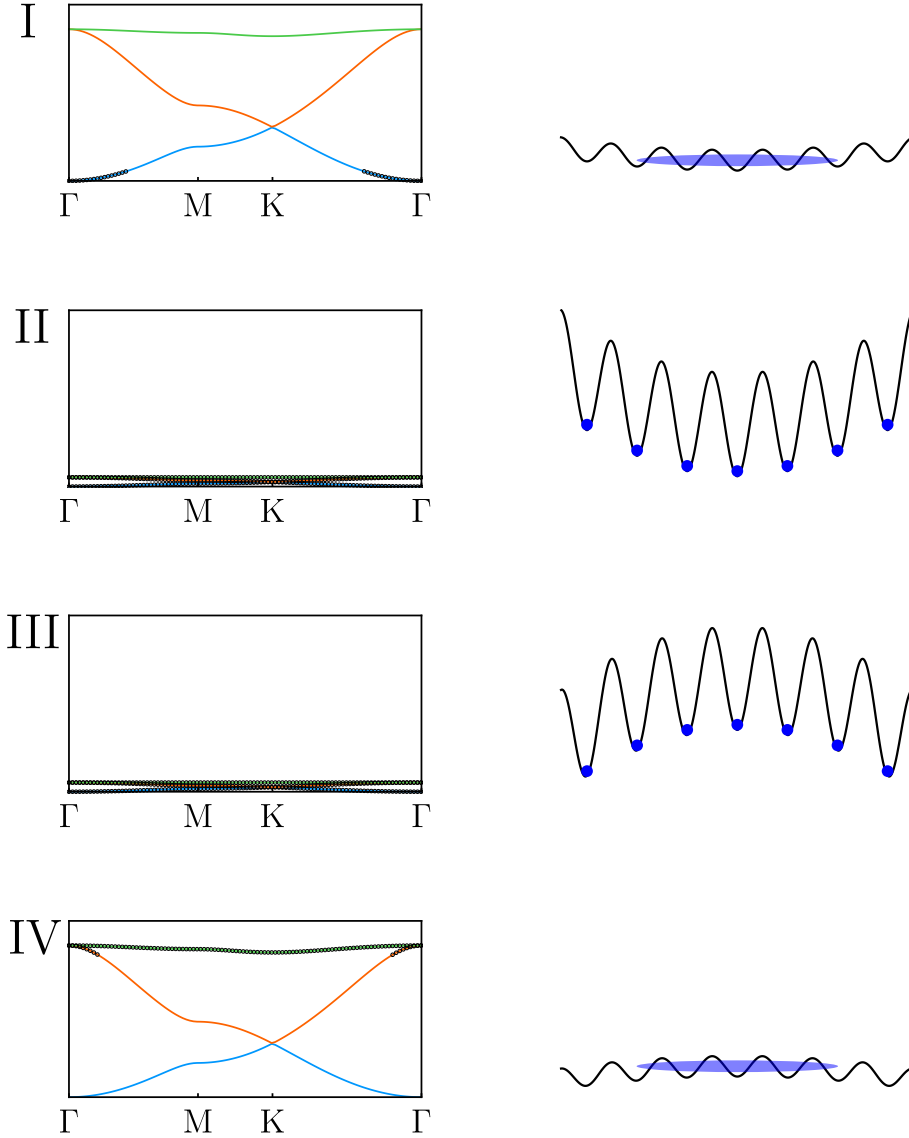


**Figure 3.2** – Schematic showing the negative temperature preparation protocol in momentum space (left) and real space (right). In the kagome lattice the lower band is dispersive and the upper band is flat. I: Positive temperature,  $0 < U \ll t, V > 0$  (superfluid). II: Positive temperature,  $U \gg t > 0, V > 0$  (Mott insulator). III: Negative temperature,  $-U \gg t > 0, V < 0$  (Mott insulator), IV: Negative temperature,  $0 < -U \ll t, V < 0$  (superfluid). The initial superfluid has a well-defined momentum, but is extended in real space. The Mott insulator state is effectively a tensor-product of maximally localized Wannier states on each site. Thus, in the Mott insulator, the particle position is well-defined, but the momentum state distribution is extended.

BECs are usually created at repulsive interactions and in a confining potential. In this case it is straightforward to create a low-entropy, positive temperature Mott insulator by simply increasing the lattice depth. In the  $n=1$  Mott insulator, the interaction energy is zero, regardless of whether the interaction is repulsive or attractive. Thus a sudden switch

from repulsive to attractive interactions will not change the distribution of particles and will not change the system's entropy. Similarly, a sudden inversion of confinement does not cause the atomic distribution to change since atoms are blocked from redistributing to compensate for a modification of the external potential.

Once we have flipped the interactions and confinement, the system will be in the highest energy state, the  $n=1$  Mott insulator at negative temperature. At this point we can change the lattice potential adiabatically to e.g. create a negative temperature superfluid [156]. Fig. 3.2 shows the steps required to create the negative temperature state in an optical lattice. Note that this protocol is agnostic with respect to lattice geometry.

**Why bother with negative temperatures?** As discussed above negative temperatures can be used to explore the highest energy states of a Hamiltonian. From the quantum simulation point of view, preparing a negative temperature state is only useful if the highest energy states of a Hamiltonian are different from the lowest energy states. In many cases, there is a symmetry between highest-lying and lowest-lying states. For example, the highest-lying states of an Ising spin Hamiltonian are simply inverted with respect to the lowest-lying states. The physics of the highest energy states is thus exactly the same as that of the lowest energy states and there is no incentive to study the highest energy states separately.

In optical lattices, we are primarily concerned with tight-binding models and so how useful it is to be able to prepare a negative temperature state comes down to whether the bottom and top of the tight-binding band structure are related by symmetry or not. One can straightforwardly prove that bipartite lattices (e.g. the square lattice, the Lieb lattice, the honeycomb lattice) always have symmetric tight-binding band structures, i.e. the upper band (highest energy states) is an inverted version of the lower band<sup>23</sup>. Thus, for bipartite lattices, the physics of the highest energy states is the same as that for the lowest energy state. On the other hand, for several non-bipartite lattices this is not true any more and the upper tight-binding band can be different from that of the lower band. Examples include the triangular and kagome lattices. In these systems, a negative temperature state is not just a symmetric version of the positive-temperature state, but can display unique properties that are not accessible via positive temperatures.

For the kagome lattice in particular, the top tight-binding band is flat, meaning that a low-entropy negative temperature state could be used to study interacting particles in a flat band in thermodynamic equilibrium [157]. We will discuss flat band physics with bosons in section 3.3 and section 3.4.

The partition function contains all relevant information about a thermodynamic system,

$$\mathcal{Z}(H, T) = f\left(\frac{H}{T}\right) = f\left(\frac{-H}{-T}\right), \quad (3.5)$$

where  $f$  is some system-specific function,  $H$  is the system's Hamiltonian, and  $T$  is the temperature. The thermodynamic properties don't change if we simultaneously invert the

---

<sup>23</sup>For a lattice with two sites per unit cell,  $H_{\text{TB}}(\mathbf{k}) = \begin{pmatrix} 0 & \alpha(\mathbf{k}) \\ \alpha^*(\mathbf{k}) & 0 \end{pmatrix} \Rightarrow E_{\mathbf{k}}^{\pm} = \pm|\alpha(\mathbf{k})|$ , i.e. the spectrum is symmetric around zero. Similar arguments can be made for other bipartite lattices.

Hamiltonian and the temperature. Applied to the Bose-Hubbard Hamiltonian this means that

$$\begin{aligned}
 \mathcal{Z}(H_{\text{BH,AFM}}, T, V, U) &= f \left[ \frac{1}{T} \left( t \sum_{\langle i,j \rangle} \hat{a}_i^\dagger \hat{a}_j + \frac{U}{2} \sum_i \hat{n}_i (\hat{n}_i - 1) + V \sum_i \hat{n}_i i^2 \right) \right] \\
 &= f \left[ \frac{1}{-T} \left( -t \sum_{\langle i,j \rangle} \hat{a}_i^\dagger \hat{a}_j - \frac{U}{2} \sum_i \hat{n}_i (\hat{n}_i - 1) - V \sum_i \hat{n}_i i^2 \right) \right] \quad (3.6) \\
 &= \mathcal{Z}(H_{\text{BH,FM}}, -T, -V, -U).
 \end{aligned}$$

Here, AFM (FM) labels the BH model with positive (negative) tunnelling. We see that we can simulate a Bose-Hubbard Hamiltonian with inverted kinetic energy,  $t < 0$ , if we are able to invert the temperature, the interaction energy and the potential (confinement) energy. Thus, a negative temperature state with attractive interactions and anti-confinement in the kagome lattice is equivalent to a repulsively interacting, harmonically confined cloud in a flat band.

### 3.2 Kagome flat band signatures

We will now discuss what signatures a negative temperature state of non-interacting particles will have and how these can be probed experimentally. Since we are working within the single-particle framework, we will assume that all flat band Bloch states are equally occupied. We will see in [section 3.3](#) that finite dispersion and interactions will cause the flat band degeneracy to be lifted.

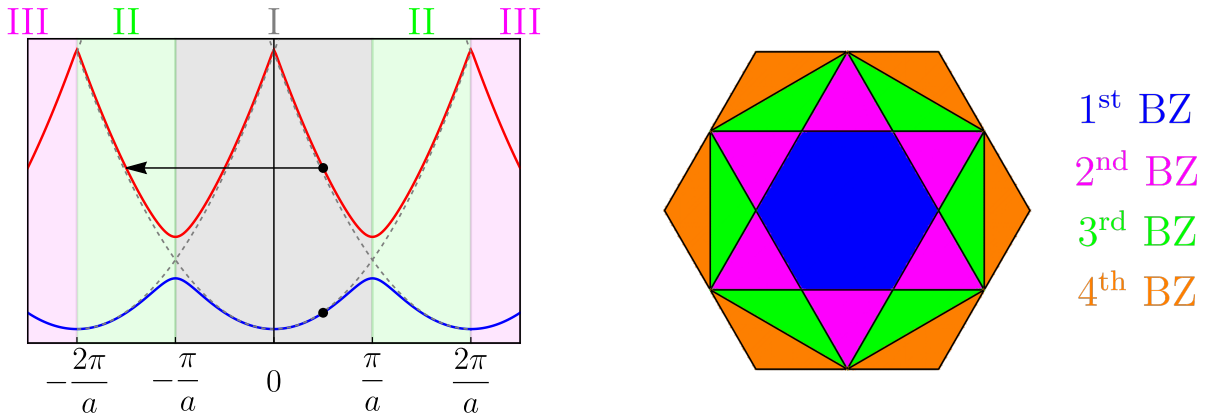


**Figure 3.3** – Left: band-mapping in 1D. I, II, and III label the 1<sup>st</sup>, 2<sup>nd</sup>, and 3<sup>rd</sup> Brillouin zone, respectively. Grey, dashed lines show the plane-wave dispersion. Bloch functions with momentum  $k$  in the first band (blue line) are mapped onto a plane wave with momentum  $k$ . Particles with momentum  $k$  in the second band (red line) are mapped onto the plane wave dispersion centred at  $\frac{2\pi}{a}$  or  $-\frac{2\pi}{a}$ , i.e. they are mapped onto the plane wave with momentum  $k - \frac{2\pi}{a}$  or  $k + \frac{2\pi}{a}$ , depending on the sign of  $k$ . Right: first four Brillouin zones (BZs) of the kagome lattice in the extended zone scheme<sup>24</sup>. Atoms in the  $n^{\text{th}}$  band are mapped to the  $n^{\text{th}}$  region of the extended zone scheme.

**Momentum space (band-mapping)** A well-established technique in optical lattice experiments to measure the population of a motional band is band-mapping. In band-mapping, the quasimomentum distribution of atoms in the optical lattice is mapped onto real momentum. The momentum of an atom occupying the  $n^{\text{th}}$  band of the optical lattice is mapped onto a momentum in the  $n^{\text{th}}$  Brillouin zone (see Fig. 3.3), making it possible to extract the population of individual bands [151, 158, 159].

To map the quasimomentum distribution onto real momentum at the end of an experiment, the lattice depth is slowly switched off before performing a time-of-flight measurement<sup>25</sup>. The population of the different Brillouin zones can be extracted and converted into band occupation in the optical lattice.

**Band-mapping of the flat band** Assuming we have populated the flat band of the kagome lattice with a non-interacting gas, we would expect only the 3<sup>rd</sup> Brillouin zone (green region in Fig. 3.3) to be occupied. In the real experiment we will inevitably also populate the upper regions of the second band (corners of the star formed by the 2<sup>nd</sup> Brillouin zone, see Fig. 3.3) due to residual interactions, lattice inhomogeneities and experimental imperfections. However, this is a crucial signature of flat band population and can be directly used to optimize the experimental sequence for higher flat band occupations.

The distribution of non-interacting particles in the flat band is also expected to be very homogeneous (due to its flatness), which is another property that can be measured via band-mapping. In the kagome tight-binding model, the classical thermal occupation of a given momentum state  $\mathbf{k}$  is given by

$$n_i(\mathbf{k}) = \frac{1}{\mathcal{Z}} e^{-\frac{E_i(\mathbf{k})}{k_B T}}, \quad (3.7)$$

where  $i \in \{1, 2, 3\}$  denotes the band index and band 3 is assumed to be the flat band. The partition function,  $\mathcal{Z}$ , is defined as

$$\mathcal{Z} = \sum_{i=1}^3 \int_{\mathbf{k} \in \text{BZ}} e^{-\frac{E_i(\mathbf{k})}{k_B T}} d\mathbf{k}. \quad (3.8)$$

We can evaluate the integral in Eq. 3.8 numerically,

$$\int_{\mathbf{k} \in \text{BZ}} e^{-\frac{E_i(\mathbf{k})}{k_B T}} d\mathbf{k} \approx \sum_{\mathbf{k}_i} e^{-\frac{E_i(\mathbf{k}_i)}{k_B T}}, \quad (3.9)$$

where  $\{\mathbf{k}_i\} \in \text{BZ}$  is a random sample of momentum states in the first Brillouin zone. Fig. 3.4 shows the band-mapped momentum distribution in the tight-binding limit of the kagome lattice for a small positive and a small negative temperature. Note that for positive temperatures, low-energy momenta are predominantly occupied, indicating that the cloud is in the lowest band (around the  $\Gamma$  point). For negative temperatures, high-energy momentum states dominate the distribution, indicating that the third (flat) band

<sup>24</sup>Note that the Brillouin zone structure for the triangular and honeycomb lattices is the same as for the kagome lattice.

<sup>25</sup>A switch-off ramp is chosen that is fast enough to avoid atoms redistributing in the band and slow enough to avoid atoms being excited to other bands [160].

is populated. States in the flat band have the same energy (in the tight-binding limit), causing them to be equally occupied.

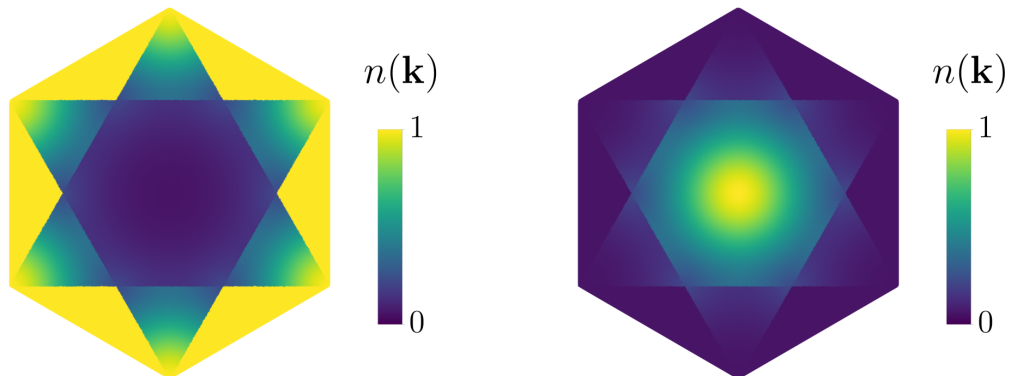


**Figure 3.4** – Left (right): numerically calculated, band-mapped momentum distribution of the tight-binding Hamiltonian at a temperature of  $-t/k_B$  ( $t/k_B$ ), where  $t$  is the tunnelling energy. The distribution is normalized to the maximum value.

Using Eq. 3.7, we can also extract the three bands' filling fractions. The filling fraction of band  $i$  at temperature  $T$  is given by

$$n_i(T) = \int_{\mathbf{k} \in \text{BZ}} n_i(\mathbf{k}, T) = \frac{\int_{\mathbf{k} \in \text{BZ}} e^{-\frac{E_i(\mathbf{k})}{k_B T}}}{\sum_{i=1}^3 \int_{\mathbf{k} \in \text{BZ}} e^{-\frac{E_i(\mathbf{k})}{k_B T}}}. \quad (3.10)$$

We can express  $T$  in units of the tunnelling energy  $t$  to find how the thermal population of the three bands scales with temperature (see Fig. 3.5).

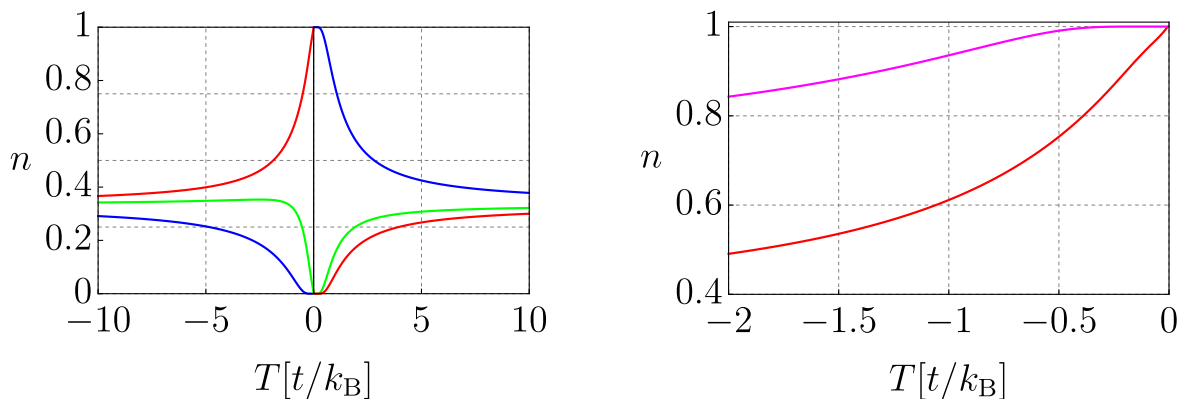


**Figure 3.5** – Band population as a function of temperature. Blue, green, red, and magenta lines are the occupation of the first, second, third, and upper two bands (second & third), respectively. For small positive (negative) temperatures, the lowest (highest) energy band, Band 1 (Band 3), is predominantly occupied. The population of Band 1 (Band 3) tends to 1 as  $T \rightarrow 0^+$  ( $T \rightarrow 0^-$ ).

At a temperature of  $-2t$  ( $-0.5t$ ) we can expect a combined excited state (bands 2 & 3) population of 0.9 (0.99) and a flat band population of 0.56 (0.75).

**Bloch state momentum distribution** By suddenly switching off the lattice potential, a Bloch state with quasimomentum  $\mathbf{k}$  is mapped onto plane wave states with momentum  $\mathbf{k} + n\mathbf{g}_1 + m\mathbf{g}_2$ , where  $\mathbf{g}_1$  and  $\mathbf{g}_2$  are the reciprocal lattice vectors. Fig. 3.6 shows the numerically obtained momentum distribution of Bloch states in the flat band of the kagome lattice.

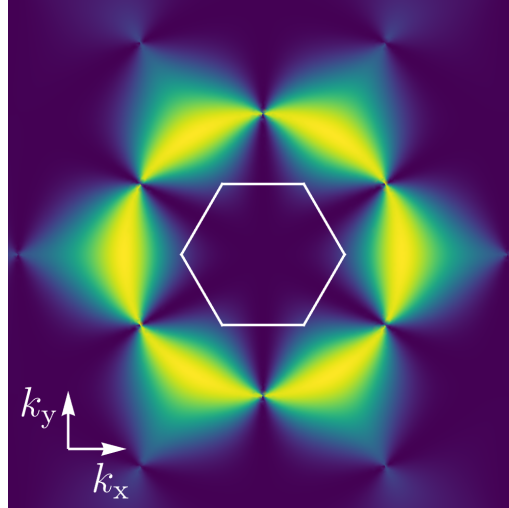


**Figure 3.6** – Predicted momentum distribution of the flat kagome band, where all Bloch states are equally occupied. This image shows the average of 5,000 flat band Bloch state momentum distributions at a lattice depth of  $s_L = s_S = 10$ . The white hexagon indicates the first BZ.

### 3.3 Flat band BEC (high density)

**Bose-Einstein distribution and flat band** Instead of looking at a classical thermal distribution as we did in chapter 3.2 we can also ask what happens when we consider bosons and the Bose-Einstein distribution.

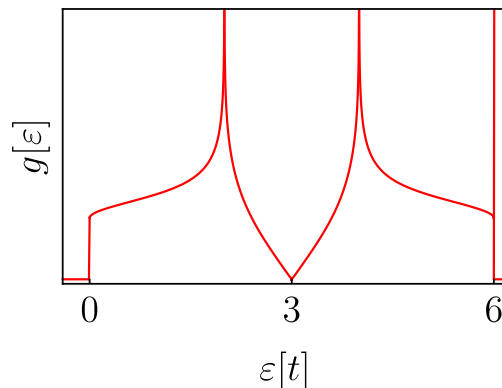


**Figure 3.7** – Analytical density of states for the tight-binding model on the kagome lattice. This is a modified version of the density of states derived for the honeycomb lattice in [161]. The flat band is located at  $\varepsilon = 6t$ . The kagome lattice additionally displays Van Hove singularities at  $\varepsilon = 2t$  and  $\varepsilon = 4t$  and a vanishing density of states at the Dirac points at  $\varepsilon = 3t$ .

The canonical approach would be to determine the density of states of the system and combine it with the Bose-Einstein distribution to obtain thermodynamic quantities such as total energy, total atom number and condensed and thermal fractions. The density of states of the tight-binding model on the kagome lattice is shown in Fig. 3.7. Using the tight-binding density of states to determine thermodynamic properties is obviously an ill-fated endeavour, since both the (negative-temperature) Bose-Einstein distribution as well as the density of states diverge as  $\varepsilon \rightarrow 6t$ . However, as we showed in section 2.3, the optical kagome lattice only approaches the tight-binding limit for deep lattices. For shallow lattices, the flat band is dispersive with a maximum around  $\Gamma$  ( $(k_x, k_y) = (0, 0)$ ). Fig. 3.8 shows the second and third bands of the numerically calculated band structure in the vicinity of  $\Gamma$ .

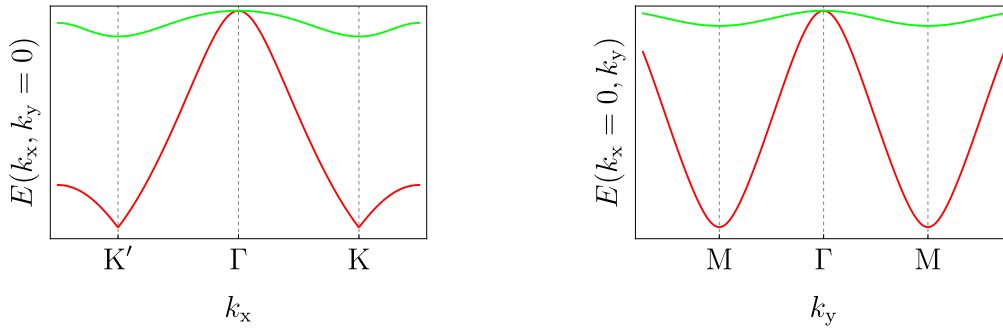


**Figure 3.8** – 1D cuts through the numerically calculated band structure of the kagome lattice with  $s_S = s_L = 3$ . Green and red lines are the third and second band, respectively.

All three bands are quadratic around  $\Gamma$  and we can therefore determine an effective mass for these bands,

$$m_{ij}^* = \hbar^2 \left( \frac{\partial^2 E(k_x, k_y)}{\partial k_i \partial k_j} \right)^{-1}. \quad (3.11)$$

Fig. 3.9 shows the numerically calculated effective mass of the three kagome bands as a function of lattice depth.

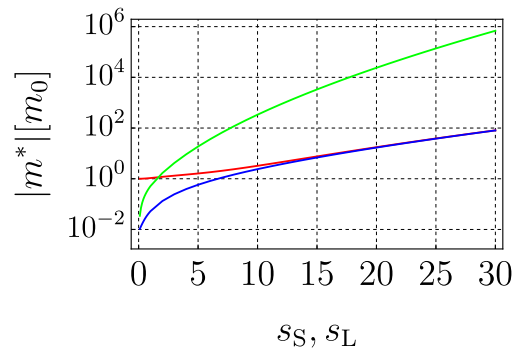


**Figure 3.9** – Absolute value of the effective mass at  $\Gamma$  for the first (red), second (blue), and third (green) band of the kagome lattice. For deep lattices, the second band is the inverted version of the first band. Thus, the effective masses approach each other, but have opposite sign, as the lattice depth is increased. The curvature of the dispersion and, consequently, the effective masses, are symmetric around  $\Gamma$ , i.e.  $m_{xx}^* = m_{yy}^*$ .

Note that the effective masses of the second and third bands are negative. The effective mass in the third band can be varied by several orders of magnitude by changing the lattice depth between 0 and  $30E_R$ . Note also that the third band's effective mass very quickly becomes orders of magnitude larger than that of the other two bands. In the presence of external harmonic confinement, e.g. due to Gaussian lattice beams, the lattice Hamiltonian around  $\Gamma$  approaches that of a harmonic oscillator (HO),

$$H = \frac{\hbar^2 k^2}{2m^*} + \frac{1}{2}m\omega^2 r^2 = \frac{\hbar^2 k^2}{2m^*} + \frac{1}{2}m^* \omega_{\text{eff}}^2 r^2, \quad (3.12)$$

where  $m^*$  is the effective mass and  $\omega_{\text{eff}}^2 = \frac{m}{m^*}\omega^2$  is the effective HO frequency. Thus, for low enough temperatures, bosons in a (2D) optical lattice are expected to display the same physics as bosons in a 2D HO trap. Since it is possible to create BECs in a 2D harmonic oscillator, one might expect there to be a BEC phase transition at a non-zero, critical temperature  $T_c$ . The critical temperature can be calculated analytically [162] and is given by

$$T_c = \sqrt{\frac{6N}{\pi^2} \frac{\hbar\omega_{\text{eff}}}{k_B}} = \sqrt{\frac{6N}{\pi^2} \frac{\hbar\omega}{k_B} \sqrt{\frac{m}{m^*}}}, \quad (3.13)$$

where  $N$  is the atom number. Expressed in units of  $t/k_B$ , the critical temperature is

$$T_c^t = \sqrt{\frac{6N}{\pi^2} \frac{\hbar\omega}{t} \sqrt{\frac{m}{m^*}}}. \quad (3.14)$$

This shows that the critical temperature decreases for increasing effective mass and vanishes for a perfectly flat band.

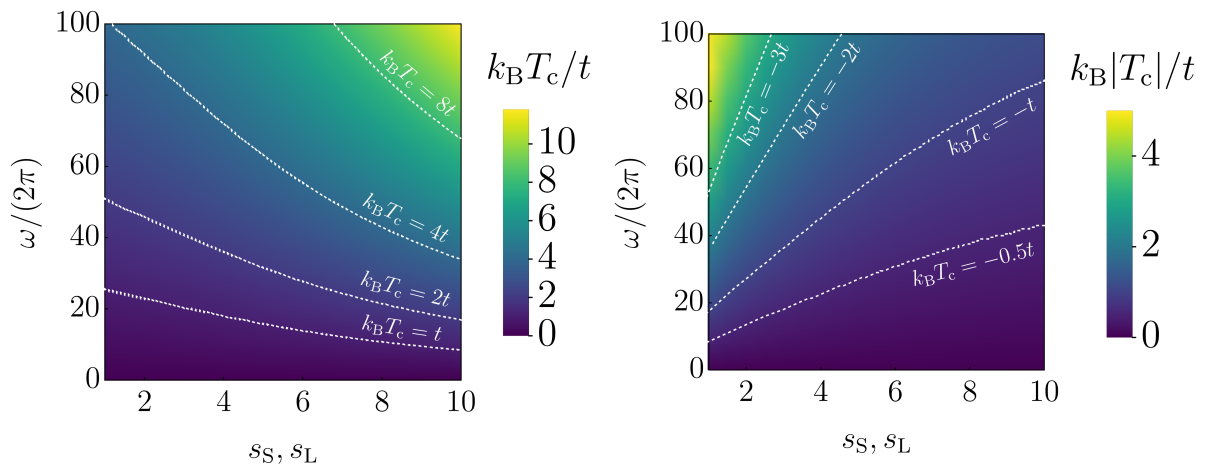


**Figure 3.10** – Critical temperature ( $T_c^t$ ) of the BEC transition in the first (left) and third (right) band for a positive and negative temperature state, respectively. Note that the value of  $t$  decreases with increasing  $s$ . In the third band, the critical temperature is reduced as the lattice depth is increased due to the exponential increase of the effective mass. These plots assume an atom number of  $10^4$  and broadly agree with what was derived in [163] for the square lattice.

We express the critical temperature in terms of  $t/k_B$ , as this is what we generally extract from our fits to the thermal momentum distribution (see section 7.1.2). Fig. 3.10 shows  $T_c^t$

as a function of lattice depth and harmonic confinement for the first band of the kagome lattice at positive temperature and for the third band of the kagome lattice at negative temperatures<sup>26</sup>. In both cases, the critical temperature increases with increasing harmonic confinement. The two cases starkly differ in their behaviour with increasing lattice depth. While the critical temperature in units of  $t$  increases with lattice depth for the first band, it quickly decreases for the third band. This is due to the third band becoming exponentially flat as the lattice depth increases, causing the effective HO frequency to decrease. Thus as the lattice depth is increased, in the third band, more and more states need to be filled before the excited states are saturated and a BEC can form. Assuming we are able to prepare the same atom number and temperature in the third band and can vary the lattice depth independently, we expect the BEC to ‘melt’ above some critical lattice depth. This critical lattice depth depends on the temperature of the cloud and the initial atom number. The temperature required to see a BEC emerge at the  $\Gamma$  point is feasible with our machine. We reach temperatures of roughly  $0.5k_{\text{B}}t$  in the triangular lattice at positive temperature (see section 7.1.2). Fig. 3.11 shows the Bloch states at  $\Gamma$  in the first and third band.

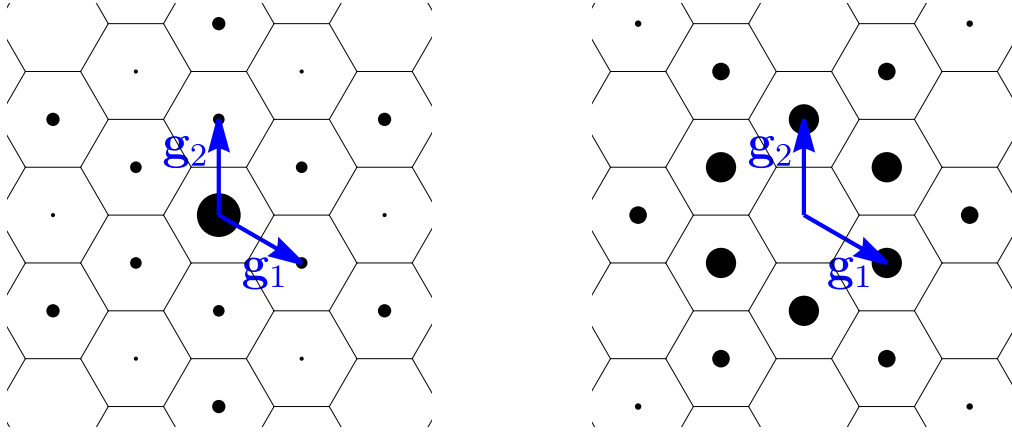


**Figure 3.11** – Expected signature of the first and third band BECs. The central hexagon is the first Brillouin zone. Left (right): Bloch state at  $\Gamma$  in the first (third) band. The size of the black points indicate the weight of the associated plane-wave. Since the second and third bands touch at  $\Gamma$ , the highest energy state is two-fold degenerate. For this image we took the superposition that has a symmetric momentum distribution.

### 3.3.1 Mean-field approach

The problem of interacting bosons in flat bands can be approached using mean-field theory. We will closely follow [152] and [88] for this calculation. To study interacting bosons in the flat band of the kagome lattice, we aim to solve the Bose-Hubbard Hamiltonian with positive tunnelling,

<sup>26</sup> $t$  in Fig. 3.10 is not calculated with Wannier states, but with the band width approximation.

$$\begin{aligned}
H_{\text{BH}} &= t \sum_{\langle \nu, \mu \rangle} (\hat{a}_\nu^\dagger \hat{a}_\mu + \text{h.c.}) + \frac{U}{2} \sum_\nu \hat{n}_\nu (\hat{n}_\nu - 1) \\
&= \sum_{\alpha, \alpha'} \sum_{i, j} t_{(i, \alpha), (j, \alpha')} \hat{b}_{i, \alpha}^\dagger \hat{b}_{j, \alpha'} + \frac{U}{2} \sum_\alpha \sum_i \hat{b}_{i, \alpha}^\dagger \hat{b}_{i, \alpha} (\hat{b}_{i, \alpha}^\dagger \hat{b}_{i, \alpha} - 1),
\end{aligned} \tag{3.15}$$

where  $i, j$  label unit cells and  $\alpha \in \{A, B, C\}$  labels the site within a unit cell. In the second line we explicitly sum over sites in the unit cell, which will make the rest easier to follow. Note that the flat band in this case has the lowest energy of the three tight-binding bands.

We already saw in [section 2.3](#) that the kinetic energy can be written as a sum over momentum states

$$H_{\text{kin}} = \sum_{\mathbf{k}} \hat{b}_{\mathbf{k}}^\dagger H(\mathbf{k}) \hat{b}_{\mathbf{k}} = \sum_{\alpha, \alpha'} \sum_{\mathbf{k}} \hat{b}_{\mathbf{k}, \alpha}^\dagger H_{\alpha, \alpha'}(\mathbf{k}) \hat{b}_{\mathbf{k}, \alpha'}, \tag{3.16}$$

where  $H(\mathbf{k})$  is as in [Eq. 2.22](#). Similarly, we can also express the interaction term in terms of momentum operators. With  $\hat{b}_{i, \alpha} = \frac{1}{\sqrt{N}} \sum_i e^{i\mathbf{k} \cdot \mathbf{r}_{i, \alpha}} \hat{b}_{\mathbf{k}, \alpha}$ ,

$$\begin{aligned}
H_{\text{int}} &= \frac{U}{2N^2} \sum_\alpha \sum_i \sum_{\mathbf{k}, \mathbf{q}, \mathbf{k}', \mathbf{q}'} \hat{b}_{\mathbf{k}, \alpha}^\dagger \hat{b}_{\mathbf{q}, \alpha} \hat{b}_{\mathbf{k}', \alpha}^\dagger \hat{b}_{\mathbf{q}', \alpha} e^{i(\mathbf{q} + \mathbf{q}' - \mathbf{k} - \mathbf{k}') \cdot \mathbf{r}_{i, \alpha}} \\
&\quad - \frac{U}{2N} \sum_\alpha \sum_i \sum_{\mathbf{k}, \mathbf{k}'} \hat{b}_{\mathbf{k}, \alpha}^\dagger \hat{b}_{\mathbf{k}', \alpha} e^{i(\mathbf{k}' - \mathbf{k}) \cdot \mathbf{r}_{i, \alpha}} \\
&= \frac{U}{2N} \sum_\alpha \sum_{\mathbf{k}, \mathbf{k}', \mathbf{q}} \hat{b}_{\mathbf{k}, \alpha}^\dagger \hat{b}_{\mathbf{q}, \alpha} \hat{b}_{\mathbf{k}', \alpha}^\dagger \hat{b}_{\mathbf{k} + \mathbf{k}' - \mathbf{q}, \alpha} - \frac{U}{2} \sum_\alpha \sum_{\mathbf{k}} \hat{b}_{\mathbf{k}, \alpha}^\dagger \hat{b}_{\mathbf{k}, \alpha} \\
&= \frac{U}{2N} \sum_\alpha \sum_{\mathbf{k}, \mathbf{k}', \mathbf{q}} \hat{b}_{\mathbf{k}, \alpha}^\dagger \hat{b}_{\mathbf{k} - \mathbf{q}, \alpha} \hat{b}_{\mathbf{k}', \alpha}^\dagger \hat{b}_{\mathbf{k}' + \mathbf{q}, \alpha} - \frac{U}{2} \sum_\alpha \sum_{\mathbf{k}} \hat{b}_{\mathbf{k}, \alpha}^\dagger \hat{b}_{\mathbf{k}, \alpha},
\end{aligned} \tag{3.17}$$

where we made the substitution  $\mathbf{q} \rightarrow \mathbf{k} - \mathbf{q}$ . To calculate the mean-field energy as a function of momentum, we substitute  $\hat{b}_{\mathbf{k}, \alpha}$  and  $\hat{b}_{\mathbf{k}, \alpha}^\dagger$  for mean-field amplitudes  $\sqrt{N} \psi_{\mathbf{k}, \alpha}$  and  $\sqrt{N} \psi_{\mathbf{k}, \alpha}^*$ , respectively. Additionally, we assume that bosons are condensed, i.e. that  $\hat{b}_{\mathbf{k}, \alpha}^\dagger \hat{b}_{\mathbf{k} - \mathbf{q}, \alpha} \hat{b}_{\mathbf{k}', \alpha}^\dagger \hat{b}_{\mathbf{k}' + \mathbf{q}, \alpha} \neq 0$  only when  $\mathbf{q} = 0$  and  $\mathbf{k} = \mathbf{k}'$ . The resulting mean-field energy functional is

$$E_{\text{MF}}(\mathbf{k})[\psi_{\mathbf{k}}] = \psi_{\mathbf{k}}^* H(\mathbf{k}) \psi_{\mathbf{k}} + \frac{U}{2} (|\psi_{\mathbf{k}, A}|^4 + |\psi_{\mathbf{k}, B}|^4 + |\psi_{\mathbf{k}, C}|^4), \tag{3.18}$$

where  $\psi_{\mathbf{k}} = (\psi_{\mathbf{k}, A}, \psi_{\mathbf{k}, B}, \psi_{\mathbf{k}, C})^T$ . The mean-field energy at some momentum  $\mathbf{k}$  with fixed  $U$  and particle density  $\rho = |\psi_{\mathbf{k}, A}|^2 + |\psi_{\mathbf{k}, B}|^2 + |\psi_{\mathbf{k}, C}|^2$ , is obtained by minimizing the mean-field energy functional over  $\psi_{\mathbf{k}}$ . Note that  $\rho$  is the particle density per unit cell. [Fig. 3.12](#) shows the mean-field energy along a path through points of high symmetry in momentum space.

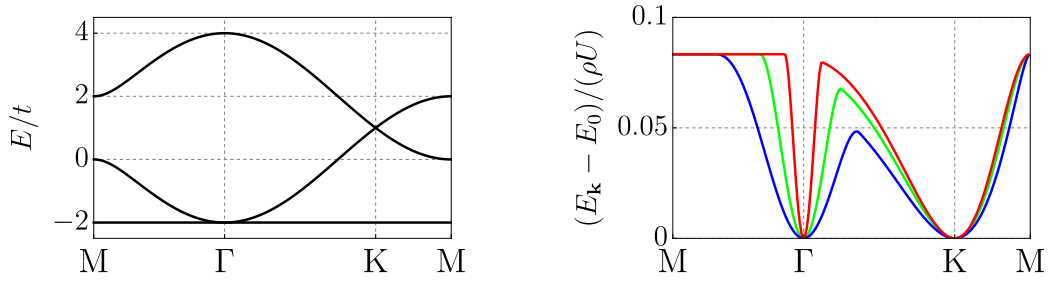


**Figure 3.12** – Left: tight-binding band structure for non-interacting particles. We define the lowest single-particle energy as  $E_0 = -2t$ . Right: lowest mean-field energy of interacting bosons in the kagome lattice. Red, green, and blue lines show the mean-field energy for  $\rho U = 0.2t$ ,  $\rho U = t$ , and  $\rho U = 3t$ , respectively.

Fig. 3.12 shows that interactions lift the degeneracy of the flat band such that the energy at the K and  $\Gamma$  points is minimal, with  $\psi_K = \frac{1}{\sqrt{3}}(-1, -1, 1)^T$  and  $\psi_\Gamma = \frac{1}{\sqrt{3}}(1, e^{\pm \frac{2\pi}{3}i}, e^{\mp \frac{2\pi}{3}i})^T$ . At these momenta, the Bloch functions simultaneously minimize kinetic and interaction energy. Interactions prefer wave functions that have equal amplitude on the three sublattices, while the kinetic energy term in Eq. 3.18 imposes a 3-colour phase pattern on the wave function, i.e. the phase on neighbouring sites differs by  $2\pi/3$ . The 3-colour phase arrangement is a manifestation of kinetic energy frustration and is analogous to antiferromagnetically interacting spins in the classical XY model on a geometrically frustrated lattice.

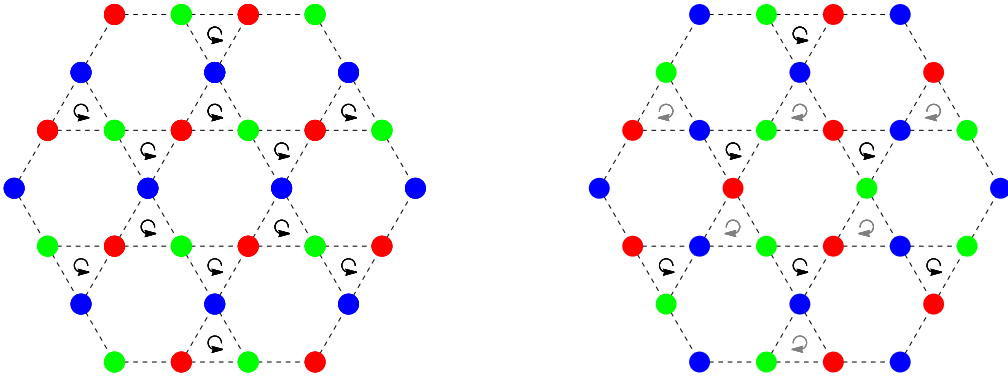


**Figure 3.13** – Left (right): vortex ferromagnet/ $\Gamma$ -point wave function (vortex antiferromagnet/ $K$ -point wave function) on the kagome lattice. Red, green, and blue points represent phases  $0$ ,  $\frac{2\pi}{3}$ , and  $\frac{4\pi}{3}$ , respectively. This state is equivalent to the  $q = 0$  ( $q = \sqrt{3} \times \sqrt{3}$ ) state in the AFM XY model on the kagome lattice [91, 123]. The circular arrows indicate vorticity. Note that both the  $\Gamma$  and  $K$  wave functions are two-fold degenerate, corresponding to the freedom in choosing vortices or anti-vortices.

Fig. 3.13 shows the phase pattern of the  $\Gamma$  and  $K$  wave functions, which can be regarded as a ferromagnetic and antiferromagnetic arrangement of vortices, respectively<sup>27</sup>. As we

<sup>27</sup>Both the  $\Gamma$  and  $K$  wave functions have  $U(1) \times \mathbb{Z}_2$  symmetry. The  $U(1)$ -symmetry arises out of the freedom to choose a global phase, while the  $\mathbb{Z}_2$ , chiral symmetry is due to the freedom to have either vortices or anti-vortices.

mentioned in [chapter 1](#), the mean-field Hamiltonian in the flat band of the kagome lattice maps onto the classical AFM XY model. The emergence of the three-colour pattern and vortex ferro- and antiferromagnets and their properties, such as the (topological) order parameters and the BKT transition temperature, have been extensively studied elsewhere [[91](#), [164](#), [165](#)] and many parallels can be drawn to the bosonic case.

The flat band degeneracy is lifted by interactions, but there is still an unresolved degeneracy between the K and  $\Gamma$  points. This degeneracy is lifted when we take into account quantum fluctuations. To this end, we expand  $H_{\text{BH}}$  around the mean-field energy and only keep terms to second order that couple to the BEC at  $\mathbf{k}_c$ <sup>28</sup>, which we assume is macroscopically occupied, i.e.  $\hat{b}_{\mathbf{k}_c, \alpha} = \sqrt{N\rho} \langle \alpha | \psi_{\mathbf{k}_c} \rangle$ . Here,  $\langle \alpha | \psi_{\mathbf{k}_c} \rangle$  is the amplitude of  $\psi_{\mathbf{k}_c}$  on sublattice  $\alpha$ , and is equal to  $1/\sqrt{3}$  for both  $\mathbf{k}_c = \text{K}$  and  $\mathbf{k}_c = \Gamma$ . We are left with terms proportional to  $\hat{b}_{\mathbf{k}_c+\mathbf{k}, \alpha}^\dagger \hat{b}_{\mathbf{k}_c+\mathbf{k}, \alpha}$ ,  $\hat{b}_{\mathbf{k}_c-\mathbf{k}, \alpha}^\dagger \hat{b}_{\mathbf{k}_c-\mathbf{k}, \alpha}$ ,  $\hat{b}_{\mathbf{k}_c-\mathbf{k}, \alpha} \hat{b}_{\mathbf{k}_c+\mathbf{k}, \alpha}$ , and  $\hat{b}_{\mathbf{k}_c+\mathbf{k}, \alpha}^\dagger \hat{b}_{\mathbf{k}_c-\mathbf{k}, \alpha}^\dagger$ , and obtain a Bogoliubov Hamiltonian for the excited states of the form [[89](#)]

$$H_{\text{B}}(\mathbf{k}) = \frac{1}{2} \sum_{\mathbf{k} \neq \mathbf{k}_c} \Psi_{\mathbf{k}}^\dagger H_{\text{B}}(\mathbf{k}) \Psi_{\mathbf{k}}, \quad (3.19)$$

with

$$\begin{aligned} H_{\text{B}}(\mathbf{k}) &= \begin{pmatrix} H(\mathbf{k}) - \mu_{\text{eff}} & \Delta \\ \Delta^* & H(2\mathbf{k}_c - \mathbf{k}) - \mu_{\text{eff}} \end{pmatrix}, \\ \Psi_{\mathbf{k}} &= (b_{\mathbf{k}, \text{A}}, b_{\mathbf{k}, \text{B}}, b_{\mathbf{k}, \text{C}}, b_{2\mathbf{k}_c - \mathbf{k}, \text{A}}^\dagger, b_{2\mathbf{k}_c - \mathbf{k}, \text{B}}^\dagger, b_{2\mathbf{k}_c - \mathbf{k}, \text{C}}^\dagger)^{\text{T}}, \\ \Delta_{i,j} &= \delta_{i,j} U \rho \langle \alpha | \phi_0 \rangle^2 = \delta_{i,j} \frac{U \rho}{3}, \\ \mu_{\text{eff}} &= (-2t - \frac{U \rho}{3}) \delta_{i,j}. \end{aligned} \quad (3.20)$$

Here, we substituted  $\mathbf{k} - \mathbf{k}_c$  for  $\mathbf{k}$ , so that the minimum of  $H_{\text{B}}(\mathbf{k})$  is located at  $\mathbf{k}_c$  and not at  $\mathbf{k} = 0$ . The Bogoliubov spectrum of the K and  $\Gamma$  condensates is shown in [Fig. 3.14](#).

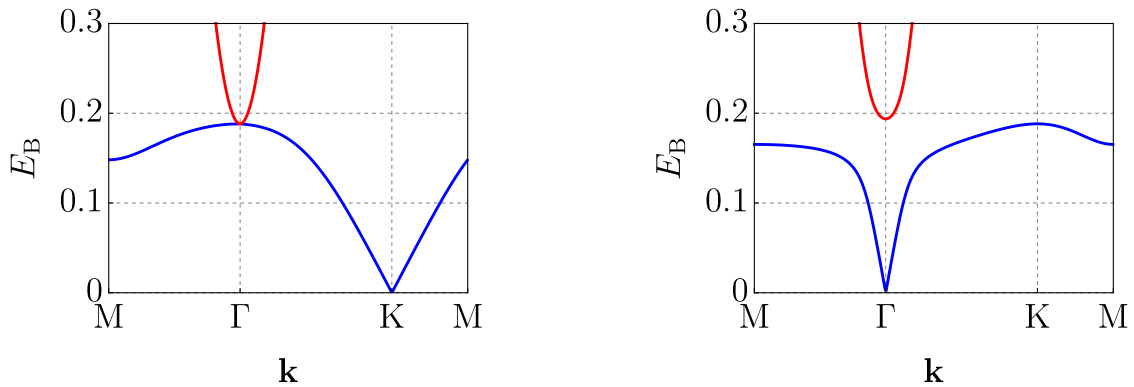


**Figure 3.14** – Left (right): Bogoliubov spectrum of the K ( $\Gamma$ ) condensate for  $U\rho = 0.6t$ . Note that the positive branch of the eigenvalues of  $\sigma_z H_{\text{B}}(\mathbf{k})$ , which preserves bosonic commutation relations [[89](#), [166](#)], is plotted here. Zero energy corresponds to the mean-field energy of K and  $\Gamma$ .

<sup>28</sup>We assume that  $\mathbf{k}_c = \text{K}$  or  $\mathbf{k}_c = \Gamma$ .

The Bogoliubov dispersion around K is less steep, i.e. the sound velocity is lower<sup>29</sup>. In the presence of quantum fluctuations, the K BEC thus has lower zero-point energy (ZPE)<sup>30</sup> than the  $\Gamma$  condensate [88]. The difference in ZPE between the  $\Gamma$  and K condensate is expected to be on the order of  $\sim 10^{-3}t$  [88].

Condensation into the K-point BEC can be understood as a manifestation of the order-by-disorder mechanism [167, 168]. Given a system in which the ground state is degenerate, states with energetically lower-lying excitations will be preferred. The presence of thermal fluctuations, or quantum fluctuations due to interactions, causes particles to ‘explore’ some of the excited states. In a quantum system at zero temperature, quantum fluctuations cause a shift in ZPE depending on the energy of the excited states. In classical systems, the free energy  $F$ , defined as  $F = U - TS$ , where  $U$  is the internal energy,  $T$  is temperature, and  $S$  is entropy, is similarly affected by the density of excited states. The lower the energy of the excited states, the higher the entropy at some temperature and the smaller the free energy.

In the context of the classical XY model on the kagome lattice, it has been shown that ferromagnetic NNN interactions or order-by-disorder through spin-wave fluctuations similarly cause the vortex-antiferromagnet state ( $q = \sqrt{3} \times \sqrt{3}$ ) to be energetically favourable to the vortex-ferromagnet ( $q = 0$ ) [122, 164].

**Flat band BECs and quantum metric** Julku et al. [89] recently found that the sound modes (Bogoliubov spectrum) in a flat band are intimately related to geometric properties of the flat band Bloch states. We will focus on the K BEC, i.e.  $\mathbf{k}_c = \text{K}$ . From Fig. 3.12 it is apparent that there is a large gap separating the flat band K point from higher bands. For small momenta around the K BEC and for weakly interacting particles we can therefore project the Bogoliubov Hamiltonian onto the lowest (flat) band [89],

$$L_p(\mathbf{q}) := P(\mathbf{q})^\dagger (\sigma_z H(\mathbf{q})) P(\mathbf{q}) = \frac{U\rho}{3} \begin{pmatrix} 1 & \alpha(\mathbf{q}) \\ -\alpha^*(\mathbf{q}) & -1 \end{pmatrix}, \quad (3.21)$$

where  $\alpha(\mathbf{q}) = \langle u_1(\text{K} + \mathbf{q}) | u_1(\text{K} - \mathbf{q}) \rangle$  and  $u_1(\mathbf{k})$  is the flat band eigenstate at momentum  $\mathbf{k}$ . The projection operator  $P$  is given by

$$P(\mathbf{k}) = \begin{pmatrix} |u_1(\mathbf{k})\rangle \langle u_1(\mathbf{k})| & 0 \\ 0 & |u_1(2\text{K} - \mathbf{k})\rangle \langle u_1(2\text{K} - \mathbf{k})| \end{pmatrix}. \quad (3.22)$$

The energy of the flat band Bogoliubov mode can thus be written as

$$E(\text{K} + \mathbf{q}) = \frac{U\rho}{3} \sqrt{1 - |\alpha(\mathbf{q})|^2} = \frac{U\rho}{3} \tilde{D}(\mathbf{q}). \quad (3.23)$$

Here,  $\tilde{D}(\mathbf{q}) = \sqrt{1 - |\langle u_1(\mathbf{k}_c + \mathbf{q}) | u_1(\mathbf{k}_c - \mathbf{q}) \rangle|^2}$  [152]. This is equal to the quantum distance between the flat band Bloch states at  $\mathbf{k}_c + \mathbf{q}$  and  $\mathbf{k}_c - \mathbf{q}$  [169] and is plotted in Fig. 3.15.

<sup>29</sup>This can already be seen in Fig. 3.12, where the curvature of the dispersion is consistently higher around the  $\Gamma$  point compared to the K point.

<sup>30</sup>The zero-point energy scales as the square of the speed of sound [166].

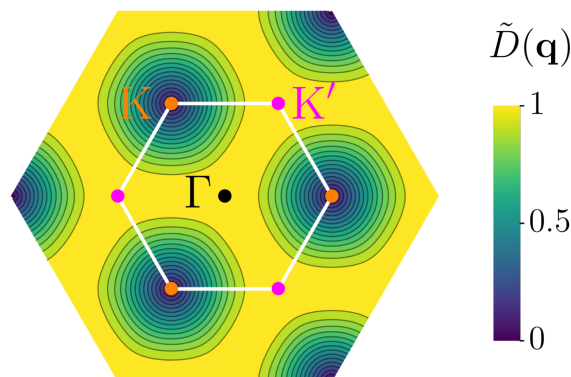


**Figure 3.15** – Quantum distance  $\tilde{D}(\mathbf{q})$  from the K-point condensate. The quantum distance is zero for  $\mathbf{q} = \mathbf{K}$ . Note that the quantum distance, and thus the excitation fraction, is finite around the K point. The K' wave function has opposite chirality to the K wave function. The derivation used to extract properties of the K BEC is equally applicable to the K' BEC.

The speed of sound is given by the derivative of the dispersion relation with momentum at K,

$$c_s = \frac{U\rho}{3} \lim_{\mathbf{q} \rightarrow \mathbf{K}} \frac{\tilde{D}(\mathbf{q})}{\mathbf{q}} = \frac{U\rho}{3} \lim_{\mathbf{q} \rightarrow \mathbf{K}} \sqrt{\frac{\tilde{D}^2(\mathbf{q})}{\mathbf{q}^2}} = \frac{U\rho}{3} \sqrt{g^1(\mathbf{K})}, \quad (3.24)$$

with

$$\begin{aligned} g^1(\mathbf{K}) &:= g_{xx}^1(\mathbf{K}) = g_{yy}^1(\mathbf{K}), \\ g_{\mu\nu}^1(\mathbf{k}) &= \langle \partial_\mu u_1(\mathbf{k}) | (1 - |u_1(\mathbf{k})\rangle \langle u_1(\mathbf{k})|) | \partial_\nu u_1(\mathbf{k}) \rangle, \end{aligned} \quad (3.25)$$

and  $\partial_\mu = \frac{\partial}{\partial k_\mu}$  [152]. We see that for the flat band BEC at K, the speed of sound is determined entirely by the quantum metric of the flat band ( $g_{\mu\nu}^1$ ), i.e. the infinitesimal quantum distance [169]. Additionally, the speed of sound scales linearly with the interaction strength instead of with  $\sqrt{U}$  as encountered in the weakly interacting BEC [166].

Geometry in Bloch bands always boils down to taking some specific scalar product of Bloch states and governs how Bloch states evolve when transported. The Berry curvature and quantum distance can be thought of as the imaginary and real part of a generalized quantum geometric tensor [169, 170]. The quantum metric quantifies the infinitesimal change of the overlap between Bloch states while the Berry curvature quantifies the infinitesimal change of the Bloch functions' phase [171]. In a flat band the effect of dispersion vanishes and the speed of sound depends entirely on geometric properties of the Bloch waves. A finite speed of sound simultaneously implies that there is a finite overlap between the condensed state and neighbouring states even in the limit of vanishing interactions [89]<sup>31</sup>. This means that there is a non-zero excited state fraction in the flat-band BEC, even in the non-interacting limit. This is in stark contrast to BECs in dispersive bands, where the excited state fraction necessarily tends to zero as the interactions are reduced

<sup>31</sup>The fraction of particles in the excited state can be calculated by adding up all the Bogoliubov modes.

[166]. Thus, the flat band causes quantum fluctuations to be strongly enhanced compared to a dispersive band [89]. On the other hand, the quantum geometry of the Bloch band stabilizes the flat band BEC even in the non-interacting limit. Taking quantum geometry into account thus leads us to conclude that flat band BECs should exist even for deep lattices, when the band structure approaches the tight-binding limit.

**Introducing temperature** We have so far only discussed the ground state properties of the flat band BEC. We will briefly discuss the results found by You et al. [88] that calculate the consequences of finite temperature in the kagome flat band.

Via the mean-field approach we found two states that fulfil the three-colour rule and thus minimize kinetic energy. However, there are many more three-colour arrangements on the kagome lattice that are non-periodic<sup>32</sup> and have the same mean-field energy as the  $\Gamma$  and K points. In fact, any wave function that has equal amplitude on all lattice sites and whose phases in each triangle obey the three-colour rule minimizes kinetic energy and is a valid mean-field ground state. By finding the eigenvalues of a real-space Bogoliubov Hamiltonian<sup>33</sup>, You et al. [88] showed numerically that all three-colour arrangements<sup>34</sup> have a ZPE between that of the K and  $\Gamma$  points, with a small gap between the absolute ground state, K, and the other states. This gap was calculated to be on the order of  $10^{-3}t$ , where  $t$  is the tunnelling parameter. At temperatures significantly below this value a BEC will form at the K point. The associated long-range order of the wave function phase will lead to sharp peaks in the momentum distribution at the K point.

At elevated temperatures,  $J \ll T \ll t$ , where  $J$  is the gap between the ZPEs of the K and  $\Gamma$  condensates, all wave functions that obey the three-colour pattern will be roughly equally occupied. This state was dubbed the ‘trion superfluid’ as it displays long-range order in  $\hat{b}_i^3$  instead of  $\hat{b}_i$  and has a finite ‘trion’ superfluid density,  $\rho_S^3 = \lim_{|i-j| \rightarrow \infty} \langle (\hat{b}_i^\dagger)^3 \hat{b}_j^3 \rangle \neq 0$  [88, 91]. Since the phase colouring is imposed by the kinetic energy, it should remain stable up to temperatures on the order of  $t$ .

Finally, as the temperature is increased beyond  $t$ , the system undergoes a BKT transition to a disordered state in which the three-colour rule no longer holds [88, 91]. To estimate the critical temperature for the BKT transition, we can look at the free energy,  $F = U - TS$ . If the interaction energy is much larger than the kinetic energy, we can assume that the sublattice density is homogeneous and that any change in internal energy is due to a deviation from the three-colour pattern. For low temperatures, the ordered states which have low entropy and minimize the kinetic energy will be preferred. However, above a critical temperature  $T_{KT}$ , the entropy contribution to the free energy dominates the kinetic energy term and the system goes into a high-entropy, disordered state. Consequently, above  $T_{KT} \sim t$ , vortices will proliferate and break the three-colour rule, thus destroying long-range trion correlations. The random distribution of phases among the lattice sites then leads to a normal, thermal state and the trion superfluid density,  $\rho_S^3$ , vanishes.

<sup>32</sup>and thus not captured by the mean-field treatment, which only can give us lattice-periodic wave functions.

<sup>33</sup>This real-space Bogoliubov Hamiltonian is analogous to the momentum-space version we derived previously with the difference that non-periodic phase colourings can be analysed as well.

<sup>34</sup>from the trial wave functions that were considered.

### 3.4 CDW & supersolid (low density)

For the following considerations, we will again use the Hubbard model as written in Eq. 3.15 and find the ground state in the low density regime. As shown previously, this Hamiltonian is equivalent to an attractively interacting Bose-Hubbard model at negative temperature.

**Constructing localized eigenstates** We start by deriving the localized states associated with the flat band of the kagome lattice which we alluded to in chapter 1 and section 2.4. The Bloch states of the kagome lattice flat band can be written as

$$\hat{\gamma}_{\mathbf{k}} = u_1(\mathbf{k}) \cdot \left( \hat{b}_{\mathbf{k},A}, \hat{b}_{\mathbf{k},B}, \hat{b}_{\mathbf{k},C} \right), \quad (3.26)$$

where  $\hat{b}_{\mathbf{k},A}$ ,  $\hat{b}_{\mathbf{k},B}$ , and  $\hat{b}_{\mathbf{k},C}$  are the Bloch state annihilation operators on sublattices A, B, and C, respectively. In the tight-binding limit,  $u_1(\mathbf{k})$  is given by

$$u_1(\mathbf{k}) = \frac{1}{\mathcal{N}(\mathbf{k})} \begin{pmatrix} \sin(\mathbf{k} \cdot \boldsymbol{\delta}_{BC}) \\ \sin(\mathbf{k} \cdot \boldsymbol{\delta}_{CA}) \\ \sin(\mathbf{k} \cdot \boldsymbol{\delta}_{AB}) \end{pmatrix}, \quad (3.27)$$

where  $\boldsymbol{\delta}_{AB}$ ,  $\boldsymbol{\delta}_{BC}$  &  $\boldsymbol{\delta}_{CA}$  are the same as in section 2.3 (see also Fig. 3.16) and

$$\mathcal{N}(\mathbf{k}) = \sqrt{\sum_i \sin^2(\mathbf{k} \cdot \boldsymbol{\delta}_i)}. \quad (3.28)$$

Any arbitrary superposition of flat band states will again be a flat band state. To obtain the localized states, we take a weighted superposition of all Bloch states,

$$\begin{aligned} \hat{\Gamma}_i &= \sum_{\mathbf{k}} 2i\mathcal{N}(\mathbf{k})\hat{\gamma}(\mathbf{k})e^{i\mathbf{k}\cdot\mathbf{r}_i} \\ &= \sum_{\mathbf{k}} 2i(\sin(\mathbf{k} \cdot \boldsymbol{\delta}_{BC})\hat{b}_{\mathbf{k},A} + \sin(\mathbf{k} \cdot \boldsymbol{\delta}_{CA})\hat{b}_{\mathbf{k},B} + \sin(\mathbf{k} \cdot \boldsymbol{\delta}_{AB})\hat{b}_{\mathbf{k},C})e^{i\mathbf{k}\cdot\mathbf{r}_i} \\ &= \underbrace{\sum_{\mathbf{k}} e^{i\mathbf{k}\cdot(\mathbf{r}_i+\boldsymbol{\delta}_{BC})}\hat{b}_{\mathbf{k},A}}_{\hat{h}_{i,1}} - \underbrace{\sum_{\mathbf{k}} e^{i\mathbf{k}\cdot(\mathbf{r}_i-\boldsymbol{\delta}_{BC})}\hat{b}_{\mathbf{k},A}}_{\hat{h}_{i,4}} + \underbrace{\sum_{\mathbf{k}} e^{i\mathbf{k}\cdot(\mathbf{r}_i+\boldsymbol{\delta}_{CA})}\hat{b}_{\mathbf{k},B}}_{\hat{h}_{i,5}} \\ &\quad - \underbrace{\sum_{\mathbf{k}} e^{i\mathbf{k}\cdot(\mathbf{r}_i-\boldsymbol{\delta}_{CA})}\hat{b}_{\mathbf{k},B}}_{\hat{h}_{i,2}} + \underbrace{\sum_{\mathbf{k}} e^{i\mathbf{k}\cdot(\mathbf{r}_i+\boldsymbol{\delta}_{AB})}\hat{b}_{\mathbf{k},C}}_{\hat{h}_{i,3}} - \underbrace{\sum_{\mathbf{k}} e^{i\mathbf{k}\cdot(\mathbf{r}_i-\boldsymbol{\delta}_{AB})}\hat{b}_{\mathbf{k},C}}_{\hat{h}_{i,6}} \\ &= \frac{1}{\sqrt{6}} \sum_{j=1}^6 (-1)^j \hat{h}_{i,j}. \end{aligned} \quad (3.29)$$

Here,  $\mathbf{r}_i$  is the position of the centre of the  $i^{\text{th}}$  hexagon (see Fig. 3.16). The last line shows that the localized state is confined to a hexagon and has alternating phases on the hexagon sites.

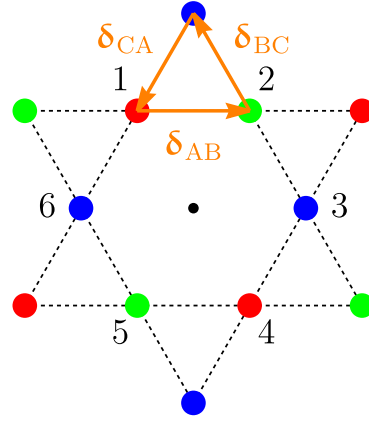


**Figure 3.16** – The black point in the centre marks the centre of a hexagon in the kagome lattice, i.e. the point to which  $\mathbf{r}_i$  points. Red, green, and blue points are A, B, and C sites, respectively.

The localized state is a direct result of Fourier transforming the momentum-space representation of the flat band Bloch states  $(\hat{\gamma}_{\mathbf{k}})^{35}$ . Any superposition of localized states is again a localized state, as shown in Fig. 3.17.

**Effect of interactions** For a non-interacting system we expect all Bloch states in the flat band to be equally occupied, which should manifest itself in momentum space as the distribution shown in Fig. 3.6. In the case of repulsively interacting bosons at a filling fraction<sup>36</sup> ( $\nu$ ) below 1/9, the energy is minimized when atoms occupy non-overlapping hexagon states. The momentum distribution can be calculated by taking a weighted sum over all real-space coherences,

$$n(\mathbf{k}) = \sum_{\alpha, \alpha'} \langle \hat{b}_{\mathbf{k}, \alpha}^\dagger \hat{b}_{\mathbf{k}, \alpha'} \rangle = \frac{1}{M} \sum_{\alpha, \alpha'} \sum_{n, m} \langle \hat{b}_{n, \alpha}^\dagger \hat{b}_{m, \alpha'} \rangle e^{i\mathbf{k} \cdot (\mathbf{r}_{m, \alpha} - \mathbf{r}_{n, \alpha'})}, \quad (3.30)$$

where the sum is taken over all lattice sites and  $M$  is a normalization constant. As the particle density is increased from zero, the average spatial extent of the particle wave function must necessarily decrease to avoid wave function overlap, which would introduce interaction energy. The momentum distribution thus evolves from Fig. 3.6 to the distribution shown on the left side of Fig. 3.17. The interacting case is subtly different from the non-interacting case, since, in the non-interacting case, the sum in Eq. 3.30 also contains states that have long-range coherence. At  $\nu=1/9$ , bosons are densely packed and any increase in density will cause a penalty to either interaction energy (if particle wave functions overlap) and/or kinetic energy (if the added particle is not a flat band state, i.e. violates the hexagon arrangement). Using Eq. 3.30, we can calculate the momentum distribution of the charge-density wave (CDW) at  $\nu=1/9$  to be

$$n(\mathbf{k}) = n_0 \left( \cos\left(\frac{ak_x}{2}\right) - \cos\left(\frac{\sqrt{3}ak_y}{2}\right) \right)^2 \sin^2\left(\frac{ak_x}{2}\right), \quad (3.31)$$

<sup>35</sup>We can also think of the localized state as being the Fourier transform of a constant in momentum space. We are effectively creating a delta function in real space.

<sup>36</sup>The number of particles per site.

where  $\mathbf{k} = (k_x, k_y)^T$  and  $a$  is the spacing between lattice sites.

The CDW momentum distribution does not display any sharp peaks due to the absence of long-range coherence. Fig. 3.17 shows the localized hexagon state and an example of a superposition of hexagon states that is suppressed in the tightly-packed case.

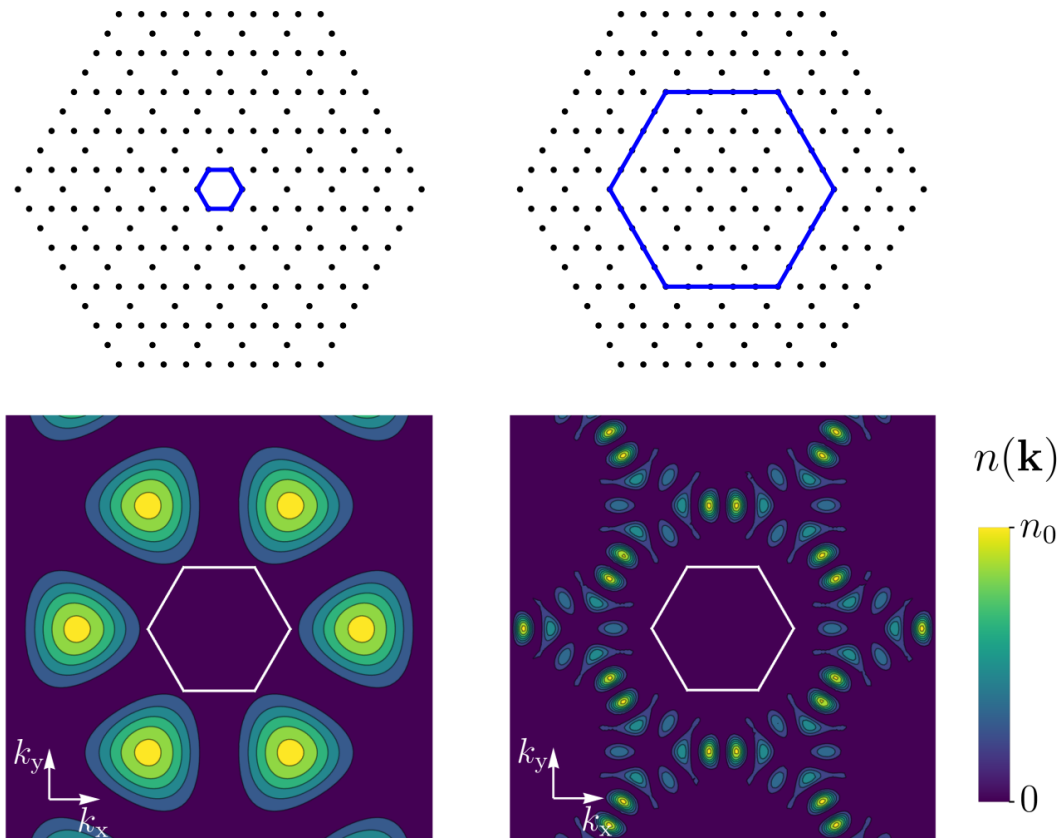


**Figure 3.17** – Left: maximally localized hexagon state in real space (top) and momentum space (bottom). This momentum distribution is expected for a filling fraction of  $1/9$  and repulsive interactions. Right: example of a superposition state of maximally localized hexagon states in real space (top) and momentum space (bottom). The state on the right is a ground state of a low-density or non-interacting system, whereas it is not a ground state in a system with repulsive interactions close to the critical density.

Note that occupation at the reciprocal lattice vectors is suppressed due to destructive interference of the alternating phases between nearest neighbours in the hexagon state.

The tightly packed CDW can be seen as a Wigner crystal of bosons [83, 97]. Wigner crystals are usually discussed in the context of 2D electron gases where below certain particle densities electrons crystallize into triangular patterns [172, 173], thereby breaking continuous translational symmetry. In the case of the flat band CDW the discrete  $\mathbb{Z}_3$  symmetry associated with the three different valid CDW configurations is broken (see Fig. 3.18).

**Superfluid peaks above critical density** Huber et al. [84] showed that doping the CDW with particles above the critical filling ( $\nu=1/9$ ) leads to the emergence of superfluid order without destroying CDW order. Additional bosons condense into interstitial sites

between the localized states. Fig. 3.18 shows that the interstitial sites form a kagome lattice, albeit rotated and with a lattice spacing that is  $\sqrt{3}$  times larger with respect to the underlying kagome lattice. A system displaying both diagonal (CDW) and off-diagonal (superfluid) long-range order is commonly referred to as being supersolid.

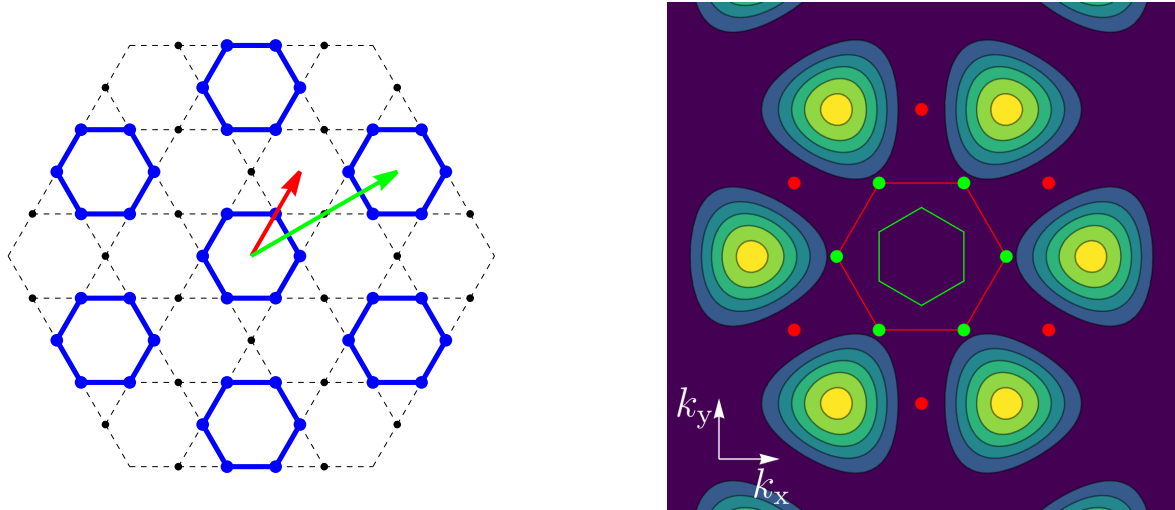


**Figure 3.18** – Left: densely-packed CDW. The red (green) arrow indicates one of the kagome (CDW) lattice vectors. Bosons are expected to condense into the interstitial sites above a critical density of  $1/9$ . Right: first Brillouin zones of the underlying kagome lattice (red) and the kagome lattice formed by the interstitial sites of the CDW (green). Beyond a filling of  $1/9$  and in the presence of repulsive interactions, a BEC forms at the reciprocal lattice vectors of the CDW, which coincide with the K, K' points of the underlying lattice.

The hexagons of the kagome lattice form a triangular lattice. The tightly packed CDW is thus equivalent to a triangular lattice in which only every third site is occupied. Huber et al. showed that particle doping causes an effective AFM interaction between the triangular lattice sites to emerge [84], causing the ground state to display the familiar three-colour arrangement of phases. In the underlying kagome lattice this three-colour arrangement can be thought of as the ‘locking’ of relative phases between hexagons, which is unlike in the pure CDW state where there is no phase coherence between hexagon states. The long-range phase coherence due to the three-colour arrangement manifests itself as peaks at the K or K' points (depending on the chirality of the three-colour pattern) of the triangular lattice Brillouin zone<sup>37</sup> or, equivalently, at the  $\Gamma$ -points of the CDW Brillouin zone (see Fig. 3.18). The occupation at the  $\Gamma$ -points is strictly zero, due to both the destructive interference of hexagon states due to their alternating phases, and the destructive interference of the three-colour phase pattern of the superfluid. Perfect CDW order and perfect superfluid order are mutually exclusive, but they can coexist together, albeit imperfectly in the regime  $\nu > 1/9$ .

We previously discussed the mean-field approach on the kagome lattice and found that interactions cause a flat-band BEC to emerge in the ground state. Mean-field theory on

<sup>37</sup>The triangular lattice of hexagons of the kagome lattice is the same as the Brillouin zone of the kagome lattice itself.

the kagome lattice breaks down at low densities because we exclude the possibility of there being spatially non-uniform density distributions such as the hexagon and CDW states. It is not entirely clear if and at what density CDW order vanishes and how to reconcile the results found in [84] with those of [88] and [152]. More precise results in the intermediate regime between low and high densities, e.g. via exact diagonalization [84], could shed light on how these two regimes are connected.

**Which phases can our machine observe?** In this chapter we introduced negative temperatures as a means to prepare ultracold atoms in the flat band of the kagome lattice. We then summarized previous theoretical work studying the ground state of the Bose-Hubbard model on the kagome flat band in different density regimes and showed measurable signatures of the predicted flat band BEC, trion superfluid and supersolid states. While we have shown that we can create negative temperature states with our machine (see [section 7.1.2](#)), it is still unclear which of the above models we will be able to implement. There are several ways in which our preparation of the kagome flat band could cause discrepancies between our system and the ideal models.

Firstly, we are always working at a finite temperature. If the gap between the ground and excited states is too small, we will not be able to prepare the ground state using adiabatic methods. This is likely true for the flat band BEC, which requires temperatures below  $10^{-3}t$ , which is currently not feasible in cold-atom experiments. However, since the trion superfluid is predicted to exist up to temperatures of roughly  $0.1t$ , it should be possible to observe this state with our machine provided there are no other limitations to our approach. The CDW has a gap on the order of  $U$  or  $t$  (whichever is smaller), so it should be fairly straightforward to observe from a temperature point of view.

Secondly, it is unclear if we can reach the bosonic flat band phases by melting a Mott insulator, which is at the heart of our negative temperature preparation scheme [174]. Specifically, it is not clear whether the frustrated phase pattern will appear with high fidelity from the initial Mott insulating state. It might be that it takes prohibitively long for the frustrated phase pattern to emerge. Based on previous experiments with Floquet shaking in a triangular lattice [47] and our experiments with the triangular lattice, the frustrated phase arrangement is indeed realizable, so this should also apply to the kagome lattice.

Finally, the kagome flat band is only asymptotically flat and always displays some finite dispersion. Especially in the case of the flat band BEC at  $\Gamma$ , with only a small energy difference to the K state, the fact that the optical kagome lattice flat band always has slightly higher energy at  $\Gamma$  than at K could cause the K BEC to be experimentally unobtainable (never mind the temperatures needed!). However, this should not affect the emergence of a trion superfluid which should be robust even in the presence of finite flat band dispersion.

Given these constraints, it seems feasible to observe the kagome trion superfluid with our protocol. Immediate goals are to observe a stable population inversion by band-mapping. If at this point our temperature is sufficiently low, we might be able to also observe the trion superfluid.

One way to prepare a K condensate despite large temperatures could be to prepare the K wave function directly via a Wilson line, i.e. non-adiabatic transport in momentum space. As calculated in [appendix D](#), there is a Wilson line that connects the Bloch state

of the kagome lattice at  $\Gamma$  in the lowest band (where the positive temperature BEC forms) to the flat band Bloch state at K. Such a diabatic protocol has been shown to be effective in preparing higher-band states in the honeycomb lattice [175]. Direct preparation of the K condensate might also prevent the  $\Gamma$ -point from becoming occupied, since the  $\Gamma$  and K wave functions are topologically distinct<sup>38</sup>.

---

<sup>38</sup>They are topologically distinct because it would require a phase transition to change the vortex antiferromagnet (K) to a vortex ferromagnet ( $\Gamma$ ).

## 4 Machine design

This chapter gives a detailed account of the kagome machine as it currently stands. Our machine has gone through roughly four build stages after each of which we ran sequences and performed experiments.

Our first operational machine configuration consisted of just the 2D and 3D MOT chambers. On the experimental side we achieved MOTs of  $^{87}\text{Rb}$ ,  $^{39}\text{K}$ , and  $^{40}\text{K}$ , evaporative cooling of  $^{87}\text{Rb}$  and hybrid trapping and Bose-condensation of  $^{87}\text{Rb}$ . During this time we made various decisions concerning implementation of the kagome lattice and the microscope including whether to put the objective in or out of vacuum, whether to use one or two objectives and which wavelength to use for the lattice. We also designed the science chamber, installed our experiment control software<sup>39</sup>, built and tested optical transport on a test setup and designed and tested the microscope objective<sup>40</sup>.

The second operational machine configuration began when the science chamber was incorporated and baked. In this stage we optically transported atoms into the science chamber, made  $^{87}\text{Rb}$  BECs in the science chamber, installed the Feshbach and gradient coils, condensed  $^{39}\text{K}$ , and installed the vertical lattice and the monolithic mount. For this stage, while we were designing the final layout of optics around the science chamber, we used a temporary dipole trap<sup>41</sup>.

Shortly before we received the lattice laser, we rebuilt the dipole trap to conform to our comprehensive plan detailing the layout of the optics around the science cell. We installed most of the lattice optics hereafter, but were still waiting for lenses to obtain our desired beam waists. During this third stage of development the lattice beams had waists of only 30  $\mu\text{m}$ . We took our first Kapitza-Dirac superlattice images and managed to produce a superfluid in the 532 nm triangular lattice. We were still missing some electronics to be able to adiabatically load the 1064 nm honeycomb lattice and electronics needed for phase-stabilization. We also did not have the phase stations installed at this point<sup>42</sup>.

The fourth operational machine configuration is the current state of the experiment. We have installed the correct lattice optics and phase stations and incorporated the vertical dipole beam. Achievements include implementing active phase stabilization and creating a superfluid and Mott insulator of  $^{87}\text{Rb}$  and  $^{39}\text{K}$  in the kagome lattice and observing a negative temperature state in the triangular lattice.

Future machine upgrades will focus on including various elements required for single-site resolved imaging, such as the imaging lattice, imaging optics, and Raman beams (more about this in [chapter 8](#)). This upgrade will likely only happen after we have taken some data on negative temperatures in the triangular and kagome lattices.

### 4.1 Vacuum system

The vacuum system is at the heart of the kagome machine and is designed specifically to implement a kagome lattice quantum gas microscope with bosonic  $^{39}\text{K}$  and  $^{87}\text{Rb}$ , and fermionic  $^{40}\text{K}$ . It should be seen as the next version in a long line of vacuum chambers

<sup>39</sup>QControl3 (python-based); kindly provided by the Max-Planck-Institute for Quantum Optics.

<sup>40</sup>MOT chamber bake-out started on 22/09/2018, science chamber bake-out finished on 18/12/2020.

<sup>41</sup>This stage lasted roughly from early January 2021 to mid-August 2021.

<sup>42</sup>This stage lasted roughly from mid-August 2021 to late November 2021.

that have been proven to work for optical lattice experiments. Our vacuum chamber is based on our group's quasicrystal machine [176, 177], which itself is in large parts copied from a previous experiment based in Munich [160, 178]. We also drew inspiration from numerous other quantum gas microscope experiments when we designed our microscope chamber [179–187].

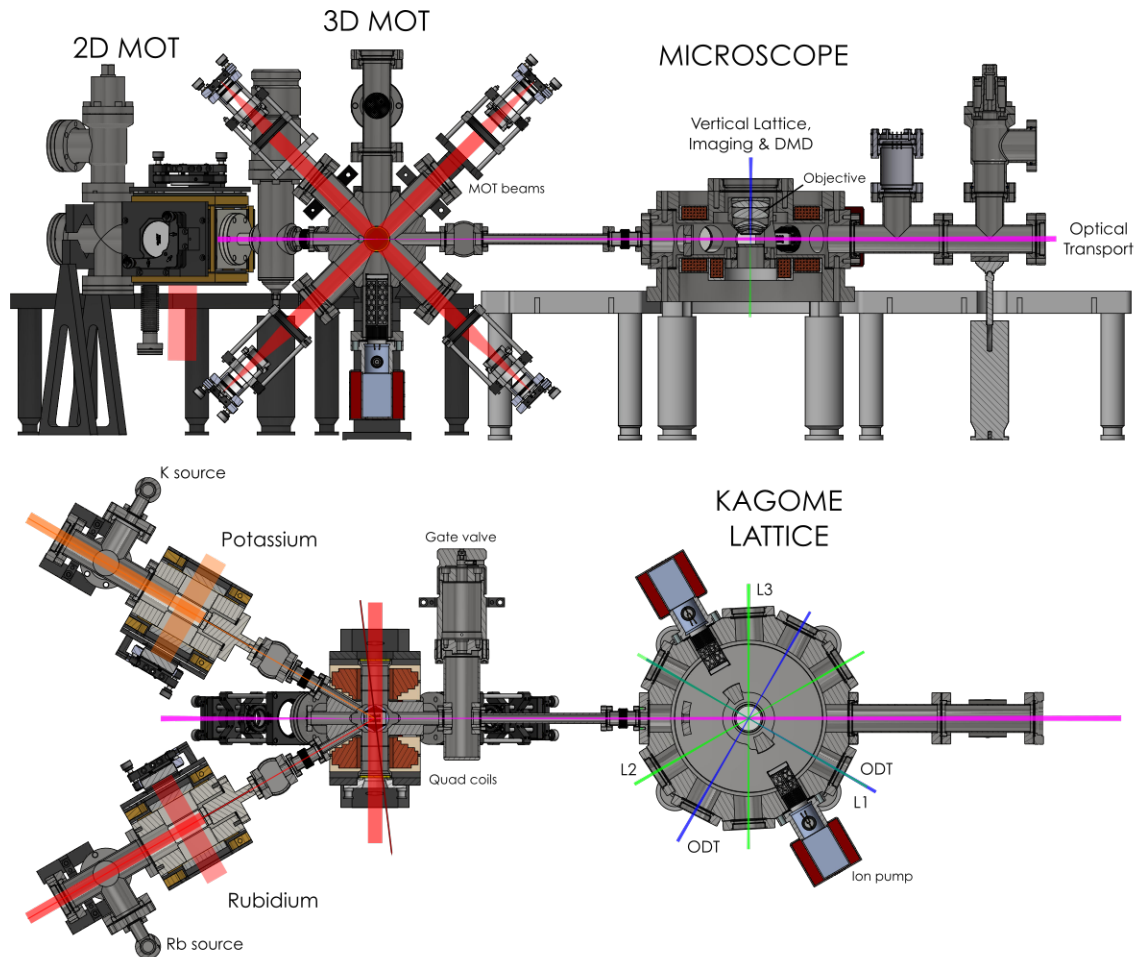


**Figure 4.1** – Diagram of the full vacuum chamber. Taken from [140].

Fig. 4.1 shows a model of the full vacuum chamber. It consists of four different chambers connected via differential pumping sections.

We use two 2D MOTs, one for  $^{87}\text{Rb}$ , one for  $^{39}\text{K}$  and  $^{40}\text{K}$ . This allows us to independently tune the temperature, and therefore the vapour pressure inside the two 2D MOTs. The 3D MOT chamber is at the centre of the vacuum system. The main purpose of the 3D MOT chamber is to cool down atoms from room temperature to a few  $\mu\text{K}$ , and even to quantum degeneracy if desired. The science chamber is the largest chamber and is connected to the 3D MOT chamber via a long differential pumping section.

Apart from these main chambers, there are various smaller active and passive components that in their entirety seal the vacuum system, maintain and measure the internal pressure and allow for optical access for the  $\sim 50$  different laser beams we need during the sequence.

Each of the four chambers is connected to a respective CF40 valve<sup>43</sup>, providing independent access to each chamber from the outside<sup>44</sup>. Each chamber can also be isolated from all of the other chambers via CF16 valves<sup>45</sup>, which was particularly important for baking out the science chamber while keeping the MOT chamber under UHV conditions.

The MOT and science chambers are actively pumped with ion pumps and non-evaporable getters (NEGs)<sup>46</sup> and the pressure in both chambers is measured using an ion gauge<sup>47</sup>.

Finally, the chamber was designed to incorporate various coils we require for producing magnetic fields and by the overarching principle of compactness and simplicity, to give us as much room as possible to place optics outside the vacuum chamber.

The entire vacuum chamber is mounted onto a floatable, non-magnetic optical table<sup>48</sup> such that its central plane is horizontal and 270 mm above the optical table. We chose 270 mm as the height of the vacuum chamber's central plane such that our standard optics, with a nominal height of 70 mm, will work for our vacuum chamber when placed on 200 mm tall breadboards. The breadboards give us more room to operate and place optics, which is necessary considering that a large part of the experiment table is occupied by the vacuum chamber.

**Material** Our vacuum components are, where possible, manufactured out of 316LN steel, which has a magnetic susceptibility  $<5 \times 10^{-3}$  [188]. We use non-magnetic steel to minimize stray magnetic fields caused by magnetization. Our coils can produce magnetic fields up to 750 G which is sufficient to magnetize normal steel to such a level that it is detrimental to our experiments<sup>49</sup>. Our 2D MOTs are made of titanium which is an artefact from previous chamber designs. Titanium and aluminium are two metals that have negligible magnetic susceptibilities and thus would be even better than 316LN steel for a cold-atom vacuum chamber. However, titanium is much more expensive and aluminium is only rarely used as vacuum chamber material. A future version of this chamber could be made out of aluminium, which has superior cost, weight, magnetic, outgassing and bake properties compared to steel and titanium [188, 189].

**Assembly** The chamber was assembled in two stages. In the first stage, the 2D MOTs and 3D MOTs were connected and baked out. About 2 years later we completed the chamber by connecting the science chamber and baking it. We decided to go for this approach as we quickly realized that designing the science chamber and objective would take a considerable amount of time. The parts for the first assembly stage were ordered within three months of us starting the experiment and the bake-out of the MOT chambers

---

<sup>43</sup>VAT 54132-GE02-0001

<sup>44</sup>This is only necessary for baking. After baking, the vacuum chamber ideally remains sealed until the machine is decommissioned.

<sup>45</sup>VAT 48124-CE01-0001

<sup>46</sup>1 x NEX Torr D200 in the MOT chamber and 2 x NEX Torr Z100 in the science chamber.

<sup>47</sup>VACOM BAT40C

<sup>48</sup>Newport M-RS4000 with 316 stainless steel top.

<sup>49</sup>We learned this the hard way with steel screws placed around the 3D MOT chamber. These became magnetized to such a degree as to produce gradients strong enough to affect our atomic cloud. Unfortunately removing them would require us taking out the 3D MOT coils, which is not worth the effort.

was completed about a year after starting. While designing the science chamber and the objective we got the MOT chamber side of the experiment up and running.

## Atom sources

**Rubidium ampoule** The rubidium ampoule<sup>50</sup> is commercially available and contains 1 g of rubidium in an argon atmosphere<sup>51</sup>. The sealed ampoule was placed in a custom-made holder and inserted into the rubidium source bellow. After baking out the MOT chamber (see [section 4.1.1](#) for details), we broke the <sup>87</sup>Rb ampoule by bending the source bellow, thus releasing <sup>87</sup>Rb into the chamber.

**Potassium ampoule** The potassium ampoule contains 100 mg of 3% enriched <sup>40</sup>K, the rest being predominantly <sup>39</sup>K. Sources enriched in <sup>40</sup>K are critical for reaching sufficiently large atom numbers [[190](#), [191](#)]. We proceeded in the same way with the potassium ampoule as we did with the <sup>87</sup>Rb ampoule. After breaking the ampoule in vacuum we wrapped the source bellow in aluminium foil, thin wire and another layer of aluminium foil. A small power supply drives a continuous current through the wire and causes heat to dissipate. In this way we heat the source bellow up to a temperature of 65 °C, ensuring a vapour pressure of  $\sim 1 \times 10^{-6}$  mbar [[192](#)].

**2D MOT chambers** The 2D MOT chambers are the first of the four chambers. They are kept at an estimated pressure of  $\sim 1 \times 10^{-7}$  mbar -  $1 \times 10^{-6}$  mbar<sup>52</sup> and are only pumped via the differential pumping section between 2D and 3D MOT chambers (see [Fig. 4.2](#)). The 2D MOT chambers have a rectangular cross section, with their long axis pointing toward the 3D MOT chamber and the short axes being the directions of collimation. The apertures and windows on the rectangular sides of the 2D MOT chambers are also rectangular and allow for the 2D MOT cooling and repump beams to enter. The windows were glued onto the 2D MOT chambers using vacuum-compatible epoxy<sup>53</sup> and cured at 150 °C for 1 day. Trapped air in the glue was removed by exposing the glue to a low vacuum ( $\sim 2 \times 10^{-2}$  mbar) in a desiccator before application to the 2D MOT frames. Thin spacers made of kapton were immersed in the glue and the window was placed on top. The thin spacers of kapton were used to ensure that there is no direct contact between chamber and window, which might lead to a bad vacuum seal.

The 2D MOT chambers are each connected to respective differential pumping sections<sup>54</sup> which in turn are connected to the 3D MOT chamber via a respective valve. We glued a 1" polarizer and 1" mirror onto the 2D MOT side of each differential pumping section (see [Fig. 4.2](#)) and drilled holes into these mirrors and polarizers through which the atoms travel on their way to the 3D MOT. The mirror and polarizer are used to reflect a variable amount of axial 2D MOT cooling light back along the 2D MOT chamber axis. The 2D MOT chamber components are identical on the rubidium and potassium side.

<sup>50</sup><https://www.alfa.com/en/catalog/044214/>

<sup>51</sup>The natural abundance of <sup>87</sup>Rb is 27.8%.

<sup>52</sup>Approximate vapour pressure of rubidium at 20 °C [[193](#)] and potassium [[192](#)] at 65 °C.

<sup>53</sup>Epo-Tek 353ND

<sup>54</sup>Inner diameter: 1.5 mm, length: 62 mm.

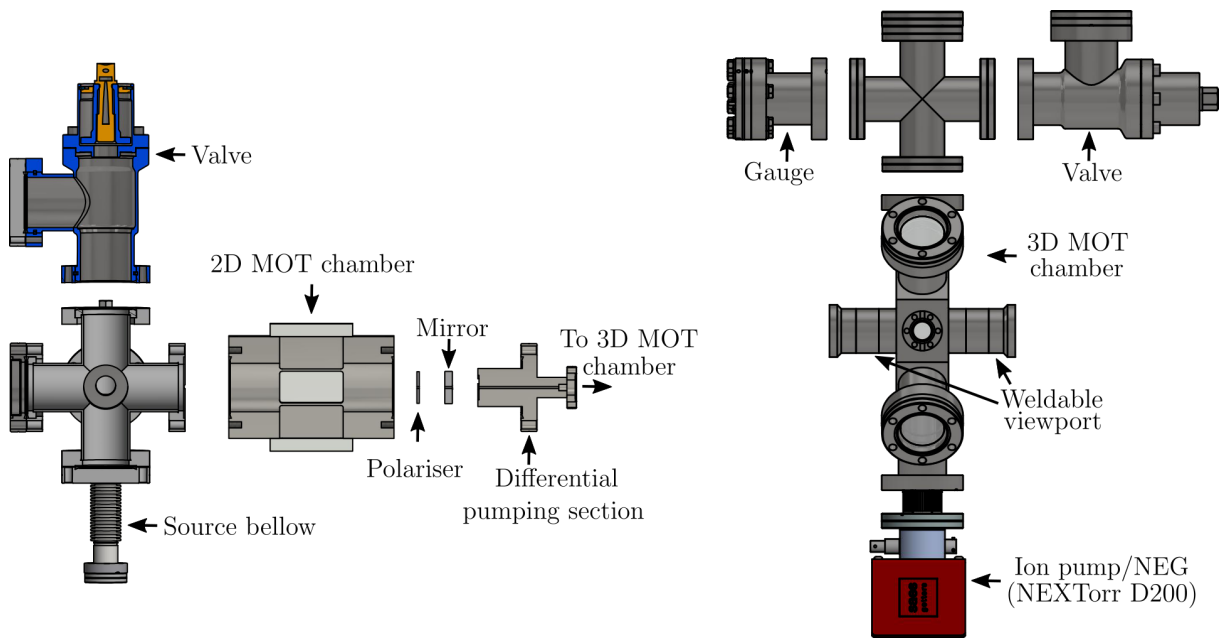


**Figure 4.2** – Left: cut through exploded view of 2D MOT chamber. Right: exploded view of 3D MOT chamber.

**3D MOT chamber** The 3D MOT chamber is located in the centre of the vacuum setup and connects to both the 2D MOT chambers and the science chamber. In the 3D MOT chamber, atoms from the 2D MOT chamber are collected, cooled down and transported to the science chamber. Its shape is primarily governed by five considerations:

- 1. Optical access for the MOT beams** The MOT requires three counter-propagating pairs of lasers, which in turn requires the 3D MOT chamber to have six viewports through which these beams can enter. The viewports must be arranged such that all beams intersect and each beam pair is perpendicular to the other two.

- 2. Space for strong quadrupole coils** In addition to the six MOT beams, the MOT requires a quadrupole field. This quadrupole field is provided by a pair of large coils. These coils also create the magnetic trap, which requires a much larger magnetic field gradient than the MOT. To reach a strong gradient, it is beneficial to have the MOT coils be very close to each other. This constrains the MOT chamber to be very narrow along one axis.

- 3. Optical transport** Optical transport requires an input and output viewport for the transport laser. We chose a CF16 viewport for the input of the transport laser, which is just about large enough to not clip the transport beam.

- 4. Connections to 2D MOTs** We decided to angle the 2D MOTs away from the science chamber (in contrast to [160, 177]) so that we have more space for optics.

**5. Pump** Finally, we had to find a way to incorporate an ion pump/getter to maintain the MOT chamber's vacuum pressure.

The design we came up with is shown in Fig. 4.1 and Fig. 4.2. The 3D MOT chamber has the shape of an octagon, its axis lying in the horizontal plane. The axial dimension of the 3D MOT chamber is narrow to allow for the 3D MOT coils to be placed close to each other. The viewports for the MOT beams are situated along the chamber axis and the 45°-faces of the octagon. Optical access for the transport beam is provided on the vertical faces of the octagon. The bottom of the chamber is connected to an SAES pump, while the top face connects to a cross which in turn connects to a gauge and a valve. The top of this cross is sealed by a viewport, giving us optical access to the MOT chamber from above. We use this top viewport primarily to measure a fluorescence signal while loading the <sup>39</sup>K, <sup>40</sup>K and <sup>87</sup>Rb MOTs. We additionally have two cameras, one each for potassium and rubidium, that can image the fluorescence<sup>55</sup>. Finally, we have two extra ports placed symmetrically and horizontally next to the input port of the transport beam. These are connected via various components to the 2D MOT chambers. The angle between the two 2D MOT ports of the 3D MOT chamber is 60°.

The 3D MOT chamber is made of 316LN steel and was manufactured by VACOM. In order to minimize the diameter of the viewports along the coil axis, we had the viewports be welded to the chamber (see Fig. 4.2). We did this so that the 3D MOT coils could have a small internal diameter which boosts the maximum obtainable magnetic field gradient. For the other viewports we use gaskets and screws, making them more bulky.

Some of the flanges, specifically the four diagonal CF40 flanges that provide optical access to the 3D MOT beams, are angled by 3°. This ensures that back-reflections from the viewports don't propagate and form a standing wave inside the chamber. It also prevents unwanted back-reflections from hitting the cloud. All our 3D MOT chamber viewports are DUV grade (Corning HPFS 7980 Fused Silica), brazed and broadband AR-coated for 650 nm-950 nm. The viewport flanges are made of 316LN steel.

The pressure in the 3D MOT chamber, as measured on our gauge and ion pump, is  $3 \times 10^{-10}$  mbar and  $1 \times 10^{-10}$  mbar, respectively.

**Science chamber** The science chamber is connected to the 3D MOT chamber via a valve, bellow and a 170 mm long differential pumping section with an inner diameter of 10 mm. Several constraints informed the design of the science chamber:

**1. Objective in vacuum** The main constraint on our chamber is that it should contain a high-NA microscope objective. This requirement immediately throws out the possibility of using a glass cell, since mechanical parts are required to mount the objective inside the vacuum chamber.

**2. Stability** It is paramount that the objective is mounted securely such that it cannot vibrate. Any vibration could cause the objective to become misaligned. Good stability requires a large mass and methods to damp vibrations.

---

<sup>55</sup>We rarely use the MOT fluorescence cameras however and usually opt for either the side fluorescence camera or one of the 3D MOT absorption cameras.

**3. Optical Access** The chamber is designed to support an optical kagome lattice, which requires at least six viewports for the lattice beams. In addition, the lattice axes should ideally not overlap with the transport axis as this would require sending lattice beams down the entire length of the chamber. If we additionally want a symmetric chamber, then the lowest-order regular polygon that fulfils the lattice beam requirement is the dodecagon.

**4. Pumps** The vacuum pressure in the science chamber should be as low as possible. The lower the background pressure, the longer the lifetime of trapped atoms, since collisions with background gases are minimized. We thus require additional ion pumps and getters attached either directly or indirectly to the science chamber.

**5. Valve and Gauge** We also need independent access to this chamber from the outside, for pumping purposes. Since we assembled the 2D and 3D MOT chambers in a first step and added the science chamber later, we wanted to be able to bake the science chamber independently of the other chambers. We therefore added another angled CF40 valve to the science chamber. In addition, we added another gauge. This helped us a lot during the science chamber bake and is useful for monitoring the pressure in the science chamber.

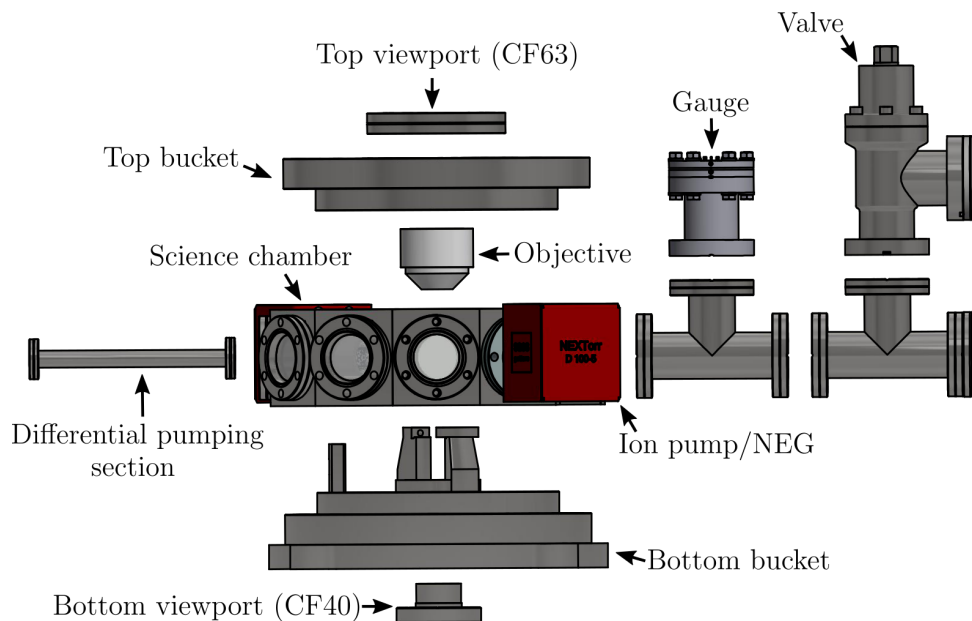


**Figure 4.3** – Diagram of the science chamber vacuum components.

A detailed schematic of the science chamber is shown in [Fig. 4.3](#). We decided to have a dodecagonal chamber with CF40 ports on each of the twelve sides and CF200 ports on the top and bottom<sup>56</sup>. The top and bottom of the science chamber are sealed by custom made CF200 ‘buckets’. The bottom bucket is attached to four 50 mm diameter aluminium posts, which are clamped to the optical table. We filled the posts supporting the science chamber with lead shot and sand to dampen any acoustic modes which might

<sup>56</sup>The science chamber was manufactured by Pfeiffer Vacuum.

be detrimental to phase stabilization<sup>57</sup>. Those faces of the science chamber to which viewports are directly attached (8 faces) are angled by  $3^\circ$  with respect to the regular dodecagon. This is to prevent any back-reflections from striking the atoms and prevents any standing waves between viewports on opposite ends of the chamber. All other faces are flat, i.e. they are not angled with respect to the regular dodecagon. The flat faces are along the transport axis (12-6) and the pump axis (2-8). The viewports are brazed and their flanges are made of 316LN steel. The windows are DUV grade fused silica and broadband anti-reflection coated on both sides for the 532 nm-1178 nm range. Since our chamber is dodecagonal, we label the faces clockwise (when looking from the top) from 1 to 12 (see Fig. 4.4).

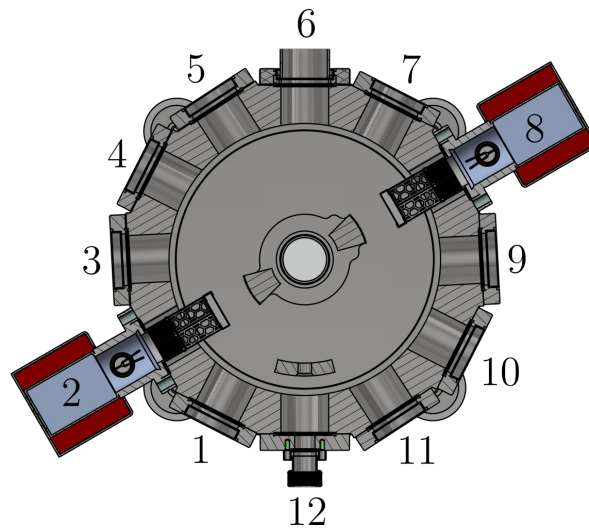


**Figure 4.4** – Looking at the science chamber from the top. The 12 faces of the science chamber are labelled 1-12, where 12 is closest to the MOT chamber.

**Objective mounting** Our objective sits on two mounts which are welded onto the bottom bucket and held in place with a vented set screw. This scheme was chosen so that the axis of the objective is naturally perpendicular to the bottom viewport. The science chamber and top bucket are only connected to the table via gaskets, which in principle could lead to small angles between these components. We tightened all connections on the science chamber metal-to-metal. It is especially important that the in-vacuum objective is well aligned to the bottom viewport, because the angle of the lattice plane is determined by the angle of the bottom viewport. For the objective to achieve maximum resolution, it is crucial that the angle between the lattice plane and the axis of the objective is as close to  $90^\circ$  as possible. More details on the objective itself can be found in [section 8.5](#).

**Pumps** We chose not to use big ion pumps or titanium sublimation pumps in addition to SAES NEX Torr pumps, since this would have significantly cut into our space to place optics. Also, since these pumps would be connected via a CF40 flange on the science chamber, the pump speed would be significantly reduced due to finite conductance.

<sup>57</sup>We used a heat gun to dry the sand before pouring it into the science chamber legs. This was to make sure we did not create steam or cause the legs to explode during the bake.

Another problem with a titanium sublimation pump is that it could potentially coat the microscope objective if they were in line-of sight with each other.

We decided to attach two SAES pumps directly to the science chamber. This minimizes loss of pump speed due to conductive elements and makes the chamber more compact, thus freeing up space for optics. One drawback of this pump configuration is that we block two of the science chambers' twelve CF40 flanges. An alternative would have been to connect the pumps via T-pieces and preserve optical access. However, we were willing to sacrifice the enhanced optical access in favour of having a more compact system and higher pump speeds.

The pumps are connected to faces 2 and 8 of the science chamber. We chose these faces for the pumps because blocking optical access from these directions was least disruptive to our optical lattice scheme.

**Valve and gauge** The valve and gauge are mounted on a respective T-piece, elongating the chamber to a total length of about 1 m. Optical access along the transport axis is thus preserved and the transport beam has a clear path to exit the chamber.

**Buckets** The top and bottom buckets<sup>58</sup> are made of 316LN steel and are connected to the science chamber via CF200 connections. The top bucket contains an annular extrusion in which the top Feshbach coil is placed. The central, non-recessed cylinder of the top bucket has an extrusion with an inner diameter of 70.1 mm, slightly wider than the outer diameter of the objective (60 mm). The central cylinder is sealed from the top by a CF63 viewport. Light collected by the objective will pass through this viewport and be collected on an EMCCD.

The science chamber is sealed from the bottom by the bottom bucket via a CF200 connection. The central region of the bottom bucket is recessed and contains a CF40 connection in its centre. The bottom bucket is sealed from the bottom by a re-entrant viewport<sup>59</sup>. This viewport reflects the vertical lattice and transmits absorption imaging light and the vertical dipole beam. Imaging light passing through this viewport is imaged onto a camera for low-resolution in-situ or time-of-flight (TOF) absorption imaging. The recessed space of the bottom bucket contains the bottom Feshbach coil on the outside and the gradient coil on the inside (more on this in [section 4.4](#)).

#### 4.1.1 Baking & vacuum maintenance

**MOT chamber bake** We baked the 2D MOTs and 3D MOT for a total of 11 days at 140°C, the main limitation to temperature being the ion pump. At the end of the bake and after turning on the ion pumps the MOT chamber gauge measured a pressure of  $1 \times 10^{-10}$  mbar. After breaking the ampoules, the pressure in the MOT chamber rose to a steady-state value of about  $3 \times 10^{-10}$  mbar as measured with the 3D MOT chamber gauge<sup>60</sup>. The valve separating the 3D MOT chamber from the (at that point non-existent) science chamber was sealed with a viewport and the valve was left open during the bake.

---

<sup>58</sup>Manufactured by VACOM.

<sup>59</sup>The re-entrant viewport was manufactured by MPF.

<sup>60</sup> $1 \times 10^{-10}$  mbar on the ion pump controller.

**Science chamber bake** Our science chamber was baked separately from the 3D MOT and 2D MOT chambers. By the time we were ready to bake the science chamber we had already installed optics and coils around the 2D and 3D MOT chambers and had produced  $^{87}\text{Rb}$  BECs and  $^{39}\text{K}$  and  $^{40}\text{K}$  MOTs in the 3D MOT chamber. We wanted to avoid taking away all the elements we had already installed around the 2D and 3D MOTs, since we would have had to rebuild and realign all these optics again. We installed a shield around the existing setup to prevent insulation and heat from disturbing the MOT optics (see [140] for more information).

The science chamber was baked for 5 weeks at  $95^\circ\text{C}$ . We chose  $95^\circ\text{C}$  because the objective is only certified up to  $100^\circ\text{C}$ . Some of the auxiliary components, such as the T-pieces, gauge, and valve were stabilized at  $115^\circ\text{C}$  while baking.

The non-evaporable getters in the science chamber were activated shortly before cooling back down to room temperature at the end of the science chamber bake. We wanted to protect the objective and prevent radiative heating from the getters to cause the objective to heat up too quickly. We first cooled down the entire chamber to  $80^\circ\text{C}$  and then started activation. We turned the current of the getters up to 4.4 A, corresponding to an estimated temperature of  $375^\circ\text{C}$  over 11 hours<sup>61</sup>. Then we kept the current running for 24 hours, after which we reduced the current in the getters back down to 0 A over 11 hours. We found that the hot getters produced a significant heat load and that we had to turn down the variacs supplying the heating tapes while increasing the current to the getters, to keep the temperature at  $80^\circ\text{C}$ <sup>62</sup>. After activation, we turned on the ion pumps and closed the valve to the turbo pump. The final pressure of the science chamber after cooling to room temperature was  $1 \times 10^{-10}$  mbar and  $<2 \times 10^{-11}$  mbar as measured on our gauge and ion pumps, respectively, and has remained there ever since.

## 4.2 Red & high power table lasers

### 4.2.1 Cooling and imaging lasers

The red table is one of our three optical tables. Laser beams prepared on the red table are mostly used for cooling and imaging and are exclusively near-resonant lasers targeting the D2 transitions of  $^{39}\text{K}$  and  $^{40}\text{K}$  at 767 nm, and of  $^{87}\text{Rb}$  at 780 nm. Compared to beams created on the high power table (discussed below), beams created on the red table are relatively low in power. Roughly one third of this table contains the lasers and optics for the preparation of  $^{87}\text{Rb}$  lasers and two thirds are used for  $^{39}\text{K}$  and  $^{40}\text{K}$  lasers. In total we have 8 home-built tapered amplifiers (TAs) and 2 home-built injection-locked diodes (IJDs). A schematic of the entire red table as it currently stands can be found in [appendix A](#).

**Transitions** Fig. 4.5 shows the atomic levels we target for cooling, repump, and imaging of  $^{87}\text{Rb}$ ,  $^{39}\text{K}$ , and  $^{40}\text{K}$ , and for spin-polarization (spin-pol) in  $^{87}\text{Rb}$ .

<sup>61</sup>The recommended activation parameters are 5 A for 1 hour.

<sup>62</sup>Once we had brought the getters up to maximum temperature, they produced almost the entire heating power.

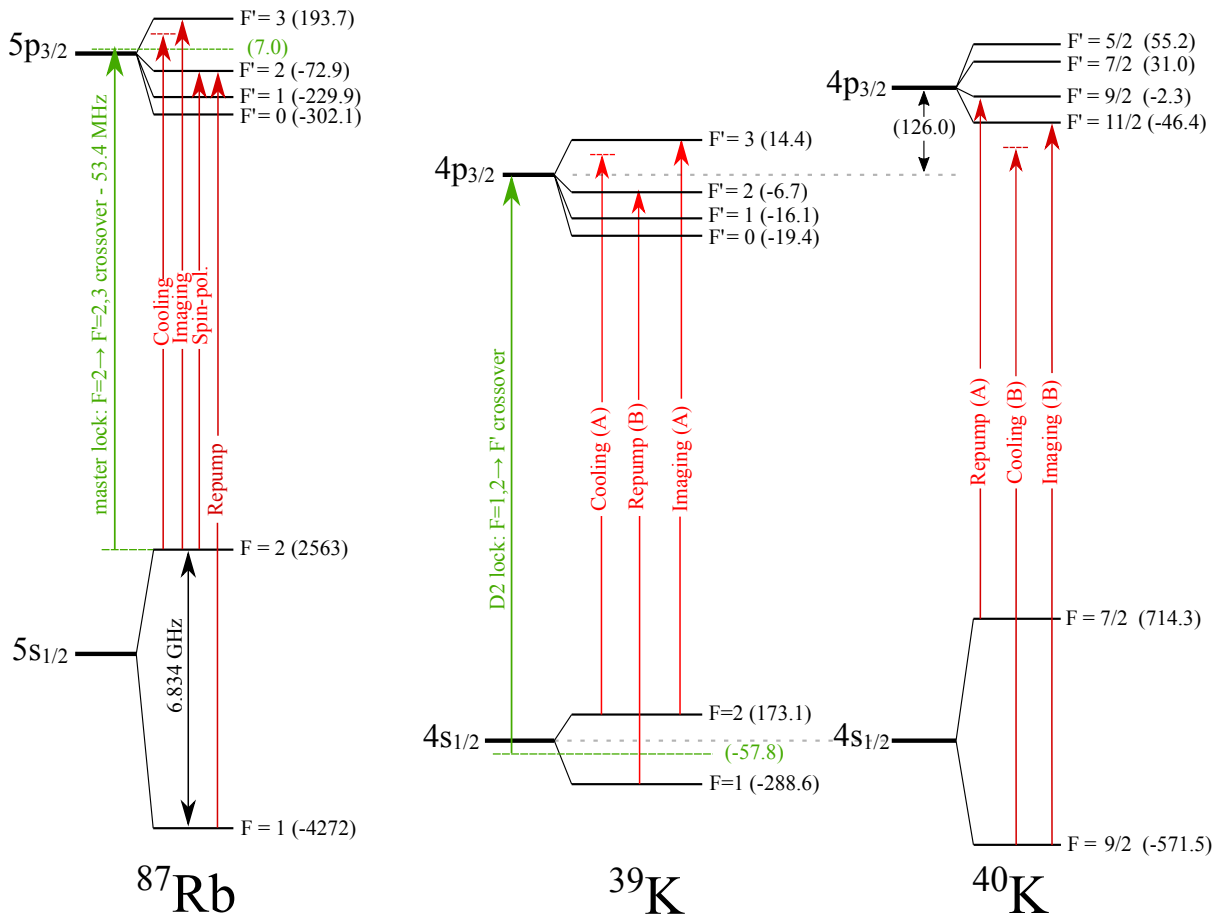


**Figure 4.5** – Level scheme for  $^{87}\text{Rb}$ ,  $^{39}\text{K}$ , and  $^{40}\text{K}$ . All numbers in parentheses are in units of MHz. Green arrows show the reference light for  $^{87}\text{Rb}$  and potassium, and red arrows indicate lasers derived from the reference light.

Our Rb cooling master light is locked to 53.4 MHz below the  $F = 2 \rightarrow F' = 2, 3$  crossover transition using saturated absorption spectroscopy [140, 177]. Rb repump master light is offset-locked to Rb cooling master light. We choose the offset frequency so that the Rb repump master is blue-shifted by 220 MHz with respect to the  $F = 1 \rightarrow F' = 2$  transition. All subsequent frequency shifts are done with acousto-optic modulators (AOMs).

Our potassium reference light is locked to the  $F = 1, 2 \rightarrow F'$  crossover transition of  $^{39}\text{K}$ <sup>63</sup>. All our  $^{39}\text{K}$  and  $^{40}\text{K}$  lasers are referenced to this master light. Note that the hyperfine structure of  $^{40}\text{K}$  is inverted with respect to  $^{39}\text{K}$ . This causes the role of repump and cooling to be ‘reversed’ between  $^{39}\text{K}$  and  $^{40}\text{K}$ . Instead of labelling the potassium lasers with ‘cooling’ and ‘repump’, which is ambiguous, we label our lasers ‘A’ and ‘B’, where ‘A’ always refers to a laser that is red-shifted with respect to the reference laser. Therefore, A (B) is cooling (repump) light for  $^{39}\text{K}$  and vice versa for  $^{40}\text{K}$ . If we want to conduct experiments with  $^{40}\text{K}$  we shift A and B light by  $-431.9$  MHz and  $+369.2$  MHz, respectively. This shifts light that was resonant to the  $|F = 2\rangle \rightarrow |F' = 3\rangle$  ( $|F = 1\rangle \rightarrow |F' = 2\rangle$ ) transition in  $^{39}\text{K}$  to be resonant with the  $|F = 7/2\rangle \rightarrow |F' = 9/2\rangle$  ( $|F = 9/2\rangle \rightarrow |F' = 11/2\rangle$ ) transition in  $^{40}\text{K}$ .

<sup>63</sup>The hyperfine splitting in the excited state is too small for us to lock to a specific line.

**Rubidium (Rb) lasers** The Rb lasers are derived from two IJDs, one for cooling and one for repump, which are locked to a small amount (3 mW-5 mW) of reference light from the quasicrystal experiment. The IJDs, which emit 150 mW of light with a linewidth of  $\sim 100$  kHz, provide light for injecting the three Rb TAs and for imaging, push and spin-pol. All Rb TAs are seeded with  $\sim 10$  mW of power and emit  $\sim 2.5$  W<sup>64</sup>.

The output of the repump IJD is sent directly to a TA whose output is split between 2D repump and 3D repump. Both 2D and 3D repump light pass through double-pass AOMs for frequency shifting. Some of the 2D repump light is picked off after the double pass AOM to provide light for imaging repump and spin-pol repump. We thus also act on the 2D repump double pass AOM to control the frequency of all additional Rb repump beams. The 3D repump light is coupled into one of the fibre cluster input fibres. The fibre cluster is a compact optics setup that evenly distributes our repump and cooling light among the six 3D MOT fibres.

A small amount of light is split off directly from the output of the Rb cooling IJD to feed Rb imaging, push and spin-pol. The rest is distributed among the 2D cooling and 3D cooling TAs. The double passes for 2D and 3D cooling light are located before their respective TAs. The 3D cooling light is coupled into the other fibre cluster input fibre. We have additional AOMs after the 2D and 3D cooling TAs for fast switching. Rb imaging, push and spin-pol also have their own respective double passes for frequency shifting. In [chapter 5](#) we list all relevant powers on the experiment table during the sequence.

**Potassium (K) lasers** Five TAs generate light for the <sup>39</sup>K & <sup>40</sup>K setup. One TA is used as a preliminary amplifier (Pre-Amp TA) that takes 25 mW of master light from the quasicrystal lab and emits roughly 1.6 W which is directed to the rest of the <sup>39</sup>K & <sup>40</sup>K setup. Some of the output of the Pre-Amp TA ( $\sim 70$  mW) is split off to feed various low-power beams, such as push, spin-pol and imaging. The rest is roughly evenly split between the A and B paths and is used to seed the K 2D A, K 2D B, K 3D A, and K 3D B TAs.

Before being split into the various paths leading to the TAs, the A and B light is directed through respective 200 MHz double pass AOMs. These double pass AOMs act as isotope switches. When running experiments with <sup>39</sup>K, the switches are off and light in the A and B paths are not frequency-shifted. When running <sup>40</sup>K sequences, A light is shifted by  $-431.9$  MHz and B light is shifted by  $+369.2$  MHz.

After the isotope switches, both A and B light is split into respective 2D and 3D paths. Seed light for the respective 2D (3D) TA is directed through a 2D (3D) double pass AOM before reaching the TA. The K 2D A, K 2D B, K 3D A, and K 3D B TAs are seeded with 20 mW-25 mW of power and emit between 1.4 W and 1.6 W.

The outputs of the K 3D TAs additionally pass through a respective 200 MHz AOM which we use for fast switching. The K 3D A (B) light is then overlapped with with Rb cooling (repump) before being coupled into the appropriate fibre cluster input fibre.

<sup>64</sup>Our TA chips are Eagleyard EYP-TPA-0780-03000-4006-CMT04-0000 for rubidium and Coherent TA-0765-2000 for potassium.

### 4.2.2 Dipole and lattice lasers

All our high power lasers (>40 W) are located on the high power (HP) table. These lasers create dipole and lattice beams for the later stages of the sequence.

**Dipole trap setup** Fig. 4.6 shows a schematic of the optics setup for producing various dipole beams on the high power table.

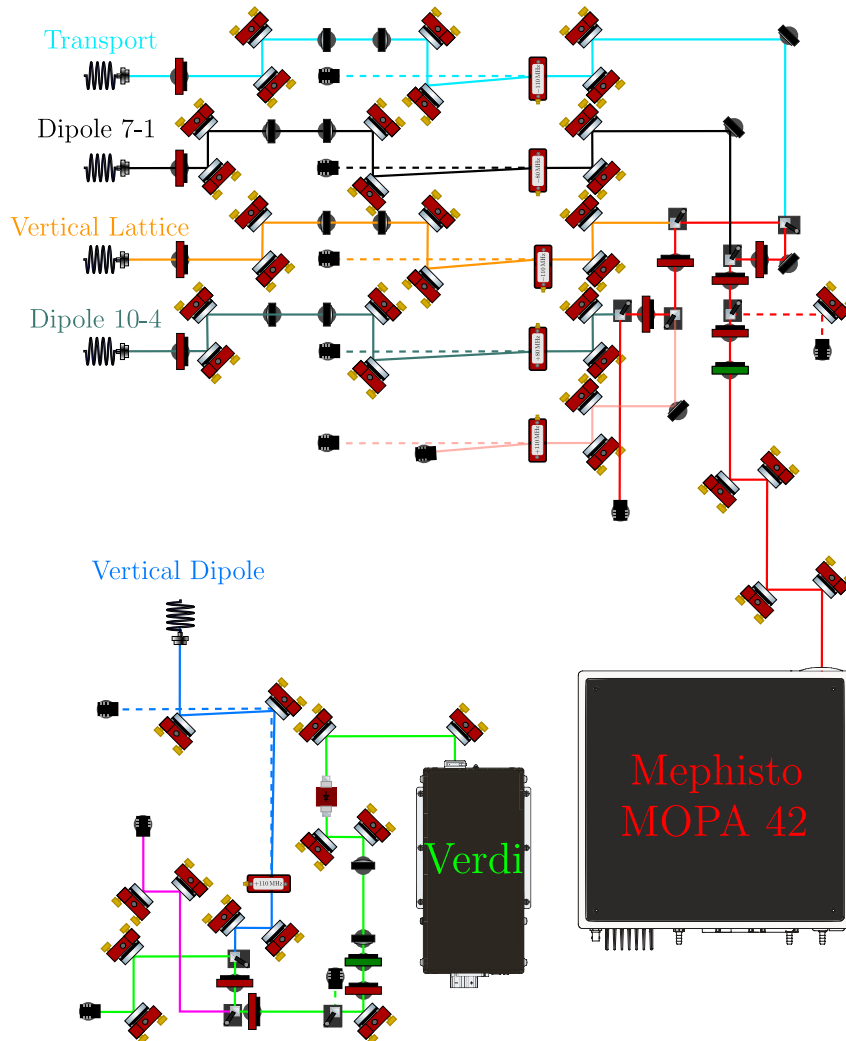


**Figure 4.6** – Transport, dipole trap, vertical lattice and vertical dipole beam setup on the high power table. A component glossary can be found in [appendix A](#).

We derive the crossed dipole trap beams, the vertical lattice and the transport beam from a Coherent Mephisto MOPA 42, which emits >42 W at 1064 nm. We use  $\lambda/2$  waveplates in conjunction with polarizing beam splitters (PBSs) to split the main beam into four different paths. Each of the four beams is diffracted by an AOM and then coupled into a respective photonic crystal fibre (PCF)<sup>65</sup> leading to the experiment table. The AOMs<sup>66</sup> in the 1064 nm path are used to stabilize and control the power of each beam. The power

<sup>65</sup>NKT Photonics LMA-PM-15

<sup>66</sup>G&H AOMO 3110-197 & 3080-197

is controlled via an analog output channel connected to the non-inverting in port of a PI controller. The power on the experiment table is measured by two photodiodes which are situated behind a respective mirror<sup>67</sup>. One photodiode is connected to the inverting in port of the PI controller, while the other provides an independent (witness) measurement. The AOMs shift the frequency of the beams by several tens of MHz with respect to each other. This ensures that their mutual interference is at a frequency that is too high for the atoms to respond to. As a consequence, they only see an averaged, time-independent potential. We typically achieve >80% diffraction efficiency into the first order. We let the zeroth and first diffracted orders propagate over a distance of 15 cm-20 cm from each AOM after which we separate the diffracted beam using a mirror. The zeroth order beam is directed into a water-cooled beam dump. Due to the high powers in the 1064 nm beams, we do not use irises or shutters.

The beams are coupled into photonic crystal fibres using custom home-built couplers. These SMA couplers are used with an aspheric lens<sup>68</sup> and we typically achieve >80% coupling efficiency.

**Lattice lasers** Our optical lattice beams are derived from a Coherent Mephisto MOPA 55 and a custom second-harmonic generator (SHG) manufactured by Toptica. The Mephisto emits 57 W of 1064 nm light. We use a waveplate and a PBS to split about 6 W of 1064 nm light to use for the 1064 nm lattice. The remaining light is directed to the SHG, where it is converted to 532 nm. The SHG has a conversion efficiency of roughly 70%, meaning that at maximum input power we get up to 36.5 W of 532 nm light.

**Power considerations** We choose to maximize the 532 nm power while still giving us a small amount of light to use for the 1064 nm lattice. During fluorescence imaging (i.e. single-site resolved imaging) we intend to pin the atoms solely in the 532 nm triangular lattice. We don't expect that we will need the 1064 nm lattice for fluorescence imaging. To achieve sufficiently small tunnelling rates we initially planned for a 532 nm lattice beam power of 3 W. Considering the higher than expected output power of the SHG, we should be able to get up to 5 W per lattice beam, assuming that we lose 50% of the power between the SHG and the atoms<sup>69</sup>.

Since 1064 nm lattice light will only be used for physics (and not for imaging), we will only need a few hundred mW in each beam. Diverting 6 W into the 1064 nm lattice path should thus give us about 1 W per 1064 nm lattice beam at the atoms.

**Optics setup** A schematic of the optical lattice setup on the high power table is shown in [Fig. 4.7](#)

<sup>67</sup>The 1064 nm beam is intense enough for light to be transmitted through our AR coated mirrors.

<sup>68</sup>Thorlabs CME280-1064

<sup>69</sup>80% AOM efficiency, 80% coupling efficiency, 80% due to losses at optical interfaces (i.e. mirrors, lenses, cubes, waveplates).

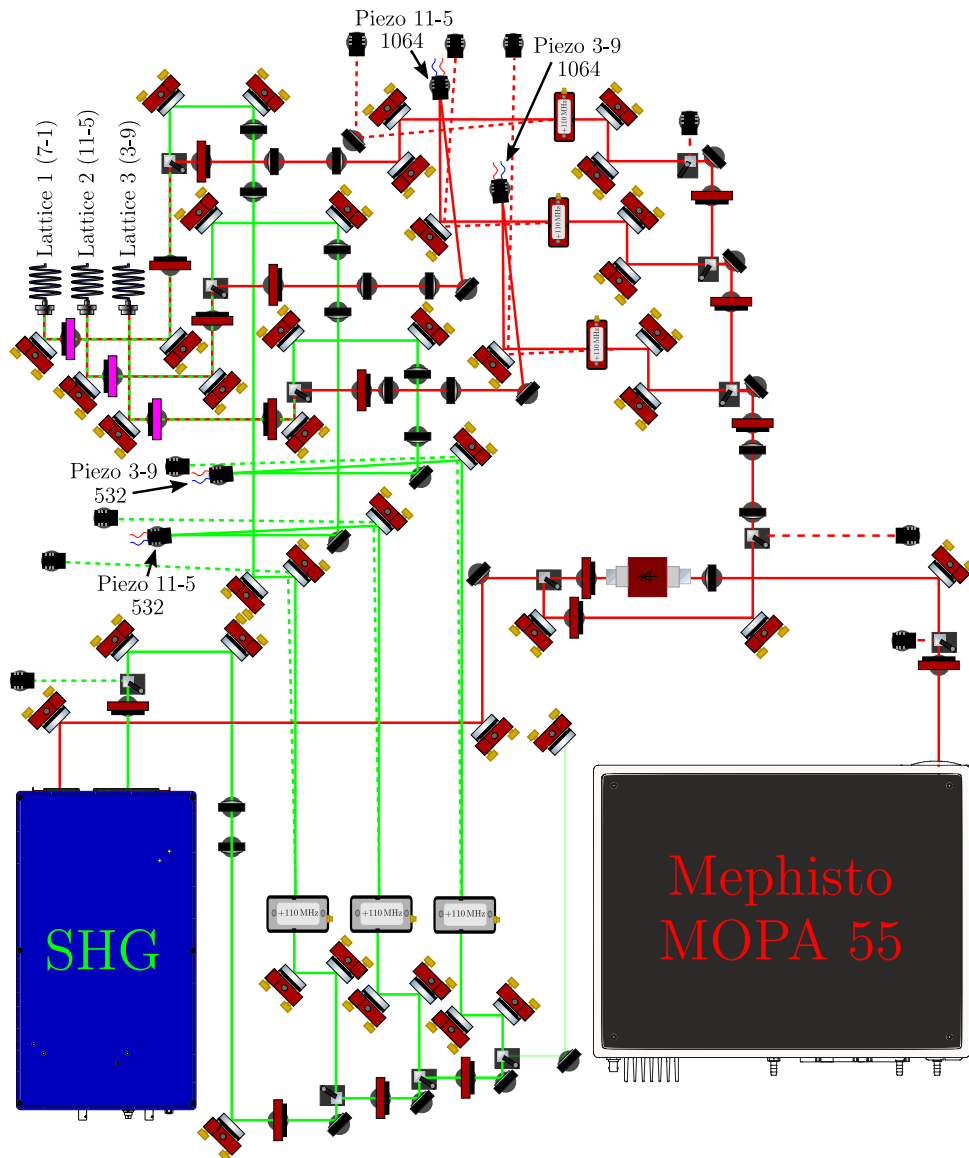


**Figure 4.7** – Optical lattice setup on the high power table. Green: 532 nm. Red: 1064 nm. A component glossary can be found in [appendix A](#).

The 532 nm and 1064 nm lattice setups are functionally identical. An initial beam passes through an attenuation stage and is split into the three lattice paths. Each of the three lattice beams passes through a respective AOM<sup>70</sup>. We allow the zeroth and first diffraction orders of the 1064 nm (532 nm) AOMs to propagate for  $\sim 15$  cm ( $\sim 40$  cm) after which the orders are separated with a mirror (see [Fig. 4.7](#)). The zeroth orders are dumped while the first orders are used as lattice beams.

After passing through a respective telescope, the three pairs of 532 nm and 1064 nm lattice beams are overlapped on a PBS. After the overlapping PBS, the 532 nm and 1064 nm lattice beams have orthogonal polarizations. We therefore use a multiple-order waveplate, that acts as a  $\lambda$ -waveplate for 1064 nm and a  $\lambda/2$  waveplate for 532 nm, to make

<sup>70</sup>MCQ110-A2-VIS from AA Opto-Electronic for 532 nm, AOMO 3110-197 from G&H for 1064 nm. We use a Minicircuits ZHL-03-5WF+ as a power amplifier for the RF input of the 532 nm AOMs.

the beam polarizations equal. We additionally have a dual-wavelength half-waveplate, which is  $\lambda/2$  for both 532 nm and 1064 nm, to polarization-maintain the optical fibre.

We installed piezo-mirrors on two of the 532 nm lattice beam paths and two of the 1064 nm lattice beam paths. These are actuated to actively stabilize the lattice phases. The interferometer signals measured on the experiment table are fed to PI controllers that feed back on the high power table piezo mirrors.

**Lattice fibres** We send the lattice beams through three photonic crystal fibres (PCFs)<sup>71</sup>. Each PCF carries one 532 nm and one 1064 nm lattice beam. The PCFs are capable of delivering both 532 nm and 1064 nm at high power.

We achieve coupling efficiencies of 70%-80% for both 532 nm and 1064 nm in the three lattice fibres. There are additional 2:1 telescopes on the three 532 nm paths before overlapping with 1064 nm<sup>72</sup>. The second lens of the telescope is mounted on a translation stage. This extra degree of freedom allows us to compensate for the focal shift of the coupling lens.

An open question is how the PCFs perform at high power. We know from using PCFs for the dipole trap that they can handle 1064 nm powers above 25 W, with coupling efficiencies above 80%. What we do not currently know is how the fibres perform at 532 nm at high power. The fibres need to be able to handle up to 6 W of 532 nm at the input for single-site resolved imaging. An open question is at what power stimulated Brillouin scattering starts to limit the output power and what the minimum bend radius is. We tested the fibres up to an input power of 1.2 W at 532 nm and found that the coupling efficiency does not noticeably drop.

**Vertical dipole** To create stable negative temperature states, we need to create an anti-confining potential (see [section 3.1.2](#)). We use a 532 nm beam for this purpose which we call the ‘vertical dipole’ beam. This beam is derived from the output of a Coherent Verdi G8. It is sent through an AOM for intensity stabilization and coupled into a standard optical fibre leading to the experiment table.

## 4.3 Experiment table optics

### 4.3.1 MOT

**2D MOT** 2D MOTs are an established component of most modern cold-atom experiments involving rubidium and potassium [194–196]. Apart from being more compact, our 2D MOTs are identical to those in the quasicrystal experiment [176, 177]. Both the Rb and K 2D MOTs are set up in the 2D<sup>+</sup> configuration [194] with an additional push beam. The cooling, repump and push beams are brought to the experiment table from the red table via standard optical fibres.

<sup>71</sup>NKT Photonics LMA-PM-15

<sup>72</sup>The mode-field diameter of the PCF is roughly equal at 532 nm and 1064 nm.

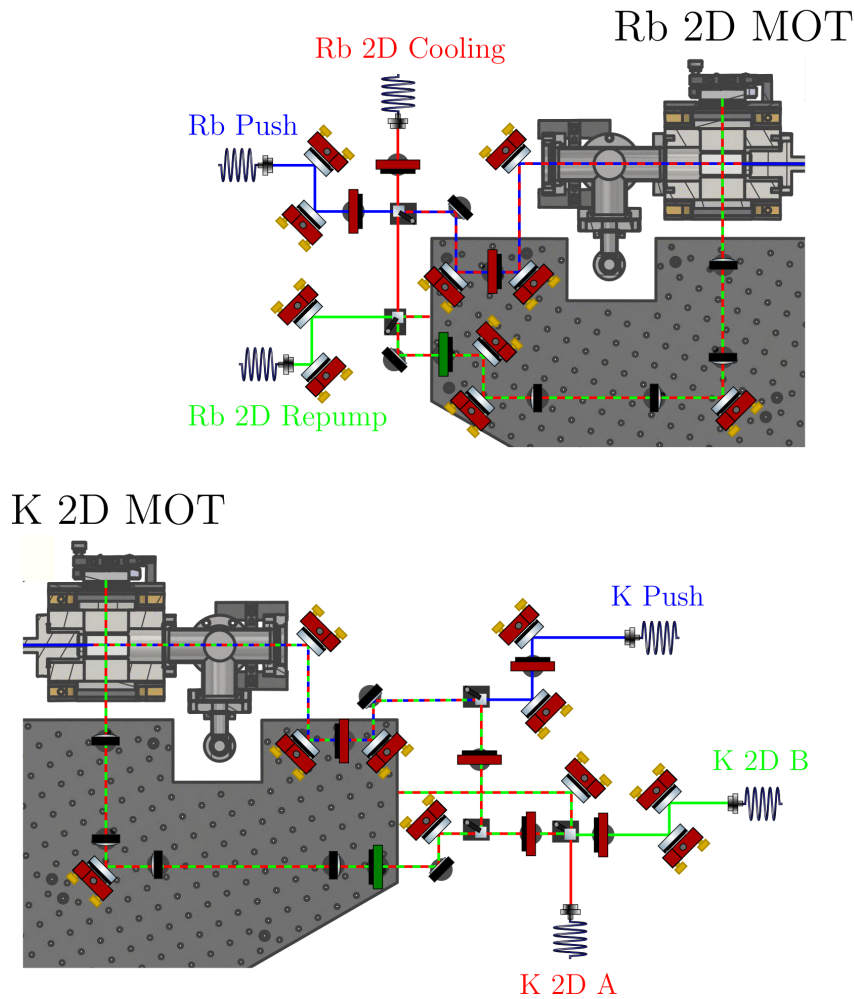


**Figure 4.8** – 2D MOT optics for  $^{87}\text{Rb}$  (top), and  $^{39}\text{K}$  and  $^{40}\text{K}$  (bottom). A component glossary can be found in [appendix A](#).

**Rubidium (Rb) 2D MOT** On the experiment table, a small amount of Rb 2D cooling light is diverted and overlapped with the push beam and is used for axial cooling. The rest of the power is overlapped with 2D repump on a 50:50 beam splitter. The two output beams of the 50:50 beam splitter serve as the transverse cooling and repump beams for the 2D MOT. Both the vertical and horizontal 2D MOT beams go through the same series of telescopes. One telescope uses circular lenses ( $-50\text{ mm}$  &  $250\text{ mm}$ ) to increase the beam size by a factor of 5. The other telescope is cylindrical ( $-75\text{ mm}$  &  $150\text{ mm}$ ) and increases the horizontal beam waist by a factor of 2, for a final beam waist of  $20\text{ mm} \times 10\text{ mm}$  (horizontal  $\times$  vertical)<sup>73</sup>. The transverse beams travel through the 2D MOT chamber and a  $52\text{ mm} \times 27\text{ mm}$ , rectangular, zero-order, quarter waveplate and are retro-reflected through the 2D MOT (see [Fig. 4.8](#)). The quarter waveplate ensures that the polarization is rotated to the correct circular polarization. The 2D MOTs are very compact, which allowed us to place them in the v-shape shown in [Fig. 4.1](#). It also ensures that we have enough optical access to install the transport beam optics.

<sup>73</sup>In the remainder of this section, we will always quote cylindrical beam waists such that the horizontal (vertical) beam waist is the first (second) number.

The axial cooling beam propagates along the axis of the 2D MOT chamber and through a polarizer in vacuum before being retro-reflected by a mirror attached to the 2D MOT differential pumping section (see Fig. 4.2). The beam is linearly polarized and its polarization can be adjusted with a  $\lambda/2$ -waveplate. The amount of light retro-reflected into the 2D MOT chamber depends on the polarization of the axial cooling beam. The waveplate thus allows us to control the amount of light being retro-reflected. The motivation behind this feature is that we want to create an imbalance of forces along the axial direction so that the cloud feels a force towards the MOT chamber.

We found that the push beam does not lead to substantial improvements in MOT loading and decided not to use it. We did however find that the power, alignment and polarization of the axial cooling beam has a strong influence on MOT loading.

**Potassium (K) 2D MOT** The K 2D MOT is set up in exactly the same way as the Rb 2D MOT, apart from the fact that K 2D A and K 2D B light are overlapped on a 50:50 beam splitter before light is split off for axial cooling. This ensures that cooling light for both  $^{39}\text{K}$  and  $^{40}\text{K}$  propagates along the axial direction of the 2D MOT.

We also found that the K push beam does not significantly improve  $^{39}\text{K}$  MOT loading, so we do not currently use it. We have not checked whether K push increases the  $^{40}\text{K}$  MOT loading as of yet.

A list of powers, detunings and field gradients for the 2D MOTs is provided in [chapter 5](#).

**3D MOT** Our 3D MOT is composed of six individual beams, each being connected to a respective fibre cluster output port. The configuration of beams is slightly unconventional in that four of the MOT beams propagate along axes  $45^\circ$  rotated with respect to the principal axes. This configuration gives us optical access along the transport axis. The MOT beams have a waist of 1 cm. Two of the beams propagate along the axis of the MOT coils. The optics for these beams consist of the fibre couplers, a collimating lens, two 2" mirrors and a quarter waveplate (see Fig. 4.9). The optics for each of the four other MOT beams are mounted in ‘fibre launchers’, consisting of the fibre out-coupler, a quarter waveplate and a collimating lens. The fibre launchers are rigidly connected to the MOT chamber (see Fig. 4.1) This is a compact solution, but also means that we are lacking degrees of freedom to steer the MOT beams<sup>74</sup>.

**Imaging** Since the machine is designed to evaporatively cool atoms and can produce  $^{87}\text{Rb}$  BECs in the MOT chamber, we implemented absorption imaging in the MOT chamber. With absorption imaging, we can accurately determine the atom number and precisely align the transport beam<sup>75</sup>. The imaging beam passes through a lens and a PBS for polarization cleaning before passing through the MOT chamber. The imaging beam and atoms are then imaged on a camera<sup>76</sup>. We use a  $4f$ -imaging system [177] with a magnification of 75:250.

<sup>74</sup>We often wished that we had these extra degrees of freedom when aligning the MOT beams, i.e. it is probably good to have them.

<sup>75</sup>See [197] for a comprehensive explanation of absorption imaging.

<sup>76</sup>IDS UI-3252LE

**Spin-pol** Like the imaging beam, the spin-pol beam propagates through the MOT chamber at a slight angle with respect to the 3D MOT coil axis. The polarization of the beam is cleaned with a PBS and then made circular with a quarter waveplate. Spin-pol is used for  $^{87}\text{Rb}$  when running  $^{87}\text{Rb}$  alone, but not used for  $^{87}\text{Rb}$  or  $^{39}\text{K}$  in the dual-species scripts.

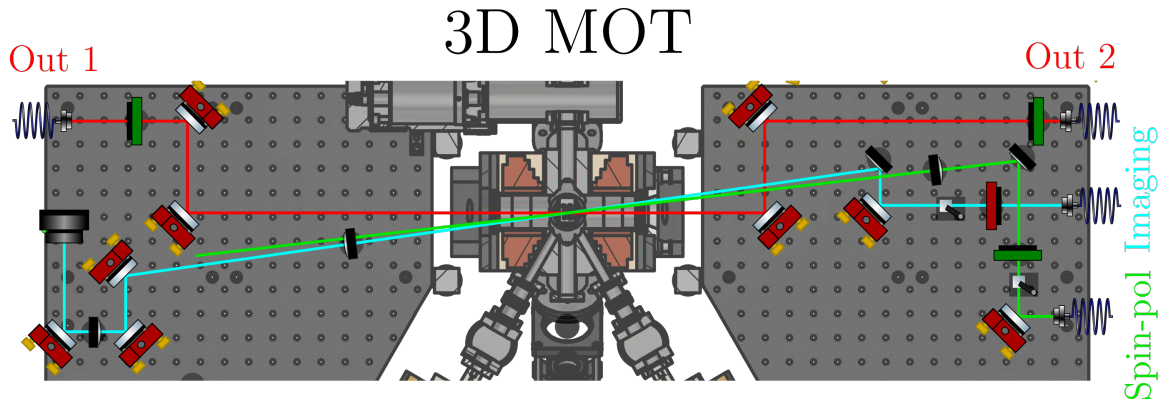


**Figure 4.9** – Horizontal 3D MOT beams (Out 1 & Out 2), absorption imaging and spin-pol in the 3D MOT chamber. A component glossary can be found in [appendix A](#).

A list of powers, detunings and field gradients for the 3D MOT is provided in [chapter 5](#).

### 4.3.2 Optical transport

**Theory** We transport atoms from the MOT chamber to the science chamber by shifting the focus position of a high power ( $>5\text{ W}$ ) 1064 nm beam with a focus-tunable lens<sup>77</sup> (FTL). Optical transport has been successfully implemented in several cold-atom machines to date [68, 198, 199] and is attractive due to its simplicity and speed compared with magnetic transport [200, 201]. Using FTLs for optical transport is a relatively recent development [68, 69]. They can be used for optical transport without a mechanical stage and therefore promise to be more reliable and create fewer vibrations during transport. The FTL changes its focal length in response to an applied current. Our current supply is custom-built, can be programmed via ethernet from our timing system and allows for correction of temperature drifts and thermal lensing. Additionally, we actively stabilize the temperature of the FTL mount to  $25^\circ\text{C}$  using a Peltier element. More details on the design of the FTL current source can be found in [202] and [140]. The transport sequence is discussed in [chapter 5](#). We found that stabilizing the temperature of the FTL mount sufficed to get transport working reliably and that we do not need to change the FTL current to correct for temperature drifts or thermal lensing.

At its core, optical transport consists of only one laser beam and two lenses, one static and one focus-tunable (see [Fig. 4.10](#)). The focus position ( $x_F$ ) and waist ( $w_F$ ) of a beam, with initial waist  $w_0$  and wavelength  $\lambda$ , passing through two lenses with focal lengths  $f_1$  and  $f_2$  and separated by a distance  $d$  are given by<sup>78</sup>

<sup>77</sup>Optotune EL-16-40-TC

<sup>78</sup>This can be straightforwardly calculated using ray transfer matrices.

$$x_F = \frac{d^2 f_1^2 \lambda^2 (d - f_2) + \pi^2 w_0^4 (d - f_1 - f_2) (d^2 - d f_1 - f_1 f_2)}{f_1^2 \lambda^2 (d - f_2)^2 + \pi^2 w_0^4 (-d + f_1 + f_2)^2},$$

$$w_F = \sqrt{\frac{f_1^2 f_2^2 \lambda^2 w_0^2}{f_1^2 \lambda^2 (d - f_2)^2 + \pi^2 w_0^4 (-d + f_1 + f_2)^2}}. \quad (4.1)$$

Here,  $x_F$  is the distance between the first lens and the position of the focus after the second lens. This shows that we can change the position of the focus by varying either  $f_1$  or  $f_2$ .

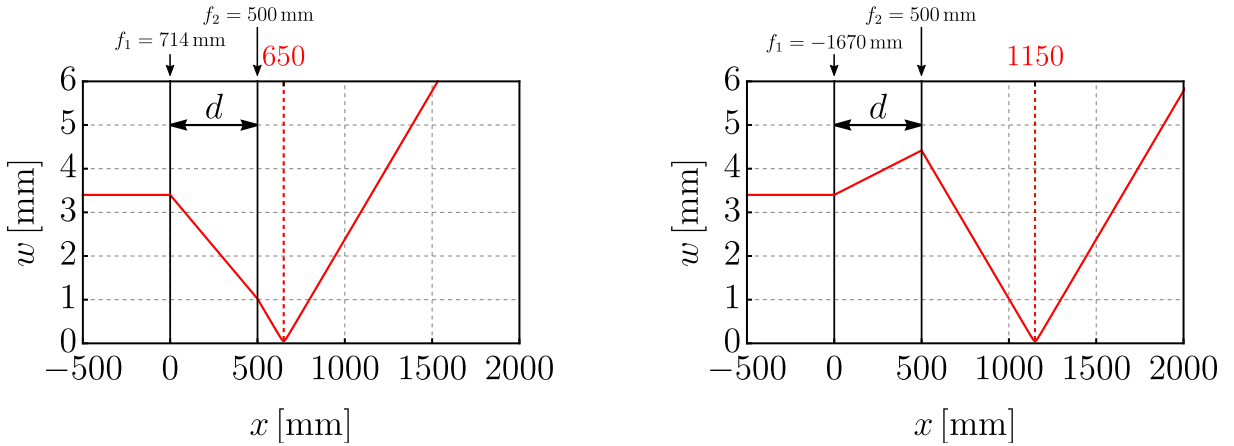


**Figure 4.10** – Approximate beam waist propagation at the beginning (left) and end (right) of transport. The black line at  $x = 0$  mm ( $x = 500$  mm) indicates the focus-tunable (static) lens.

We ideally want the trap shape to stay the same during transport which entails keeping the beam waist constant. This holds true when  $d = f_2$ , for which the equations above simplify to

$$x_F = f_2 \left( 2 - \frac{f_2}{f_1} \right), \quad w_F = \frac{\lambda}{\pi w_0} f_2. \quad (4.2)$$

In this case we can change the position of the focus by simply changing  $f_1$  which simultaneously keeps the beam waist constant. We chose to separate the centres of the MOT and science chambers by 50 cm and wanted a transport beam waist of  $50 \mu\text{m}$ . We therefore use a final lens with a focal length of 500 mm ( $f_2$ ). Fig. 4.10 shows a schematic of the transport beam waist as a function of distance when focused in the MOT and science chambers.

**Optics setup** Fig. 4.11 shows the transport beam path on the experiment table. The transport beam is emitted from a photonic crystal fibre (PCF) on the experiment table. It is directed through a waveplate and a Glan-Laser-Prism<sup>79</sup> to clean its polarization. The beam waist is then expanded via a telescope to  $w_0 \approx 3.5$  mm before passing through the

<sup>79</sup>Thorlabs GL10-C26

FTL. The FTL is mounted horizontally to avoid gravitational sag of the FTL liquid, which can lead to severe aberrations. Finally, the beam is directed via two mirrors onto the final 500 mm lens placed a few mm away from the CF16 viewport of the MOT Chamber<sup>80</sup>. The final lens focuses the beam down to a waist of roughly 50  $\mu\text{m}$ . The transport beam power is stabilized with light transmitted through a mirror.

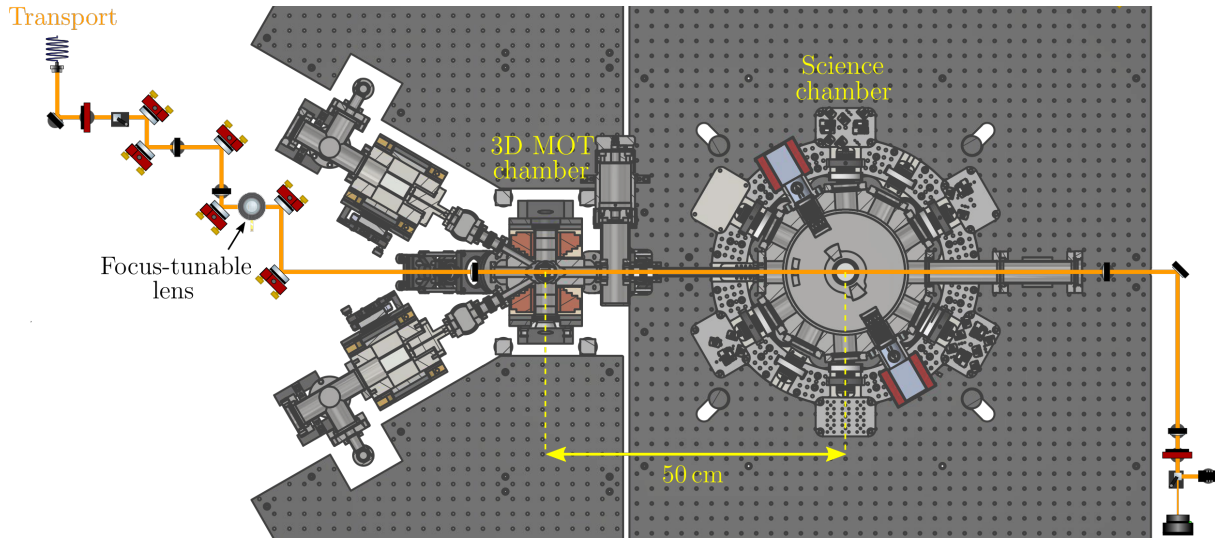


**Figure 4.11** – Optics setup around the vacuum chamber for optical transport. Note that the FTL is mounted horizontally and that the transport beam height changes from 70 mm to 270 mm before the chamber and back to 70 mm after it passes through chamber. A component glossary can be found in [appendix A](#).

We deflect  $>99\%$  of the transport beam power into a beam dump after the chamber. The remaining  $<1\%$  can be imaged with a camera to e.g. indirectly infer the waist of the transport beam during transport.

### 4.3.3 Dipole trap

The dipole trap is formed by two 1064 nm beams, which we label dipole 10-4 and dipole 7-1 according to their input and output ports (see [Fig. 4.4](#)), intersecting at a right angle to each other. The dipole trap optics are built around the lattice optics and are designed to have waists of 200  $\mu\text{m}$  x 50  $\mu\text{m}$ . Similar to the transport beam, the dipole beams pass through a Glan-Laser prism for polarization cleaning and are stabilized with light transmitted through a mirror. [Fig. 4.12](#) shows the optics layout for the dipole trap, lattice, and imaging lattice<sup>81</sup> as well as various absorption imaging beams we use for alignment.

<sup>80</sup>The mirror before the final lens is mounted in a 2", piezo-actuated mirror mount (Newport New Focus 8821).

<sup>81</sup>At the time of writing the imaging lattice had not been installed.

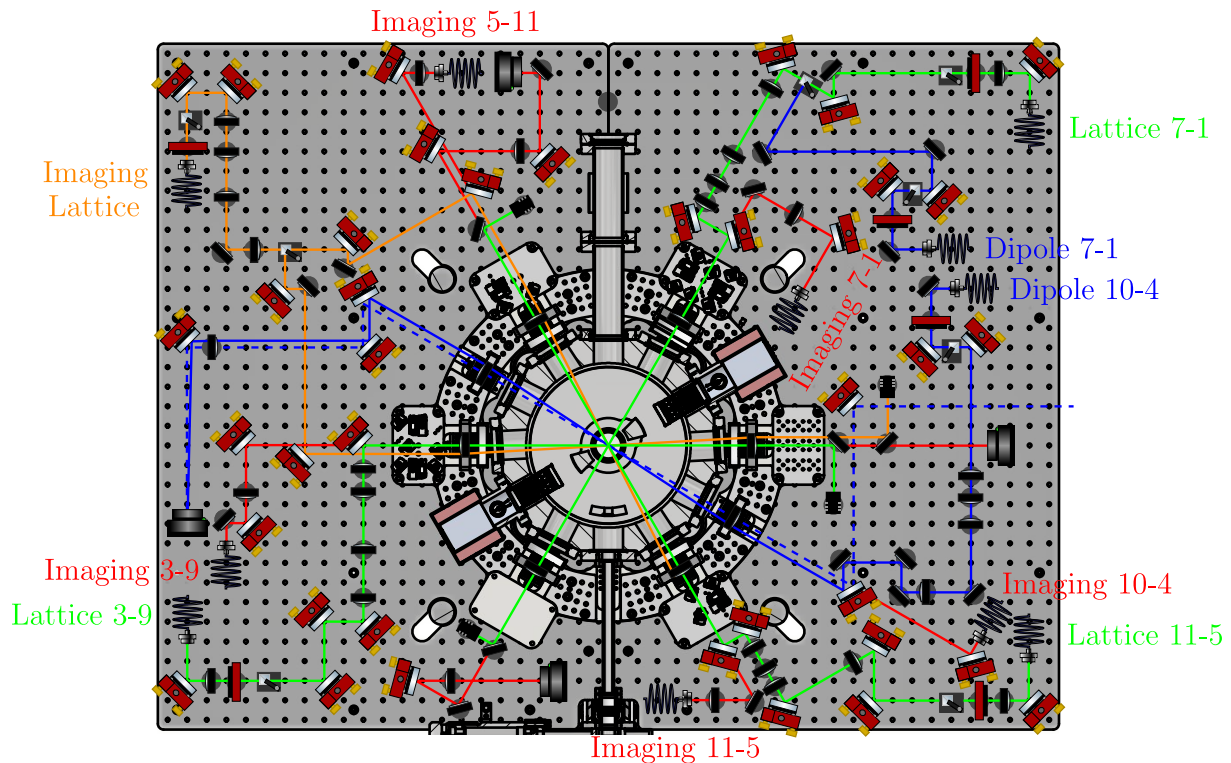


**Figure 4.12** – Optics layout for the dipole trap (blue), kagome lattice (green), and imaging lattice (orange) around the science chamber. Imaging beams are shown in red. Transfer path optics are not shown (see Fig. 4.16 instead). A component glossary can be found in appendix A.

#### 4.3.4 Kagome lattice

**Kagome lattice optics** The three bichromatic pairs (532 nm & 1064 nm) of lattice beams propagate along the 7-1, 11-5 and 3-9 axes of the science chamber (see Fig. 4.12).

Each lattice beam goes through the same set of lenses. Both colours along one axis are coupled into a respective fibre, i.e. each fibre emits both 532 nm and 1064 nm lattice light. The mirrors, cubes and lenses after the lattice fibres are coated for both 532 nm and 1064 nm. We have design waists of  $100\ \mu\text{m} \times 50\ \mu\text{m}$  (horizontal and vertical) for the lattice beams at the atoms, which requires both spherical as well as cylindrical telescopes. The lenses and distances between the optics were chosen so that both 532 nm and 1064 nm have the same waist and are focused in the centre of the science chamber.

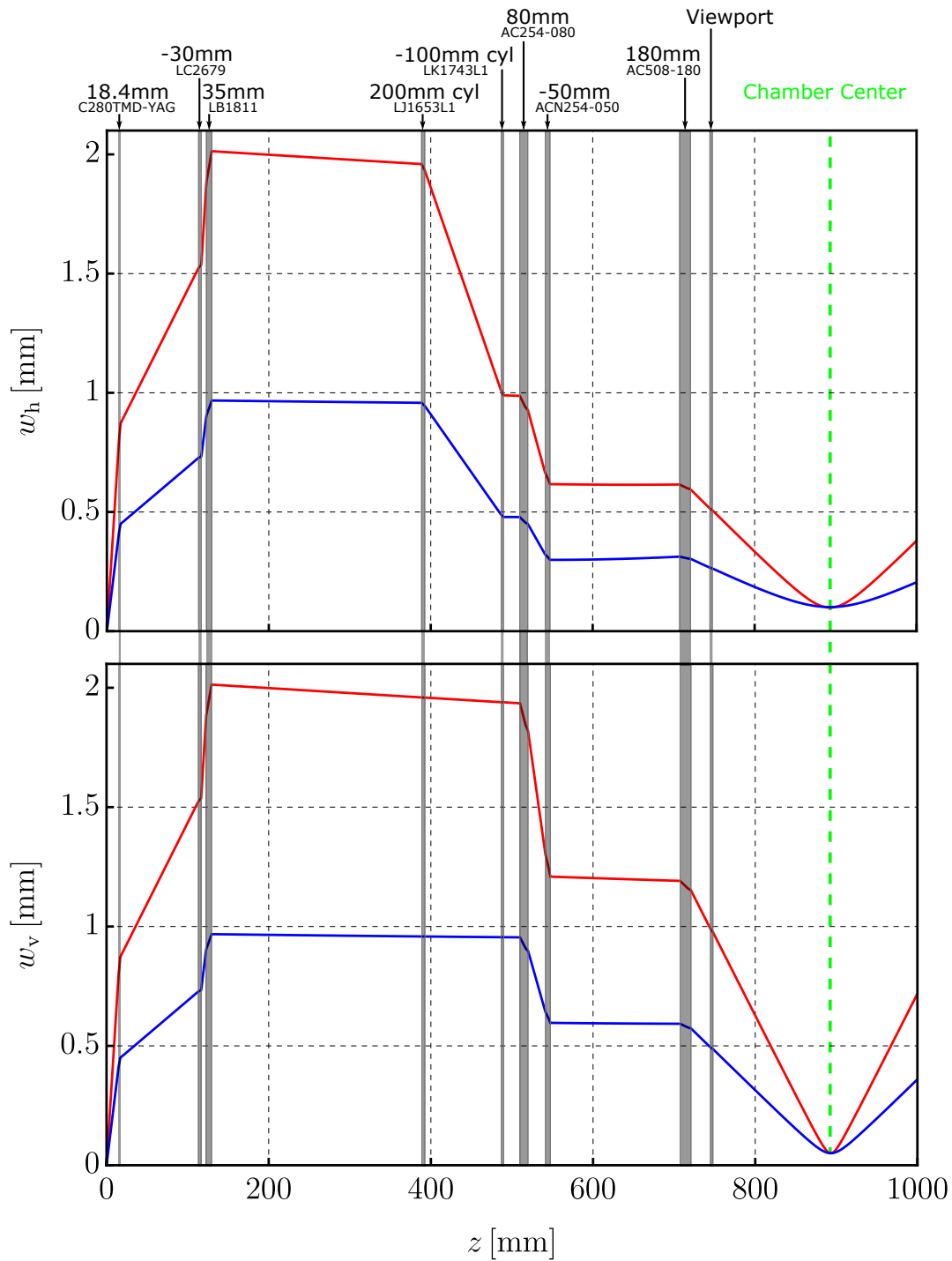


**Figure 4.13** – Top (bottom): theoretically calculated evolution of a lattice beam’s horizontal (vertical) beam waist as it propagates through the lattice optics. Blue (red): 532 nm (1064 nm) lattice beam. All lattice axes are built with the same optics. Lens part numbers are shown at the top.

The distances between the lenses were optimized using Zemax<sup>82</sup> (see Fig. 4.13). Where

<sup>82</sup>Special thanks to Luca Donini who determined the required lenses and performed the Zemax simulations.

necessary, we prioritized that the 532 nm lattice beams be closer to design specifications and pushed any extra uncertainty onto the 1064 nm lattice beams. For the microscope, it is more important that the 532 nm lattice beam waists are close to the design waists, since even small increases in waist will lead to a substantial reduction in maximum lattice depth.

The lattice beams emitted from the couplers are not simultaneously collimated. This is rectified by adding a doublet lens consisting of a biconvex and a plano-concave lens after the coupler. After the doublet, the 532 nm and 1064 nm lattice beams are collimated (though not perfectly).

We bought standard uncoated optics from Thorlabs and had them custom coated for 532 nm and 1064 nm. Using these optics we calculate that the two colours should have the same waist at the focus to within  $2\ \mu\text{m}$  and should be focussed at the same axial position to within  $5\ \mu\text{m}$  (see Fig. 4.14).

Propagation of the beam from the coupler through the coupler lens, doublet, cylindrical and spherical telescopes, the final focusing lens and the viewport were taken into account when optimizing the beam waists and focus positions in Zemax.

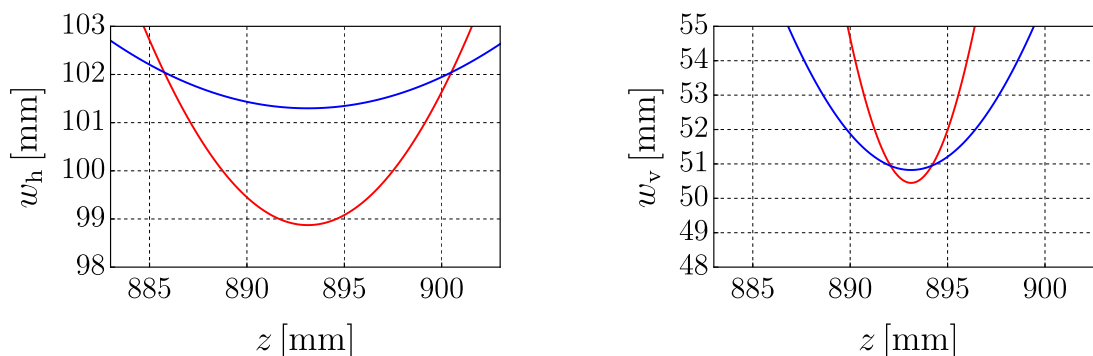


**Figure 4.14** – Left (right): simulated horizontal (vertical) waist of the lattice beams around the focus position. The calculated focal shift between 532 nm (blue) and 1064 nm (red) lattice beams is less than  $5\ \mu\text{m}$  for both the horizontal and vertical waist and for the two colours.

#### 4.3.5 Phase stabilization

As we showed in chapter 2, it is critical that we can control the lattice beams' relative phases. Any phase drifts between the 532 nm and 1064 nm lattices will cause these to move with respect to each other and thus will lead to the kagome pattern being distorted (see Fig. 4.15). Phase stabilization of optical lattices is a significant technical challenge and has only been successfully implemented in a handful of machines [36, 203]. To understand why this is the case, let us look at the example of 532 nm and 1064 nm travelling through air. For 532 nm, the index of refraction in air changes by about 1ppm when the temperature changes from  $21.5^\circ\text{C}$  (our table temperature) to  $22.5^\circ\text{C}$ . This change in refractive index is enough to change the phase of a 532 nm beam by  $\pi$  over a distance of 30 cm. For 1064 nm the phase shift is slightly less than half of this value. The absolute (equivalent) displacement is therefore 285 nm for 532 nm and 281 nm for 1064 nm. The relative displacement between the two colours is thus 4 nm over a distance of 30 cm and a temperature change of  $1^\circ\text{C}$ . This shows that in general the absolute phase shift of the

individual colours is much larger than the relative phase shift. Humidity and air pressure affect the index of refraction as well.

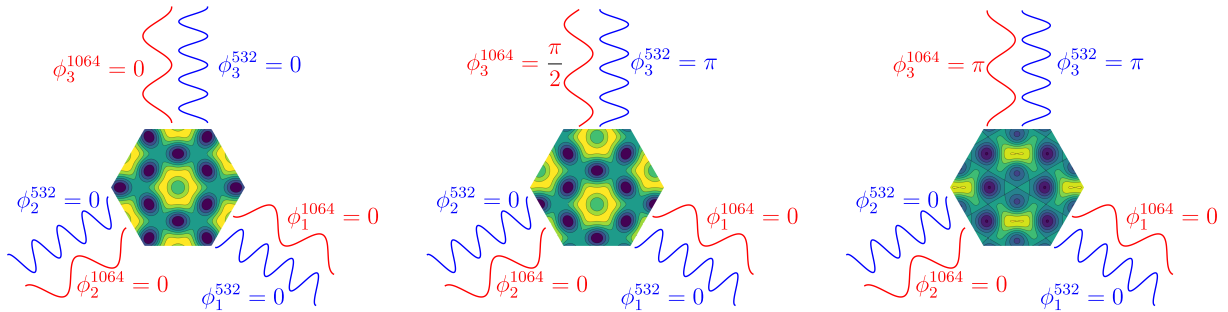


**Figure 4.15** – Effect of changing the lattice beam phases on the lattice potential. Left: phases chosen such that a kagome lattice is formed. Centre: change in absolute position of kagome lattice. Right: change in relative phase between 532 nm & 1064 nm lattice. A relative phase shift between colours changes the optical potential.

Another source of phase instability is fluctuations in the distance of unstabilized paths. These are caused by mechanical vibrations from water-cooling and air-conditioning or expansion and contraction of optical elements due to temperature fluctuations. These distance fluctuations only have an effect if they are not common mode. Common mode phase noise does not affect the absolute position of an interfering triangular lattice. It is therefore important that any unstabilized path length is equal for all three paths. To this end, we minimized the unstabilized path in each beam and installed the phase sensitive optics on a solid ring of titanium that fits around the science chamber<sup>83</sup>. Titanium has a small coefficient of thermal expansion and, due to the symmetry of the monolithic mount, expansion and contraction due to temperature fluctuations are common mode (see [140] for more information).

**Phase stabilization design** As discussed in section 2.2 the interfering kagome lattice has four phase degrees of freedom. To ensure that the lattice is stable in space and the kagome pattern is preserved, these four phases need to be stabilized. Our experimental implementation of phase stabilization follows that of [36] very closely. The basic idea is to pick off a small amount of light from the input of each lattice beam and interfere the pick-offs from different lattice beams on a photodiode. The resulting voltage will depend on the relative phase between the two lattice beams,

$$V_{ij}^{\lambda} \propto \cos^2 \left( \frac{1}{2}(\phi_i^{\lambda} - \phi_j^{\lambda}) \right), \quad (4.3)$$

where  $\lambda \in \{\lambda_S, \lambda_L\}$  and  $i, j \in \{1, 2, 3\}$  are the wavelength and lattice index, respectively. We can now build an active feedback loop in which e.g. a piezo-actuated mirror changes the path lengths of one of the interferometer paths in response to the photodiode voltage.

<sup>83</sup>We refer to this ring as the ‘monolithic mount’. More details are provided in [140].

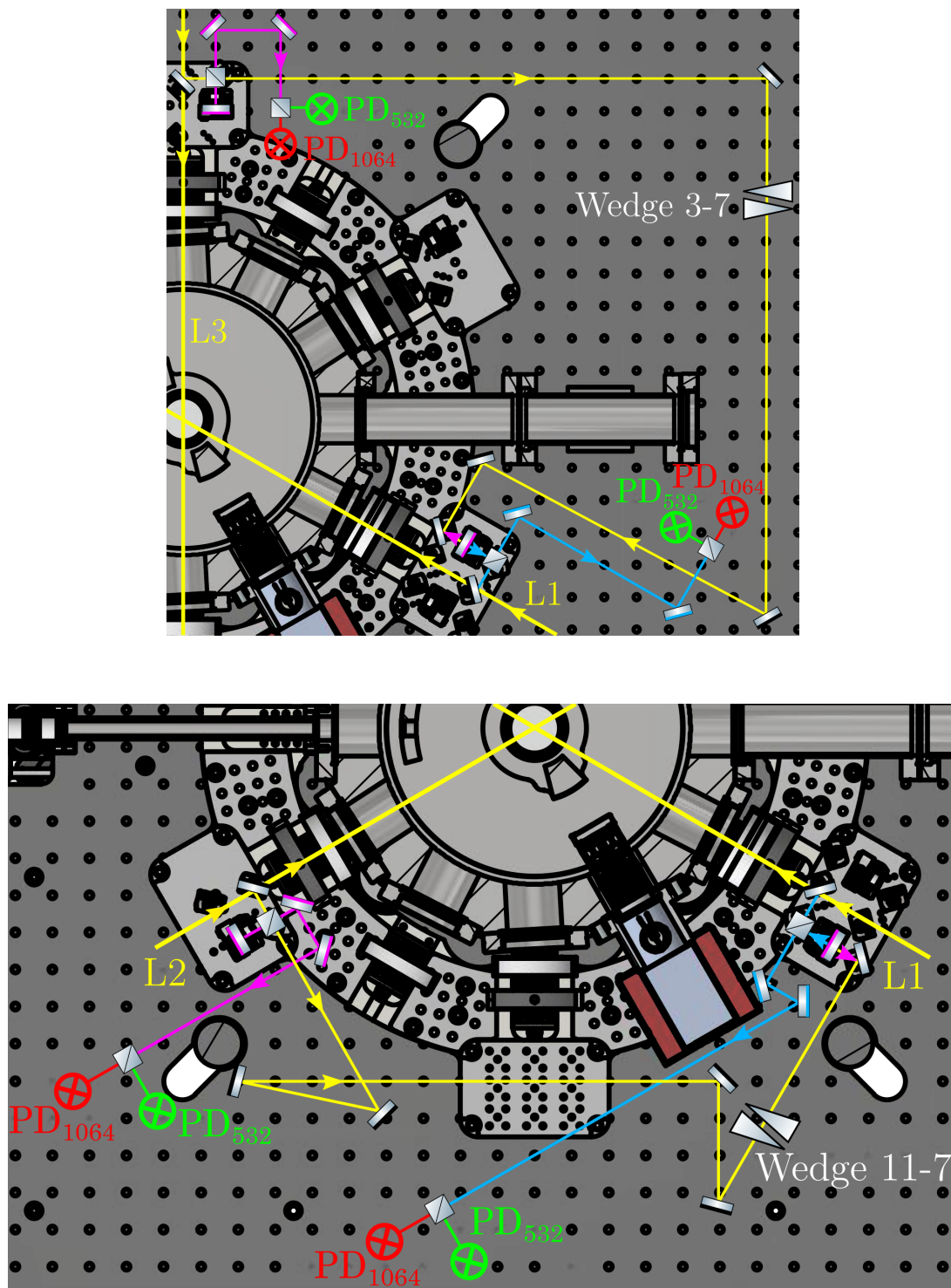


**Figure 4.16** – Top: 3-7 transfer path. Bottom: 11-7 transfer path. Yellow, magenta, blue: 532 nm & 1064 nm overlapped, red: 1064 nm, green: 532 nm. Components and beam paths that are magenta (blue) are part of only the Michelson (Mach-Zehnder) interferometers. A component glossary can be found in [appendix A](#).

The voltage change per unit phase shift is maximized when the phase difference between the two lattice beams is  $\pi/2$ . Therefore, the feedback loop will be most sensitive to

phase shifts when it is told to lock at  $\pi/2$  and the phase can be locked with higher precision. For more information about how this lock is implemented on our machine, see Dan Reed’s thesis [140]. Since we split the lattice beams before the lattice AOMs (see Fig. 4.7) and recombine them on the experimental table to measure the relative phases, we have effectively built four Mach-Zehnder (MZ) interferometers (yellow and blue-coloured components in Fig. 4.16).

For the Mach-Zehnder interferometer feedback loops, we actuate piezo-actuable mirrors before the fibres (see Fig. 4.7). We have piezo mirrors in all but the 532 nm 7-1 and 1064 nm 7-1 paths. We thus lock the 11-5 and 3-9 phases to the 7-1 beam. Provided all phases are locked, any change in the 7-1 beam phase will not result in a change in potential, since the interfering kagome lattice only cares about relative phase shifts between different lattice beams (see chapter 2).

In an ideal world, we would only need four interferometers to lock the four phase degrees of freedom. However, in the real world (and in our experiment), there will always be some path difference between where the light is picked off and where it is made to interfere. This path difference is also susceptible to phase fluctuations due to fluctuations in e.g. air temperature, humidity and pressure and microscopic movement of the optics in this path. We thus have another four phase degrees of freedom, two for each colour, associated with what we call the ‘transfer paths’, i.e. the paths between the pick-off elements and the elements combining the pick-offs. We measure and lock the transfer path phases via four Michelson interferometers in addition to the MZ interferometers (see the yellow and magenta-coloured components in Fig. 4.16).

One issue with locking the transfer path phases is that the two colours of each lattice axis are overlapped when they are emitted from their respective fibres. This prevents us from having two separate piezo-actuated mirrors in each transfer path to fix the phase of the two colours separately. We instead opted to install only one piezo-actuated mirror in each transfer path which only locks the transfer path phase of one of the colours. On a timescale of a few hours, we rely on the passive stability of the relative phase between 532 nm and 1064 nm along the transfer path. Over long times (a few days) we observe that the relative phase can drift significantly<sup>84</sup>. To correct for relative phase shifts between colours, we use movable glass wedges in the transfer paths (see Fig. 4.16). Using glass wedges for relative phase adjustment is problematic since beams are displaced from each other and propagate in different directions after passing through the wedge. We rectify this issue by using two wedges in each transfer path, one of which is fixed and the other moveable [151].

### 4.3.6 Imaging breadboard

The vertical lattice beam is derived from the dipole Mephisto (see section 4.3.3) and is transported to the imaging breadboard via a PCF. The imaging breadboard sits above the science chamber. On the imaging breadboard, the vertical lattice passes through a Glan-Laser cube, an optical isolator and a telescope before being sent through the hole in the objective onto the atoms. The design waist at the atoms is 100  $\mu\text{m}$ . The vertical lattice beam is retro-reflected off the bottom viewport, propagates back through the hole in the objective, and is rejected and dumped at the optical isolator. Fig. 4.17 shows the

<sup>84</sup>chapter 6 contains more information on how we measure relative phases.

vertical lattice optics on the imaging breadboard.

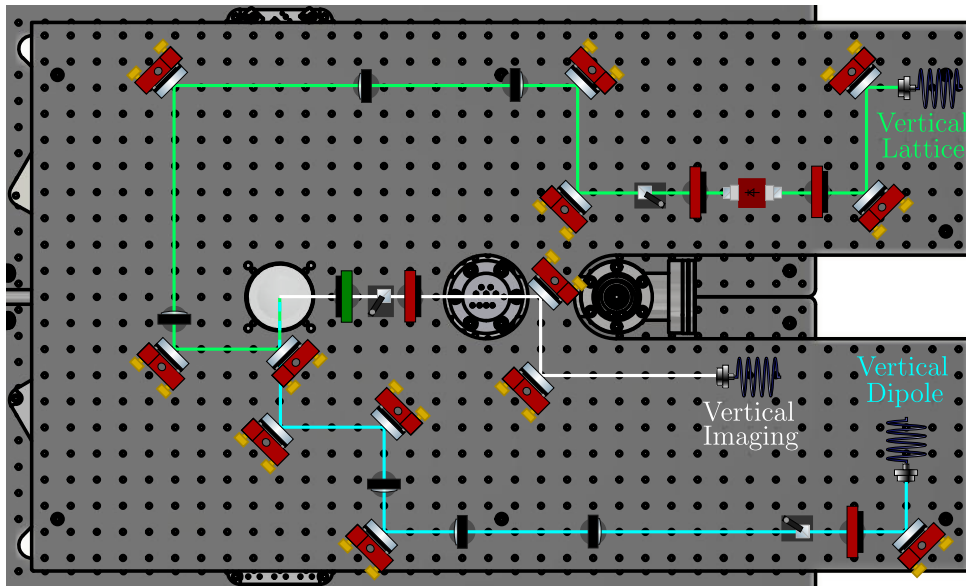


**Figure 4.17** – Vertical lattice, absorption imaging and vertical dipole setup on the imaging breadboard. A component glossary can be found in [appendix A](#).

Our Verdi laser creates the vertical dipole beam which we use to create an anti-confining potential. The vertical dipole beam propagates through a telescope, through the hole in the objective and through the bottom viewport, after which it is dumped. The design waist is 50  $\mu\text{m}$ .

Finally, we have a vertical imaging beam for absorption imaging which also passes through the hole in the objective and the bottom viewport. This imaging beam can be directed onto either an in-situ camera<sup>85</sup> or a camera for TOF<sup>86</sup>. Most of the experimental images shown in [chapter 6](#) and [chapter 7](#) are taken with these two cameras.

#### 4.4 Experiment coils

Cold-atom experiments typically operate with fields of up to 1000 G (0.1 T) and gradients of up to 400 G/cm, which can be readily reached with compact solenoids. These fields typically require currents of up to 200 A and usually the coils need to be water-cooled if they are operated for several seconds in a sequence.

We use hollow-core wire for all our ‘big’ coils, i.e. the 3D MOT coils, Feshbach coils and the gradient coil<sup>87</sup>. For all the other coils, including 2D MOT offset coils, 2D MOT quadrupole coils, 3D MOT offset coils, spin-pol coils, science chamber offset coils, and the Stern-Gerlach coil, we use 1 mm thick, enamelled copper wire.

The 2D MOT offset, MOT chamber offset and science chamber offset coils are supplied by standard, low-power current supplies and are continuously running. The power supplies

<sup>85</sup>IDS UI-3252

<sup>86</sup>Andor Zyla 5.5

<sup>87</sup>Our hollow-core wire has a square profile with a side length of 4 mm and a (circular) hole diameter of 2.5 mm.

for the 2D quadrupole coils are programmable. Finally, we use discharge units<sup>88</sup> to supply the spin-pol coil and Stern-Gerlach coils. These only need to be on for a few ms during the sequence during which they produce a relatively strong field.

We will only elaborate on the high-current coils in what follows. [Table 4.1](#) specifies the number of windings and the fields of the 3D MOT, Feshbach, and gradient coils.

	Windings (per coil)	Field (G/A)	Gradient (G/cm/A)
3D MOT coils	46	N/A	1.5
Feshbach coils	32	3.81	0.61
gradient coil	28	1.5	0.48

**Table 4.1** – Select parameters of the high-current coils.

We added values for both the gradient and offset field for the Feshbach coil because we intend to use these coils in both the Helmholtz- and anti-Helmholtz configurations (see [section 8.4](#)). The gradient coil produces both an offset field as well as a gradient.

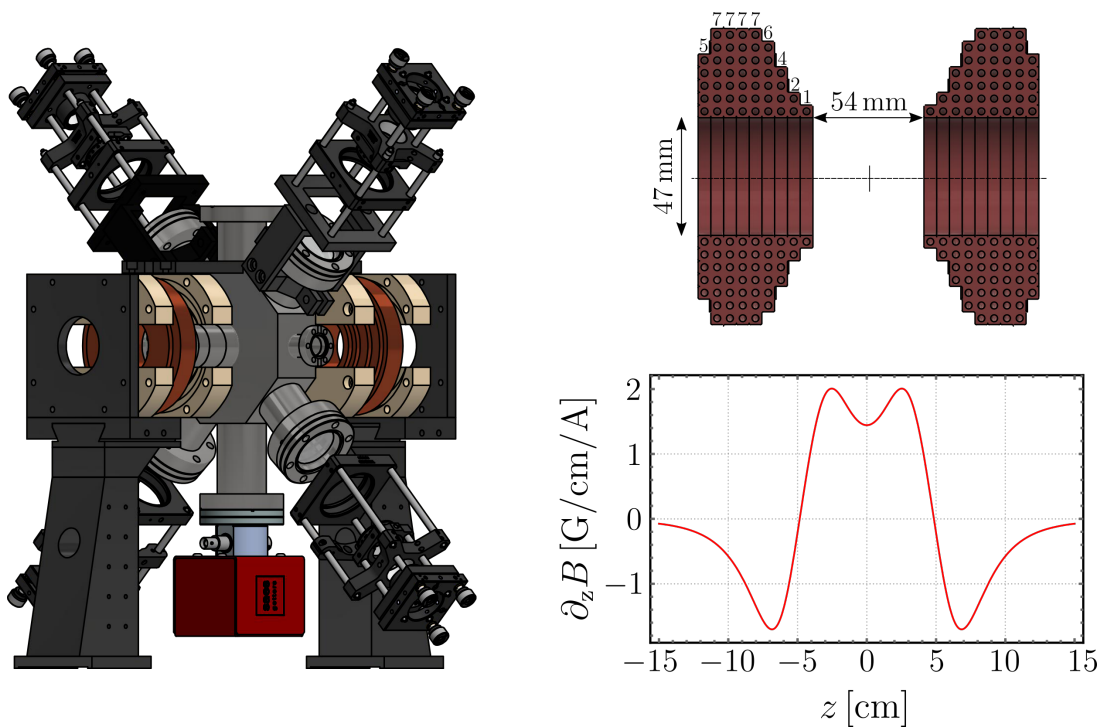


**Figure 4.18** – Left: exploded view of the 3D MOT chamber with its mounts, the 3D MOT coils and the fibre launchers. Top right: 3D MOT coil drawing with number of radial windings in each layer. Bottom right: calculated, on-axis magnetic field gradient of the 3D MOT coils.

**3D MOT coils** The 3D MOT coils are the machine’s most powerful. They also have the most complicated shape (see [Fig. 4.18](#)). The somewhat unusual shape is a consequence

<sup>88</sup>A discharge unit is effectively a capacitor in series with a resistor and can supply 10 A-20 A for a few ms.

of the 3D MOT chamber's angled connections leading to the 2D MOT chambers. The 3D MOT coils produce a magnetic field gradient of 1.5 G/cm/A. The maximum current they operate at is 200 A, during the magnetic trap stage, corresponding to a maximum field gradient of 300 G/cm. Their inner and outer diameters are 47 mm and 107 mm, respectively.

The 3D MOT coils are held in place by casts that connect to a moveable dovetail clamp on a short rail. The axial position of the 3D MOT coil can thus be changed by a few mm if required. Both the 3D MOT and the Feshbach coils are supplied by the same power supply<sup>89</sup>. For fast switch-off of the MOT coil current, we use dedicated MOSFETs. A schematic of the power supply, coil, and MOSFET wiring is shown in Fig. 4.19. We installed two MOSFET boxes in parallel to reduce the load on each individual MOSFET. This increases the lifetime of the MOSFETs, especially if we are running sequences where the duty cycle of the power supply is high. We toggle between the two MOSFETs at the start of every sequence using a multiplexer (see Fig. 4.19).

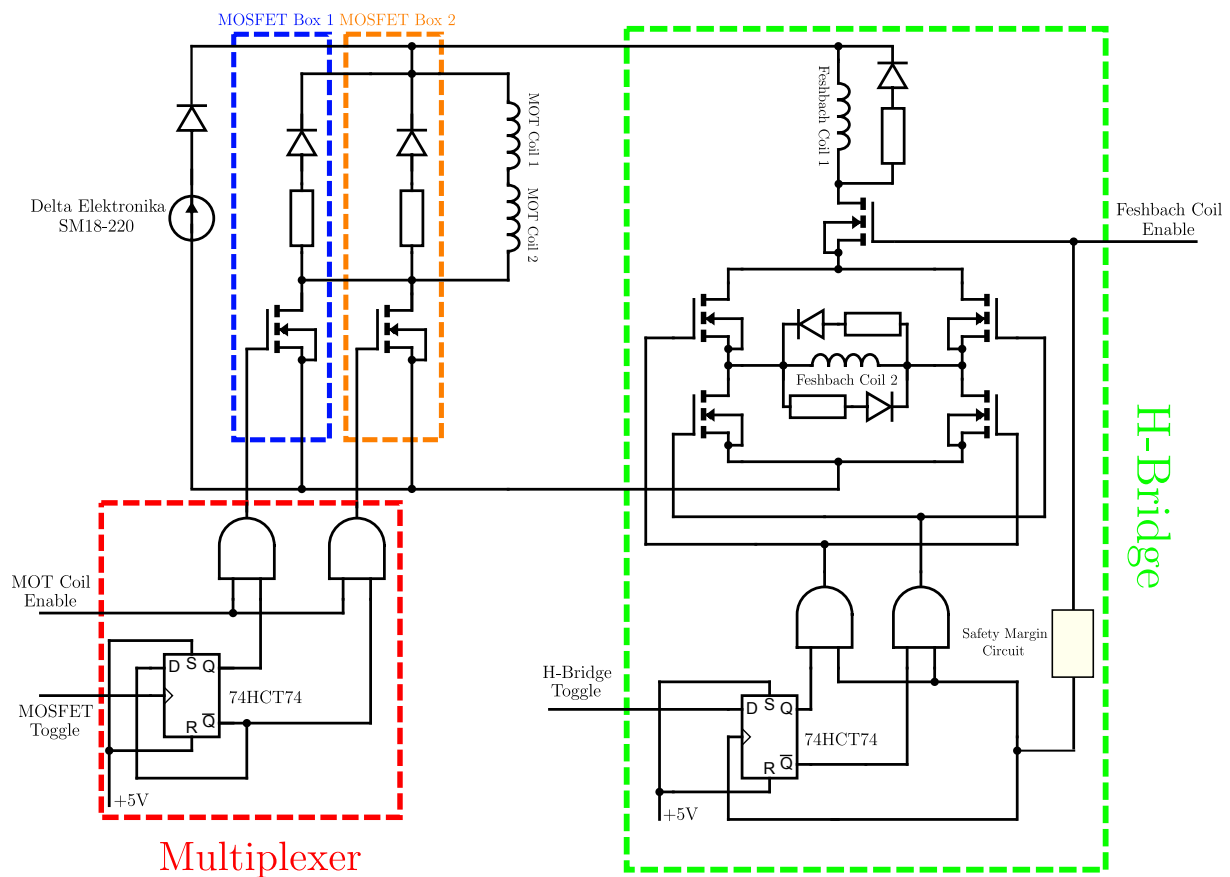


**Figure 4.19** – Circuit diagram of the 3D MOT coils and Feshbach coils. The safety margin circuit ensures that the H-bridge polarity cannot be switched while current is still flowing.

**Feshbach coils** Our Feshbach coils have a simple cylindrical shape. Each coil has 8 radial windings and 4 layers (32 windings in total). The inner (outer) diameter is 118 mm

<sup>89</sup>Delta Elektronika SM 18-220. We can use the same power supply for both the 3D MOT and Feshbach coils since they are only needed in separate parts of the sequence.

(186 mm) and the height is 17 mm. The coils are placed as close to the ideal Helmholtz configuration as possible in order to minimize radial field curvature. After they were wound, we cast the coils in resin<sup>90</sup> (see Fig. 4.20). Casting our Feshbach coils ensures the coils' rigidity and makes them easier to install on the science chamber. They are held in place by custom, acetal coil mounts that push the Feshbach coil casts against the chamber<sup>91</sup>. Wherever possible, we chose the inner and outer diameters of the casts and Feshbach coil mounts to fit tightly into the buckets so that the room to move is minimized and the axes of the coils and the chamber are as well aligned as possible.

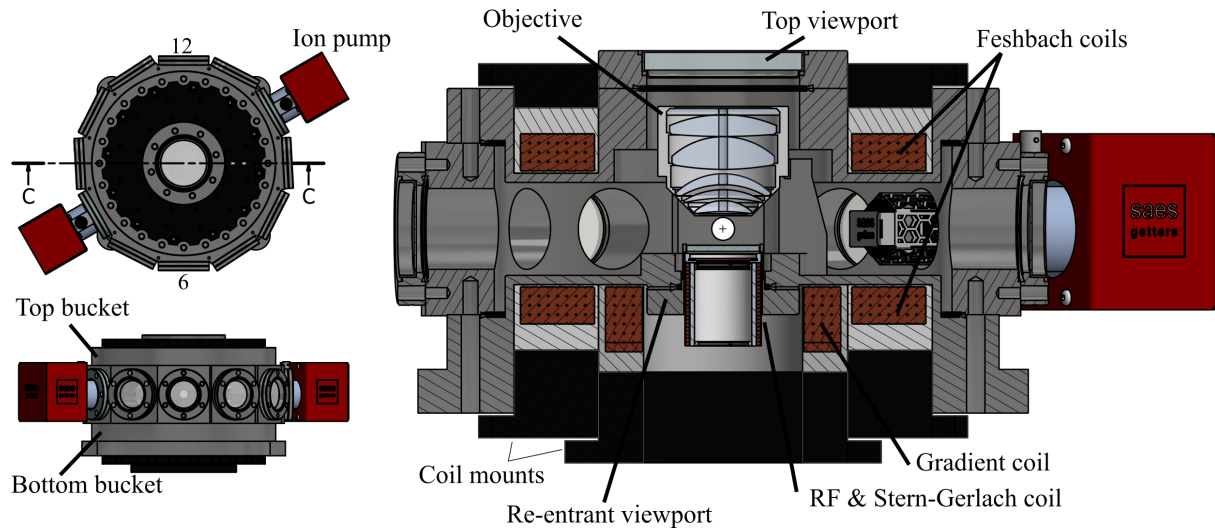


**Figure 4.20** – Diagram of the science chamber, microscope objective, and gradient and Feshbach coils. Figure adapted from [140].

Using a simple voltage divider circuit, we measured the inductance of each Feshbach coil to be  $155 \mu\text{H}$ . Switch off times from 100 A are on the order of  $100 \mu\text{s}$ . However, we believe that eddy currents persist for several ms upon switching off the Feshbach coils. We see that it takes 10 ms - 15 ms after switch-off until we are able to see the cloud in absorption imaging at the zero-field imaging frequency.

The polarity of one of the Feshbach coils can be flipped via an H-bridge (see Fig. 4.19). The H-bridge will be used for our single-layer selection scheme (see section 8.4).

**Gradient coil** The last of the ‘big’ coils is the gradient coil, which will be used for single layer selection. It is located in the bottom bucket between the CF40 (re-entrant) viewport and the inner surface of the bottom Feshbach coil cast (see Fig. 4.20). It has 4 radial windings and 7 layers, an inner diameter of 37 mm, an outer diameter of 54 mm, and a height of 30 mm. Like the Feshbach coils, the gradient coil is cast in resin. It is held in place by a cylindrical acetal mount that presses the gradient coil cast against the science chamber and holds it in place. We measured the inductance of the gradient coil to be around  $85 \mu\text{H}$ . The current in the gradient coil is generated by a power supply<sup>92</sup> with a nominal relative current stability of  $1 \times 10^{-5}$ .

<sup>90</sup>Polytek EasyFlo 60

<sup>91</sup>We chose acetal to minimize eddy currents.

<sup>92</sup>FuG NLN 700-6,5.

## 4.5 RF and MW setup

We have various components dedicated to the delivery of microwave (MW) and radio-frequency (RF) radiation.

**MW in the 3D MOT chamber** We use MW radiation between 6.500 GHz and 6.850 GHz for forced evaporative cooling of  $^{87}\text{Rb}$  on the  $F = 1 \rightarrow F = 2$  transition. A local oscillator signal of 6.850 GHz is mixed with the output of a DDS. The output of the mixer is amplified and sent through a circulator before being emitted by a MW antenna placed close to the MOT chamber. The circulator prevents reflected power, e.g. due to a mismatch of impedances, from making it back into the amplifier.

Fig. 4.21 shows a schematic of the MW setup for the 3D MOT chamber.

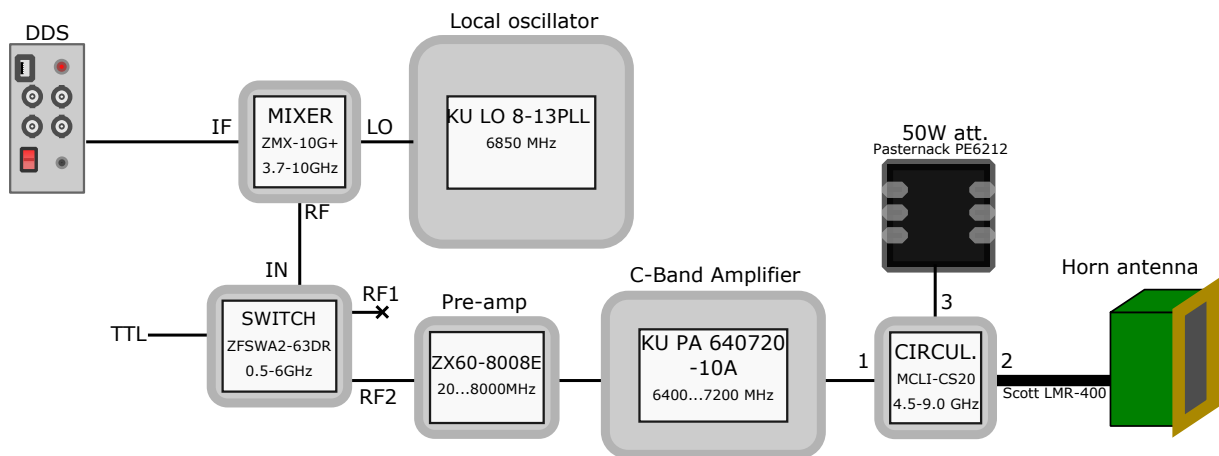


Figure 4.21 – MW setup in the MOT chamber.

**RF & MW in the science chamber** To transfer atoms between  $m_F$  states and, in particular, to prepare the atoms in the absolute ground state after transport, we use a RF antenna mounted close to the bottom viewport of the science chamber. The output of a DDS is amplified and coupled into the RF antenna. We use the RF setup for frequencies between 500 kHz and 300 MHz. In addition to RF radiation, we can also send MW radiation in the range 500 MHz-1.4 GHz through the RF antenna. MW radiation in the science chamber will be used to target the  $4s_{1/2}$  hyperfine transition of  $^{39}\text{K}$  and  $^{40}\text{K}$  for single layer selection (see section 8.4). We mix the output of a DDS with a programmable local oscillator and send the mixed signal through a 6 W amplifier. The amplifier output is then sent through one of two circulators (depending on the isotope) and to the RF antenna. Fig. 4.22 shows a functional diagram of the RF and MW setup for the science chamber.

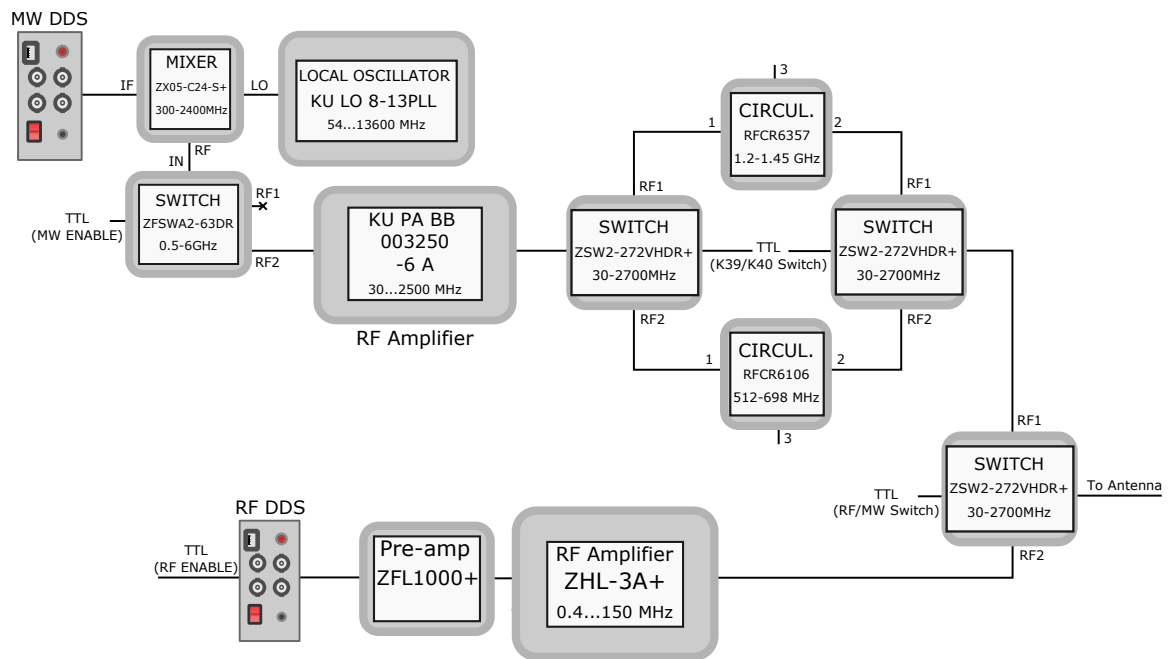


Figure 4.22 – RF and MW setup for the science chamber.



## 5 Experimental sequence

This chapter details the different stages in the experimental sequence for creating BECs of  $^{87}\text{Rb}$  and  $^{39}\text{K}$  and for loading the optical lattice. Most of the sequence time ( $\sim 28\text{ s}$ ) is dedicated to cooling atoms to quantum degeneracy and actual experiments usually only take a few 100 ms. The sequence consists of roughly five stages. First, atoms are collected from background vapour in a magneto-optical trap and cooled to roughly  $100\ \mu\text{K}$ . They are subsequently transferred to a magnetic trap and evaporatively cooled to  $10\ \mu\text{K}$ . A transport beam then moves the cloud from the MOT chamber to the science chamber. After further evaporative cooling in a crossed dipole trap a BEC is formed. Finally, the cloud is loaded into the optical lattice in which we conduct our experiments.

We have separate sequences for  $^{87}\text{Rb}$  and  $^{39}\text{K}$ , the main difference being that we control the scattering length via a magnetic offset field (which we call the ‘Feshbach field’) for  $^{39}\text{K}$ <sup>93</sup>. We will focus on the  $^{39}\text{K}$  sequence in this chapter. Note that  $^{87}\text{Rb}$  is also used in the  $^{39}\text{K}$  sequence.

### 5.1 MOT

Ultracold-atom experiments universally use magneto-optical traps (MOTs) to trap atomic clouds and cool them to  $10\ \mu\text{K}$ - $100\ \mu\text{K}$ . A MOT consists of a magnetic quadrupole field and, typically, six laser beams red-detuned with respect to a strong atomic transition (such as the D1 and D2 lines for alkali atoms). This combination causes atoms to be pushed towards the centre of the quadrupole field while simultaneously being cooled through scattering of red-detuned light [205].

At the start of our sequence, the 2D MOT and 3D MOT light is switched on along with the 2D MOT and 3D MOT coils. We load the MOT for 3 s. Table 5.1 and Table 5.2 list our MOT parameters for  $^{87}\text{Rb}$  and  $^{39}\text{K}$ , respectively. Detunings for cooling and repump are referenced to the  $|F = 2\rangle \rightarrow |F' = 3\rangle$  and  $|F = 1\rangle \rightarrow |F' = 2\rangle$  transition, respectively.

MOT load duration	3 s
2D field gradient	19 G/cm
2D cooling power	150 mW
2D cooling detuning	$-3\Gamma$ <sup>94</sup>
2D repump power	10 mW
2D axial cooling power	32 mW
2D repump detuning	0 $\Gamma$
3D cooling power	90 mW
3D cooling detuning	$-3.5\Gamma$
3D repump power	11 mW
3D repump detuning	0 $\Gamma$

**Table 5.1** –  $^{87}\text{Rb}$  MOT parameters.  
Powers are per beam.

MOT load duration	0.9 s
2D field gradient	15 G/cm
2D cooling power	90 mW
2D cooling detuning	$-3.9\Gamma$
2D repump power	110 mW
2D axial cooling power	2.2 mW
2D repump detuning	$-1.4\Gamma$
3D cooling power	20 mW
3D cooling detuning	$-1.3\Gamma$
3D repump power	41 mW
3D repump detuning	$-3.4\Gamma$

**Table 5.2** –  $^{39}\text{K}$  MOT parameters.  
Powers are per beam.

<sup>93</sup>BECs of  $^{39}\text{K}$  are not stable at zero magnetic field, since the zero-field scattering length is negative [204].

<sup>94</sup>Here,  $\Gamma \approx 2\pi \times 6\ \text{MHz}$  is the natural linewidth of the D1 and D2 transitions of  $^{87}\text{Rb}$  and  $^{39}\text{K}$ .

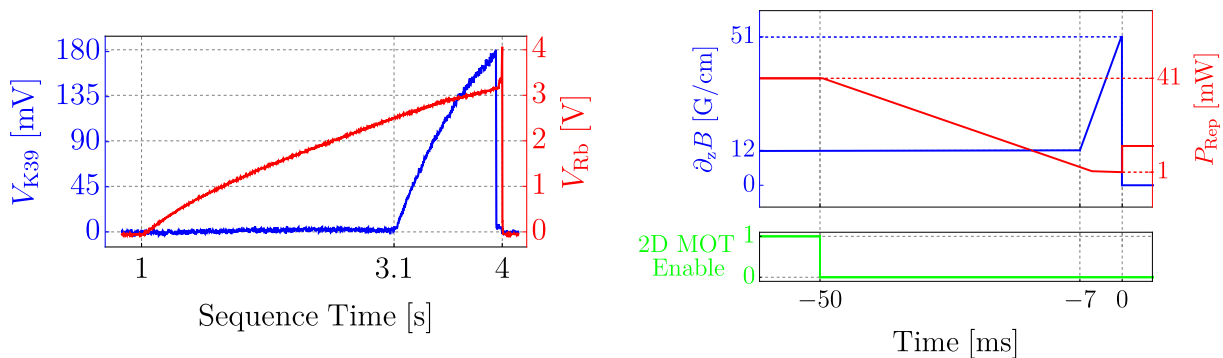


**Figure 5.1** – Left: fluorescence signal of  $^{87}\text{Rb}$  (red) and  $^{39}\text{K}$  (blue) during MOT loading. Note that MOT loading starts at 1 s<sup>95</sup>. Right: 3D MOT quadrupole gradient ( $\partial_z B$ ), repump power ( $P_{\text{Rep}}$ ) and 2D MOT Enable during the last 50 ms of MOT loading. Time 0 marks the end of the compressed MOT stage.

Fig. 5.1 shows an image of a typical MOT fluorescence signal. The 3D MOT quadrupole field is kept at 12 G/cm during MOT loading. We compress the MOT in the last 7 ms of the MOT loading stage to 51 G/cm<sup>96</sup>. 50 ms before the MOT stage is complete, we turn off the 2D MOT light and 2D quadrupole fields (i.e. 2D MOT Enable is set to 0), while simultaneously reducing the power in the  $^{39}\text{K}$  3D repump beam (see Fig. 5.1) [176, 177].

We have additional blue-detuned push beams for  $^{87}\text{Rb}$  and  $^{39}\text{K}$  that propagate along the axial directions of the respective 2D MOTs. We found however that these do not significantly increase the MOT size or reduce the MOT load duration. We therefore do not use push beams during the sequence.

## 5.2 Molasses

Molasses cooling (also known as Sisyphus cooling) is a common method for additional cooling after the MOT loading stage. During the molasses stage, atoms selectively absorb lower energy photons than they emit through spontaneous emission [207]. This cools the cloud to a temperature of typically a few tens of  $\mu\text{K}$ .

3D cooling power	18 mW
3D cooling detuning	$-11.8 \Gamma$
3D repump power	5 mW
3D repump detuning	$-8.3 \Gamma$
Final atom number	$\sim 4 \times 10^9$
Final temperature <sup>97</sup>	40 $\mu\text{K}$

**Table 5.3** –  $^{87}\text{Rb}$  molasses parameters.

3D cooling power	2.8 mW
3D cooling detuning	$+0.2 \Gamma$
3D repump power	1.7 mW
3D repump detuning	$-11.4 \Gamma$
Final atom number	$\sim 4 \times 10^8$
Final temperature	90 $\mu\text{K}$

**Table 5.4** –  $^{39}\text{K}$  molasses parameters

After MOT loading is complete, we switch off the 3D MOT coil current but keep the 3D MOT light enabled. We suddenly change the detuning of the cooling and repump light

<sup>95</sup>We reserve 1 s at the beginning of each sequence to send commands to various devices connected via ethernet.

<sup>96</sup>This compressed MOT stage is a common element of experiments with  $^{39}\text{K}$  [206].

for both species and additionally reduce their power. The total duration of the molasses stage is 5.5 ms. Table 5.3 and Table 5.4 list the molasses parameters for  $^{87}\text{Rb}$  and  $^{39}\text{K}$ , respectively.

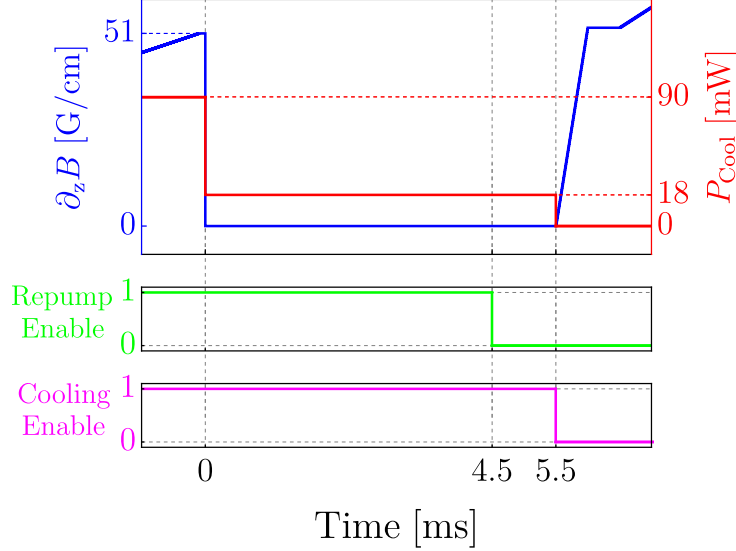


**Figure 5.2** – Quadrupole field strength ( $\partial_z B$ ), Rb 3D cooling power ( $P_{\text{Cool}}$ ), and 3D cooling and repump enables during the molasses stage. Time 0 marks the end of the compressed MOT stage.

At the end of molasses, the  $^{87}\text{Rb}$  ( $^{39}\text{K}$ ) cloud contains  $\sim 4 \times 10^9$  ( $\sim 4 \times 10^8$ ) atoms and has a temperature of 40  $\mu\text{K}$  (90  $\mu\text{K}$ ). We switch off the 3D repump light 1 ms before switching off the cooling light (see Fig. 5.2). This pumps atoms into the  $|F = 1\rangle$  hyperfine manifold. At this point, the atoms are evenly distributed among the three  $m_F$  states of the  $|F = 1\rangle$  hyperfine manifold.

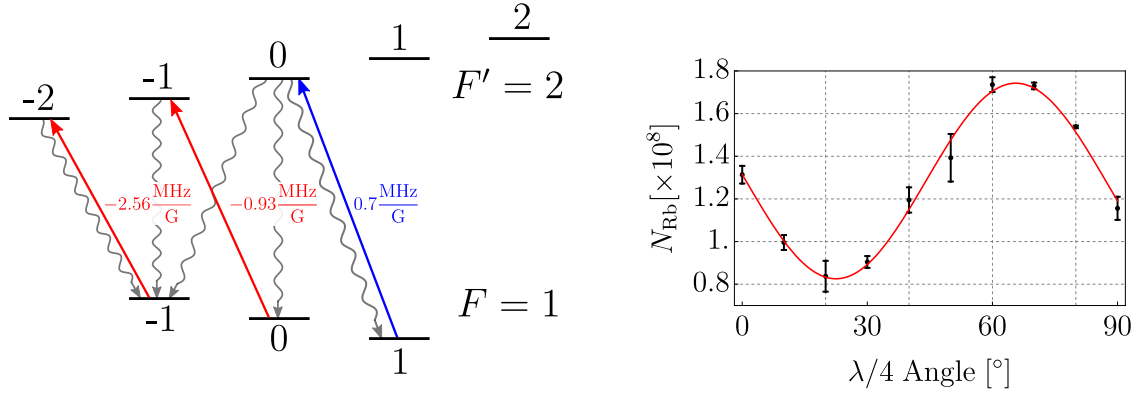
**Spin-pol** In the  $^{87}\text{Rb}$  sequence we have an additional spin-polarization (spin-pol) stage that pumps atoms into the low-field seeking, and hence magnetically trappable  $|F = 1, m_F = -1\rangle$  state. In the  $^{39}\text{K}$  sequence we skip the spin-pol stage and move straight to the magnetic trap stage<sup>98</sup>. We will briefly discuss spin-pol in the  $^{87}\text{Rb}$  sequence before returning to the  $^{39}\text{K}$  sequence.

Fig. 5.3 shows how spin-pol can be used to optically pump atoms into a desired Zeeman state. 300  $\mu\text{s}$  after the end of molasses, a bias field of  $\sim 10$  G is switched on along the direction of the 3D MOT coil axis. 180  $\mu\text{s}$  later, the spin-pol beam and an overlapped spin-pol repump beam are shone onto the cloud for 245  $\mu\text{s}$  (see Fig. 5.4). During this time, atoms are pumped toward the  $|F = 1, m_F = -1\rangle$  and  $|F = 2, m_F = -2\rangle$  states. The spin-pol repump beam is then switched off so that the still-present spin-pol light can pump atoms out of the  $|F = 2\rangle$  manifold. This final pumping stage lasts for 275  $\mu\text{s}$ . The bias field is switched off 3 ms after the magnetic trap has started ramping up which ensures that there is always a fixed quantization axis. Adding spin-pol before the magnetic trap

<sup>97</sup>Temperature is measured for a small MOT (150 ms load duration).

<sup>98</sup>We did not find any benefit in using spin-pol for the  $^{39}\text{K}$  sequence.

increases our atom number after MW evaporation by roughly 50%. Table 5.5 lists the relevant sequence parameters.



**Figure 5.3** – Left: spin-pol schematic. Atoms can be pumped into the low-field seeking  $|F = 1, m_F = -1\rangle$  state via a red-detuned and circularly polarized laser beam. Red (blue) arrows indicate that the transition is shifted to lower (higher) frequencies as the magnetic field is increased. Note that in  $^{87}\text{Rb}$  and  $^{39}\text{K}$  atoms can also spontaneously decay into the  $F=2$  hyperfine manifold. Atoms in  $|F = 2\rangle$  ( $|F = 1\rangle$ ) are targeted by the spin-pol (spin-pol repump) beam. Right: measured  $^{87}\text{Rb}$  atom number after MW evaporation vs spin-pol waveplate angle.

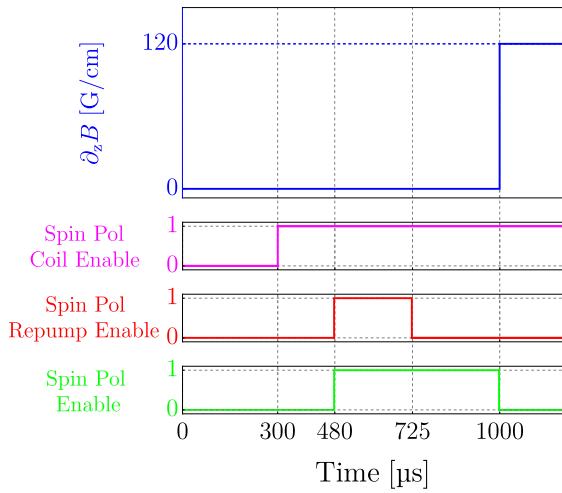


**Figure 5.4** –  $^{87}\text{Rb}$  spin-pol sequence. Time 0 marks the end of molasses.

Spin-pol power	1.3 mW
Spin-pol detuning	-4.2 MHz
Repump power	0.4 mW
Repump detuning	-12 MHz
bias field	$\sim 10$ G

**Table 5.5** – Spin-pol parameters for  $^{87}\text{Rb}$ .

### 5.3 Magnetic trap & MW evaporation

The magnetic trap is turned on in two steps. In the first step, the magnetic field is ramped up from zero to 53 G/cm in 0.5 ms. This ramp is followed by a slower, 20 ms ramp up to 270 G/cm. We initially found that  $^{39}\text{K}$  quickly leaves a strong magnetic trap within a few ms. We attributed this loss to the cloud being heated too much in the transfer

process. While not a problem for  $^{87}\text{Rb}$ , too high temperatures will cause  $^{39}\text{K}$  to probe magnetic fields at which it becomes high-field seeking and be lost as a consequence. While we could hold  $^{39}\text{K}$  in a shallow magnetic trap for a few seconds, we were not able to get sympathetic cooling to work efficiently. We solve this problem by turning on the MW field, which we use for evaporation, at large detuning ( $\Delta = -285$  MHz) from the zero-field  $|F = 1, m_F = -1\rangle \rightarrow |F = 2, m_F = -2\rangle$  transition in  $^{87}\text{Rb}$  before we ramp up the magnetic trap. This causes  $^{87}\text{Rb}$  to be evaporated in the magnetic trap loading process, which allows us to transfer a sufficient amount of  $^{39}\text{K}$  into a strong magnetic trap.

Once the magnetic trap is ramped up fully, we start increasing the MW frequency for sympathetic cooling. We target the  $|F = 1, m_F = -1\rangle \rightarrow |F = 2, m_F = -2\rangle$  transition in  $^{87}\text{Rb}$  (see Fig. 5.5) for cooling both  $^{87}\text{Rb}$  and  $^{39}\text{K}$ . By sweeping the MW frequency from a low frequency to a high frequency, we can remove the hottest atoms from the cloud, thereby effectively cooling the remaining, trapped atoms. We sweep the MW frequency from  $\Delta = -165$  MHz to  $\Delta = -105$  MHz over 450 ms and then to  $\Delta = -6.3$  MHz in 12 s. At the end of MW evaporation we are left with  $2 \times 10^7$   $^{39}\text{K}$  atoms and  $1.5 \times 10^7$   $^{87}\text{Rb}$  atoms at 18  $\mu\text{K}$  and 6  $\mu\text{K}$ , respectively.

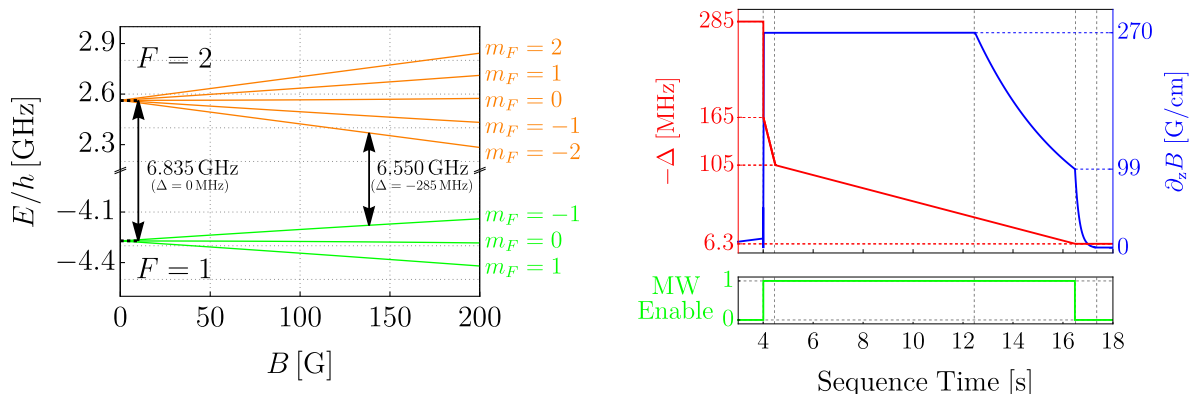


**Figure 5.5** – Left: Zeeman shift of the  $5s_{1/2}$  manifold in  $^{87}\text{Rb}$ . We target the  $|F = 1, m_F = -1\rangle \rightarrow |F = 2, m_F = -2\rangle$  transition for MW evaporation. Right: detuning of MW radiation ( $-\Delta$ ) and magnetic field gradient during the MW evaporation stage.

See section 4.5 for details on the MW electronics setup.

## 5.4 Hybrid trap

Combining a magnetic trap and a single dipole beam is commonly called a ‘hybrid’ trap, as it is part optical and part magnetic [208]. The dipole beam provides strong confinement along two axes, while confinement along the dipole axis is predominantly provided by the magnetic trap (see Fig. 5.6).

Our transport beam acts as the dipole beam in the hybrid trap and is ramped up to 7 W at the beginning of magnetic trap loading. At this stage of the sequence the transport beam has virtually no effect on temperature or atom number. However, the importance of the transport beam increases as the temperature of the cloud is reduced. Its focus is located a few tens of  $\mu\text{m}$  below the centre of the magnetic trap. At temperatures close to 1  $\mu\text{K}$ -10  $\mu\text{K}$ , the magnetic trap suffers from Majorana losses when atoms cross the zero-field region [209]. This ‘hole’ in the magnetic trap can be avoided with the transport

beam, which distorts the potential in such a way so as to spatially separate the zero-field region of the magnetic trap and the potential minimum. The potential minimum of the hybrid trap is thus located at a finite field, ensuring a well-defined quantization axis. Atoms consequently stay spin-polarized in the  $|F = 1, m_F = -1\rangle$  state.

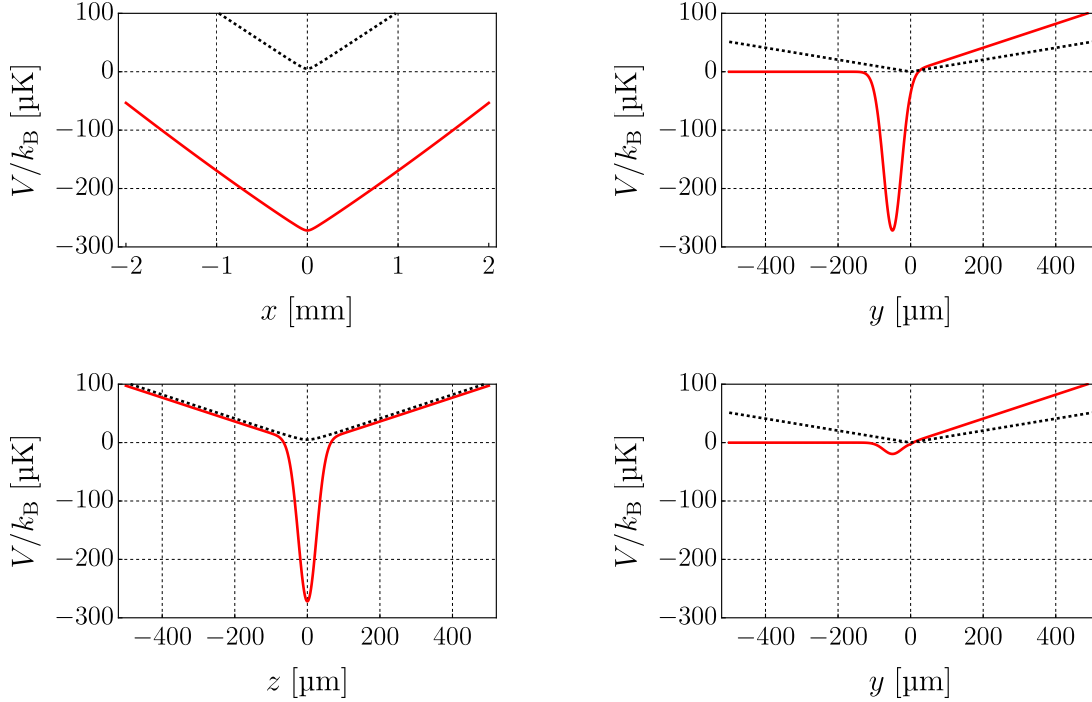


**Figure 5.6** – Hybrid trap potential for  $^{87}\text{Rb}$  before evaporation to a MOT chamber BEC along the three principal axes. We assume  $P$ ,  $w_0$ ,  $\lambda$ , and  $\partial_z B$  to be 7 W, 50  $\mu\text{m}$ , 1064 nm, and 61 G/cm, respectively.  $x$ : transport direction,  $y$ : vertical (gravity) direction,  $z$ : strong axis of MOT coils. The black dashed line shows the contribution of the quadrupole trap to the hybrid trap potential. Note the additional contribution of gravity in the  $y$ -direction. Confinement along the transport beam’s axial direction ( $x$ ) is dominated by the quadrupole field, while confinement along the other two axes ( $y$  &  $z$ ) is primarily provided by the transport beam. The cuts through the potential along the  $x$  and  $z$  directions are at the height of the trap minimum, i.e. the height of the transport beam. Bottom right: final evaporation to BEC in the hybrid trap. During evaporation, the quadrupole field is fixed to compensate for gravity, while the transport beam power is lowered.

**Potential** The total hybrid trap potential can be written as

$$\begin{aligned}
 V(x, y, z) = & \underbrace{U_0 \frac{2P}{\pi w(x)^2} e^{-\frac{2(y^2+z^2)}{w(x)^2}}}_{V_{\text{dipole}}} + \underbrace{\mu(\partial_z B) \sqrt{\frac{x^2}{4} + \frac{y^2}{4} + z^2}}_{V_{\text{mag}}} + \underbrace{mgy}_{V_{\text{grav}}}, \\
 w(x) = & w_0 \sqrt{1 + \left(\frac{\lambda x}{\pi w_0^2}\right)^2},
 \end{aligned} \tag{5.1}$$

where  $\partial_z B := \left. \frac{\partial B}{\partial z} \right|_{(x,y,z)=(0,0,0)}$  is the magnetic field gradient in the centre of the trap along the strong axis,  $P$ ,  $w_0$ , and  $\lambda$  are the power, waist, and wavelength of the transport beam,  $m$  is particle mass,  $\mu$  is the atomic magnetic moment<sup>99</sup>,  $g$  is the gravitational acceleration, and  $U_0$  is light shift per unit intensity.

**Alignment** We initially aligned the transport beam using fluorescence imaging along the transport axis. In this way, both the transport beam and the cloud in the magnetic trap can be imaged and the transport beam can be aligned precisely. For alignment, the cloud in the magnetic trap is evaporated to a very small size and measured in-situ. The centre of the cloud in-situ is assumed to be the centre of the magnetic trap. Since getting optical transport to work, we exclusively image the cloud in the MOT chamber via absorption imaging along the  $z$  axis (strong axis of the MOT coils). We align the transport beam by maximizing the atom number in the transport beam after switching off the MOT coils.

**Hybrid trap BEC** Fig. 5.6 shows the expected potential of the hybrid trap after loading is complete and before final evaporation to the BEC in the MOT chamber.

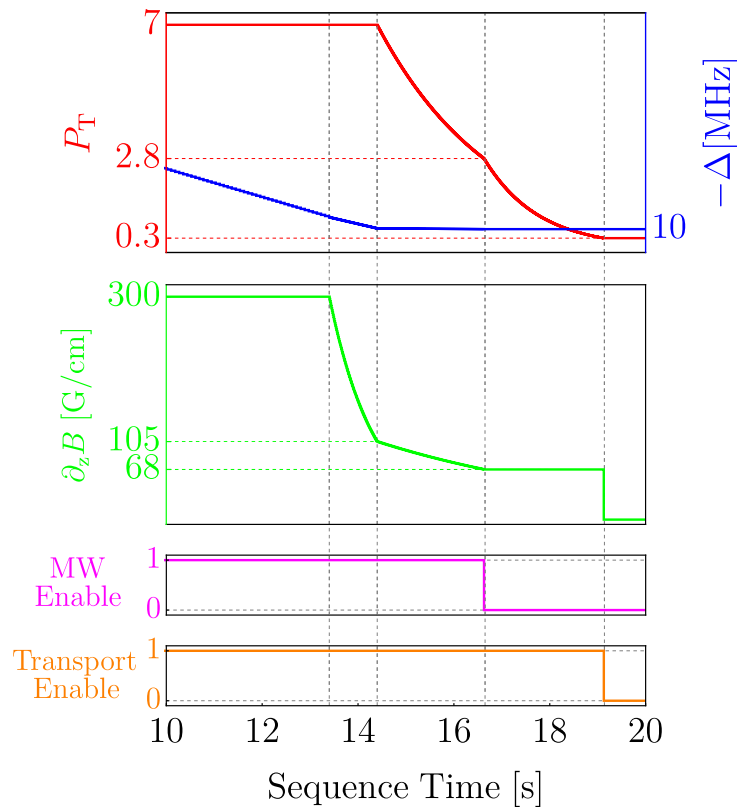


**Figure 5.7** – Hybrid trap BEC Sequence.  $P_T$ ,  $\Delta$ , and  $\partial_z B$  are the transport beam power, MW detuning, and magnetic trap gradient along the strong axis, respectively.

After MW evaporation, the magnetic trap gradient is lowered to  $\sim 68$  G/cm (strong axis)

<sup>99</sup> $\mu = \frac{1}{2}\mu_B$  for both  $^{87}\text{Rb}$  and  $^{39}\text{K}$  in the  $|F = 1, m_F = -1\rangle$  state.

until the gradient along the vertical direction exactly cancels gravity<sup>100</sup>. We call this the levitation gradient. Further evaporation to BEC is performed with the MOT coil current fixed at the levitation current, i.e. the current needed to produce the levitation gradient. We found that it is crucial to sit as close to the levitation current as possible to achieve reasonably-sized BECs. If the current is set too low, non-compensated gravity will cut into the dipole potential. If the current is too high, the hybrid trap potential will be confining in every direction and atoms will not have a way to escape the trap (though in practice they still do at slightly elevated currents).

We evaporate the  $^{87}\text{Rb}$  cloud to BEC in the hybrid trap by reducing the power in the transport beam, see Fig. 5.6 and Fig. 5.7. Atoms exclusively escape along the vertical direction, as seen by vertical streaks in the time-of-flight (TOF) images, since only this direction is untrapped beyond a certain distance from the trap minimum.

We can produce  $^{87}\text{Rb}$  BECs of up to  $6 \times 10^5$  atoms in the MOT chamber in the hybrid trap. Note however that creating the BEC in the MOT chamber is unnecessary for transport and that this stage constitutes a branch from the main sequence.

## 5.5 Transport

To load the transport beam we ramp down the magnetic trap to zero over 850 ms.

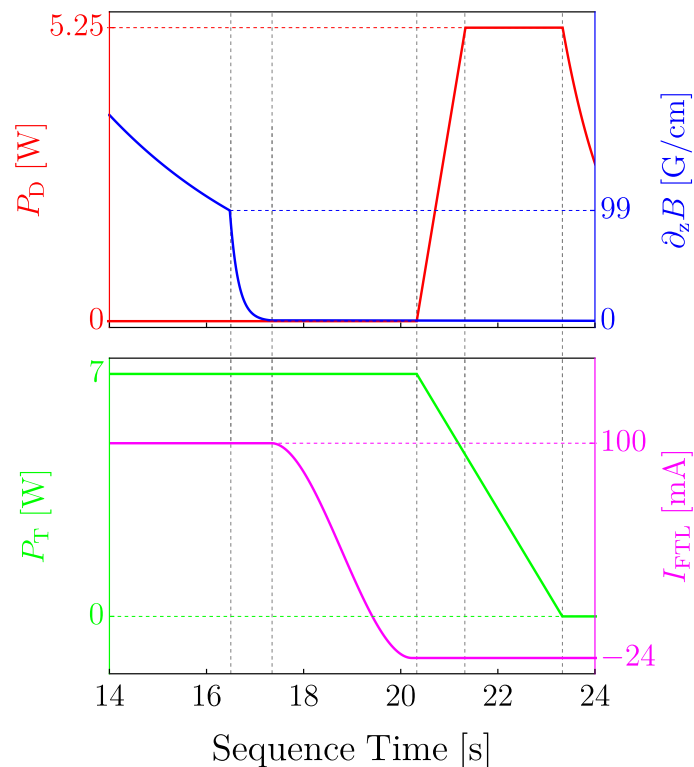


**Figure 5.8** – Transport beam power ( $P_T$ ), dipole trap power ( $P_D$ ), FTL current ( $I_{FTL}$ ), and MOT coil field gradient ( $\partial_z B$ ) during transport loading, transport, and dipole trap loading. Transport loading, transport, and dipole trap loading end at roughly 17.4s, 20.3s, and 23.3s, respectively.

<sup>100</sup>The levitation current depends on the atomic species; the quoted levitation gradient value is for  $^{87}\text{Rb}$ . Since  $^{39}\text{K}$  requires a Feshbach field, we can only create a hybrid trap BEC with  $^{87}\text{Rb}$ .

We transport by ramping the current supplied to the focus-tunable lens (FTL) from 100 mA (MOT chamber focus) to  $-24$  mA (science chamber focus) in an s-shaped ramp (see Fig. 5.8). This current ramp causes the transport laser’s focus to be displaced by 50 cm (see Fig. 5.9).

Temperature before transport	10 $\mu$ K
$N(^{87}\text{Rb})$ before transport	$1 \times 10^7$
$N(^{39}\text{K})$ before transport	$1.6 \times 10^7$
Temperature after transport	13 $\mu$ K
$N(^{87}\text{Rb})$ after transport	$7 \times 10^6$
$N(^{39}\text{K})$ after transport	$8 \times 10^6$

**Table 5.6** – Atom numbers and temperatures before and after transport. Note that the two species have the same temperatures.

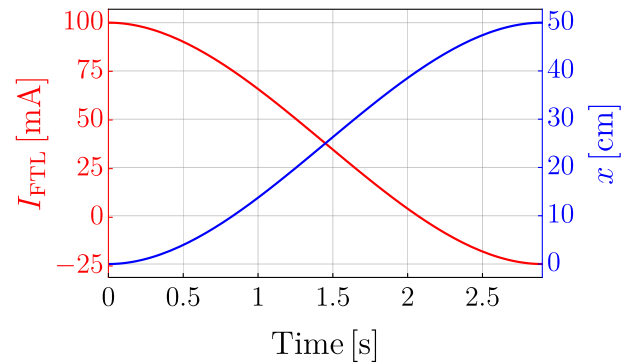


**Figure 5.9** – FTL current (red) and transport distance (blue) as a function of time during optical transport. Time 0 marks the beginning of transport.

We tried several different ramp shapes and found that the ramp used in [68] gave us both the best transport efficiency and the shortest transport times. Table 5.6 lists our typical transport parameters. In addition, as part of our transport optimization, we measured the lifetime of the cloud at various positions between MOT and science chamber. To this end, we transported the atomic cloud from the MOT chamber to a variable distance between MOT and science chamber, held for some time and moved the cloud back to the MOT chamber. We then imaged the cloud and extracted the atom number. As seen in Fig. 5.10, we get a steady increase in lifetime as the distance to the MOT chamber increases. This is consistent with the vacuum pressure in the science chamber being lower than in the MOT chamber, as we mentioned in section 4.1.1. For a more detailed discussion, see [210].

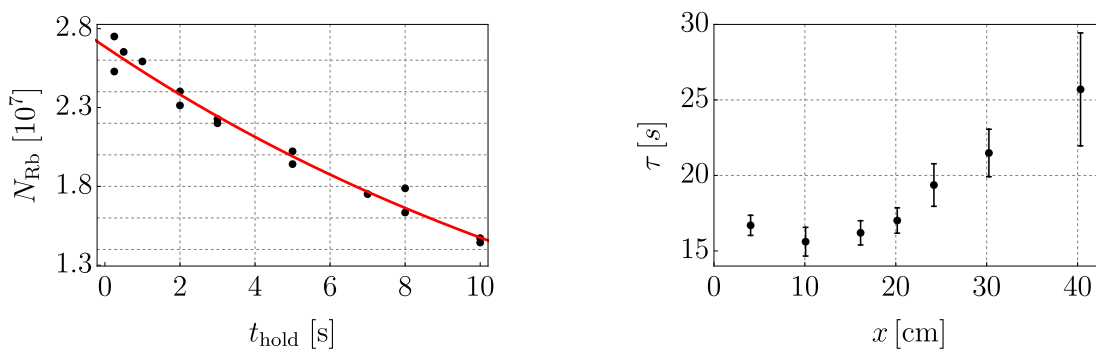


**Figure 5.10** – Left: decay of atom number ( $N_{\text{Rb}}$ ) in transport beam with hold time ( $t_{\text{hold}}$ ) at a distance of 5 cm from the MOT chamber. Right:  $\frac{1}{e}$ -lifetime ( $\tau$ ) of atomic cloud in transport beam vs transport distance ( $x$ ).

### 5.5.1 RF transfer

In the magnetic trap and during transport, atoms occupy the  $|F = 1, m_F = -1\rangle$  state. We find that transport does not change the  $m_F$  state of the atomic cloud despite the fact that we do not apply an offset field around the differential pumping section connecting the MOT and science chambers. At the end of transport, we turn on an RF field and sweep the frequency from 1000 kHz to 700 kHz in a 1 G-1.5 G bias field over 100 ms<sup>101</sup>. This transfers both  $^{87}\text{Rb}$  and  $^{39}\text{K}$  with nearly perfect efficiency to the  $|F = 1, m_F = 1\rangle$  state. Note that the frequency needs to be swept from high to low, as the  $m_F = -1 \rightarrow m_F = 0$  transition is at a higher frequency than the  $m_F = 0 \rightarrow m_F = 1$  transition. We confirm that RF transfer is successful by using a Stern-Gerlach field and TOF to spatially separate different  $m_F$  states and measure their respective populations.

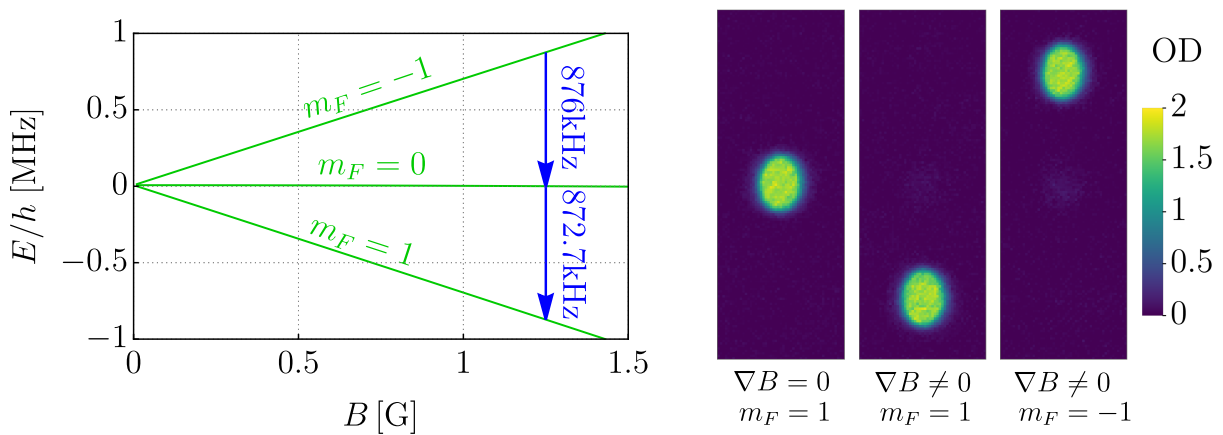


**Figure 5.11** – Left: Zeeman level splitting at low field for  $^{39}\text{K}$  and  $\Delta m_F = 1$  transition frequencies for a field of 1.25 G. Right: images of  $^{87}\text{Rb}$  BECs in the  $m_F = 1$  or  $m_F = -1$  state with ( $\nabla B \neq 0$ ) and without ( $\nabla B = 0$ ) a Stern-Gerlach pulse before imaging. Images are taken after 25 ms of TOF. The atomic density is proportional to the optical density (OD), which is extracted from absorption images [197].

## 5.6 Dipole trap

**Loading from the transport beam** In the science chamber, the two beams of the crossed dipole trap are ramped up to 5.25 W immediately after transport is complete (see Fig. 5.8). We simultaneously ramp down the transport beam power. Roughly 50% of atoms are transferred from the transport beam to the dipole trap. We end up with roughly  $3 \times 10^6$   $^{39}\text{K}$  atoms and  $3 \times 10^6$   $^{87}\text{Rb}$  atoms at 6  $\mu\text{K}$  in the dipole trap.

**Evaporation** The Feshbach field is ramped from 0 G to 316 G at the end of transport to target the  $^{87}\text{Rb}$  -  $^{39}\text{K}$  inter-species Feshbach resonance at 318 G [211]. At this field, the scattering length is  $170 a_0$ , where  $a_0$  is the Bohr radius. The dipole trap power is then lowered exponentially over 3 s to evaporatively cool the cloud. As the dipole trap power is lowered, the potential minimum is shifted downward due to gravity. The relative separation between the potential minima of  $^{87}\text{Rb}$  and  $^{39}\text{K}$  also increases (See Fig. 5.12). If

<sup>101</sup>The bias field is on continuously.

the separation becomes too large, the overlap between the  $^{87}\text{Rb}$  and  $^{39}\text{K}$  clouds is small and evaporative cooling becomes less efficient. This is one reason we chose cylindrical beam waists with a horizontal to vertical waist ratio of 4:1 for our dipole trap beams. Since  $^{87}\text{Rb}$  is heavier than  $^{39}\text{K}$ ,  $^{87}\text{Rb}$  is less strongly trapped and will be primarily evaporated during the dipole trap ramp down. Thus,  $^{39}\text{K}$  is sympathetically cooled with  $^{87}\text{Rb}$ .

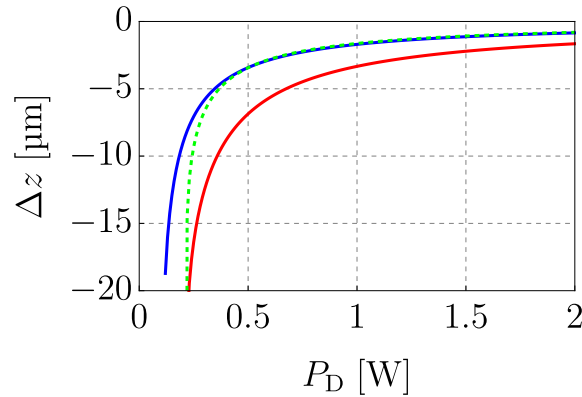


**Figure 5.12** – Gravitational sag of  $^{87}\text{Rb}$  (red) and  $^{39}\text{K}$  (blue) in a 1064 nm crossed dipole trap with waists of  $200 \mu\text{m} \times 50 \mu\text{m}$  as a function of dipole beam power. The green, dashed line shows the relative displacement.

**$^{39}\text{K}$  BEC** Below a certain trap depth,  $^{87}\text{Rb}$  drops out of the trap and only  $^{39}\text{K}$  is left (see Fig. 5.13). At this point we increase the strength of the Feshbach field to 394 G (intra-species scattering length of  $160 a_0$ ), thereby targeting the intra-species Feshbach resonance at 402 G [212] of  $^{39}\text{K}$  atoms in the  $|F = 1, m_F = 1\rangle$  state.

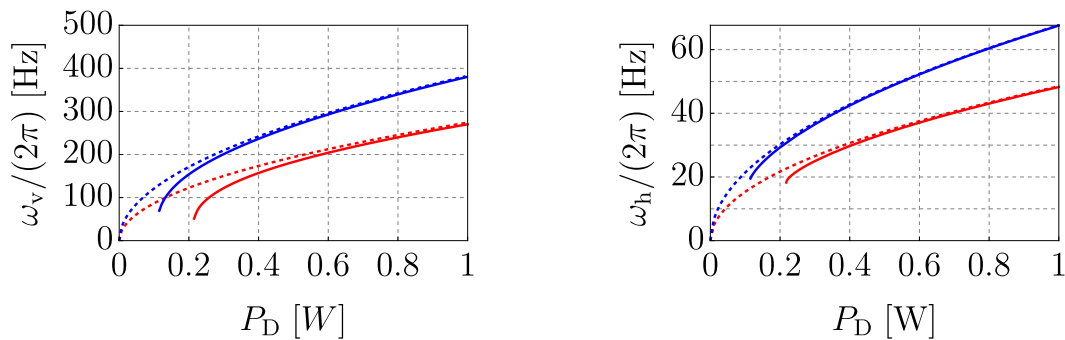


**Figure 5.13** – Left (right): vertical (horizontal) trap frequency in a 1064 nm crossed dipole trap with waists of  $200 \mu\text{m} \times 50 \mu\text{m}$  as a function of dipole beam power. Solid (dashed) lines are calculated trap frequencies with (without) taking into account gravitational sag. For high powers, the exact trap frequency approaches the theoretical value without gravitational sag. As the power approaches the drop-out power, the exact trap frequency increasingly diverges from the zero-gravity approximation.

After 2 s of evaporation at the intra-species Feshbach field a pure BEC of up to  $1.5 \times 10^5$   $^{39}\text{K}$  atoms is formed (see Fig. 5.14 and Fig. 5.15).

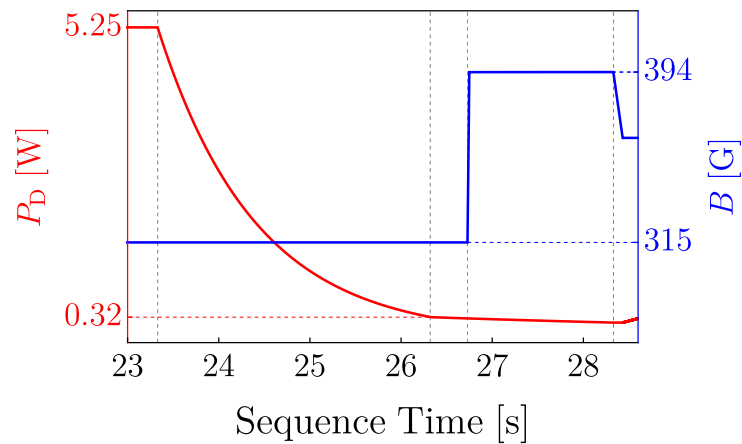


**Figure 5.14** – Dipole trap power ( $P_D$ ) and Feshbach field ( $B$ ) during evaporation to BECs of  $^{39}\text{K}$ . The  $^{39}\text{K}$  BEC emerges at around 26 s.

To get  $^{87}\text{Rb}$  BECs we run a dedicated  $^{87}\text{Rb}$  sequence, which is optimized to get large  $^{87}\text{Rb}$  BECs. We can get  $^{87}\text{Rb}$  BECs with up to  $1.2 \times 10^6$  atoms<sup>102</sup>. The BEC transition for  $^{87}\text{Rb}$  is shown in Fig. 5.15.

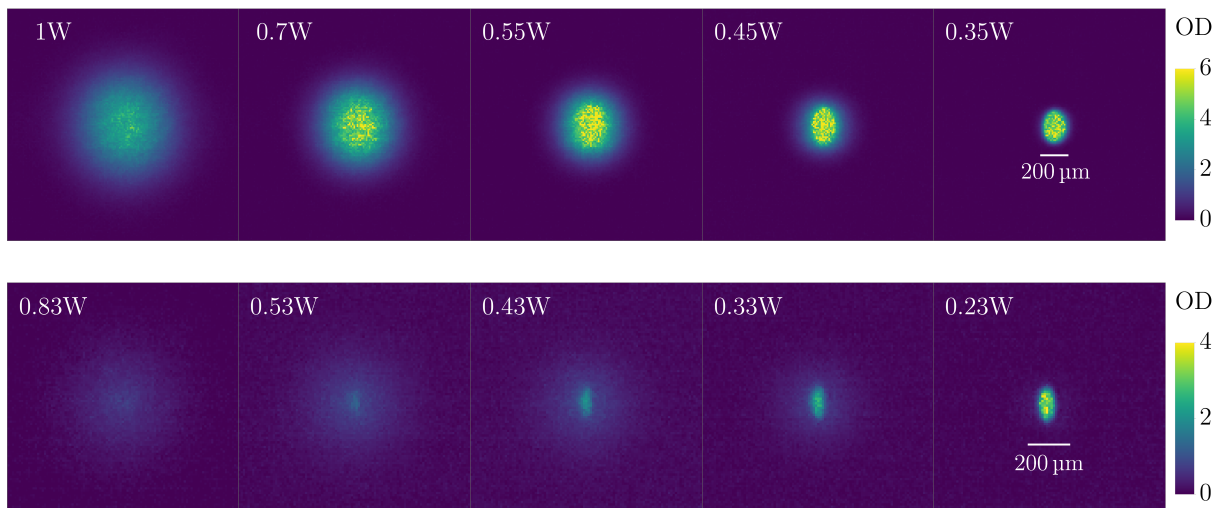


**Figure 5.15** – Onset of  $^{87}\text{Rb}$  (top) and  $^{39}\text{K}$  (bottom) BECs as the dipole trap power is lowered. Note the emergence of a sharp boundary and an aspect ratio different from 1. Images are taken after 25 ms (23 ms) of TOF for  $^{87}\text{Rb}$  ( $^{39}\text{K}$ ).

## 5.7 Lattice

For our lattice scripts, we ramp the intra-species scattering length to  $10 a_0$  over 100 ms immediately after the  $^{39}\text{K}$  BEC has formed. After holding the BEC for 100 ms, we ramp up the dipole trap to 0.5 W over 500 ms. At this point the lattice sequences diverge depending on whether we load the lattice adiabatically or perform lattice pulses for Kapitza-Dirac. We will only describe the lattice sequences in broad terms since we are still in the process of optimizing them.

<sup>102</sup>Measured after recompressing the dipole trap.

Apart from the Feshbach field, our  $^{87}\text{Rb}$  lattice scripts are identical to those used for  $^{39}\text{K}$ . For all  $^{87}\text{Rb}$  lattice sequences there is only a small 1 G-1.5 G offset field.

**Adiabatic loading** For the vertical, triangular and honeycomb lattice experiments, we ramp up the lattice beam powers exponentially over a few tens of ms to some lattice depth and hold for a few ms. We then ramp the lattice powers down linearly to zero over a few tens of ms. Fig. 5.16 shows an example lattice ramp up sequence. We switch off all lattice beams at some variable time during the final ramp down.

We control which combinations of lattice beams we want enabled during adiabatic loading, i.e. we can switch easily between running the triangular only or the honeycomb only or the triangular and vertical lattice or the honeycomb and vertical lattice.

If we want to create a superfluid, we ramp up the desired lattice beams to a shallow lattice depth, hold and switch off the lattice beams when ramp down starts (see Fig. 5.16). For creating a Mott insulator we ramp up to deeper lattices, apart from which the sequence is the same. The final ramp down to zero power serves two main purposes. Firstly, by ramping back to zero lattice depth, it allows us to check how adiabatic our lattice sequence is. By comparing the temperature of the cloud before and after the lattice sequence is performed, we can estimate how much our protocol is heating the atomic cloud. Secondly, we can create a negative temperature superfluid if we switch the interactions and confinement during the Mott insulator stage. This ramp down from the Mott insulator is also crucial to determine the temperature of the negative temperature state.

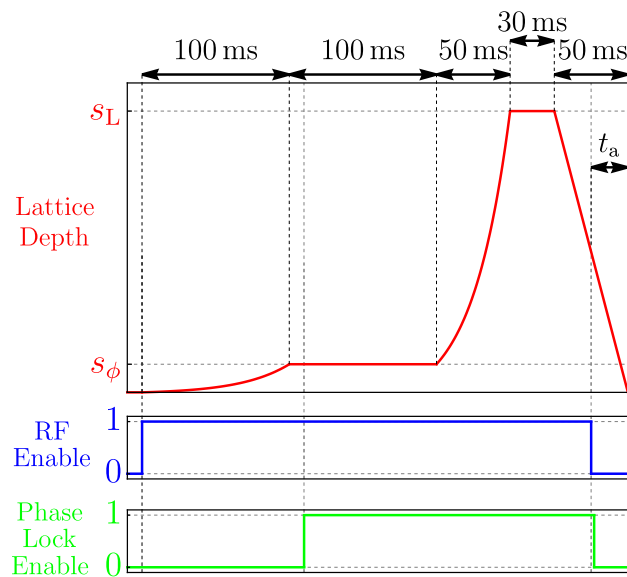


**Figure 5.16** – Sequence for adiabatic loading of the optical lattice. Here, the additional power ramp for phase stabilization is drawn. If we only work with the triangular or honeycomb lattices we skip the ramp to  $s_\phi$  and ramp directly to  $s_L$ .  $t_a$  is the time by which we advance switching off all lattice and dipole trap lasers. All times are approximate.

**Phase stabilization** To adiabatically load the kagome lattice we use a slightly modified sequence that allows us to engage phase stabilization. The phase controllers require a small amount of lattice light to enable phase locking. Thus, we ramp up the

lattice depth to  $s_\phi \sim 0.5-1$  and hold for a few ms, during which we lock the phase. We then ramp the lattices up to the full lattice depth,  $s_L$  (see Fig. 5.16). We found that locking the phase can heat the cloud to an unacceptable degree if the phase PI controllers are not properly set up. We therefore generally only use phase stabilization for the kagome lattice and not for the triangular or honeycomb lattices. A more detailed description of the phase locking protocol can be found in [140].

**Kapitza-Dirac scattering** For Kapitza-Dirac scattering we suddenly enable selected lattice beams at our desired lattice depths. Our lattice beam intensity stabilization loops typically have rise times of  $1\ \mu\text{s}$ - $1.5\ \mu\text{s}$ , which is not ideal for creating sharply bounded, rectangular pulses. The AOMs we use for intensity stabilization have rise times of  $\sim 100\ \text{ns}$ . To reduce our switch on and switch off times we use a sample & hold scheme. The PI controllers are connected to the AOM RF amplifiers via a sample & hold circuit (see chapter 4). We switch on the lattices during optical transport to the lattice powers we use for Kapitza-Dirac and engage the hold of the sample & hold board. This ‘stores’ the voltage that the PI controller supplies to the RF amplifier. The RF amplifier is now fed from this stored voltage and the PI controller is taken out of the control loop. After sampling and holding we switch off the lattice beams by switching off the RF source (usually a DDS). The sequence then proceeds through dipole trap loading, evaporation and BEC creation as described above. For the Kapitza-Dirac pulse we reenable the RF source of the AOMs, which causes the lattice power to rise to the sampled value within the rise time of the AOM. There is an additional delay of  $\sim 1\ \mu\text{s}$  due to the time it takes for the acoustic wave to travel from the transducer to the laser beam in the AOM crystal. We advance the RF switch-on and switch-off to take out this delay. Fig. 5.17 shows the behaviour of key channels during our Kapitza-Dirac sequence.

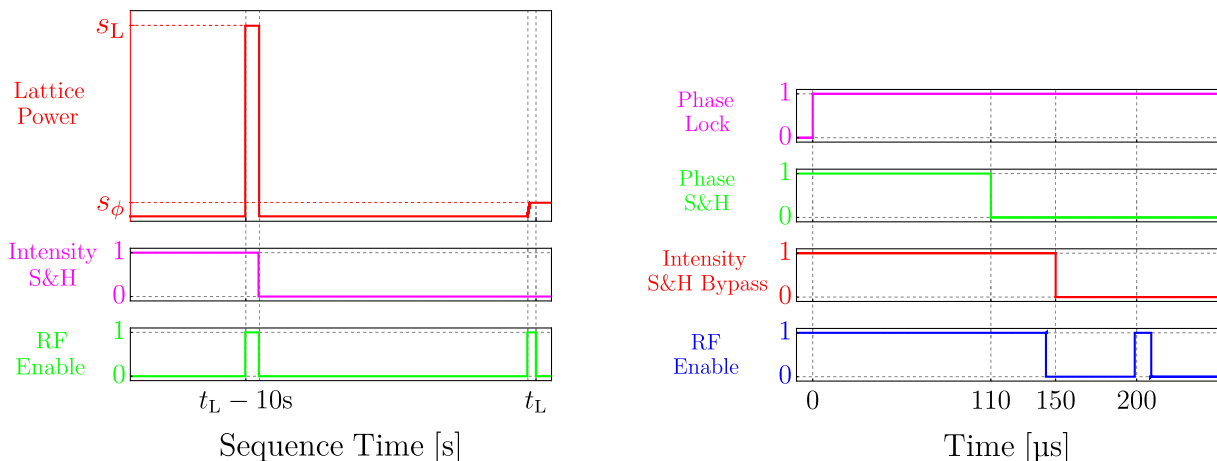


**Figure 5.17** – Key channels during the Kapitza-Dirac sequence showing both intensity (left) and phase (right) sample & hold protocols.  $t_L$  marks the time at which the phase lock is engaged. For the right plot,  $t_L = 0$ .

**Phase stabilization** Similarly to the adiabatic case, we need to engage phase stabilization for Kapitza-Dirac in 1D superlattices and the kagome lattice. We make extensive use of Kapitza-Dirac scattering with 1D superlattices to monitor and correct the relative

phase between the 532 nm and 1064 nm lattices. To stabilize the phase for Kapitza-Dirac with a superlattice we ramp up the lattice beams over 100 ms to a small depth and engage the phase lock PI controller. The sequence for this is somewhat tricky since we need to be able to bypass the sample & hold circuit to ramp up the lattice for phase locking before the actual Kapitza-Dirac pulse happens. 200  $\mu\text{s}$  before the Kapitza-Dirac pulse is triggered, the phase lock is engaged. 110  $\mu\text{s}$  later, the phase is sampled via the sample & hold circuit on the phase stabilization box (see [140]). At this point the piezo voltage is kept constant and is not being actively actuated to stabilize the phase. We do not notice any phase drift in the 90  $\mu\text{s}$  between holding the piezo voltage and the start of the KD pulse.

The RF is disabled after the phase has been sampled and the intensity sample & hold boxes are switched from bypass mode back to hold mode 50  $\mu\text{s}$  before the RF is enabled for the Kapitza-Dirac pulse. Fig. 5.17 shows a schematic of the relevant channels and sequence of events for Kapitza-Dirac with a superlattice.

## 5.8 Negative temperature protocol

As shown in Fig. 5.18 the negative temperature protocol proceeds through four stages (I-IV). After creating a BEC and ramping up the dipole trap power, we increase the scattering length to  $\sim 300 a_0$ . We then ramp up the triangular or kagome lattice to  $\sim 18E_R$  which is well above the superfluid to Mott insulator transition (see chapter 7).

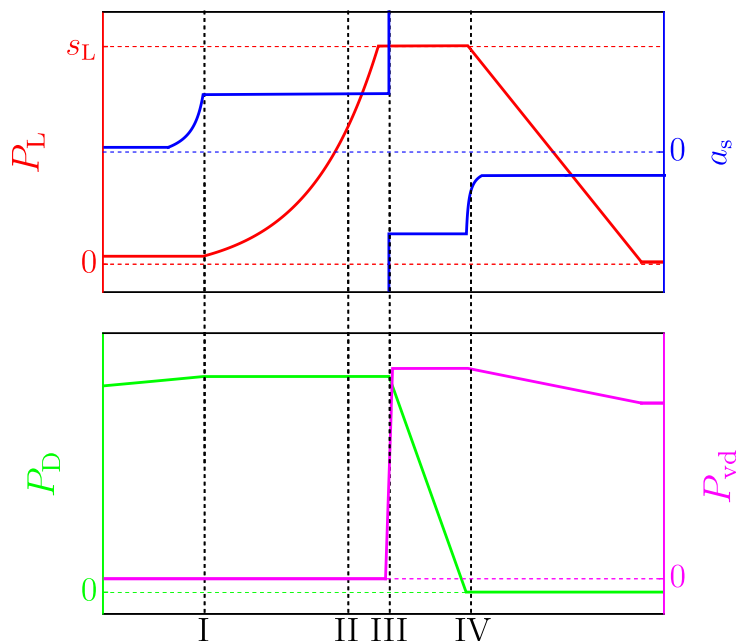


**Figure 5.18** – Negative temperature sequence.  $P_L$ ,  $a_S$ ,  $P_D$  and  $P_{vd}$  denote the lattice depth, scattering length, dipole beam power and vertical dipole power, respectively. Roman numerals correspond to steps in the negative temperature protocol (see Fig. 3.2). I: positive temperature superfluid, II: positive temperature Mott Insulator, III: negative temperature Mott Insulator, IV: negative temperature superfluid.

In the Mott insulator stage we suddenly change the Feshbach coil current from below to above the Feshbach resonance, thereby changing the scattering length from  $\sim 300 a_0$  to

$\sim -300 a_0$ . We also ramp up the vertical dipole beam in 2 ms to create an anti-confining potential. With this we have prepared the highest energy state of the system and just need to melt the Mott insulator to end up with a negative temperature superfluid. To this end, we ramp the scattering length to  $\sim -50 a_0$  and lower the lattice depth to  $\sim 6 E_R$ . The negative temperature protocol is schematically drawn in Fig. 5.18.

Fig. 5.19 shows the evolution from Mott insulator to negative temperature superfluid in the triangular lattice in momentum space. As the lattice depth ( $s_S$ ) is reduced, the central region of the Brillouin zone is depleted and atoms start to predominantly occupy the corners and edges.

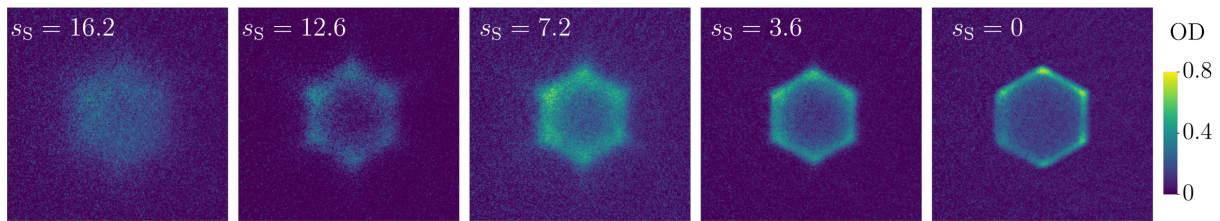


**Figure 5.19** – Melting a  $^{39}\text{K}$  Mott insulator to a negative temperature state in the triangular lattice. Images are taken after 11 ms of TOF.

We find that we can get negative temperature states even without using the vertical dipole beam. We have yet to conclusively determine the effect of the vertical dipole beam on the lifetime of the negative temperature state.

## 6 Alignment and calibration

Since our quantum simulator is designed to implement the Hubbard model, it is imperative that we know how the Hubbard parameters (‘model parameters’) depend on quantities we can program via the timing system (‘machine parameters’). In [section 2.5](#) and [section 2.6](#) we calculated Hubbard  $t$  and  $U$  as a function of lattice depth, which we expressed in units of the recoil energy. However, in practice we have control over the lattice beam power. Thus, we need to find the relationship between beam power and lattice depth to be able to compare theory with experiment. Similarly, we calibrate the scattering length as a function of Feshbach coil current, and the trap frequencies (confinement) as a function of dipole trap and lattice powers. This chapter covers our procedure for aligning the lattice beams and calibrating these parameters of the kagome quantum simulator.

### 6.1 Lattice beam alignment

On each axis, the respective 532 nm and 1064 nm lattice beams are overlapped before entering the science chamber. We therefore only need to align one of the colours to the atoms and the other colour should be automatically aligned as well. In practice we see that this is indeed the case.

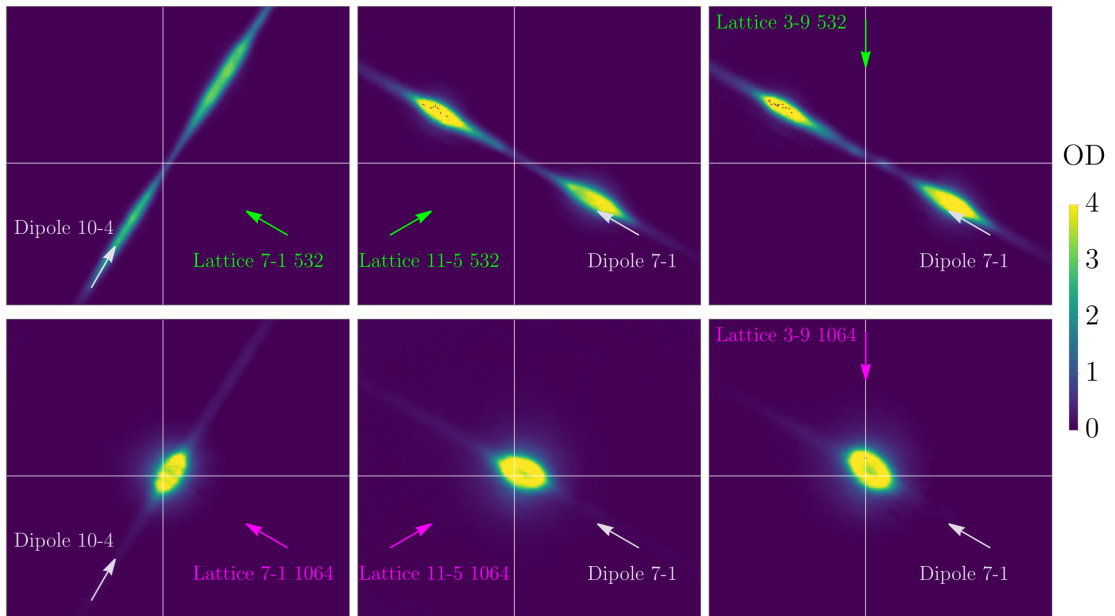


**Figure 6.1** – Alignment of lattice beams onto  $^{87}\text{Rb}$  atoms trapped in a single beam of the dipole trap. The single 532 nm lattice beams split the cloud (top) in a single dipole trap beam, while single 1064 nm lattice beams create a dipole trap when overlapped with one of the dipole trap beams. Note that because the 7-1 dipole and 7-1 lattice beams are co-propagating, we choose to overlap the 7-1 lattice beams with atoms in the dipole 10-4 beam for alignment. The white lines in each plot show the position of the  $^{87}\text{Rb}$  BEC in the crossed dipole trap.

We prioritize the alignment of the 532 nm lattice since achieving a high lattice depth

for 532 nm is critical for the microscope<sup>103</sup>. Each pair of lattice beams can be precisely aligned with piezo-actuated mirror mounts<sup>104</sup>. We align the 532 nm beams to the atoms in two steps. We first try to split a  $^{87}\text{Rb}$  cloud in a single beam of the dipole trap with each 532 nm lattice beam<sup>105</sup> (see Fig. 6.1). To load only a single beam of the dipole trap, we first evaporate in the dipole trap and then ramp one of the dipole trap beams to zero power. We image the atomic cloud in-situ along the vertical direction.

We initially found that the two colours on one axis were not well overlapped at the position of the atoms<sup>106</sup>. We managed to fix this by walking the doublet and one of the mirrors in the lattice beam path (see Fig. 4.12 for a layout of the lattice beam optics). Thus, we can independently move the 532 nm and 1064 nm lattice beams with respect to each other if necessary.

To fine-align the lattice beams to the  $^{39}\text{K}$  BEC, we split the BEC with each 532 nm lattice beam and ensure the cloud is split evenly (see Fig. 6.2).

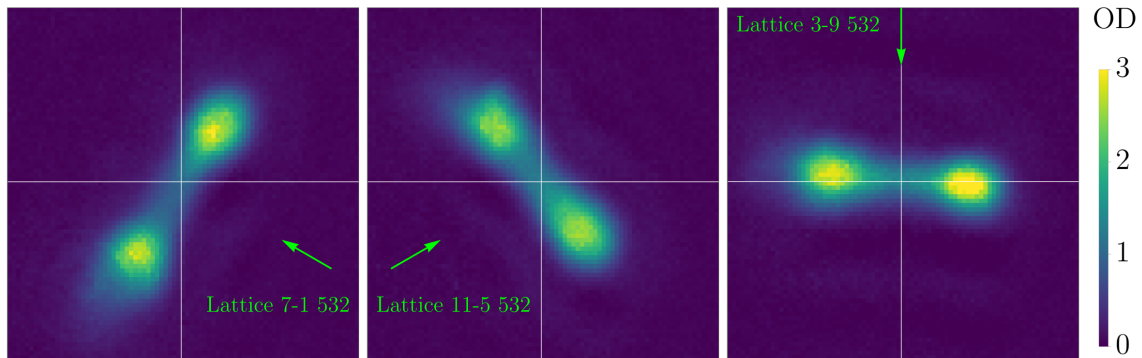


**Figure 6.2** – Final alignment of 532 nm beams onto  $^{39}\text{K}$  BEC. Each 532 nm beam splits the BEC into two equally sized parts. The white lines indicate the position of the  $^{39}\text{K}$  BEC when no lattice beams are enabled.

We align the vertical lattice by ensuring that the BEC is in the same place in the horizontal plane with and without the vertical lattice. Once the lattice beams are aligned we can proceed to calibrate the lattice depths of each of the seven lattice beams.

## 6.2 Lattice depth & phase (Kapitza-Dirac)

Kapitza-Dirac (KD) scattering is a simple and powerful method to calibrate lattice depths and is widely used in optical lattice experiments [151, 176, 213]. The protocol requires the initial preparation of a BEC. We subject the BEC to a pulse of lattice light for a few  $\mu\text{s}$ , which causes diffraction into higher momentum states. The exact distribution among the momentum states depends on the length and intensity of the pulse, allowing us to

<sup>103</sup>We also require more 532 nm power, compared to 1064 nm, to reach the same lattice depth.

<sup>104</sup>Newport 8821.

<sup>105</sup>Since 532 nm is blue-detuned with respect to the D1 and D2 transitions of  $^{87}\text{Rb}$  and  $^{39}\text{K}$ , atoms are repelled from regions of high-intensity.

<sup>106</sup>This was the first lattice axis we built. For the other lattice axes, we refined our alignment method and found that the colors were well overlapped at the atoms.

accurately calibrate each lattice beam. This technique is analogous to scattering of light off a diffraction grating, with the atoms playing the role of light and the lattice the role of the grating [214].

We use KD scattering to calibrate our vertical lattice, the 532 nm and 1064 nm lattices separately and to measure the relative phase between the 532 nm and 1064 nm lattices.

### Vertical lattice

**Theory** The Hamiltonian for a particle with momentum  $q$  and mass  $m$  in a 1D lattice with lattice depth  $V_0$  is given by

$$H(q) = \frac{\hbar^2 q^2}{2m} + V_0 \cos^2(kz), \quad (6.1)$$

where  $k$  is the lattice beam wavevector and  $z$  is the position. This Hamiltonian is commonly expressed in units of the recoil energy,  $E_R = \frac{\hbar^2 k^2}{2m}$ ,

$$\frac{1}{E_R} H(q) = \frac{q^2}{k^2} + \frac{s_0}{4} (2 + e^{2ikz} + e^{-2ikz}), \quad (6.2)$$

where

$$s_0 = \frac{V_0}{E_R} \quad (6.3)$$

is the lattice depth in units of  $E_R$ . It is straightforward to see that the lattice potential couples different plane-wave states by recognizing that

$$e^{i\mu z} |\lambda\rangle = |\lambda + \mu\rangle, \quad (6.4)$$

where  $|\lambda\rangle$  is a plane-wave state with momentum  $\lambda$ . If we assume that the system is prepared at  $q = 0$ , then the Hamiltonian can be expanded in the momentum basis  $|2n\hbar k\rangle$  ( $n \in \mathbb{Z}$ ), where  $n$  is the diffraction order,

$$H_{n,m} = 4n^2 \delta_{n,m} + \frac{s_0}{4} (\delta_{n,m+1} + \delta_{n,m-1}). \quad (6.5)$$

**Experiment** We apply the vertical lattice KD pulse to the BEC in the dipole trap. After the KD pulse is complete, the dipole trap is switched off and we wait  $\sim 25$  ms (TOF) before taking an image along the horizontal direction. During this time the different momentum states (diffraction peaks) separate in space. Fig. 6.3 shows experimental data and a least-squares fit of KD diffraction peak population as a function of vertical lattice pulse duration.

For a retro-reflected lattice, the lattice depth in units of  $E_R$  and the lattice beam power are related by

$$s_0 = \frac{V_0}{E_R} = \frac{1}{E_R} \times 4 \times \frac{2U_0}{\pi w_0^2} \times P. \quad (6.6)$$

Here,  $U_0$ ,  $w_0$ , and  $P$  are the light shift per unit intensity at the lattice wavelength, the beam waist (assuming a circular beam), and the lattice beam power, respectively<sup>107</sup>. The lattice depth thus scales linearly with lattice power and we can convert vertical lattice power (machine parameter) to lattice depth in units of  $E_R$  (model parameter).

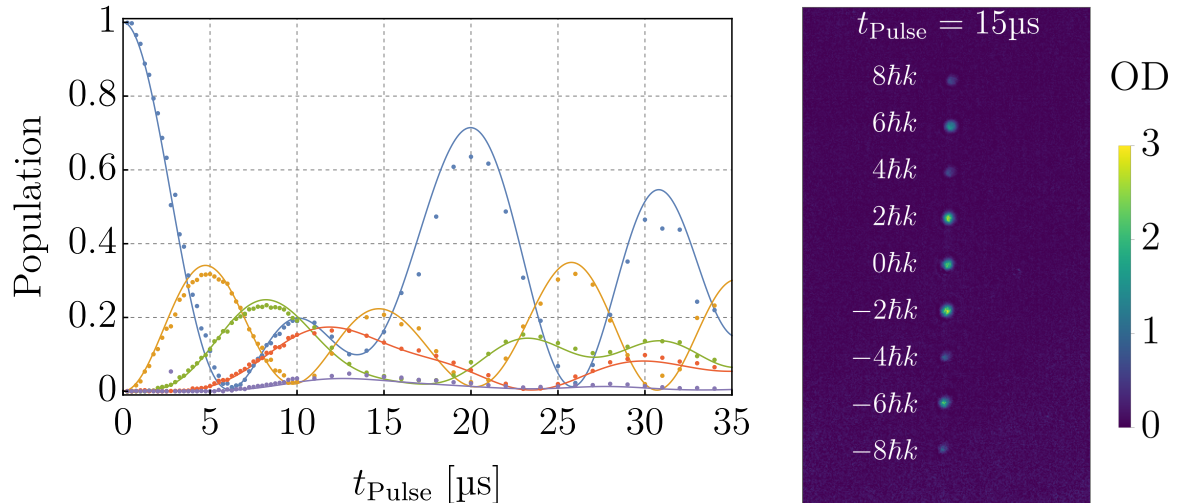


**Figure 6.3** – KD scattering of  $^{87}\text{Rb}$  in the vertical lattice. Left: normalized population in different diffraction orders (averaged over positive and negative orders) as a function of pulse duration. Blue is the zeroth order population and yellow, green, red, and purple are the average of  $\pm 2\hbar k$ ,  $\pm 4\hbar k$ ,  $\pm 6\hbar k$ , and  $\pm 8\hbar k$  diffraction peak populations, respectively. Dots indicate experimentally determined populations; lines are theory curves for a lattice depth of  $61.7 E_R$ . Right: KD image at  $15 \mu\text{s}$ . We use images like this to extract the population in different diffraction orders. Different diffraction orders have different momentum and are thus separated after TOF.

**Triangular & honeycomb lattices** Several different conventions can be used to quantify the depth of a triangular lattice. One convention is to equate the lattice depth with the difference between the maximum and minimum value of the optical lattice potential [36, 151]. This form is convenient because it normalizes the lattice potential and is simple to understand. However, it cannot be used to express lattices for which the lattice intensities are unequal. It also does not easily connect to our timing script since we define the powers of each beam individually. We therefore decided to define the individual lattice depths of the three lattice beams (similarly to [34, 90]). This means that our calibrations are more directly related to what we program and that we can also easily handle imbalanced lattices.

We calibrate the depth of the three lattice beams forming one triangular lattice<sup>108</sup> by taking three KD measurements, one with each pair of beams. Note that ‘lattice depth’ is not a well-defined quantity for single beams in an interfering lattice since any single beam does not form a lattice. ‘Depth’ is used as a way to express the beam intensity.

<sup>107</sup>The additional factor of 4 is due to the peak intensity of the retro-reflected lattice being 4 times the peak intensity of a single beam.

<sup>108</sup>We will refer to both the 532 nm triangular and 1064 nm honeycomb lattice as ‘triangular lattices’.

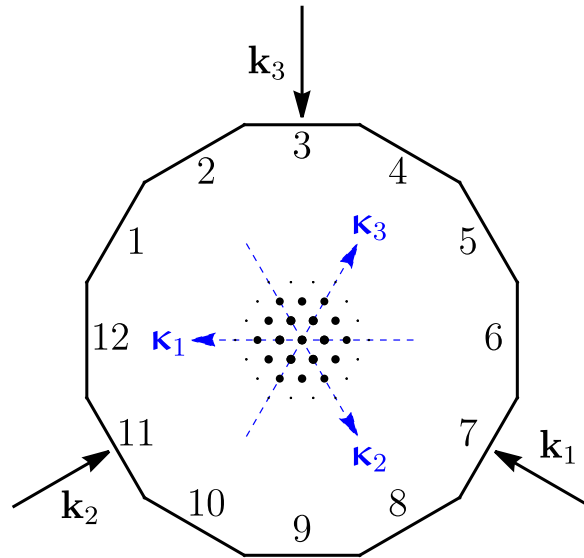


**Figure 6.4** – Schematic of KD scattering with either the triangular or honeycomb lattice in the science chamber. Vectors and diffraction pattern are not to scale. Atoms get scattered along the vectors  $\{\kappa_j\}$ , defined in Eq. 2.4.

Assuming the lattice wavevectors to be as in Eq. 2.2 (see also the arrangement in Fig. 6.4), we can write the intensity distribution created by the interference of lattices 1 & 2 as<sup>109</sup>

$$I_{12} = I_1 + I_2 - \sqrt{I_1 I_2} \cos(\sqrt{3}kx). \quad (6.7)$$

The 1D lattice potential is thus

$$V_{12} = -2U_0 \sqrt{I_1 I_2} \cos^2\left(\frac{\sqrt{3}}{2}kx\right), \quad (6.8)$$

where  $U_0$  is the light shift per unit intensity. Constant energy terms were omitted. Eq. 6.8 can be rewritten in units of  $E_R$ ,

$$\begin{aligned} V_{12} &= -\frac{2U_0 \sqrt{I_1 I_2}}{\underbrace{\frac{\hbar^2 \left(\frac{\sqrt{3}}{2}k\right)^2}{2m}}_{s_{\text{int}}}} \underbrace{\frac{\hbar^2 \left(\frac{\sqrt{3}}{2}k\right)^2}{2m}}_{E_R^{\text{int}}} \cos^2\left(\frac{\sqrt{3}}{2}kx\right) \\ &= s_{\text{int}} E_R^{\text{int}} \cos^2(k_{\text{int}}x), \end{aligned} \quad (6.9)$$

where  $k_{\text{int}} = \frac{\sqrt{3}}{2}k$ . This is the familiar form of 1D lattices that we also encountered for the vertical lattice and we can use this expression to straightforwardly determine the lattice depth of a 1D lattice in units of  $E_R^{\text{int}}$ .

<sup>109</sup>We refer to the 7-1, 11-5, and 3-9 lattice beam as lattice 1, 2, and 3, respectively.

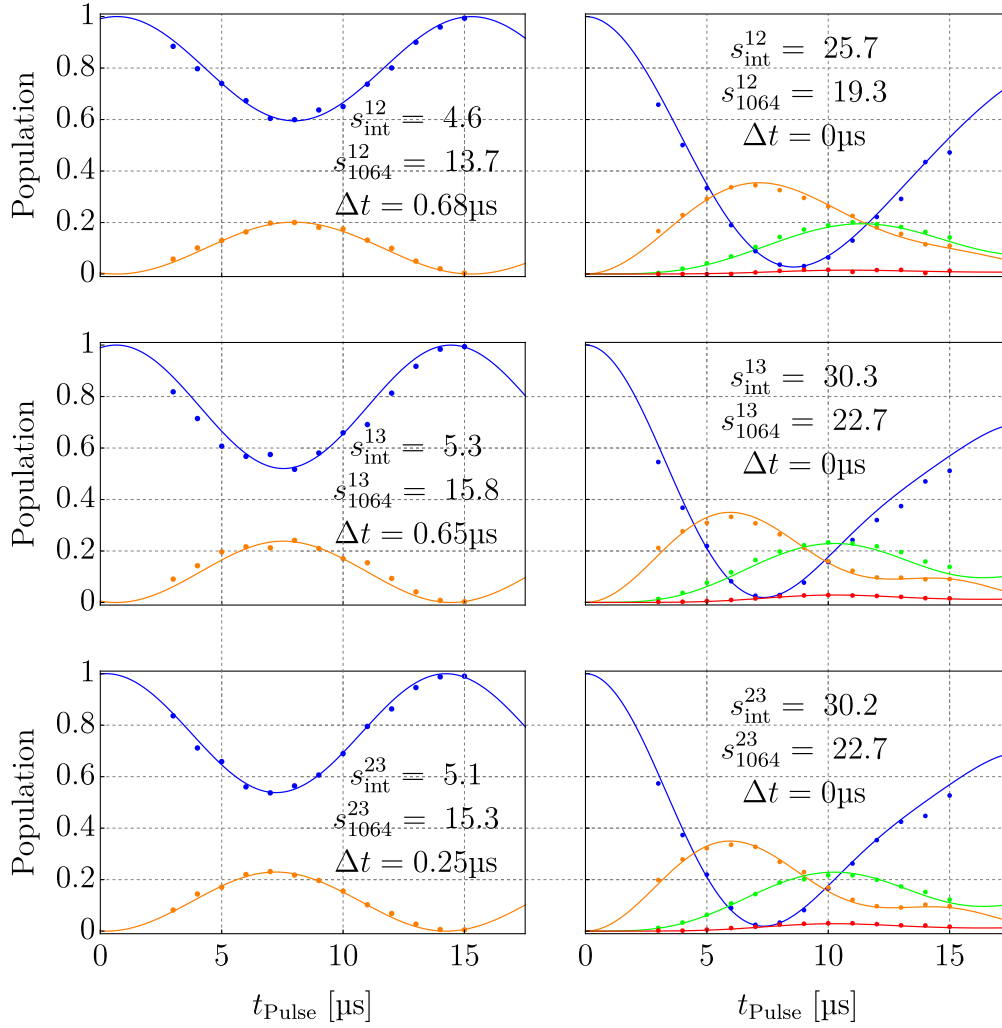


**Figure 6.5** – KD traces of 532 nm (left) and 1064 nm (right) 1D lattices for  $^{39}\text{K}$  at programmed beam powers of 400 mW and 200 mW, respectively. Blue, orange, green, and red points (lines) are experimental data (theoretical fits) for the 0<sup>th</sup> ( $0\hbar k_{\text{int}}$ ), 1<sup>st</sup> ( $\pm 2\hbar k_{\text{int}}$ ), 2<sup>nd</sup> ( $\pm 4\hbar k_{\text{int}}$ ), and 3<sup>rd</sup> ( $\pm 6\hbar k_{\text{int}}$ ) diffraction orders, respectively. We choose the lattice depth ( $s_{\text{int}}$ ) and a time delay ( $\Delta t$ ) as free parameters for the fits. For 532 nm, a small delay in the fit ensures that the fit overlaps with the data.  $s_{1064}^{ij}$  is defined in Eq. 6.11.

Since we have two triangular lattices with different wavelengths, we also have to decide which units we want to use to express our lattice depths. In this case there are again multiple different definitions we can choose from:

1. Define the lattice depth in terms of the wavelength of the lattice. This means that  $E_{\text{R}}$  would have a different magnitude for the 532 nm and 1064 nm triangular lattices.
2. Define the lattice depth in terms of the 1D lattice spacing of a 1D lattice. This makes the evaluation of 1D lattice KD data very simple, but  $E_{\text{R}}$  is different for different lattice wavelengths.
3. Define all lattice depths in units of a  $E_{\text{R}}$  at one wavelength. This makes the comparison of lattice depths between different triangular lattices straightforward. However,

the wavelength with which  $E_R$  is defined may be different from the wavelength of the lattice.

We chose the third approach, i.e. we express all our lattice depths in units of

$$E_R^{1064} = \frac{\hbar^2}{2m} \left( \frac{2\pi}{\lambda} \right)^2, \quad (6.10)$$

where  $m$  is the mass of the atomic species and  $\lambda = 1064$  nm. After extracting  $s_{\text{int}}$  from the 1D KD traces, we calculate the lattice depth in units of  $E_R^{1064}$  via

$$s_{1064}^{ij} = s_{\text{int}}^{ij} \frac{E_R^{\text{int}}}{E_R^{1064}}, \quad (6.11)$$

where  $i$  and  $j$  label the two lattice beams involved in the relevant 1D lattice. Note that  $E_R^{\text{int}}$  is different for the 532 nm triangular and 1064 nm honeycomb lattice. For the 532 nm triangular lattice and 1064 nm honeycomb lattice,  $s_{1064}^{ij} = 3s_{\text{int}}^{ij}$  and  $s_{1064}^{ij} = \frac{3}{4}s_{\text{int}}^{ij}$ , respectively. Fig. 6.5 shows data from a typical calibration run.

**Total lattice potential** From the above considerations we can see that

$$2U_0\sqrt{I_i I_j} = s_{1064}^{ij} E_R^{1064}. \quad (6.12)$$

The total triangular lattice potential can therefore be written as

$$\begin{aligned} V_{\text{tot}} &= -U_0 \left\{ \sqrt{I_1 I_2} \cos((\mathbf{k}_1 - \mathbf{k}_2) \cdot \mathbf{r}) + \sqrt{I_1 I_3} \cos((\mathbf{k}_3 - \mathbf{k}_1) \cdot \mathbf{r}) \right. \\ &\quad \left. + \sqrt{I_2 I_3} \cos((\mathbf{k}_2 - \mathbf{k}_3) \cdot \mathbf{r}) \right\} \\ &= \pm \frac{E_R^{1064}}{2} \left\{ s_{1064}^{12} \cos((\mathbf{k}_1 - \mathbf{k}_2) \cdot \mathbf{r}) + s_{1064}^{13} \cos((\mathbf{k}_3 - \mathbf{k}_1) \cdot \mathbf{r}) \right. \\ &\quad \left. + s_{1064}^{23} \cos((\mathbf{k}_2 - \mathbf{k}_3) \cdot \mathbf{r}) \right\}, \end{aligned} \quad (6.13)$$

where  $U_0 > 0$  ( $U_0 < 0$ ) for 532 nm (1064 nm) in the first line and  $-$  ( $+$ ) for 532 nm (1064 nm) in the second line. If all lattice depths are equal, i.e.  $s_{1064}^{12} = s_{1064}^{13} = s_{1064}^{23} = s_{1064}$ , the resulting potential forms a symmetric triangular (honeycomb) lattice where the difference between maximum and minimum energy is

$$V_{\text{max}} - V_{\text{min}} = \frac{9}{4} s_{1064} E_R^{1064}. \quad (6.14)$$

This last expression can be used to convert between our units ( $s_{1064}$ ) and the units used in [36, 151] ( $V_{\text{max}} - V_{\text{min}}$ ). For the remainder of this thesis we will only refer to  $E_R := E_R^{1064}$ .

<sup>110</sup>We already implicitly did this when we derived the band structure in section 2.3.

**Kagome lattice** Combining the 532 nm triangular and 1064 nm honeycomb lattices results in a six beam superlattice. As we showed in [section 2.2](#), the relative phases between the short (532 nm) and long (1064 nm) wavelength lattices determine the superlattice potential. To ensure that we reproducibly create a kagome lattice, we need to have a way of measuring what potential the atoms are experiencing. KD diffraction fortunately also gives us information about the superlattice potential. [Fig. 6.6](#) shows three KD diffraction images for which the relative phases of the superlattice are not stabilized.

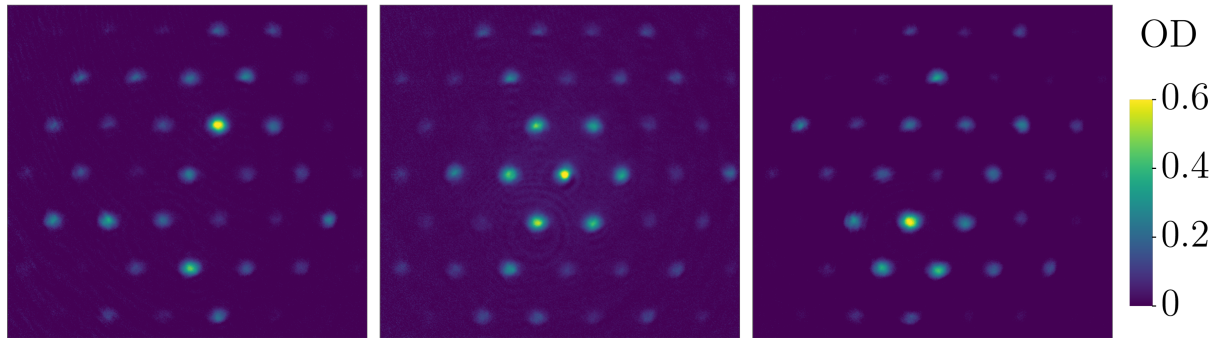


**Figure 6.6** – Different shots of KD diffraction of  $^{87}\text{Rb}$  in the unstabilized superlattice formed of the 532 nm triangular and 1064 nm honeycomb lattices. The four phase degrees of freedom fluctuate in between shots, leading to different KD diffraction patterns.

When the phases are not stabilized, the diffraction pattern changes from shot to shot. This is in contrast to diffraction patterns obtained with the triangular and honeycomb lattices individually, which are only affected by the lattice intensities, not the lattice phases. Since phase information is imparted onto the KD images of the superlattice, it is possible to extract the lattice phases and correct for any relative phase shifts.

To understand how the lattice phases play a role in KD diffraction it is instructive to look at a single 1D superlattice,

$$V(x) = V_S \cos^2(2kx) + V_L \cos^2\left(kx + \frac{\phi}{2}\right). \quad (6.15)$$

For the 1D superlattice, the KD Hamiltonian can be written as

$$H_{n,m} = 4n^2\delta_{n,m} + \frac{s_S}{4}(\delta_{n,m+2} + \delta_{n,m-2}) + \frac{s_L}{4}(e^{-i\phi}\delta_{n,m+1} + e^{i\phi}\delta_{n,m-1}), \quad (6.16)$$

where  $s_S$  and  $s_L$  are the lattice depths of the short and long lattice in units of  $E_R$ , respectively.

The population of  $|1\rangle = |2\hbar k\rangle$  is given by

$$\begin{aligned}
p_1 &= |\langle 1 | e^{-iHt} | 0 \rangle|^2 \\
&= \left| \langle 1 | \left( 1 - iHt + \frac{(iHt)^2}{2} + \mathcal{O}(t^3) \right) | 0 \rangle \right|^2 \\
&= \left| \underbrace{\langle 1 | 0 \rangle}_0 - it \underbrace{\langle 1 | H | 0 \rangle}_{\frac{s_L}{4} e^{i\phi}} - \frac{t^2}{2} \underbrace{\langle 1 | H^2 | 0 \rangle}_{s_L e^{i\phi} + \frac{s_L s_S}{8} e^{-i\phi}} + \mathcal{O}(t^3) \right|^2 \\
&= \frac{s_L^2}{16} t^2 - \frac{1}{32} s_L^2 s_S \sin(2\phi) t^3 + \mathcal{O}(t^4).
\end{aligned} \tag{6.17}$$

This shows that the population of the first order diffraction peaks depends on the relative phase of the 532 nm and 1064 nm lattices. The interference term vanishes if either of the lattices is switched off. The occupation of  $|-1\rangle = |-2\hbar k\rangle$ ,  $p_{-1}$ , can be calculated analogously to Eq. 6.17, so that

$$p_1 - p_{-1} = -\frac{1}{16} s_L^2 s_S \sin(2\phi) t^3 + \mathcal{O}(t^5). \tag{6.18}$$

Thus, we can measure the relative phase between the 532 nm and 1064 nm lattices by measuring the difference in occupation between the  $|1\rangle$  and  $|-1\rangle$  orders. To be insensitive to atom number fluctuations, we work with the imbalance between  $\pm 1$  orders, i.e.  $(p_1 - p_{-1})/(p_1 + p_{-1})$ .

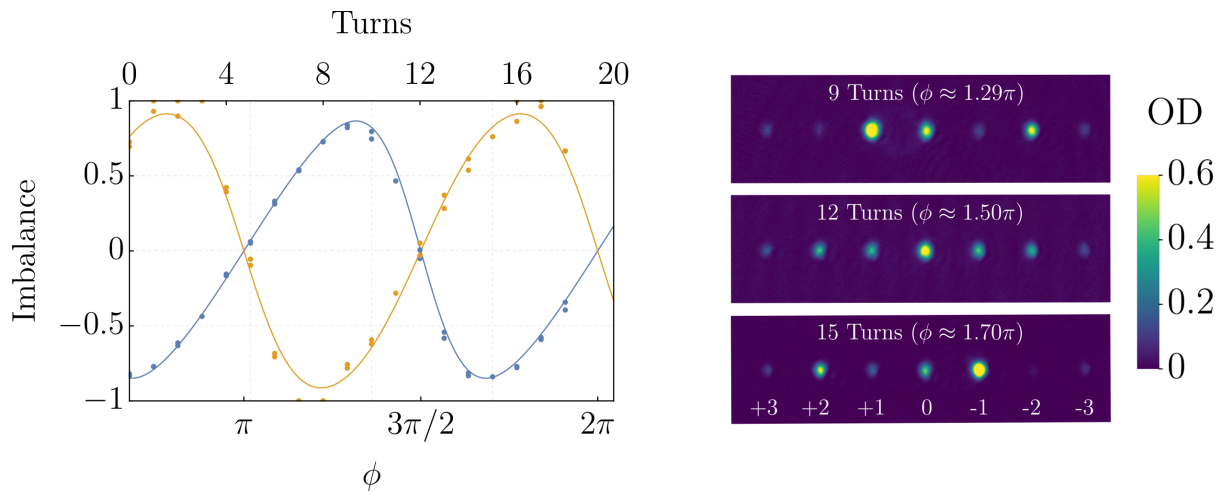


**Figure 6.7** – Left: imbalance of KD diffraction orders as a function of the wedge position/phase. Blue (yellow) points: imbalance between  $\pm 1$  ( $\pm 2$ ) orders. Lines are theoretically calculated curves for  $s_S = 12$  and  $s_L = 14.5$ . The phase changes by  $0.068\pi$  per turn (of the translation stage actuator). Since this data was taken we installed a motorized linear translation stage. Right: KD images at 9, 12, and 15 turns. The imbalance between the  $\pm 1$  and  $\pm 2$  diffraction orders visibly changes when we move the wedge. Note that we actively stabilize the phase for this data and rely on passive phase stability on the transfer path for shot-to-shot reproducibility.

We control the relative phases using moveable glass wedges in the transfer paths (see section 4.3.5). Fig. 6.7 shows the imbalance in a 1D superlattice as a function of the wedge

position. We numerically calculate the population in all diffraction orders as a function of phase, lattice depth, and KD pulse duration, which allows us to fit experimental KD data. We use our numerically calculated KD distribution to determine the pulse duration at which the first order population is most sensitive to phase and adjust the wedge at this pulse duration. When phase stabilization is engaged, the relative phases are fixed. We cannot currently change the relative phases during the sequence.

### 6.3 Calibration of Feshbach coil current

With a calibration of the lattice depth, we can precisely determine the shape of the lattice potential and can calculate the tunnelling energy  $t$ . To calculate the interaction strength in the lattice, we additionally need to know the scattering length, which is a function of the Feshbach field. Hubbard  $U$  depends linearly on the scattering length and scales roughly as the square root of the lattice depth. The Feshbach field is proportional to the Feshbach coil current (our machine parameter).

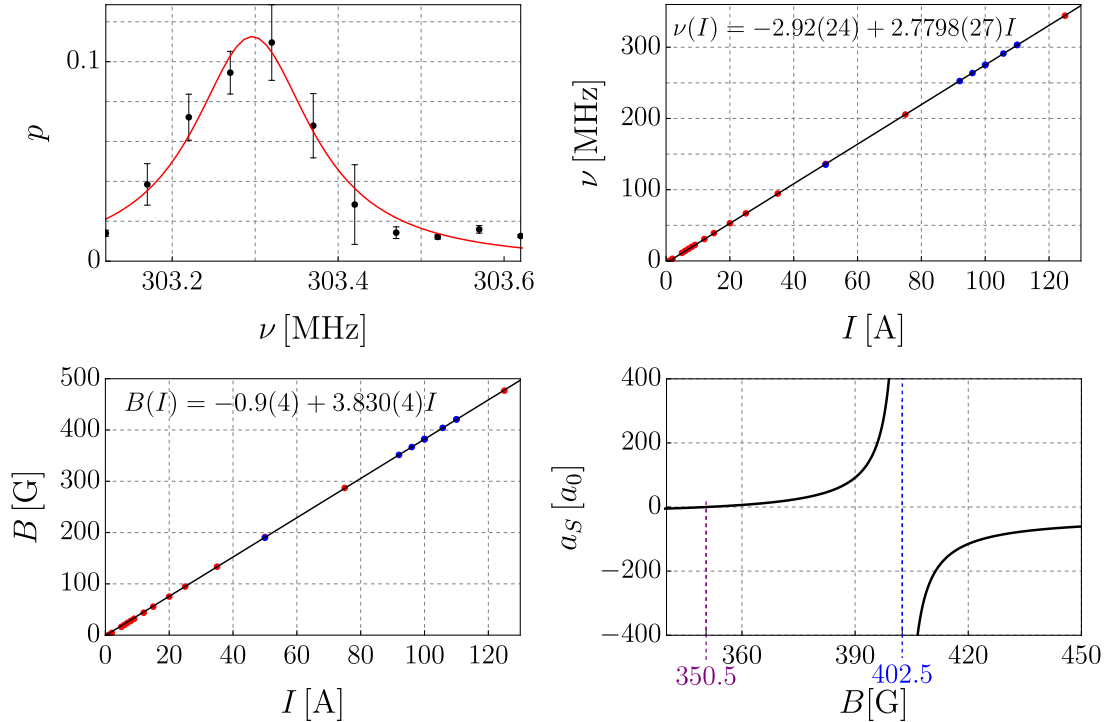


**Figure 6.8** – Top left: RF transfer efficiency ( $p$ ) vs RF frequency ( $\nu$ ) at a Feshbach coil current ( $I$ ) of 110 A. The red line shows a Lorentzian fit. The RF frequency is kept constant for 500 ms for each data point. The efficiency is broadened due to Feshbach coil current fluctuations. Top right: transition frequency ( $f$ ) of the  $|F = 1, m_F = -1\rangle \rightarrow |F = 1, m_F = 0\rangle$  transition in  $^{87}\text{Rb}$  as a function of Feshbach coil current. Blue points show the centre of a Lorentzian fit to transfer efficiency vs RF frequency data. Red points are obtained by finding the frequency at which we get maximum population transfer with LZ sweeps over a 500 kHz-wide window; the resonance is assumed to be in the centre of the LZ window. Bottom left: magnetic field ( $B$ ) vs Feshbach coil current. Bottom right: scattering length ( $a_S$ ) of  $^{39}\text{K}$  as a function of magnetic field.

We calibrated the Feshbach coils by finding the transition frequency of the  $|F = 1, m_F = -1\rangle \rightarrow |F = 1, m_F = 0\rangle$  transition in  $^{87}\text{Rb}$  for different Feshbach coil currents and compared this with the theoretically expected frequency (see Fig. 6.8). We drive the transition with RF radiation and measure the fraction of atoms in the  $|F = 1, m_F = 0\rangle$  state after a short Stern-Gerlach pulse. The resonance frequencies are then converted to magnetic fields via the theoretically calculated Zeeman splitting as a function of magnetic field. This gives us an accurate calibration of magnetic field vs Feshbach coil current.

## 6.4 Trap frequency measurements

The last parameter in the Hubbard model left to calibrate is the potential energy (or confinement). For small distances around the centre of the lattice, confinement can be considered harmonic, i.e. we can quantify confinement by a trap frequency. The dipole trap, vertical dipole, and the honeycomb, triangular, and vertical lattices all contribute to confinement and the total trap frequency ( $\omega_{\text{tot}}$ ) is generally a complicated function of five machine parameters: The dipole trap power, vertical dipole power, and the three lattice powers,

$$\omega_{\text{tot}} = \sqrt{\omega_{\text{hon}}^2 + \omega_{\text{vert}}^2 + \omega_{\text{cd}}^2 - \omega_{\text{tri}}^2 - \omega_{\text{vd}}^2}, \quad (6.19)$$

where  $\omega_{\text{tri}}$ ,  $\omega_{\text{hon}}$ ,  $\omega_{\text{vert}}$ ,  $\omega_{\text{cd}}$ , and  $\omega_{\text{vd}}$  are the trap frequencies of the triangular lattice, honeycomb lattice, vertical lattice, crossed dipole trap, and vertical dipole, respectively<sup>111</sup>.

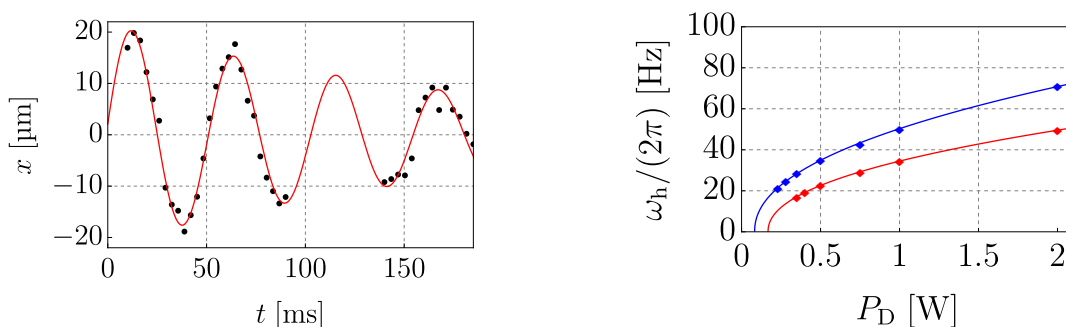


**Figure 6.9** – Horizontal trap frequencies in the dipole trap. Left: horizontal oscillations of  $^{87}\text{Rb}$  in the dipole trap at 0.4 W (programmed).  $x$  is the horizontal position of the atomic cloud and  $t$  is the oscillation duration. The red line is a sinusoidal fit used to extract the horizontal trap frequency,  $\omega_h/(2\pi)$ . Right: red (blue) diamonds show the measured trap frequencies for  $^{87}\text{Rb}$  and  $^{39}\text{K}$ , respectively, as a function of dipole trap power ( $P_D$ ). The solid lines are fits of the form  $a(P - P_0)^\alpha$ , where  $a$ ,  $P_0$ , and  $\alpha$  are fit parameters<sup>112</sup>.  $\alpha \approx 0.46$  for both species.

In practice, one of the trap frequencies in Eq. 6.19 usually dominates and we can neglect the other contributions. We are also usually only interested in the horizontal trap frequency<sup>113</sup>. Trap frequencies are commonly measured by inducing oscillations in the

<sup>111</sup>Note that  $\omega_{\text{tri}}^2$  and  $\omega_{\text{vd}}^2$  are subtracted, since the triangular lattice and vertical dipole potentials are anti-confining.

<sup>112</sup>We can use this fit to express the dipole trap power in terms of trap frequency in the lattice scripts.

<sup>113</sup>For most experiments the vertical direction is frozen out due to the vertical lattice.

atomic cloud (e.g. by suddenly moving the cloud or the trap) and recording the subsequent oscillatory motion as a function of oscillation duration. For all lattices, the lattice depth and trap frequency cannot be decoupled as they both depend on power. However, the dipole trap and vertical dipole beam can be used to tune the trap frequency independently of lattice parameters. We will thus restrict ourselves to trap frequencies in the crossed dipole trap.

Fig. 6.9 shows the horizontal trap frequency of  $^{87}\text{Rb}$  and  $^{39}\text{K}$  in the dipole trap as a function of dipole trap power. We start from a BEC and induce oscillations by quickly ( $\sim 5$  ms) ramping up the dipole trap to the desired power. We then hold the cloud in the dipole trap for a variable amount of time during which the cloud oscillates. Finally, the cloud is released and the cloud's horizontal position is recorded after TOF. The trap frequency changes roughly as the square root of power.

Similar methods can be used to determine the trap frequencies of the lattices and the vertical dipole beam<sup>114</sup>.

---

<sup>114</sup>For blue-detuned beams (which create an anti-confining potential), the trap frequency as a function of power can be inferred from a reduction in trap frequency in the dipole trap.

## 7 Kagome Mott insulators and triangular lattice negative temperatures

This chapter contains preliminary measurements involving the triangular and kagome lattices. We will first discuss results with the triangular lattice and will focus on the superfluid to Mott insulator transition and the observation of a negative temperature state. We will then walk through our measurements of the superfluid to Mott insulator transition in the kagome lattice. We only recently managed to load the lattice and implement phase stabilization, so the quality of most of the data in this section will likely be improved in the future. All quoted lattice depths were calibrated with Kapitza-Dirac measurements.

### 7.1 Triangular lattice

**Triangular & honeycomb lattice superfluid** Upon adiabatically ramping up the optical lattice, the BEC will be loaded into the ground state of the lattice. This state is a Bloch state with quasimomentum  $q = 0$ , i.e. a superposition of plane-wave states, with relative weights determined by the lattice depth<sup>115</sup>. These relative weights can be calculated numerically, as we did in [section 2.3](#). [Fig. 7.1](#) shows the momentum distribution of superfluids of  $^{39}\text{K}$  in the 532 nm triangular and 1064 nm honeycomb lattice.

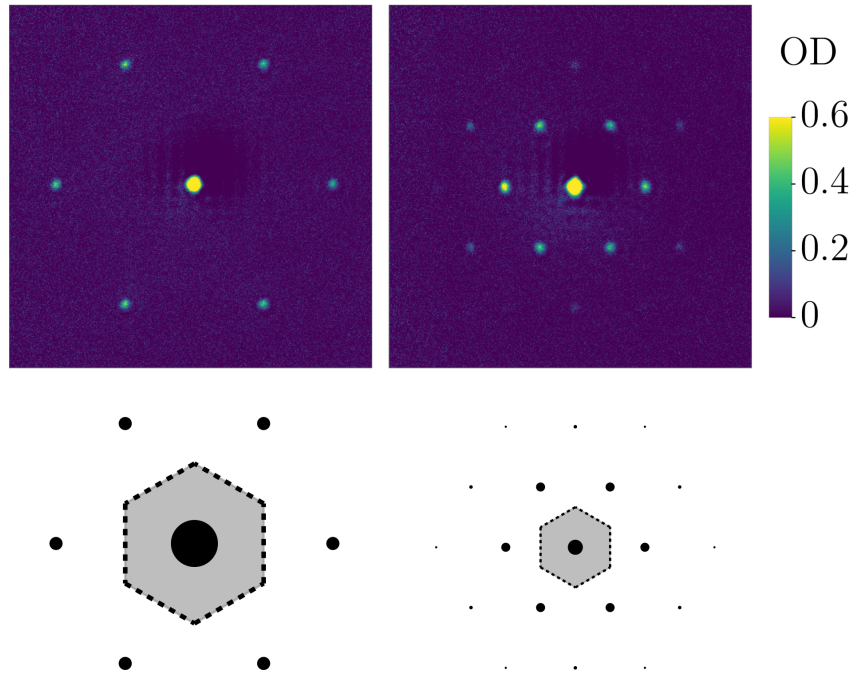


**Figure 7.1** – Experimental (top) and calculated (bottom) momentum distribution of a  $^{39}\text{K}$  superfluid in the triangular (left) and honeycomb (right) lattices at a depth of  $s = 15$ . Grey hexagons indicate the first Brillouin zones. The sizes of the black points indicate the weight of the associated plane-waves. Experimental images are taken at a TOF of 11 ms. Note that the optical density of the central peak is much higher than 0.6.

<sup>115</sup>The larger the lattice depth, the stronger the coupling between momentum states, i.e. higher-order peaks will become more populated as the lattice depth is increased.

Note that the area of the first Brillouin zone of the 532 nm triangular lattice is four times larger than that of the 1064 nm honeycomb lattice.

### 7.1.1 Superfluid to Mott insulator transition

As we showed in [section 2.5](#) and [section 2.6](#), the lattice depth determines the tunnelling energy  $t$  and, in combination with the scattering length, also the interaction strength  $U$  in the Hubbard model. Above a critical value of  $U/t$ , the system becomes Mott insulating, i.e. repulsive interactions are strong enough to localize atoms to individual sites. The transition from superfluid to Mott insulator manifests itself as a reduction and eventual elimination of long-range coherence of the many-particle wave function. This leads to a broadening of superfluid peaks [\[41\]](#). We quantify the coherence by measuring the width of the central superfluid peak and use this to determine the superfluid to Mott insulator transition point<sup>116</sup>.

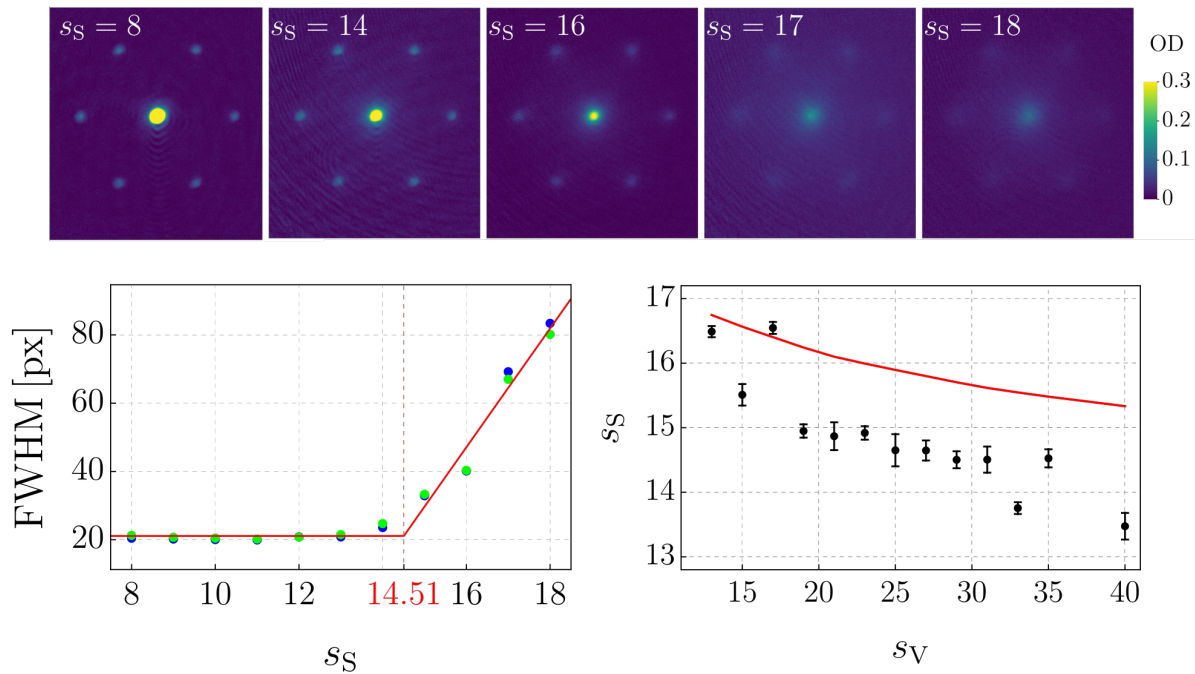


**Figure 7.2** – Superfluid to Mott insulator transition for  $^{87}\text{Rb}$  in the 532 nm triangular lattice. Top row: TOF images (25 ms) for different triangular lattice depths ( $s_S$ ) for a vertical lattice depth of  $s_V = 31$ . Bottom left: width (FWHM of Gaussian fit) of the central momentum peak as a function of triangular lattice depth. The red line shows a piecewise linear fit used to extract the transition point of the superfluid to Mott insulator transition. Bottom right: transition point of superfluid to Mott insulator transition as a function of vertical lattice depth. Each point is extracted from fits like the one shown in the bottom left image. The error bars are estimated fit errors. The red line is the theoretical superfluid to Mott insulator transition point according to [\[216\]](#) with no free parameters.

<sup>116</sup>A more precise measure of coherence is the visibility of the interference fringes [\[215\]](#). This approach unfortunately did not lend itself to our preliminary data.

**Superfluid to Mott insulator with rubidium** For  $^{87}\text{Rb}$ , we are not able to tune the interactions between particles, so the superfluid to Mott insulator transition can only be observed by changing the lattice depth. Since  $U/t$  increases with lattice depth, the system is superfluid (Mott insulating) for small (large) lattice depths. Fig. 7.2 shows how the momentum distribution of  $^{87}\text{Rb}$  in the triangular lattice evolves as the lattice depth is increased.

As expected, the sharp peaks in momentum space due to long-range coherence in the superfluid broaden and eventually disappear above a certain lattice depth. We use a piecewise linear fit to determine at which lattice depth the central peak width starts increasing and equate the position of the kink with the critical value for the superfluid to Mott insulator transition.

Since the momentum distribution of the Mott insulator is very similar to a thermal state, we made sure that we could restore coherence by ramping the lattice back to zero. Restoring the BEC after ramp down confirms that the diffuse distribution for deep lattices is not thermal [41].

Since the superfluid to Mott insulator transition point depends on the interaction strength which itself depends on the vertical lattice depth, we decided to measure the transition point as a function of vertical lattice depth. Higher vertical lattice depths cause tighter confinement and, as a result, larger interaction strengths. This behaviour is reflected in our data, which shows that the transition point is lowered as the vertical lattice depth is increased (see Fig. 7.2).

Mean-field theory predicts that the transition is located at  $(U/(zt))_c \approx 5.8$  [217], where  $z$  is the coordination number and is equal to 6 for the triangular lattice. More precise theoretical calculations predict that the transition happens at  $(U/(zt))_c \approx 4.9$  [216], which is slightly lower than the mean-field result. We use the result in [216] in conjunction with  $U$  and  $J$  calculated via Wannier states (section 2.4) to determine where the transition is theoretically supposed to occur as a function of lattice depth.

We see that both the trend and the order of magnitude between the measured and theoretically calculated data agree. However, the experimentally measured transition point is systematically lower by about  $1.2E_R$  compared to what we expect from theory. This could be explained by a systematic error in calibrating the triangular lattice depth or a discrepancy between how we define the transition point in our fits, i.e. via the kink in the piecewise linear function, and the actual location of the transition. There is also a roughly 10% uncertainty in the theoretical value of  $(U/t)_c$  [216, 218, 219]. Measurements like these are useful to reconcile our machine's behaviour with our code for determining the Hubbard parameters.

**Superfluid to Mott insulator with potassium** With  $^{39}\text{K}$  we can tune the interaction strength  $U$  independently of the tunnelling energy  $t$ . We can thus map the superfluid to Mott insulator transition as a function of lattice depth, which affects both  $U$  and  $t$ , and the scattering length, which affects only  $U$ . Fig. 7.3 shows the momentum distribution of  $^{39}\text{K}$  in the triangular lattice as a function of scattering length and lattice depth.

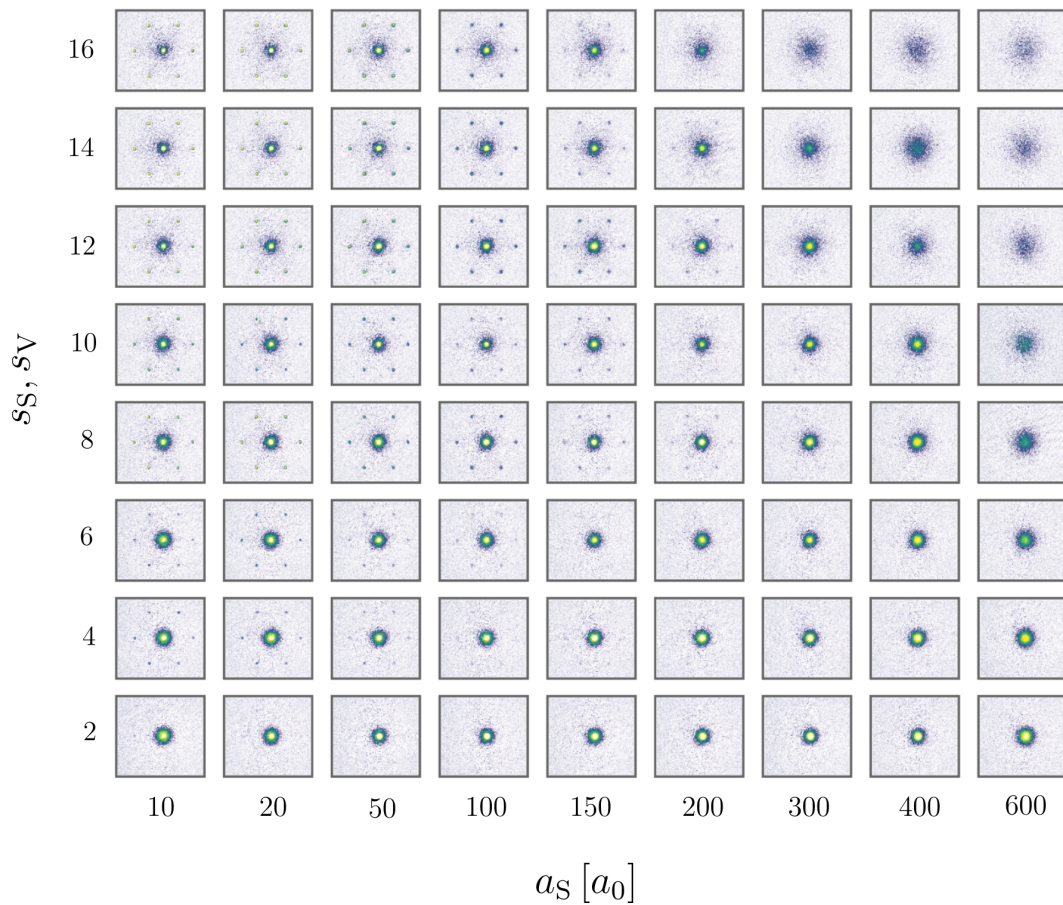


**Figure 7.3** – TOF images (11 ms) of  $^{39}\text{K}$  in the triangular lattice for different values of the scattering length  $a_S$  and the lattice depths ( $s_S, s_V$ ). The vertical and triangular lattice have equal depths.

We again quantify the coherence by measuring the width of the central peak. This is shown in Fig. 7.4. As for  $^{87}\text{Rb}$ , we use our Wannier state code to calculate the tunnelling rate and interaction strength as a function of lattice depth and scattering length. For each scattering length, we numerically determine the lattice depth required so that  $U/(zt) = 4.9$  [216]. This theoretical transition line is also shown in Fig. 7.4.

Our measured values are in good agreement with the theoretical prediction. This shows that our calibration scheme is accurate and that our code produces physically meaningful results. It would be good to extend our data to lower scattering lengths and deeper lattices to check whether theory and experiment still agree.

The critical  $U/t$  should be mass- and therefore species-independent. Comparing the theoretical transition point at  $a_S = 100a_0$  in  $^{39}\text{K}$  with the result we obtained for  $^{87}\text{Rb}$  at  $s_V \approx 16$  confirms this. Our experimental data also is consistent with a mass-independent transition point. In our units of lattice depth, the superfluid to Mott insulator transition occurs at a triangular lattice depth of roughly  $14E_R - 16E_R$ <sup>117</sup> at  $a_S = 100a_0$ .

<sup>117</sup>For vertical lattice depths of  $15E_R - 30E_R$ .

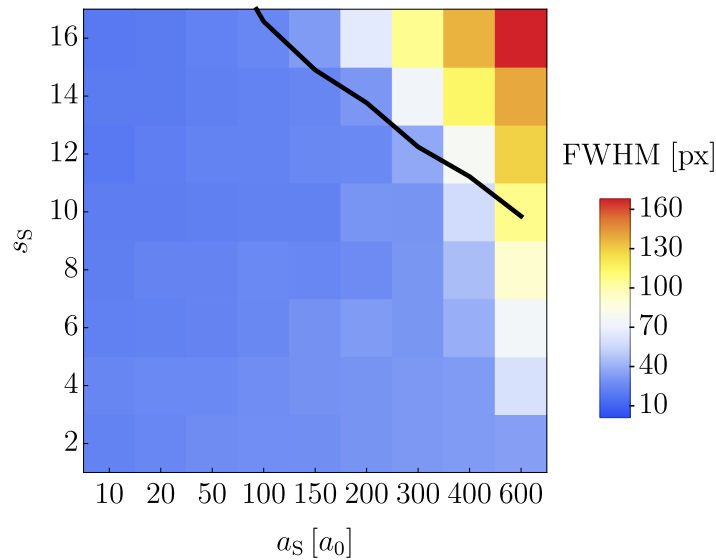


**Figure 7.4** – Measured width (FWHM) of the central peak as a function of the scattering length and the lattice depth. The black line marks the theoretically calculated transition point.

### 7.1.2 Preparation of negative temperature states

We will now discuss our recent observation of a negative temperature state in the triangular lattice. As far as we are aware, this marks the first time a negative temperature state has been prepared in a non-bipartite lattice. This should open a path towards studying bosonic and fermionic phases in a triangular lattice with inverted tunnelling. As of writing, our entropy in the negative temperature state is probably too large to properly study effects of frustrated bosonic phases on the triangular lattice.

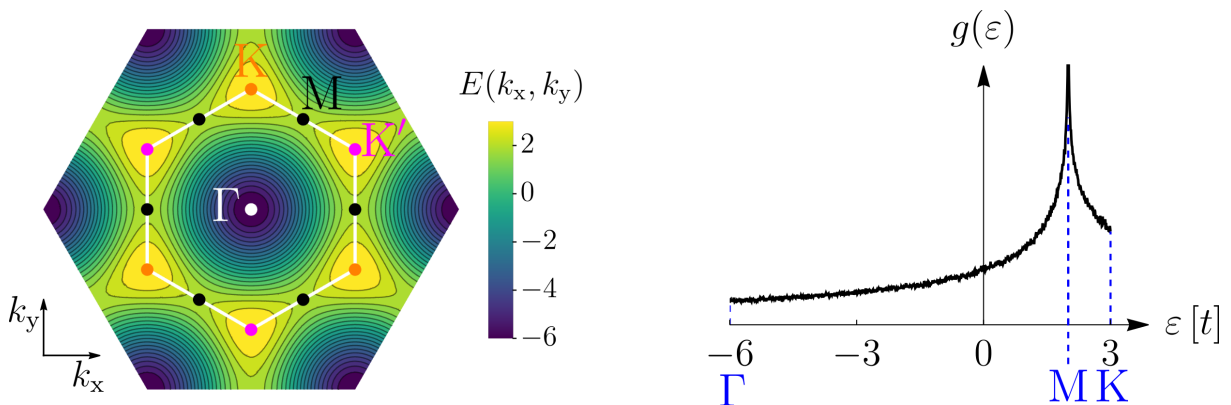


**Figure 7.5** – Left: tight-binding dispersion in the lowest band of the triangular lattice. The white hexagon indicates the BZ. Right: numerically calculated density of states of the triangular lattice in the tight-binding limit. The triangular lattice displays a van Hove singularity at the M-point.

A low-entropy, negative temperature state should cause occupation of the highest energy states. In a superfluid, for which kinetic energy dominates, we thus expect the momentum

states with the highest energies to be predominantly occupied. The triangular lattice hosts a single tight-binding band in which the highest energy states are located at the corners of the first Brillouin zone (BZ), i.e. the K and K' points (see Fig. 7.5).

The highest tight-binding energy is two-fold degenerate and condensation at negative temperatures will break the associated  $\mathbb{Z}_2$  symmetry<sup>118</sup>. The Bloch states at K and K' correspond to the vortex and antivortex antiferromagnet, both of which obey the three-colour arrangement (see section 3.3.1). Fig. 7.6 shows an image of a negative temperature state alongside the theoretically expected momentum distribution at the K and K' points.

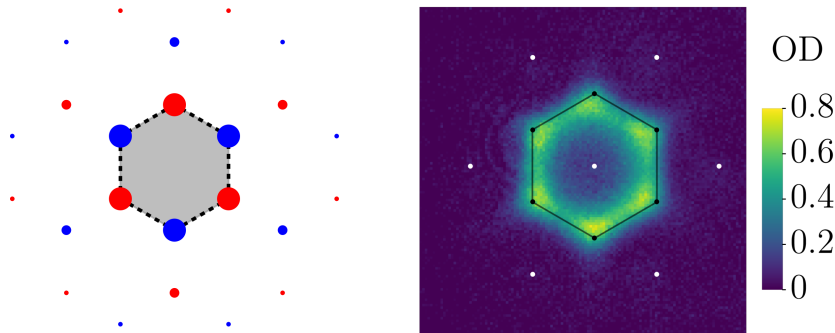


**Figure 7.6** – Left: Bloch states at K and K' (red and blue) in the lowest band of the triangular lattice. The BZ is shown in grey. Right: momentum distribution (11 ms TOF) of the negative temperature state in a triangular lattice with  $s_s = 6$ . The BZ boundary is shown in black. It is inferred from positive temperature superfluid peaks (white points).

In our system we do not see spontaneous symmetry breaking and see peaks at both K and K' simultaneously. We believe that there are two reasons for this. On the one hand, we have multiple layers in the vertical direction, which means that atoms will, at low temperatures, randomly condense into either the K or K' points in each layer<sup>119</sup>. Since we see an averaged distribution of all layers, the most probable momentum distribution will be that in which both K and K' are equally occupied. On the other hand, our entropy is likely still so high that the  $\mathbb{Z}_2$  symmetry is not globally broken. At our temperatures we could have a proliferation of domain walls between the two chiral orders [90, 220] and thus see a statistical mixture of both chiralities even in a single layer.

We also expect to see higher-order superfluid peaks similar to what was seen in [47]. We attribute our lack of superfluid peaks to excessive entropy generation during the Mott insulating stage of the negative temperature ramp. We see this heating also when we melt the Mott insulator into a positive temperature state and therefore believe that it is purely technical and fixable.

**Extracting temperature** To determine the temperature of the cloud we closely follow the approach outlined in [163] and the supplementary material of [48]. We can extract the temperature of a distribution of bosonic atoms in momentum or energy space by fitting a Bose-Einstein (BE) distribution,

<sup>118</sup>This effect was also observed in shaken triangular lattices [47]. There, the tunnelling element was inverted via Floquet shaking. We expect the physics to be the same as for a negative temperature state.

<sup>119</sup>Note that the vertical layers are effectively decoupled due to the vertical lattice, so we expect each layer to assume an individual chirality (see [90]).

$$n(\varepsilon) = f(\varepsilon)g(\varepsilon), \quad f(\varepsilon) = \frac{1}{e^{\frac{\varepsilon-\mu}{k_B T}} - 1}, \quad (7.1)$$

where  $\varepsilon$  is the energy,  $\mu$  is the chemical potential,  $f(\varepsilon)$  is the BE-distribution and  $g(\varepsilon)$  is the density of states. In practice we can only extract the momentum distribution of the atomic cloud. If we want to calculate  $f(\varepsilon)$ , we have to divide the momentum distribution by the density of states, which can be calculated numerically (see Fig. 7.5). If the lattice is deep enough, we can use the tight-binding dispersion relation to express  $f$  in terms of momentum,

$$f(\mathbf{k}) = \frac{1}{e^{\frac{\varepsilon(\mathbf{k})-\mu}{k_B T}} - 1}, \quad (7.2)$$

with

$$\begin{aligned} \varepsilon(\mathbf{k}) &= -2t \sum_{j=1}^3 \cos(\mathbf{k} \cdot \boldsymbol{\delta}_j) \\ &= -2t \left[ 2 \cos\left(\frac{\sqrt{3}}{2} a k_x\right) \cos\left(\frac{a k_y}{2}\right) + \cos(a k_y) \right] \end{aligned} \quad (7.3)$$

being the tight-binding band structure of the triangular lattice. For convenience, we express  $k_B T$  and  $\mu$  in units of the tunnelling energy,

$$\begin{aligned} f(\mathbf{k}) &= \left\{ e^{\frac{\varepsilon(\mathbf{k})-\mu}{k_B T}} - 1 \right\}^{-1} \\ &= \left\{ e^{\frac{-2t \sum_{j=1}^3 \cos(\mathbf{k} \cdot \boldsymbol{\delta}_j) - \mu}{k_B T}} - 1 \right\}^{-1} \\ &= \left\{ e^{\frac{-2 \left[ 2 \cos\left(\frac{\sqrt{3}}{2} a k_x\right) \cos\left(\frac{a k_y}{2}\right) + \cos(a k_y) \right] - \frac{\mu}{t}}{\frac{k_B T}{t}}} - 1 \right\}^{-1}. \end{aligned} \quad (7.4)$$

Here,  $a$  is the lattice spacing and effectively determines the magnification of the distribution. We fit the atomic momentum distribution with the function

$$f_{\text{fit}}(k_x, k_y) = \left\{ e^{\frac{-2 \left[ 2 \cos\left(\frac{\sqrt{3}}{2} a_{\text{fit}}(k_x - k_x^0)\right) \cos\left(\frac{a_{\text{fit}}(k_y - k_y^0)}{2}\right) + \cos(a_{\text{fit}}(k_y - k_y^0)) \right] - \mu_{\text{fit}}}{T_{\text{fit}}}} - 1 \right\}^{-1} + o_{\text{fit}}, \quad (7.5)$$

where  $a_{\text{fit}}$ ,  $\mu_{\text{fit}}$ ,  $T_{\text{fit}}$ ,  $o_{\text{fit}}$ ,  $k_x^0$ , and  $k_y^0$  are fit variables. We determine the BZ using the superfluid peaks of the positive temperature superfluid and exclude data that does not lie within it (see Fig. 7.7).

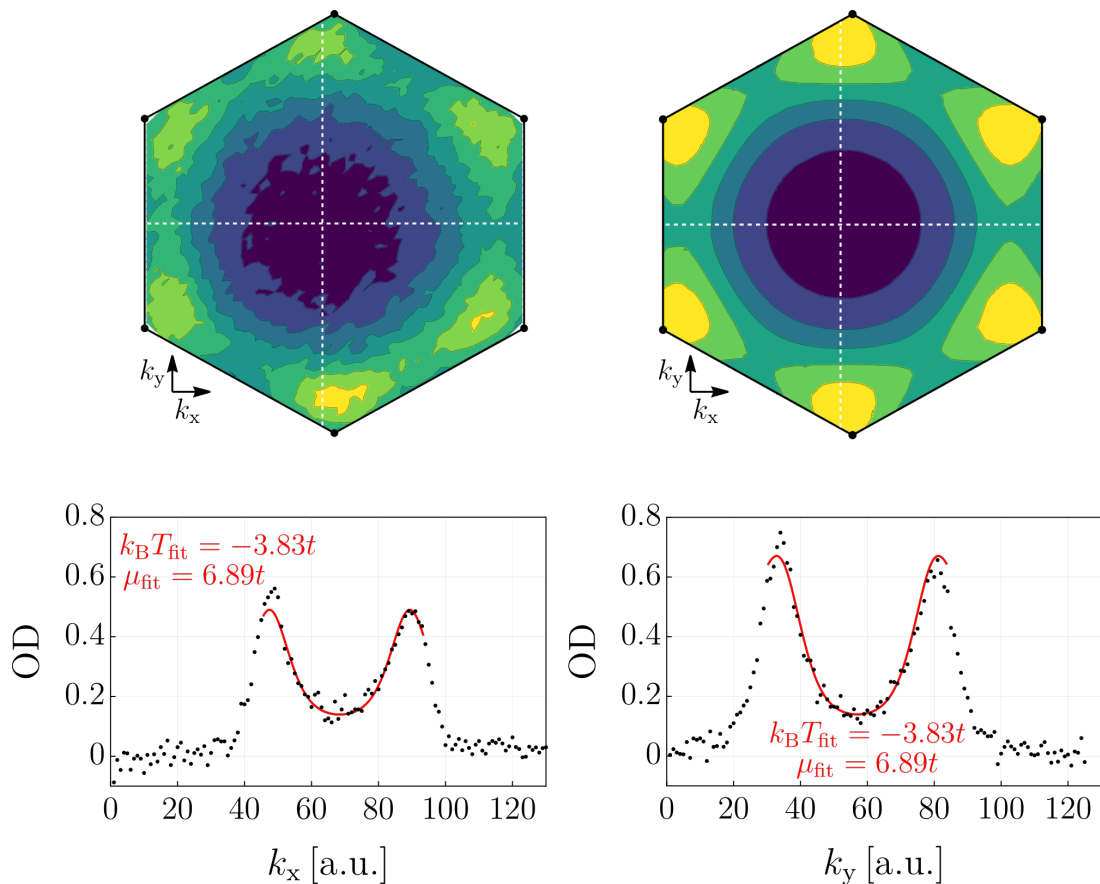


**Figure 7.7** – Top left: momentum distribution in the BZ (region enclosed by black, hexagonal line in Fig. 7.6) for the negative temperature state. Top right: contour plot of fit (Eq. 7.5) to top left image. Dashed, white lines intersect at  $(k_x = k_x^0, k_y = k_y^0)$  and indicate the positions of the 1D cuts shown in the bottom images. Bottom left (right): horizontal (vertical) cut through data (black points) and BE fit (red line). The fit is restricted to the BZ.

With our fit we determine  $T_{\text{fit}} \approx -3.8t$  and  $\mu_{\text{fit}} \approx 6.9t$ . From Fig. 7.7, we can see that the BE-distribution at negative temperatures fits the measured distribution well. The extracted chemical potential,  $\mu_{\text{fit}}$ , is also larger than the largest kinetic energy in the system, which is what we expect [163]. While the fit overlaps well with the measured data, the exact values  $T_{\text{fit}}$  and  $\mu_{\text{fit}}$  are somewhat ambiguous, as several different combinations of  $T_{\text{fit}}$  and  $\mu_{\text{fit}}$  can result in a similarly accurate fit. We are also not fitting the actual number distribution in momentum space, but only the OD image directly. In the future, we will accurately determine the atom number ( $N$ ) and fit the momentum distribution under the constraint that

$$\int_{\text{BZ}} f(k_x, k_y) dk_x dk_y = \int f(E)g(E) dE = N. \quad (7.6)$$

Note also that we fit the temperature of the Bloch wave directly which likely overestimates the absolute value of the temperature, since, by restricting the analysis to the first Brillouin zone, we don't take into account atoms that lie outside it. In a more careful experiment, we would use band-mapping to get an accurate occupation of momentum

states in the BZ.

Finally, we do not take into account the finite width of the in-situ cloud for our temperature fits. What we measure in absorption imaging after TOF is broader than the underlying momentum distribution. Our fits thus likely overestimate the absolute value of the temperature. We can take into account the finite in-situ cloud size by convolving  $f(k_x, k_y)$  with a Gaussian of some width  $\sigma$ , which can be determined independently [163].

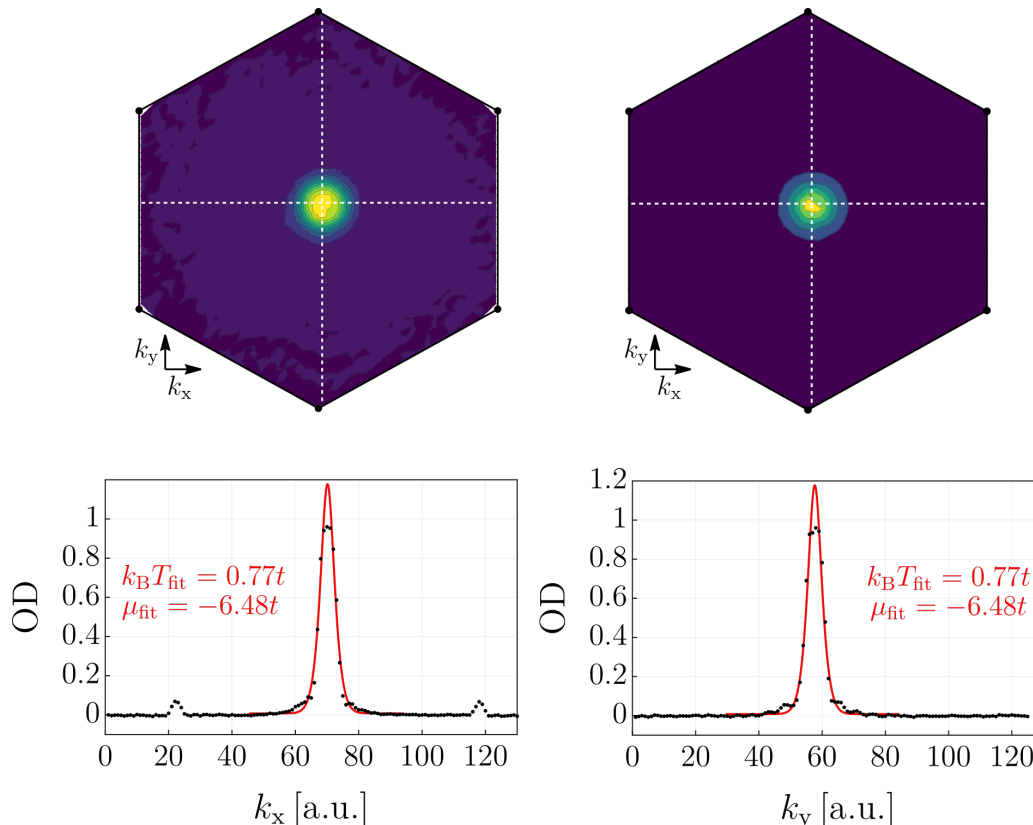


**Figure 7.8** – Positive temperature superfluid without ramping through the Mott insulator. Plots have the same meaning as Fig. 7.7.

To estimate how much the negative temperature protocol is heating the cloud, we apply the same fit (Eq. 7.5) to the positive temperature superfluid, before and after ramping to the Mott insulator. Fig. 7.8 (Fig. 7.9) shows the momentum distribution and estimated temperature for the positive temperature superfluid at  $6E_R$  without (after) ramping through the Mott insulator<sup>120</sup>. To ensure comparability of all datasets, we fix the scaling parameter,  $a_{\text{fit}}$  to the value extracted from the negative temperature fit. We extract fit values of  $T_{\text{fit}} \approx 0.8t$  ( $T_{\text{fit}} \approx 5.1t$ ) and  $\mu_{\text{fit}} \approx -6.5t$  ( $\mu_{\text{fit}} \approx -9.8t$ )<sup>121</sup>. This shows that even in the positive temperature case we significantly heat the cloud when ramping through the Mott insulator. Since, after ramping through the Mott insulator, the absolute value of the temperatures of both the positive and negative temperature states are similar,

<sup>120</sup>‘Ramping through the Mott insulator’ means that we are effectively running the same sequence as the negative temperature sequence, but do not go to attractive interactions or ramp up the vertical dipole beam.

<sup>121</sup>Note that the fitted chemical potentials are smaller than  $-6t$ , the lower bound of the tight-binding energy.

we conclude that heating is a consequence of technical noise or a sub-optimal ramping sequence, rather than of any fundamental limit affecting only the negative temperature state.

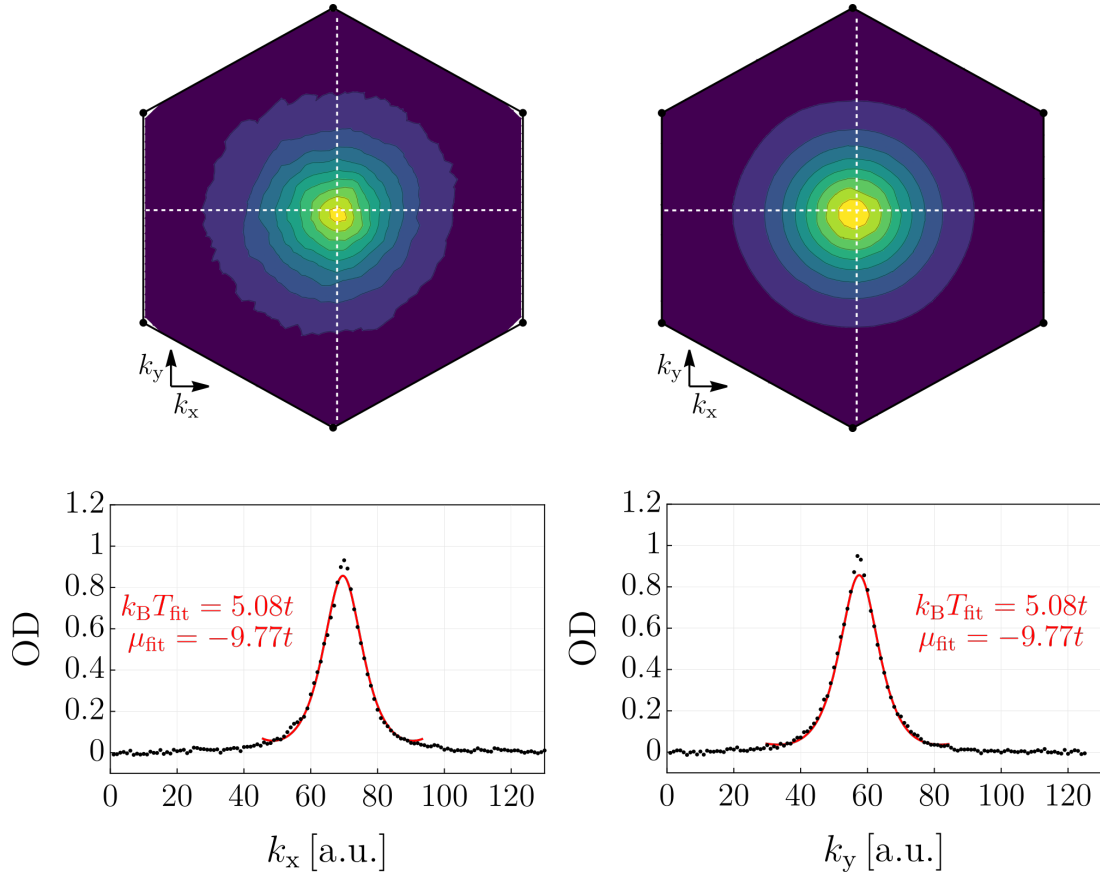


**Figure 7.9** – Positive temperature superfluid after ramping through the Mott insulator. Plots have same meaning as [Fig. 7.7](#).

## 7.2 Kagome lattice

We will conclude this chapter by briefly showing some results we obtained with  $^{87}\text{Rb}$  and  $^{39}\text{K}$  in the kagome lattice.

**Kagome superfluid** We combine the 532 nm triangular and 1064 nm honeycomb lattice to create the kagome lattice. If the relative phases are chosen correctly and are actively stabilized, the superfluid displays the distinctive momentum distribution shown in [Fig. 7.10](#).

The width of the superfluid peaks at finite TOF is affected by the in-situ cloud size, which itself depends on the interaction strength. Stronger repulsive interactions cause a larger in-situ cloud size [166]. One benefit of  $^{39}\text{K}$  is that the superfluid peaks can be made to be much sharper than for  $^{87}\text{Rb}$ , due to the ability to reduce the scattering length.

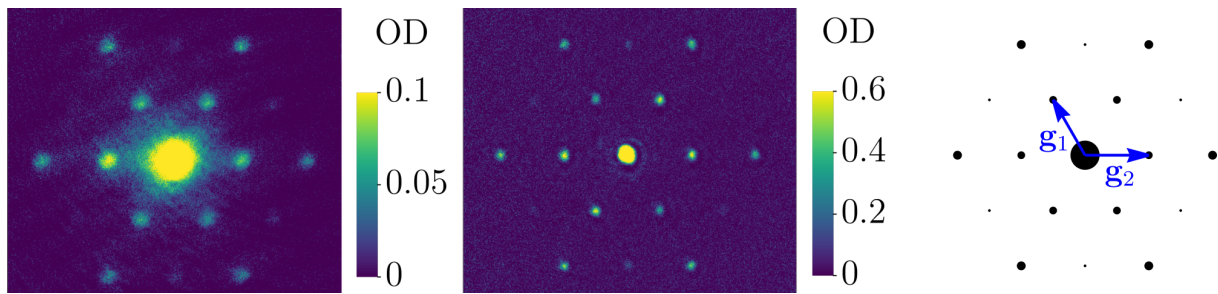


**Figure 7.10** – Superfluid of  $^{87}\text{Rb}$  (left) and  $^{39}\text{K}$  (centre) in the kagome lattice. Right: calculated momentum distribution of the Bloch state at  $\Gamma$  for a lattice with  $s_S = s_L = 15$ .

**Varying the superlattice phase** With our ability to control the relative phases between the triangular and honeycomb lattices, we can also realize other lattice potentials. For this, we move the wedge in the transfer paths (see [section 4.3.5](#)). Note that we still engage our active phase stabilization for lattices other than the kagome lattice, so as to create the same superfluid every shot. [Fig. 7.11](#) shows superfluids of different, highly symmetric superlattices.

Very similar measurements were taken with  $^{87}\text{Rb}$  in Berkeley [\[36\]](#). Under normal conditions, the stabilized superlattice phases do not vary noticeably over the course of a day. More on the stability of our relative phases can be found in Dan Reed’s thesis [\[140\]](#).

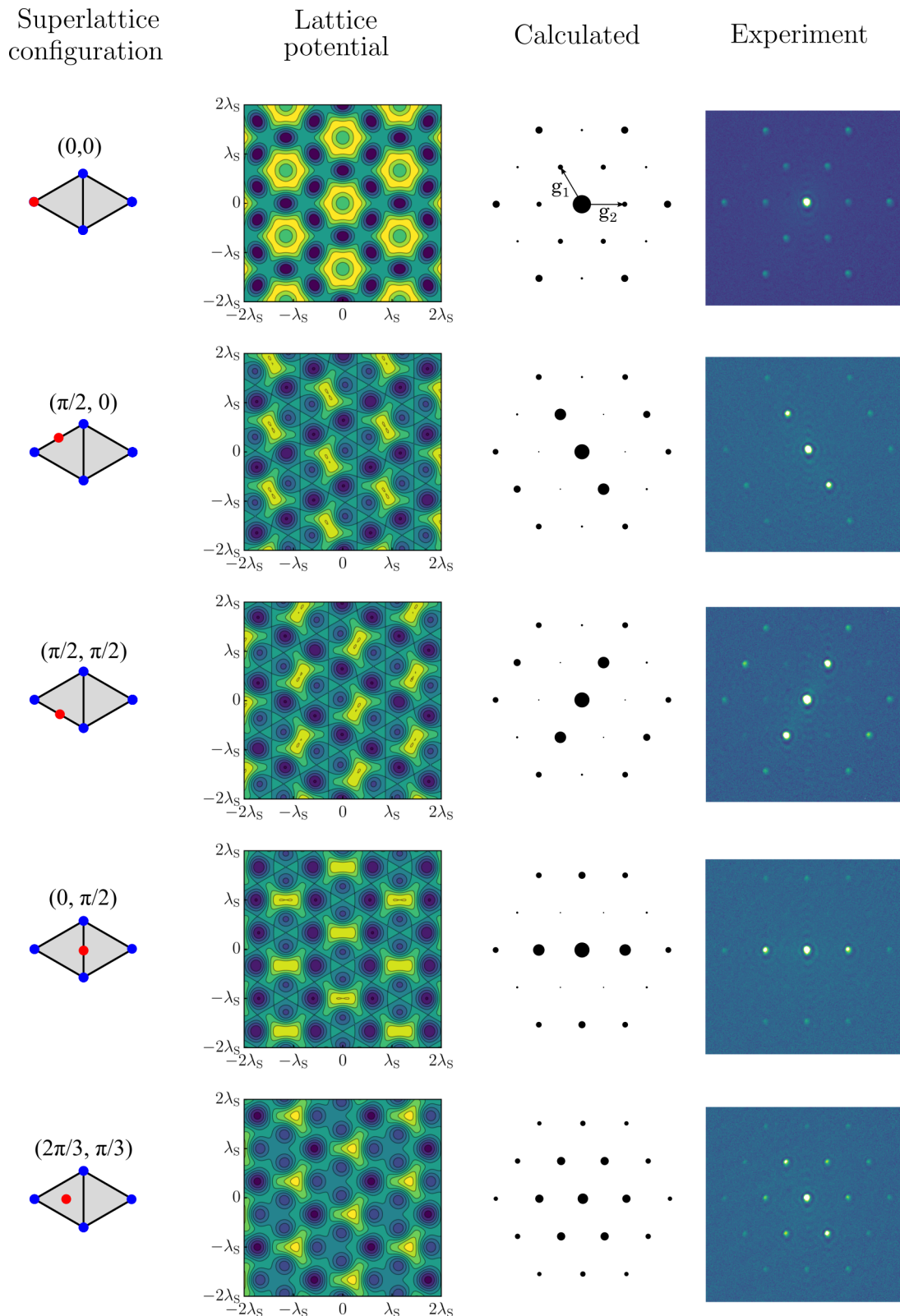


**Figure 7.11** – Superfluid of  $^{39}\text{K}$  in different superlattice potentials. The left column indicates the position of the 1064 nm, ‘repulsive’, triangular lattice sites (red) and the 532 nm ( $\lambda_s$ ), ‘attractive’, triangular lattice sites (blue). The right columns show the corresponding Bloch state momentum distributions at  $\Gamma$ . The experimental images are single shots, i.e. not averaged. Adapted from [140].

### 7.2.1 Superfluid to Mott insulator transition

Finally, we will discuss the superfluid to Mott insulator transition in the kagome lattice. Fig. 7.12 shows the momentum distribution of  $^{87}\text{Rb}$  in the kagome lattice for different lattice depths.

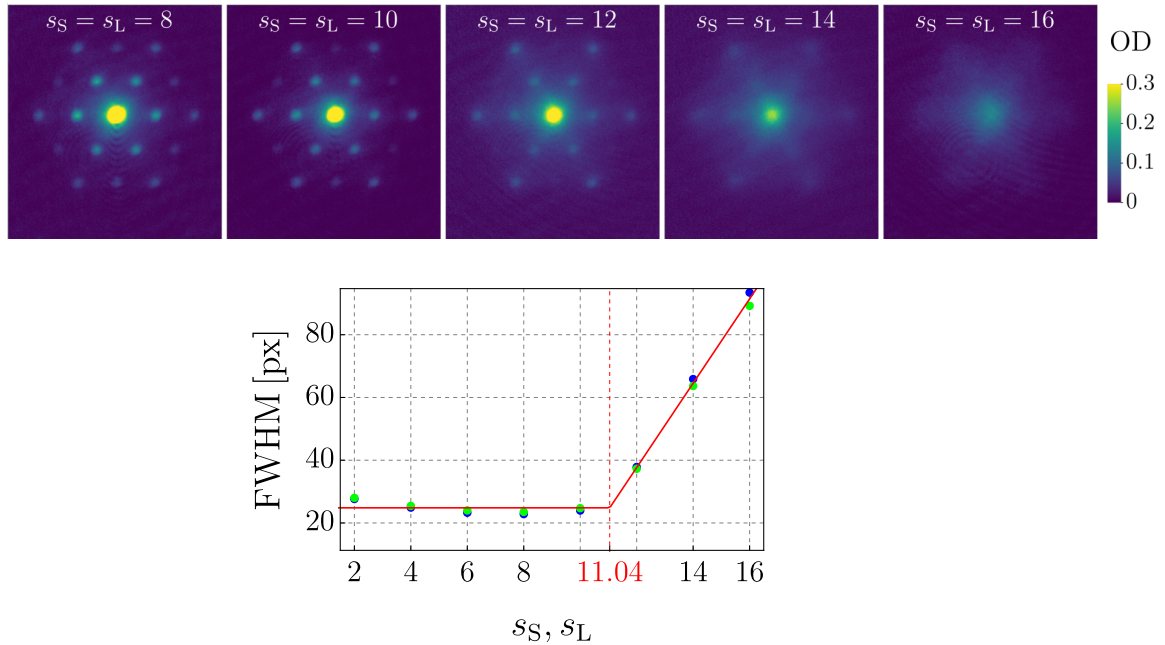


**Figure 7.12** – Top: superfluid to Mott insulator transition with  $^{87}\text{Rb}$  in momentum space (25 ms TOF). The 532 nm and 1064 nm lattice depths are equal, i.e.  $s_S = s_L$ . The vertical lattice depth is  $s_V = 20$ . Bottom: FWHM of the central peak vs lattice depth. The red line is a piecewise linear fit and the kink is assumed to be the transition point.

As in the triangular lattice, we see that the central peak of the momentum distribution starts to increase linearly above a certain lattice depth. We confirm that the diffuse distribution is a Mott insulator by ramping down the lattice from  $s_S = s_L = 16$ , which recovers the BEC. Compared to the triangular lattice case, we expect the transition to happen for lower lattice depths, since the lattice’s connectivity is lower<sup>122</sup> [137]. Lin et al. calculate that  $(U/(zt))_c \approx 4.46$  [216], where  $z = 4$  for the kagome lattice. Using the Wannier states, we calculate that  $(U/(zt)) = 4.46$  for  $s_S = s_L = 14.1$  and  $s_V = 20$ , so at significantly higher lattice depths than we observe experimentally. We are still trying to figure out why we have this discrepancy.

With the Mott insulator in the kagome lattice we are now one step away from creating a negative temperature state and populating the flat band. We did in fact go through the same protocol as with the triangular lattice, but did not find a clear population inversion. We only found that the entire Brillouin zone was occupied, consistent with an infinite temperature state. We already saw that the triangular lattice negative temperature state suffers from a lot of ‘heating’ when ramping over the Mott insulator. We think that reducing the heating for the triangular lattice will also lead to lower entropies in the kagome negative temperature state.

<sup>122</sup>Triangular lattice sites have six nearest neighbours, while the kagome lattice sites have four.



## 8 Towards quantum gas microscopy for the kagome lattice

This chapter covers our progress towards implementing a kagome lattice quantum gas microscope (QGM). Many of the design decisions we made stemmed from the desire to have single-site resolved imaging. The first choice we had to make was what wavelength to use for the kagome lattice. Current QGMs with alkali atoms almost universally use 1064 nm lattice light [50, 55–60], due to easy availability of high powers (50 W+). The lattice spacing for a square lattice formed with 1064 nm beams is 532 nm. This is just at the edge of what is feasible in terms of resolution  $R$ , which is commonly defined as the distance between maximum and first minimum of the Airy disk (Rayleigh criterion),

$$R \approx 0.61 \frac{\lambda}{\text{NA}}, \quad (8.1)$$

where  $\lambda$  is the imaging wavelength and NA is the numerical aperture of the imaging lens/objective<sup>123</sup>. The principal transitions of alkali atoms range from 589 nm (Na D2) to 895 nm (Cs D1). Thus, using a typical objective NA of 0.6-0.85, single-site resolved imaging of 532 nm-sized features is just about possible<sup>124</sup>. If the lattice spacing is much smaller than 532 nm, conventional single-site resolved imaging will not be possible. On the other hand, if lattice spacings are much larger than 532 nm, the tunnelling rate is suppressed, which is detrimental to conducting experiments. Ideally, the lattice spacing is small enough to be able to achieve tunnelling rates of up to 1 kHz, but large enough to be resolved with a 0.7-0.8 NA objective operating at the D1/D2 transitions of the atomic species. Unfortunately, the list of suitable lattice wavelengths is very short due to power availability; a lattice for quantum gas microscopy usually requires several watts of power per beam.

For potassium, a tunnelling rate of 1 kHz requires a lattice spacing on the order of 500 nm [184, 185]. A triangular lattice of 1064 nm lattice beams has a lattice spacing of 709 nm (614 nm) in the interfering (retro-reflected) case. Even in the retro-reflected case, the lattice spacing is larger than ideal. We therefore opted for a lattice wavelength of 532 nm in interfering configuration, which gives us a lattice spacing of 355 nm (good for physics) and is available at high power (good for imaging). However, this lattice spacing is too small to resolve with a conventional QGM.

Given a fixed lattice wavelength, there are two ways in which the ‘resolution’ can be increased: either the lattice spacing is artificially increased, e.g. by tilting the lattice [60] or an imaging transition with a smaller wavelength is used, such as the 4s  $\rightarrow$  5p transition in <sup>39</sup>K and <sup>40</sup>K [184].

Tilting the lattice is a simple way of increasing the lattice spacing without sacrificing lattice depth. However, this means that the lattice beams need to be tilted out of plane and requires a more complicated vacuum chamber design. In addition, it limits the maximum tunnelling rate<sup>125</sup>.

<sup>123</sup>A stricter bound on resolution is given by the Sparrow limit, which defines resolution as the distance between two identical point sources at which the intensity at the mid-point between their Airy disks is flat [221].

<sup>124</sup>Rayleigh resolutions of 450 nm-910 nm with these parameters.

<sup>125</sup>In section 2.3, we show that the tunnelling rate scales as  $\frac{1}{a^2}$ , where  $a$  is the lattice spacing.

Imaging on the  $4s \rightarrow 5p$  line in potassium (405 nm) would allow us to resolve features below 400 nm. This raises a number of complications however, one of which is that this transition is not closed for alkali atoms [222]. Therefore, a full treatment of the imaging process requires taking into account the lifetimes, polarisabilities, and scattering rates of all intermediate transitions. The intermediate transitions make this calculation much more involved. In the case of the  $4s \rightarrow 5p$  transition for K, absorption of a 1064 nm lattice photon or another imaging photon also causes ionization, complicating the imaging process even further.

We decided not to pursue these routes and instead found a way to increase our resolution without having to resort to the tilted lattice approach or to using a different imaging transition. Inspired by super-resolution microscopy techniques in cold atoms [223], we decided to use a separate imaging lattice that causes only a subset of sites to fluoresce while other sites are dark. Instead of taking one image to resolve all atoms, we intend to take three images, each one capturing one third of all sites. The benefit of this approach is that for each of the three images, the spacing of imaged atoms is increased to well above the diffraction limit for D1 & D2 light. One drawback is that our imaging times are longer. However, imaging times should be significantly reduced in blue detuned lattices compared to those in lattices made of 1064 nm light (see below).

To accurately reconstruct the distribution of atoms in an optical lattice, each atom has to scatter on the order of a few thousand photons. Scattering causes heating and will eventually cause atoms to tunnel to neighbouring sites or be lost altogether. For this reason, it is imperative that the atoms are cooled during imaging. Raman sideband cooling (RSC) has emerged as the method of choice for cooling fermionic alkali atoms in optical lattices [15, 43] and we intend to implement it for our machine.

## 8.1 Imaging transition

Since we want to stick with the D1 ( $4s_{1/2} \rightarrow 4p_{1/2}$ ) and D2 ( $4s_{1/2} \rightarrow 4p_{3/2}$ ) lines for imaging, we now have to figure out which transitions to use for imaging and RSC. We intend to use RSC on the D2 line and imaging (repump) on the D1 line, for the following reasons:

**(1) Light shifts of the excited state** During imaging, atoms will spend a significant amount of time in the excited state of the imaging transition. Ideally, atoms in the excited state will see the same lattice as atoms in the ground state. This ensures that each individual atom is still trapped even when it is in the excited state of the imaging transition. For atoms in the ground and excited states to see the same potential, the AC Stark shifts of the two levels at the lattice wavelength need to have the same sign. This is the case for a lattice formed of 532 nm beams, but not for a lattice formed of 1064 nm beams (see Fig. 8.1). For a 1064 nm lattice, the potential felt by  $^{39}\text{K}$  and  $^{40}\text{K}$  in the excited state is not only inverted with respect to the ground state, but is about five times stronger. In first-generation fermionic QGMs this presents a major problem to the imaging process. The amount of time an individual atom spends in the excited state has to be limited drastically to ensure that atoms remain trapped on average. This is one of the reasons why RSC is needed for fermionic QGMs using  $^6\text{Li}$  or  $^{40}\text{K}$ . This approach severely limits the scattering rate of imaging light and thus leads to long imaging times

of  $\sim 1$  s which, in turn, limits reconstruction fidelity [49, 57, 59].

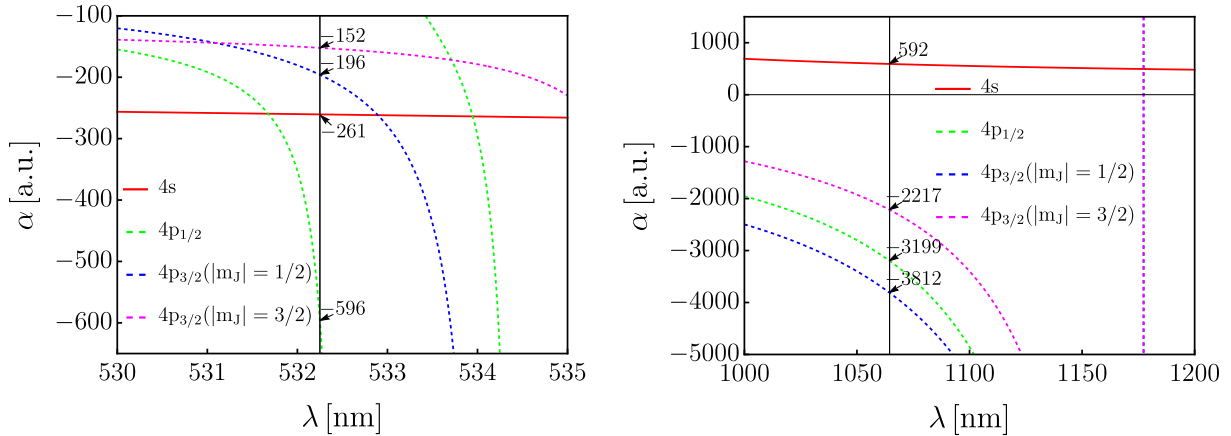


**Figure 8.1** – Left (right): polarizability of  $^{39}\text{K}/^{40}\text{K}$  around 532 nm (1064 nm). The red, green dashed, blue dashed, and magenta dashed lines are the polarizabilities of  $4s_{1/2}$ ,  $4p_{1/2}$ ,  $4p_{3/2}(|m_J| = 1/2)$ , and  $4p_{3/2}(|m_J| = 3/2)$ , respectively. Vertical black lines indicate wavelengths of 532.25 nm (short lattice) and 1064.5 nm (long lattice).

Fig. 8.1 shows that the  $4s$  and  $4p_{1/2}$  states are shifted in the same direction at a lattice wavelength of 532.25 nm<sup>126</sup>. This is about 0.22 nm detuned from the weak  $4p_{1/2} \rightarrow 8s_{1/2}$  transition, which might cause scattering in the  $4p_{1/2}$  state to be unacceptably high. However, since the lattice is blue-detuned, atoms will sit at points of zero lattice intensity which should suppress scattering of lattice photons in the  $4p_{1/2}$  state. The shift of the  $4p_{1/2}$  state at 532.25 nm is significantly stronger than that of the  $4p_{3/2}$  state. Atoms in the  $4p_{1/2}$  state are thus more strongly trapped at 532.25 nm, making the D1 transition preferable for imaging.

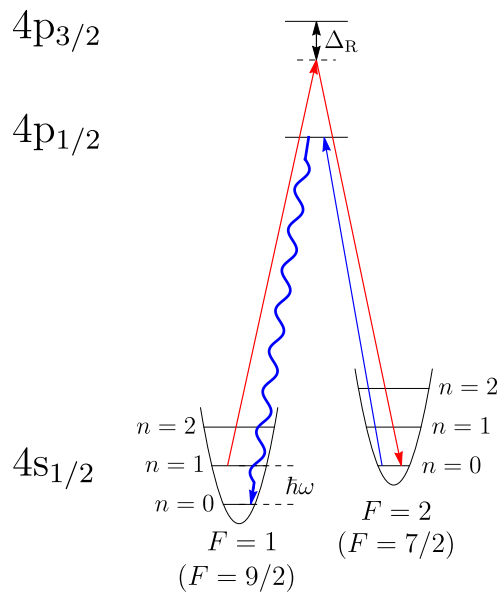
Similar to potassium in a 532 nm lattice, the Stark shifts of the ground and excited states of Yb at 1082 nm have the same sign, but the Stark shift in the excited state is 200 times larger [51]. Therefore, atoms in the excited state are trapped much more strongly than in the ground state. This greatly benefits the imaging process because the imaging transition can be driven strongly while still keeping atoms pinned to individual lattice sites. Thus, it is possible to image without needing additional cooling, because enough photons can be collected before any individual atom is lost from a site and imaging times can be reduced to 100  $\mu\text{s}$  [51] (instead of conventional exposure times on the order of 1 s [56–58]). A 532.25 nm lattice for potassium might similarly help reduce imaging times and improve reconstruction fidelities.

**(2) Excited state hyperfine splitting** The minimum splitting between levels in the D2 manifold of  $^{39}\text{K}$  and  $^{40}\text{K}$  is 3.3 MHz and 24.2 MHz, much smaller than for the D1 levels at 55.5 MHz and 155.3 MHz, respectively. To suppress off-resonant excitations it makes more sense to use the D1 line for imaging and the D2 line for RSC. RSC is not affected by the level splitting in the excited state since the Raman beams are far detuned from the hyperfine manifold.

<sup>126</sup>Based on the Coherent Mephisto MOPA manual, the laser frequency is  $\sim 281.63$  THz at a crystal temperature of 30°C, corresponding to a vacuum wavelength of 1064.5 nm.

**(3) Separability of D1 and D2 light** D1 (770 nm) and D2 (767 nm) light can be split using a line/edge filter. This means that if the Raman transition targets either D1 or D2 and the imaging transition targets the other, it is possible to separate Raman and imaging light during imaging. This is especially useful considering the difference in power levels between Raman and repump beams: Raman power is on the order of a few hundred mW, while imaging power is on the order of a few hundred  $\mu$ W. Therefore it is important that stray Raman light be strongly attenuated before reaching the camera. Targeting a separate transition for Raman and repump makes the separation process much easier. Using a filter for Raman and repump is also done in [56, 57].

**(4) Precedent** Other QGMs with potassium have successfully used D1 for imaging and D2 for RSC/EIT<sup>127</sup> [56, 57].



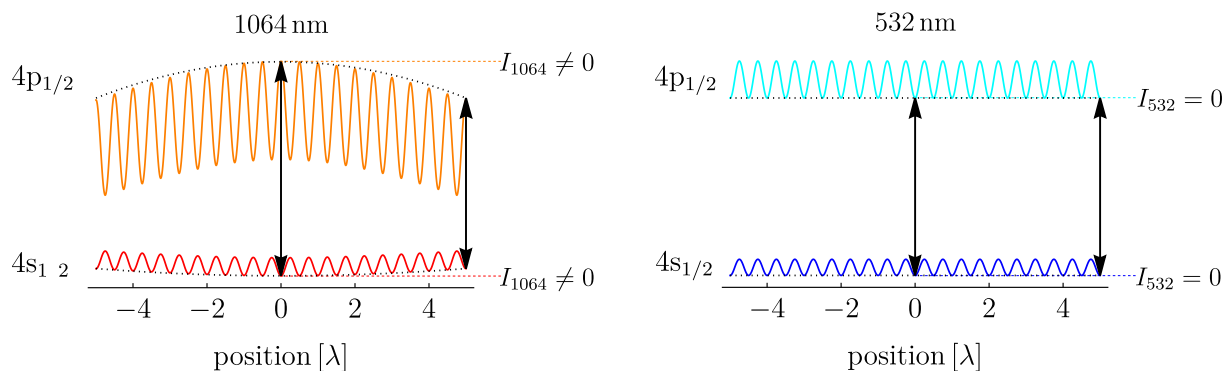
**Figure 8.2** – Raman sideband cooling and repump on the D2 ( $4s \rightarrow 4p_{3/2}$ ) and D1 ( $4s \rightarrow 4p_{1/2}$ ) line of  $^{39}\text{K}$ , respectively. States in parentheses are for  $^{40}\text{K}$ . The Raman beams (red) transfer atoms from one ground state hyperfine level to the other while additionally removing a motional quantum. Repump and spontaneous decay (blue) close the cycle. The imaging system collects spontaneously emitted photons to form an image.

Fig. 8.2 shows how Raman sideband cooling can be used to cool atoms in an optical lattice during fluorescence imaging. The Raman beams couple the two ground-state hyperfine levels and target the red sideband of the  $|F=1\rangle \rightarrow |F=2\rangle$  ( $|F=9/2\rangle \rightarrow |F=7/2\rangle$ ) transition in  $^{39}\text{K}$  ( $^{40}\text{K}$ ), corresponding to a removal of motional energy. Repump light populates the excited state and spontaneous emission closes the imaging cycle.

<sup>127</sup>EIT: electromagnetically induced transparency. EIT is very closely related to RSC [224, 225].

## 8.2 Blue vs red-detuned lattices

For  $^{39}\text{K}$  and  $^{40}\text{K}$  there are several advantages in using 532 nm to pin atoms for fluorescence imaging. Firstly, as pointed out previously, the sign of the AC Stark shift of both the ground and excited states is the same in a 532 nm lattice. Secondly, atoms are repelled from regions of high intensity and sit at the zero-intensity points. This suppresses heating due to scattering of lattice light. Finally, residual lattice curvature is minimized and a larger number of sites can be imaged. Fig. 8.3 shows a comparison of the three effects in  $^{39}\text{K}$  for 532 nm and 1064 nm light.



**Figure 8.3** – Schematic of the potential created by a 1064 nm (left) and 532 nm (right) lattice in the 4s (bottom) and  $4p_{1/2}$  (top) states of potassium. For 1064 nm (532 nm), the potential minima are located at maximum (zero) intensity and the  $4p_{1/2}$  state potential is inverted (not inverted) with respect to the 4s state. Black arrows indicate the imaging frequency shift between different sites of the lattice. For 1064 nm, this shift is substantial, while for 532 nm the imaging frequency shift is zero.

In contrast to a red-detuned lattice, the fluorescence rate in a blue-detuned lattice is not site-dependent. While the imaging transition should not be shifted between lattice sites in a blue-detuned lattice, the Raman resonance will shift due to the harmonic oscillator spacing also being affected by lattice beam curvature. This is an effect that equally affects red and blue detuned lattices and cannot be easily compensated for. In practice this means that the cooling efficiency will be reduced away from the centre of the lattice (provided the Raman lasers are resonant with the lattice’s central region).

## 8.3 Imaging lattice

To selectively suppress fluorescence from a subset of lattice sites we will use an imaging lattice with a wavelength close to the  $4p_{1/2} \rightarrow 3d_{3/2}$  transition. This lattice ideally induces a large shift in the imaging transition ( $4s_{1/2} \rightarrow 4p_{1/2}$ ) while minimally affecting the lattice potential that atoms in the  $4s_{1/2}$  state experience. We intend to use a tunable laser between 1168 nm and 1178 nm for our imaging lattice that can emit a few watts of power, which we can use to target both the  $4p_{1/2} \rightarrow 3d_{3/2}$  and the  $4p_{3/2} \rightarrow 3d$  transitions.

**Imaging lattice geometry** The geometry of the imaging lattice has to be compatible with the geometry of the kagome lattice, i.e. the imaging lattice sites have to line up with

kagome lattice sites. We opted for a simple 1D imaging lattice formed of two interfering beams.

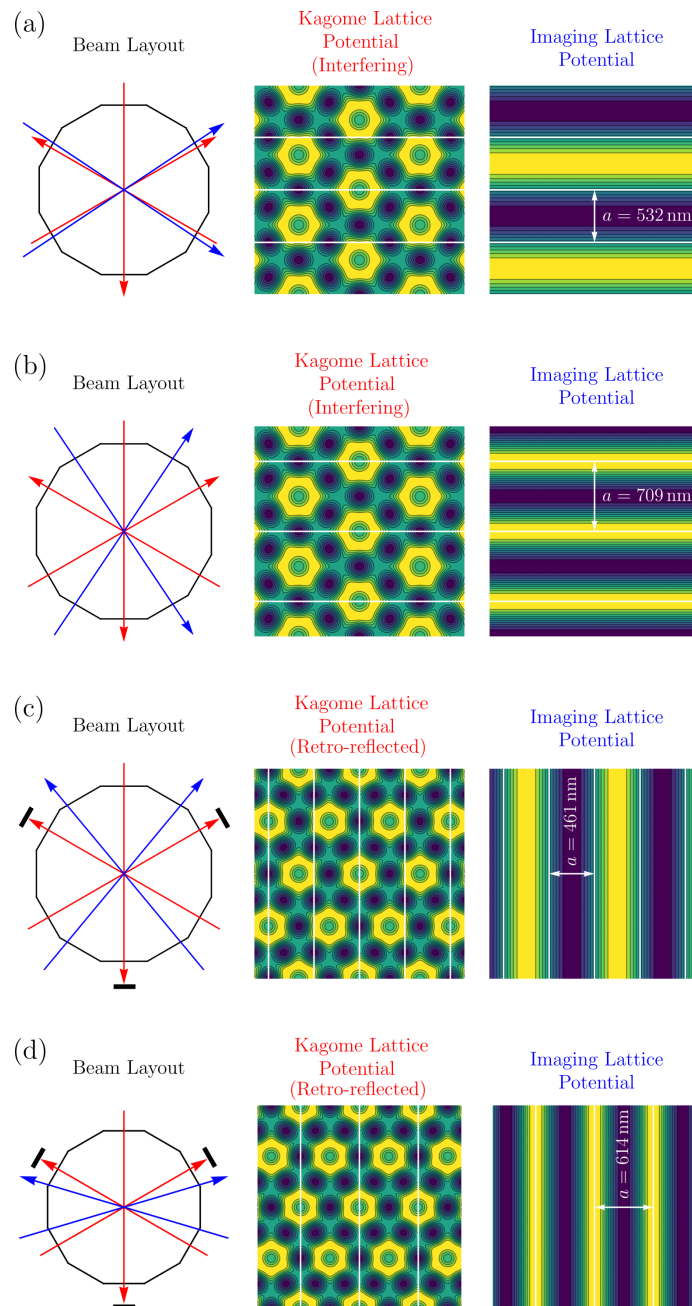


**Figure 8.4** – Each row shows the configuration of the kagome (red) and imaging lattice (blue) beams around the science chamber (black outline of dodecagon) (left) and the resulting potentials (centre: kagome, right: imaging). (a) interfering kagome lattice; full imaging requires three images. Effective lattice spacing: 614 nm. (b) interfering kagome lattice; full imaging requires four images. Effective lattice spacing: 709 nm. (c) retro-reflected kagome lattice; full imaging requires three images. Effective lattice spacing: 532 nm. (d) retro-reflected kagome lattice; full imaging requires four images. Effective lattice spacing: 614 nm.

Since we intend to use the D1 transition for imaging, the wavelength of the imaging lattice is fixed to be close to the  $4p_{1/2} \rightarrow 3d_{3/2}$  transition. We can change the imaging lattice spacing by adjusting the angle of incidence between the imaging lattice beams. We also need to ensure that the imaging lattice is compatible with our science chamber. Fig. 8.4 shows different configurations of the imaging and kagome lattices.

Only the first configuration in Fig. 8.4 is compatible with our science chamber, which is the main reason we decided to implement the kagome lattice with interfering beams. In this configuration we need to take three images with an effective lattice spacing of  $614 \text{ nm}$ <sup>128</sup>.

This configuration is slightly unusual in that the imaged sites do not lie at the maxima or minima of the imaging lattice but rather at the half-intensity lines. This is illustrated in Fig. 8.5. This leads to the extra complication that the excited state atoms reside on a strong slope instead of either a maximum or minimum. This can be resolved (if necessary) by taking six images instead of three and selecting imaged sites via the minimum (or maximum) of the imaging lattice.

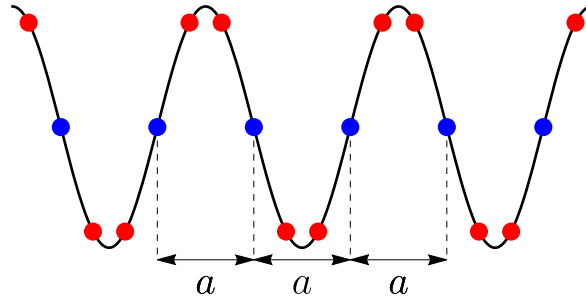


**Figure 8.5** – Schematic of the imaging lattice with imaged (blue) and unimaged (red) sites.

Fig. 8.5 makes apparent that the imaging lattice shifts the imaging transition also on imaged sites. The imaging light has to thus be shifted accordingly.

Using a single additional imaging lattice is one of the simpler ways to achieve super-resolution microscopy. We came up with an even simpler scheme that does not require an imaging lattice but achieves super-resolution with kagome lattice beams only. This is discussed in detail in [appendix B](#).

**Imaging transition shift** The shift induced by the imaging lattice between imaged and unimaged sites depends strongly on the imaging lattice wavelength. On the one hand, being close to the  $4p \rightarrow 3d$  resonance leads to strong shifts in the excited state even at low powers. However, this can cause severe scattering of imaging lattice light and therefore heating and atom loss. On the other hand, we can suppress scattering of imaging lattice photons by using larger detunings from the  $4p \rightarrow 3d$  resonance. This means that more power is required to get the same shift of the imaging transition. Too much imaging lattice power will also start to affect atoms in the  $4s$  state, which we want to avoid. The exact parameters will thus be a compromise between imaging lattice

<sup>128</sup>Note that while the spacing between imaging lattice half-intensity lines is  $532 \text{ nm}$ , the imaged lattice sites are at a distance of  $\frac{2}{\sqrt{3}} \times 532 \text{ nm} = 614 \text{ nm}$ .

power and wavelength. Fig. 8.6 shows the polarizability of  $^{39}\text{K}/^{40}\text{K}$  between 1165 nm and 1180 nm. The  $4p_{1/2} \rightarrow 3d_{3/2}$ ,  $4p_{3/2} \rightarrow 3d_{3/2}$ , and  $4p_{3/2} \rightarrow 3d_{5/2}$  transitions are located at 1169.34 nm, 1177.29 nm, and 1177.61 nm, respectively.

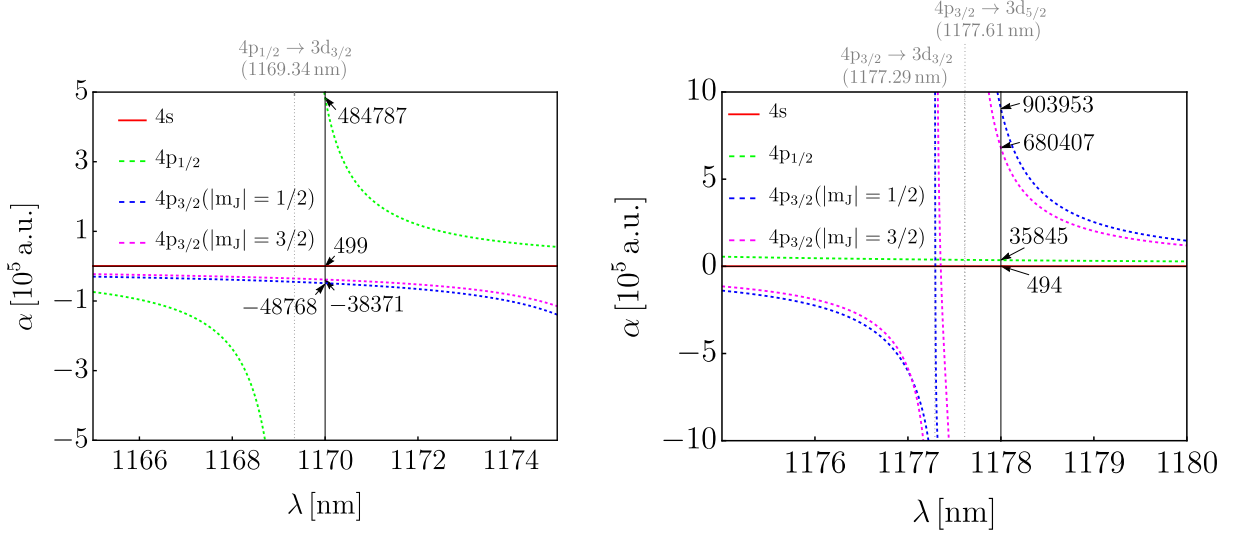


**Figure 8.6** – Left (right): polarizability of potassium around 1170 nm (1178 nm). The red, green dashed, blue dashed, and magenta dashed lines are the polarizability of  $4s_{1/2}$ ,  $4p_{1/2}$ ,  $4p_{3/2}(|m_J| = 1/2)$ , and  $4p_{3/2}(|m_J| = 3/2)$  in  $^{39}\text{K}/^{40}\text{K}$ , respectively. Vertical black lines indicate wavelengths of 1170 nm and 1178 nm (imaging lattice).

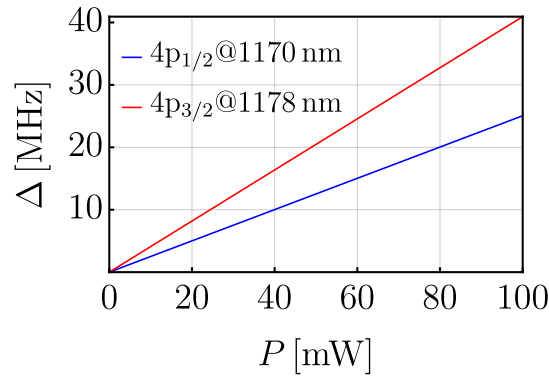


**Figure 8.7** – AC Stark shift as a function of imaging lattice power for the  $^{39}\text{K}/^{40}\text{K}$   $4s \rightarrow 4p_{1/2}$  transition at 1170 nm (blue) and the  $4s \rightarrow 4p_{3/2}$  transition at 1178 nm (red). We assume that the imaging lattice is formed of circular beams with a beam waist of 100  $\mu\text{m}$ .

The imaging lattice potential is given by

$$\begin{aligned}
 V_{T,\lambda}(x, y) &= U_{T,\lambda} \frac{2P}{\pi w_0^2} \left| e^{ik(\cos(\alpha)x + \sin(\alpha)y)} + e^{ik(\cos(\alpha)x - \sin(\alpha)y)} \right|^2 \\
 &= U_{T,\lambda} \frac{8P}{\pi w_0^2} \cos^2(k \sin(\alpha)y),
 \end{aligned} \tag{8.2}$$

where  $\lambda$  is the wavelength of the imaging lattice,  $\alpha$  is the angle between imaging lattice beams,  $T$  is the target atomic level,  $P$  is the power in each beam, and  $w_0$  is the beam waist<sup>129</sup>.

We assume that the polarizations are along the  $z$ -direction, i.e. out-of-plane. Note also that the imaging lattice spacing is given by  $a = \frac{\pi}{k \sin(\alpha)} = 1064$  nm. The difference in light shift between an imaged and unimaged site is given by  $\Delta = V_{T,\lambda}(0, a/2) - V_{T,\lambda}(0, 2a/3)$ . Fig. 8.7 shows the resulting light shift for the D1 transition at 1170 nm and the D2 transition at 1178 nm.

This shows that we can shift the imaging transition by several times the natural linewidth with moderate powers of the imaging lattice. Considering that for small powers the scattering rate of imaging light as a function of detuning is

$$R_{\text{scatt}} \propto \frac{\Gamma}{2} \frac{I}{1 + \frac{4\Delta^2}{\Gamma^2}}, \quad (8.3)$$

where  $\Gamma$  is the natural linewidth of the D1 transition ( $\sim 6$  MHz),  $I$  is the intensity of the imaging light, and  $\Delta$  is the detuning from the imaging transition, a shift of 12 MHz would suppress fluorescence on unimaged sites by 94% compared to imaged sites.

**Total potential** In the presence of the imaging lattice, the  $4p_{1/2}$  lattice sites are shifted by a few nm with respect to those in the ground state (see Fig. 8.8). This shift will cause atoms to move and gain momentum during the imaging process. Additionally, the effective lattice site depth is reduced in the  $4p_{1/2}$  state due to the imaging lattice.

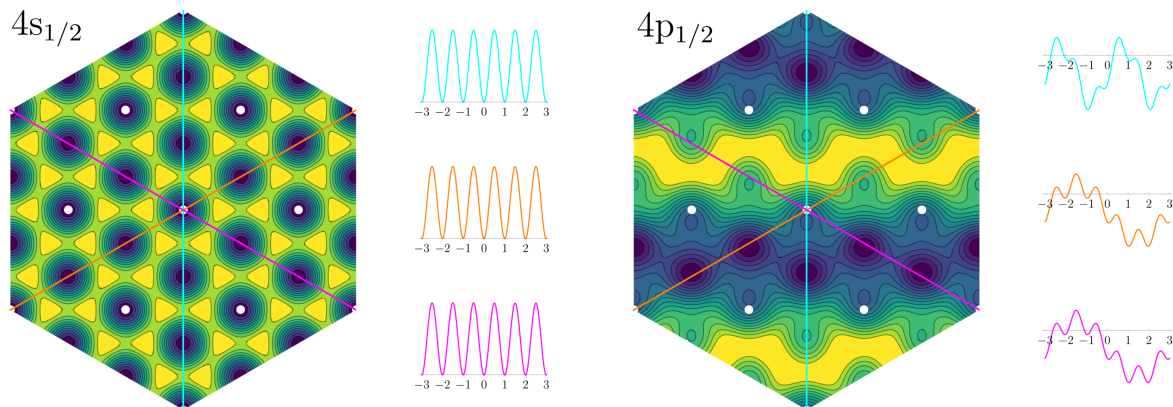


**Figure 8.8** – Left: potential seen by atoms in the  $4s$  state of  $^{39}\text{K}/^{40}\text{K}$  in a 3 W, 532 nm triangular lattice and 48 mW per beam of the 1170 nm imaging lattice (same beam parameters as in Fig. 8.7). The configuration of imaging lattice beams is as in Fig. 8.4 (a). Right: potential seen by atoms in the  $4p_{1/2}$  state at the same lattice powers. The imaging lattice shifts the  $4p_{1/2}$ -state on the unimaged sites with respect to the imaged sites (white points) by roughly 12 MHz. Note also that the minima of imaged sites in the  $4p_{1/2}$  state are translated with respect to those in the  $4s$  state. Cyan, orange, and magenta-coloured lines indicate 1D cuts through the potential along different directions.

Note that the imaging lattice technique will require us to change the imaging lattice phase between exposures. We already showed that we can reliably stabilize the kagome lattice

<sup>129</sup>The beam is assumed to be circular.

phases with piezo mirrors and can lock the phase over a large range of lattice powers (see [chapter 5](#)). We intend to use either piezo mirrors or AOM frequency modulation for phase control of the imaging lattice.

## 8.4 Single-layer selection

To obtain a reliable image of the atomic distribution, it is vital to prepare only a single horizontal layer in the focus of the microscope objective [58, 59]. Fluorescence from multiple layers blurs the image and makes it difficult to determine site-occupation in the target layer. We intend to prepare a single layer via a magnetic gradient, MW radiation, and an optical removal scheme. This technique is robust and commonly used in other QGMs [50, 56, 57]. The first step of the single-layer selection protocol is to transfer atoms in all layers to a different ground-state hyperfine level via a MW Landau-Zener (LZ) sweep. A magnetic offset field and gradient are then switched on, so that only the target layer is affected by a second LZ sweep and the target layer is selectively transferred back to the initial hyperfine level. Finally, atoms in unwanted layers are removed with resonant light and only atoms in the target layer remain.

**MW transfer** MW radiation for single-layer selection targets the ground state fine structure manifold,  $4s_{1/2}$  for  $^{39}\text{K}$  and  $^{40}\text{K}$  (see [Fig. 8.9](#)). The derivative of the MW transition frequency ( $\nu$ ) with respect to the magnitude of a magnetic offset field ( $B$ ), i.e.  $\frac{d\nu}{dB} = \frac{1}{h} \frac{dE}{dB}$  is maximized for the stretched state (Black arrows in [Fig. 8.9](#)). In addition,  $\frac{d\nu}{dB}$  is independent of  $B$  for the stretched state but varies for all other MW transitions in the ground state fine structure manifold. Using the stretched state to target an individual layer minimizes the magnetic field gradient required for single-layer selection and allows us to work at an arbitrary offset field. This freedom in choosing the offset field means we can maximize the minimum field stability required to deterministically prepare a single layer.

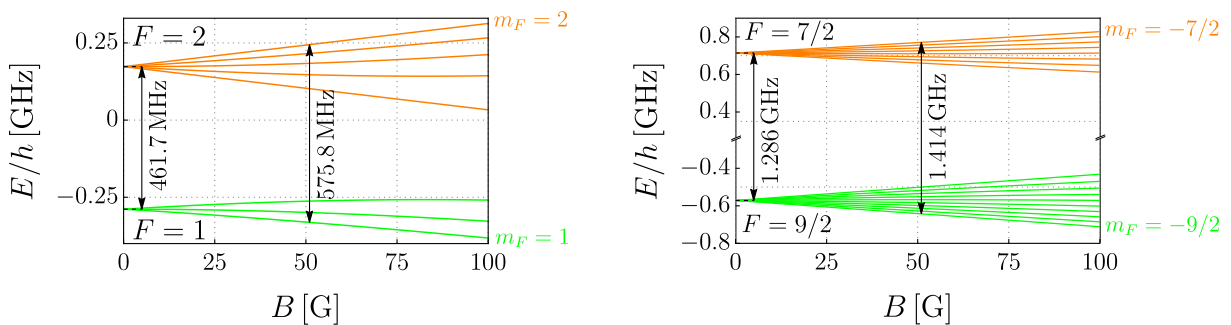


**Figure 8.9** – Left (right): Zeeman level splitting in the ground state manifold of  $^{39}\text{K}$  ( $^{40}\text{K}$ ) as a function of magnetic field. For single-layer preparation, we target the  $|F=1, m_F=1\rangle \rightarrow |F=2, m_F=2\rangle$  and  $|F=9/2, m_F=-9/2\rangle \rightarrow |F=7/2, m_F=-7/2\rangle$  transitions for  $^{39}\text{K}$  and  $^{40}\text{K}$ , respectively. Black arrows show the stretched state transition frequency for 0 G and 51 G.

In an ideal system, the first, layer-independent transfer to the excited state and the subsequent single-layer-selective transfer to the ground state can be done with a resonant

Rabi-pulse. However, the real system will invariably suffer from magnetic field inhomogeneities leading to a broadening of the resonance (see Fig. 8.10). A Rabi-pulse will thus fail to fully transfer all atoms to the target  $m_F$  state. A solution to this problem is to use a LZ sweep in which the MW frequency is ramped over some frequency range that spans the resonant frequencies of all atoms in the target layer.

To ensure that only atoms in the target layer are affected by step two of the single layer selection process, the offset magnetic field, which fixes the resonant frequency of the MW transition, needs to be very homogeneous in space and very stable in time.

**Stability requirements** There are two independent conditions on the offset magnetic field. The first requirement is that the magnetic field is sufficiently homogeneous in space. Every magnetic field displays some curvature and it is important that this curvature is minimized. The amount of curvature permissible is fixed by the size of the target region and the difference in magnitude of the magnetic field between adjacent layers (see Fig. 8.10). The second requirement is that the magnetic field is stable in time. Since the magnetic field is created by a current running through a solenoid, stability of the magnetic field translates into current stability. A general expression for the highest permissible fractional magnetic field instability can be written as

$$s = \frac{a\partial_z B - \Delta B}{B_0} \quad (8.4)$$

where  $a = 532\text{ nm}$  is the vertical lattice spacing,  $\partial_z B$  is the gradient along the vertical direction,  $\Delta B$  is the spatial variance of the magnetic field over the target region (chosen to have a diameter of  $100\text{ }\mu\text{m}$  in the following calculations) and  $B_0$  is the magnitude of the offset field in the centre of the target region (see Fig. 8.10). The parameter  $s$  gives us a convenient way to express the required current stability, making the choice of a suitable power supply straightforward.

We decided to use the Feshbach coils in anti-Helmholtz configuration to create a strong gradient and use the gradient coil to provide the offset field<sup>130</sup>. Fig. 4.20 shows the location of the gradient and Feshbach coils around the science chamber. We determine the optimum offset current, i.e. the current that maximises  $s$  in Eq. 8.4, numerically. Fig. 8.11 shows  $s$  as a function of the gradient coil current  $I_{\text{grad}}$  at a Feshbach coil current of  $150\text{ A}$ .

The gradient coil current at which  $s$  is maximized is  $34\text{ A}$ , corresponding to an offset field of  $51\text{ G}$  and a field gradient of  $16.3\text{ G/cm}$ . The Feshbach and gradient coil field gradients are assumed to have equal sign.

The current through the Feshbach coils provides a strong gradient and does not have to be particularly stable. However, the current in the gradient coil, which creates the offset field, has to be stable to less than  $59\text{ ppm}$ . Fortunately, power supplies that can achieve this current stability are commercially available (see section 4.4) and we do not have to implement a current stabilization scheme as in [179, 184].

<sup>130</sup>This might seem counter-intuitive given the nomenclature. The Feshbach coil can be switched from Helmholtz to anti-Helmholtz configuration via an H-bridge (see section 4.4).

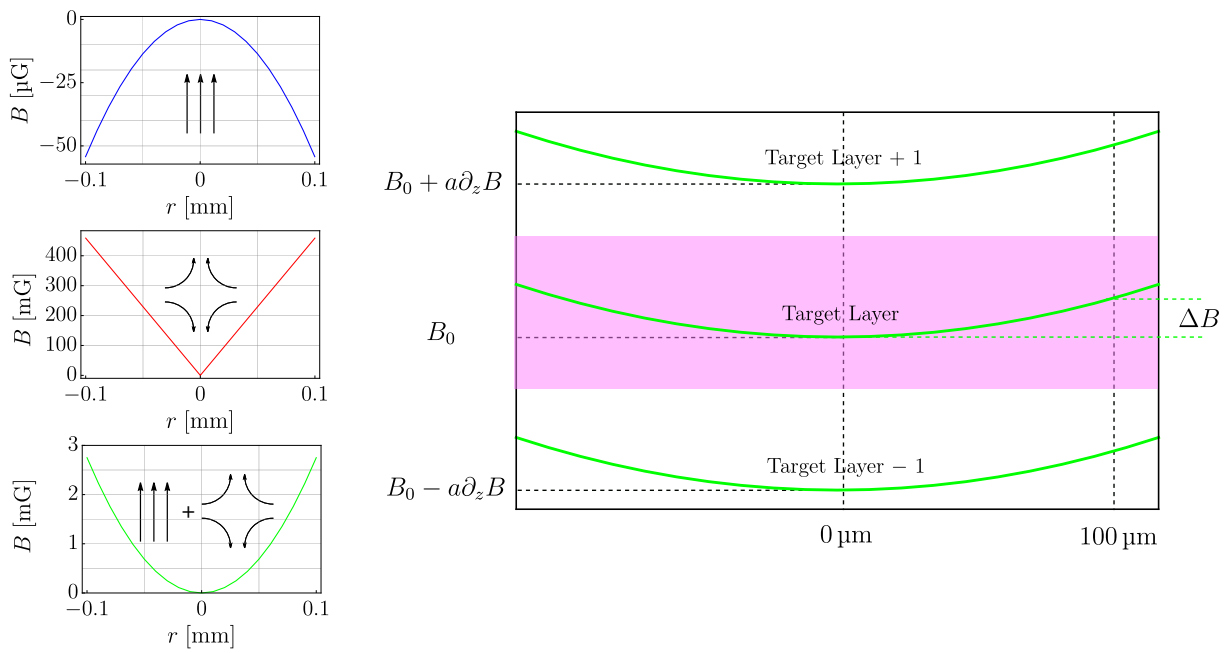


**Figure 8.10** – Left: curvature of B-field magnitude vs radial distance ( $r$ ) for the gradient coil at 34 A only (top), Feshbach coil in quadrupole configuration at 150 A only (centre), and gradient coil and Feshbach coil combined (bottom). The field at  $r = 0$  mm (on-axis) is subtracted. Note that the offset field of the gradient coil causes the combined field of gradient coil and Feshbach coil to have a smaller radial curvature than the Feshbach field itself. Right: combined magnetic field of the gradient coil and Feshbach coil as a function of radial distance for the target layer and adjacent layers. The magenta-coloured region indicates the target region for the LZ-sweep. Fluctuations in the offset magnetic field ( $B_0$ ) can cause adjacent layers to move into the region affected by the LZ-sweep, causing imperfect single-layer preparation.

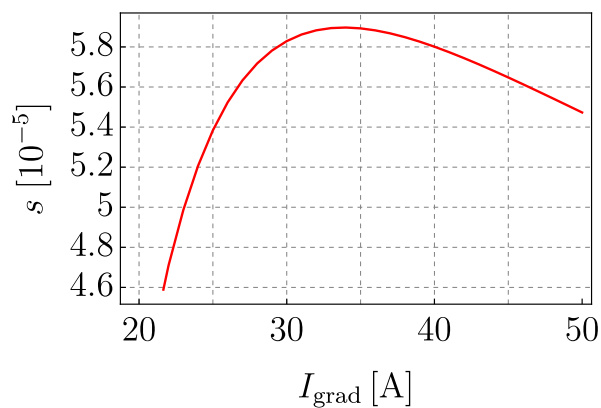


**Figure 8.11** – Required current stability for single-layer selection as a function of gradient coil current. The Feshbach coil is in anti-Helmholtz configuration with a current of 150 A (field gradient of 91.5 G/cm).

## 8.5 Microscope objective

Our microscope objective has a numerical aperture of 0.75 with a working distance of 6 mm and was made by Special Optics. We had a 4 mm diameter hole drilled through the objective<sup>131</sup> to allow absorption imaging light and the vertical lattice to pass through without clipping the lenses. The objective has a diameter of 60 mm and a height of 50 mm (see Fig. 8.12). Its housing is made of Macor, which has a low thermal expansion coefficient, low outgassing rate, is non-magnetic, and does not conduct electricity. Non-conductivity prevents eddy currents from being induced in the objective when ramping the Feshbach field. The objective lenses are AR coated at 767 nm-780 nm and 532 nm and the objective performance is optimized for 532 nm and 768.5 nm. We intend to use 532 nm light to project potentials onto the atoms on a length-scale of the lattice constant. Our calculated minimum projected feature size is  $\sim 350$  nm.

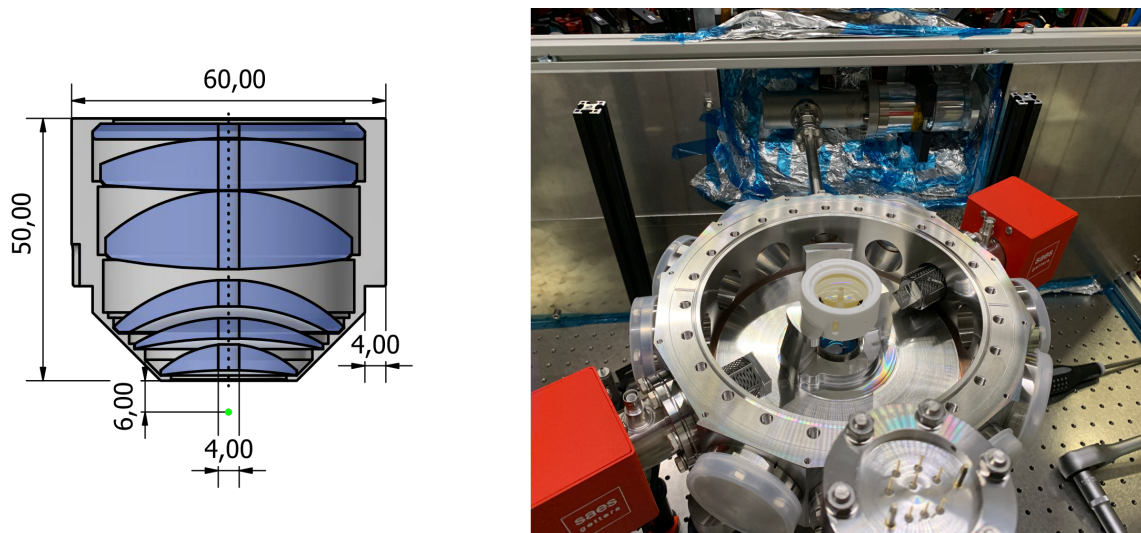


**Figure 8.12** – Left: sketch of objective. All dimensions are in millimetres. The indicated dimensions are correct; the lenses are different from the actual objective for proprietary reasons. The green dot indicates the objective’s focal point. Two pillars in the vacuum chamber support the objective via its 4 mm ledge. Right: objective placed in the science chamber.

The point spread function (PSF), depth of field (DOF) and field of view (FOV) were numerically determined in Zemax<sup>132</sup>. To quantify our resolution we use the Sparrow limit (defined above) and find a minimum resolution of 478 nm and a FWHM of the PSF of 489 nm. We calculate that the resolution decreases with increasing distance from the objective axis (see Fig. 8.13). We define the FOV as twice the distance between the objective axis and the radius at which the resolution increases to 614 nm, i.e. the effective lattice spacing of each of the three fluorescence images. The DOF is defined similarly as the distance between two planes either side of the objective’s focal point and perpendicular to the objective axis which have a Sparrow limit of 614 nm. We calculate the FOV and

<sup>131</sup>Also done by Special Optics.

<sup>132</sup>Many thanks to Dr Tiffany Harte who performed the Zemax calculations and provided data for this chapter.

DOF to be  $180\ \mu\text{m}$  and  $2\ \mu\text{m}$ , respectively. To bring the atoms into the focus of the objective, we will have to carefully move the lattice, since the objective is not moveable.

We tested the resolution of the objective by imaging a USAF test target<sup>133</sup> and a custom star test target<sup>134</sup>. Fig. 8.13 show images of the USAF test target taken with the objective outside of vacuum.

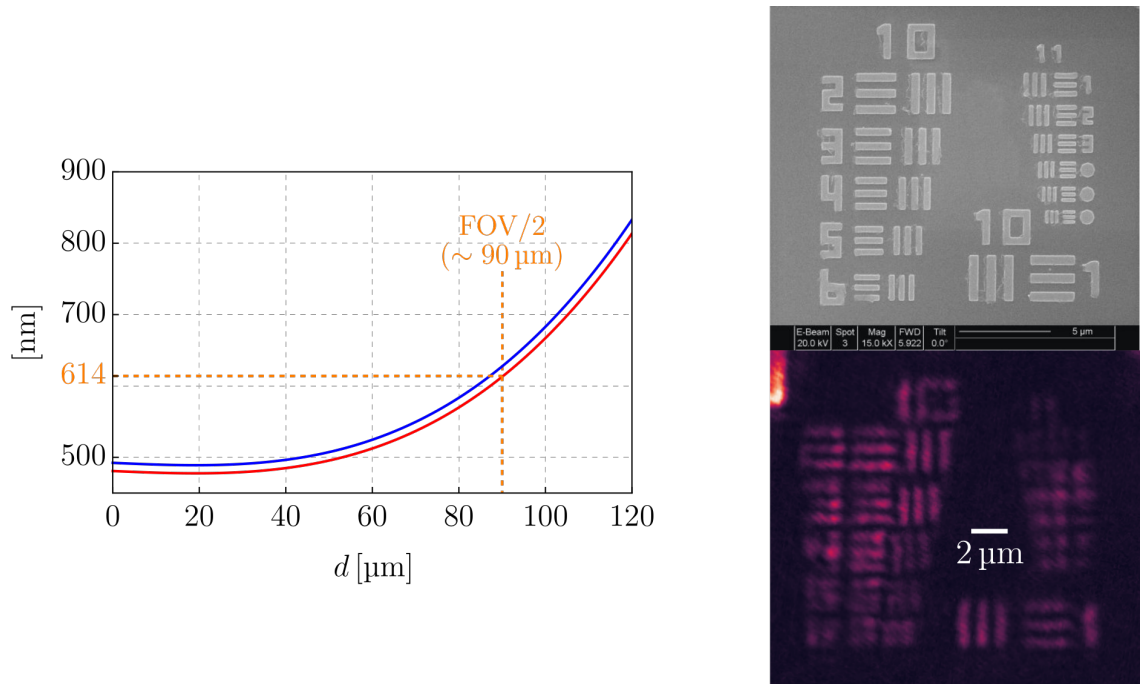


**Figure 8.13** – Left: calculated Sparrow limit (red) and PSF FWHM (blue) as a function of distance from the objective axis. We define the FOV as the distance at which the Sparrow limit increases to 614 nm. Top right: scanning electron microscope image of a USAF test target [226], similar to the one we used for resolution tests. Bottom right: image of a USAF test target with our objective using incoherent light at 767 nm. The white bar indicates the length scale in the image. Contrast is fully lost for feature sizes smaller than  $\sim 350\ \text{nm}$ .

Our star test consisted of a substrate patterned with groups of microscopic holes whose diameters ranged from 270 nm to 650 nm. For the group with an average hole diameter of 350 nm, we found that the average FWHM of the imaged intensity distribution is on the order of 550 nm, which, when deconvolved with the hole size gives a PSF FWHM of  $\sim 510\ \text{nm}$ , which is very close to the simulated value (see [140] for more information).

In addition to the resolution tests, we measured the alignment of the objective lenses via an interferometric probe. Our setup for interferometric alignment is adapted from a technique used at Harvard [227]. The idea is to combine an incoherent source with a delay line so that only reflections from two select optical surfaces can interfere with each other. From the resulting interference pattern, we can reconstruct the relative angle between the lenses in the objective and between the objective and the science chamber

<sup>133</sup>Newport HIGHRES-1.

<sup>134</sup>Kindly provided by the Cavendish NanoPhotonics group.

viewports. More information about the exact implementation of our incoherent source and interferometric alignment can be found in [228].

The performance of the objective depends sensitively on the relative angle between the objective and the vertical lattice planes, or, equivalently, between the objective and the bottom viewport. We therefore ensured that the alignment between the objective and the bottom viewport was within  $0.1^\circ$  after we placed the objective in the science chamber<sup>135</sup>. Before we baked the science chamber, we recorded all discernible interference patterns between the bottom viewport and the objective, and between internal surfaces of the objective. When we performed the same measurements after the bake, we found that the interference patterns were unchanged.

---

<sup>135</sup>Our Zemax simulations indicate a maximum acceptable tilt angle of  $0.5^\circ$ .



## 9 Conclusion & outlook

Despite the vast abundance of theoretical work dedicated to elucidating quantum phases of the kagome lattice, experimental implementations have so far been scarce. To rectify this discrepancy, we have built a versatile quantum simulator to study bosonic and fermionic quantum many-body physics in optical triangular, honeycomb, and kagome lattices. While features are still being added to make our machine even more capable, we have already shown that we can create superfluids and Mott insulators of  $^{87}\text{Rb}$  and  $^{39}\text{K}$  in the optical triangular and kagome lattices and can create negative temperature states in the triangular lattice. These achievements make our machine unique among current optical lattice quantum simulators.

This thesis serves as both a technical manual detailing the theoretical foundations (chapter 2), design (chapter 4), operation (chapter 5 & chapter 6), and current capabilities (chapter 7) of the Cambridge kagome machine, and as a guide for future scientific experiments (chapter 3) and apparatus upgrades (chapter 8).

We will briefly discuss the current goals and possible future developments in the Cambridge kagome lab.

**First measurements** We are currently working on reducing the entropy in the negative temperature state, which we attribute to easily fixable technical noise. Our first objective is to reduce entropy to the point where we see negative temperature superfluid peaks in the triangular lattice. We expect images similar to those observed in [47]. Provided our lifetimes are long enough, we will then move on to negative temperatures in the kagome lattice and check via band-mapping whether we can populate the third band. Atoms in the flat band should condense at the  $\Gamma$  point for shallow lattices and form a trion superfluid for deeper lattices. These signatures are readily observable in momentum space. The BEC at  $\Gamma$  in the third band breaks the  $\mathbb{Z}_2$  symmetry associated with the interchange of vortices with anti-vortices. This should manifest itself in the momentum distribution, provided we can measure the momentum distribution of single layers or manage to sync the phase between different layers. We will also want to explore how phase coherence builds up in the triangular and kagome lattices when melting the negative temperature Mott insulator and should be able to measure the BKT transition temperature.

To prepare the K BEC in the flat band, we could make use of a Wilson line. If we want to stabilize the K BEC, we will have to find a way to prepare a negative temperature state in addition to traversing the Wilson line. At this point, we can measure the geometric properties of flat bands. We should be able to measure the fraction of non-condensed atoms in the flat band as a function of interaction strength and as a function of quantum distance to the K BEC. Additionally, we might determine the Bogoliubov spectrum via e.g. Bragg spectroscopy experiments [229, 230]. This would give us direct access to the speed of sound which is predicted to depend on the flat band quantum metric and should scale linearly with interaction strength [152]. To make use of Wilson lines, we will have to think carefully about how to do frequency ramps (for transport in momentum space) while keeping the relative phase of the kagome lattice locked. We think that our existing hardware will suffice for these measurements.

**Medium term developments** Once we have exhaustively characterized the negative temperature state at unity filling, we will attempt to study the supersolid phase of the flat band at low densities. Preparing low densities in the flat band could prove to be tricky as our negative temperature protocol requires a  $n=1$  Mott insulator. To prepare lower density samples in the flat band, we could prepare a  $n=1$  Mott insulator at positive temperature with some initial confinement. When melting the Mott insulator again in the negative temperature regime we can adjust the overall density via the final trap frequency. In this way, we use the freedom to choose the magnitude of confinement to adjust the effective volume and, consequently, the particle density. Another option would be to lower the density by selectively removing atoms via additional light potentials such as a digital micromirror device (DMD) or the imaging lattice. With the imaging lattice, we should be able to remove five out of every six atoms. The resulting density is well in the regime of the supersolid phase [84]. Our DMD will allow us to selectively remove any desired subset of atoms in the lattice and will therefore enable us to vary the density between experimental runs.

We can measure both CDW and superfluid order via TOF images. We will want to measure their relative weights in the supersolid state as a function of particle density, interaction strength, and temperature. We are also especially interested in the intermediate density regime, between those discussed in [88, 152] and [84], and want to measure how high the boson density has to be for CDW order to vanish.

For the CDW it would be particularly useful to measure local correlators. For this we will have to implement fluorescence imaging with the high-NA objective. We are currently missing a Raman laser for RSC and are still missing the imaging lattice laser. However, even without the imaging lattice it might be possible to measure CDW order, since the unit cell of the CDW is much larger than the lattice spacing. We should also be able to resolve low-density samples in the kagome and triangular lattices.

For high-density samples we will likely need the imaging lattice. In addition, we will install an accordion lattice [231], which has already been tested without the atoms [232]. The accordion lattice will act as an intermediate stage between dipole trap and lattice and will boost the atom number within the single plane in the focus of the objective.

Should the imaging lattice not work as expected, we will likely replace our current 532 nm/1064 nm lattice with a guide star lattice (see [appendix B](#)). Alternatively, it might be possible to use recently developed, machine learning-based, single image super-resolution techniques [233, 234] to achieve single-site resolution in spite of the lattice spacing being smaller than the diffraction limit. With the objective in place, the SHG producing plenty of 532 nm power, and the single-layer selection hardware installed, we are in an excellent position to upgrade to fluorescence imaging soon.

**Long term experiments** In the long term we will move on to  $^{40}\text{K}$  to study fermionic physics in the triangular, honeycomb, and kagome lattices. The path to creating degenerate Fermi gases of  $^{40}\text{K}$  is relatively straightforward, considering that we can already create MOTs. The next steps are achieving sympathetic cooling in the magnetic trap, optical transport, and evaporative cooling in the science chamber. To load the flat band of the kagome lattice we can either use negative temperatures, as in the bosonic case, or set the Fermi level to lie in the flat band by controlling the particle density [235]. This will allow us to prepare flat band fermionic superfluids and, potentially, to test BCS theory in flat

bands.

Once we are able to load fermions into the flat band, we could employ Floquet shaking to induce complex next-to-nearest neighbour tunnelling and engineer a topological flat band [19, 117]. This would give us access to fractional Chern insulator and Laughlin state physics [110, 111]. Laughlin states should be discernible from density correlations which can be resolved by the microscope [236, 237].

For a balanced spin mixture at half filling and strong repulsive interactions, we expect to create an effective spin-1/2 Heisenberg antiferromagnet (HAFM). With the microscope we can measure in-situ spin-correlations and spin structure [20]. It would be especially interesting to measure how the staggered magnetization evolves as temperature is reduced in the kagome lattice. The ground state is expected to be an RVB-state or spin-liquid lacking long-range order. While we will likely not be able to prepare the ground state due to the prohibitively small singlet-gap [129], we might be able to make statements about the emergence of long-range order in the kagome lattice by comparing its behaviour with that in the triangular lattice. The triangular lattice HAFM is expected to have finite staggered magnetization at low temperatures [238], in contrast to the kagome lattice HAFM.

Frustrated systems suffer from the sign problem [239] and so are not easily simulated on classical computers. Our measurements could help to benchmark and improve numerical algorithms designed for frustrated systems, similar to what has already been done for square lattices [12]. We should also be able to prepare and probe doped systems [240], which are likely too complex to simulate classically.

**Other experiments** Finally, while we have focussed most of our discussion on the kagome lattice, we can also perform experiments with the triangular and honeycomb lattices. In the near future we will map the superfluid to Mott insulator transition for the honeycomb lattice and reconcile the measured transition point with the theoretically expected value. This measurement, along with the triangular and kagome transition points will serve to further calibrate and benchmark our quantum simulator. We might also decide to study the trimerized kagome lattice [138], which we can easily do by changing the polarization of the 1064 nm lattice. If we are able to prepare fractional fillings, as we will in any case need to do for supersolid physics, we should be able to study the fractional Mott insulator transition on the trimerized kagome lattice [241].



## A Optics glossary and red table optics layout

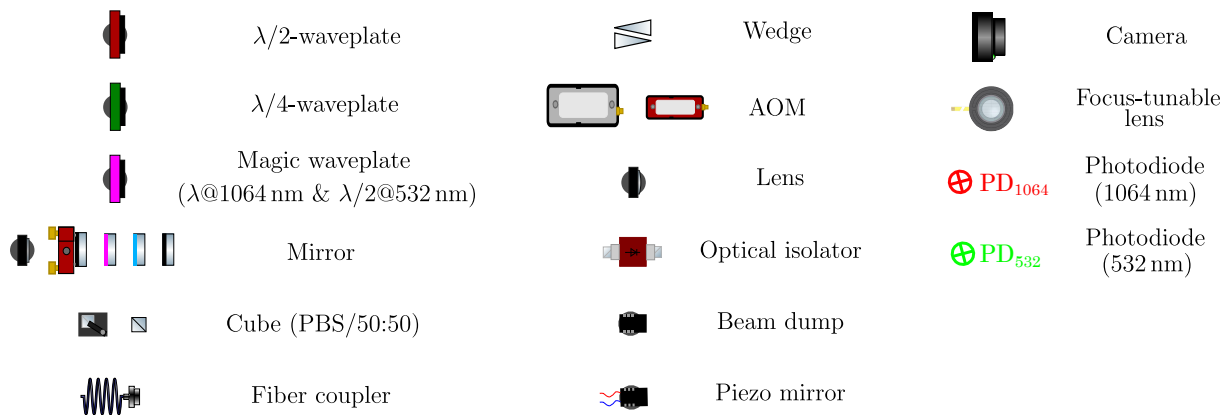


**Figure A.1** – Component glossary



## B Guide star lattice

In this section we introduce a scheme that would allow for super-resolution microscopy of the kagome lattice without needing an additional imaging lattice. The key idea is to implement the kagome lattice with a long lattice wavelength close to the  $4p \rightarrow 3d$  transitions of potassium around 1170 nm-1178 nm. During the imaging process, atoms are pinned in the short-wavelength lattice and the long-wavelength lattice is used to shift the imaging transition out of resonance on two out of every three sites. In this way we can ensure that only every third site fluoresces. The full distribution is recovered by taking three images, each with an effective lattice spacing that is well above the resolution of our imaging system (see Fig. B.1). During exposures, to change which sublattice is imaged, the long-wavelength lattice is moved by changing the phases of the lattice beams. Alternatively, a sublattice can be selected by simply switching off one of the long-wavelength lattice beams.

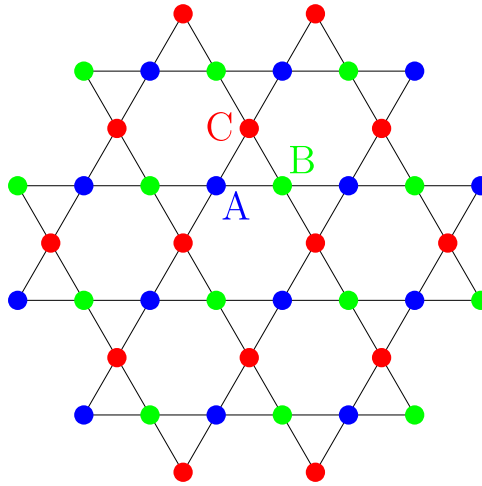


**Figure B.1** – Super-resolution imaging of the kagome lattice. Each exposure captures the fluorescence from one sublattice (A, B, or C sites). After three exposures, the full atom distribution can be reconstructed.

**Deciding on a lattice wavelength** To narrow down which lattice wavelength is optimal for this super-resolution scheme, we will impose a number of constraints.

1. The imaging transition should be on the D1 line and the Raman beam on the D2 line. In section 8.1 we motivated why this configuration is beneficial. This condition constrains the long-wavelength lattice to be a few nm detuned from the  $4p_{1/2} \rightarrow 3d_{3/2}$  transition in potassium ( $\sim 1169.3$  nm).
2. The kagome lattice should be implemented with retro-reflected lattice beams. This increases our lattice depth compared to the interfering case and gives us more flexibility due to the extra phase degrees of freedom.
3. Atoms on imaged sites should be trapped in both the ground ( $4s_{1/2}$ ) and excited ( $4p_{1/2}$ ) states.

4. Atoms should sit at zero intensity in both the ground and excited states to avoid scattering of lattice light. This constrains the wavelength of the long-wavelength lattice to be smaller than that of the  $4p_{1/2} \rightarrow 3d_{3/2}$  transition, since the polarizability for the  $4p_{1/2}$ -state is negative in this region (see Fig. B.2)<sup>136</sup>. This condition also ensures that the potential that atoms in the  $4s_{1/2}$  state experience is unaffected by the long-wavelength lattice.
5. The shift of the imaging transition on unimaged sites should be several tens of MHz. This constrains the long-wavelength lattice to be within 1 nm-2 nm of the  $4p_{1/2} \rightarrow 3d_{3/2}$  transition

A long-wavelength lattice at 1168 nm fulfils all these constraints and we will proceed to calculate various properties of a retro-reflected kagome lattice with lattice wavelengths of 584 nm and 1168 nm.

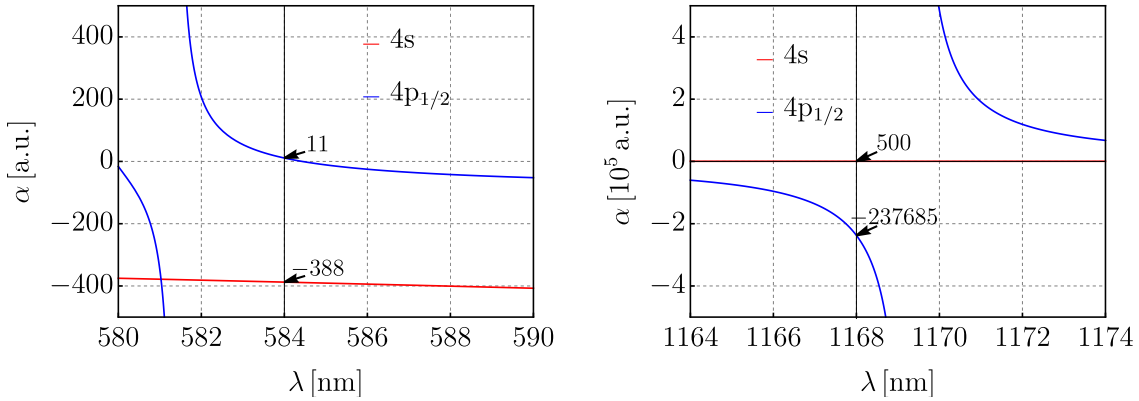


**Figure B.2** – Polarizabilities of the potassium  $4s_{1/2}$ -state (red) and  $4p_{1/2}$ -state (blue) around 584 nm (left) and 1168 nm (right). At 1168 nm, the polarizability in the  $4p_{1/2}$  is  $-475$  times the polarizability in the  $4s_{1/2}$  state.

As we can see in Fig. B.2, the polarizability of the  $4s_{1/2}$ - and  $4p_{1/2}$ -states is inverted at 1168 nm. This means that the long lattice is a repulsive triangular lattice for the s-state, which in combination with the short lattice, forms a kagome lattice. For the  $4p_{1/2}$ -state however, the long lattice is an attractive triangular lattice, which is the configuration we desire for imaging. We thus do not have to invert the potential between physics and imaging, because the polarizations are such that we automatically get the kagome lattice in the s-state and a site-selective lattice in the p-state. Note that the same holds true for the interfering kagome lattice where we are not able to invert potentials via a phase change.

**Calculations** The lattice and sublattice spacings of the 584 nm/1168 nm kagome lattice are 337 nm and 674 nm, respectively. Fig. B.3 shows the calculated tunnelling rate and band gap as a function of lattice depth and lattice beam power.

<sup>136</sup>Note that while a retro-reflected triangular lattice allows us to invert the potential, the lattice has to be blue-detuned to create a triangular lattice potential where the lattice sites have zero intensity.

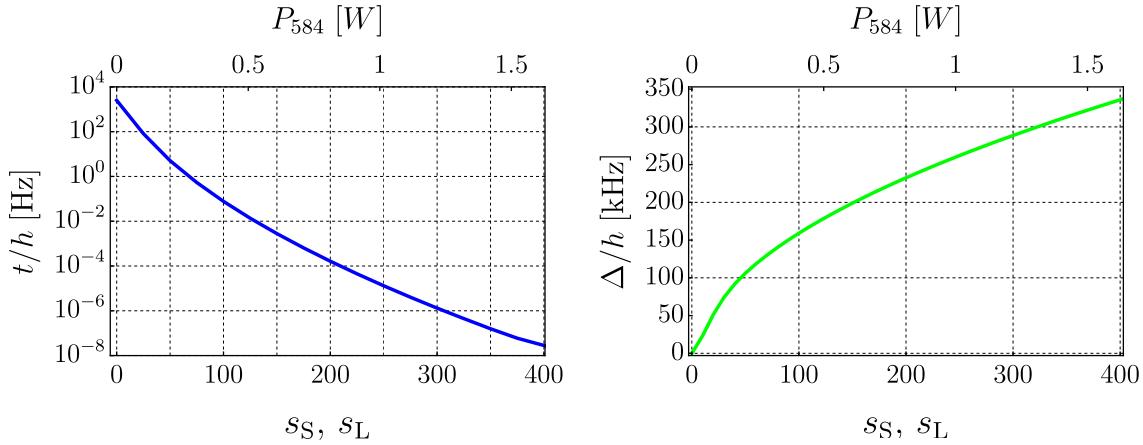


**Figure B.3** – Tunnelling rate,  $t$ , (left) and band gap,  $\Delta$ , (right) as a function of lattice depth and lattice beam power for the 584 nm/1168 nm, retro-reflected kagome lattice. We assume lattice beam waists of  $100 \mu\text{m} \times 50 \mu\text{m}$  (horizontal  $\times$  vertical) and equal lattice depths for the short- and long lattice, i.e.  $s_S = s_L$ .

Since we are working with a retro-reflected lattice and the polarizability of potassium is  $\sim 50\%$  larger at 584 nm than at 532 nm, we only require  $\sim 40\%$  of 584 nm power compared to 532 nm to achieve similar tunnelling rates.

Even for low 1168 nm powers, the imaging transition can be shifted by several MHz on unimaged sites. For a long lattice with 55 mW per beam we calculate that the imaging transition on unimaged sites is shifted by roughly  $10\Gamma$ <sup>137</sup>, while the imaged sites remain unaffected. During imaging it should thus be possible to completely suppress fluorescence on unimaged sites. This technique can be easily adapted to other atomic species (provided the appropriate wavelengths are available) and other superlattice geometries.

An open question is whether there are lasers that can emit sufficient power at 1168 nm to get a sufficient amount of frequency-doubled 584 nm power. Fortunately, commercial lasers for 589 nm/1178 nm already exist<sup>138</sup>, which are commonly used as laser guide stars on large terrestrial telescopes, and can deliver  $>20$  W at 589 nm. It should therefore also be possible to construct a laser that can deliver similar powers at 584 nm/1168 nm.

**Raman-Selective Imaging** One could also target the Raman transition instead of the imaging transition to selectively suppress fluorescence from unimaged sites. The idea here is to shift the sidebands of imaged and non-imaged sites with respect to each other and ensure that the Raman lasers only target the sidebands of the imaged sites. The shift between sideband frequency and carrier is equal to the on-site trap frequency (see Fig. B.4). Shifting the sidebands between imaged and non-imaged sites thus requires the ability to selectively change the trap frequency of a subset of lattice sites. In a superlattice (and in particular, in the kagome lattice), the long-wavelength lattice can be used to shift the trap frequencies of a subset of sites in the short-wavelength lattice. As discussed previously, quantum gas microscopes require some process that ensures that the atoms are fluorescing, i.e. that atoms are pumped into the imaging transition. If the red sideband is driven exclusively, eventually atoms will end up in the motional ground state and will

<sup>137</sup> $\Gamma \approx 6$  MHz is the natural linewidth of the imaging transition.

<sup>138</sup>Toptica SodiumStar

become dark to the Raman transition, which in turn prevents them from being pumped into the ground state of the repump transition. In this case fluorescence quickly ceases and not enough photons are scattered to image the atom distribution. A common fix to this problem is to broaden out the Raman transition or shift the Raman resonance somewhere between the red sideband and the carrier transition. While the red sideband is still predominantly driven, occasionally atoms will be excited via the carrier transition and be repumped, causing fluorescence.

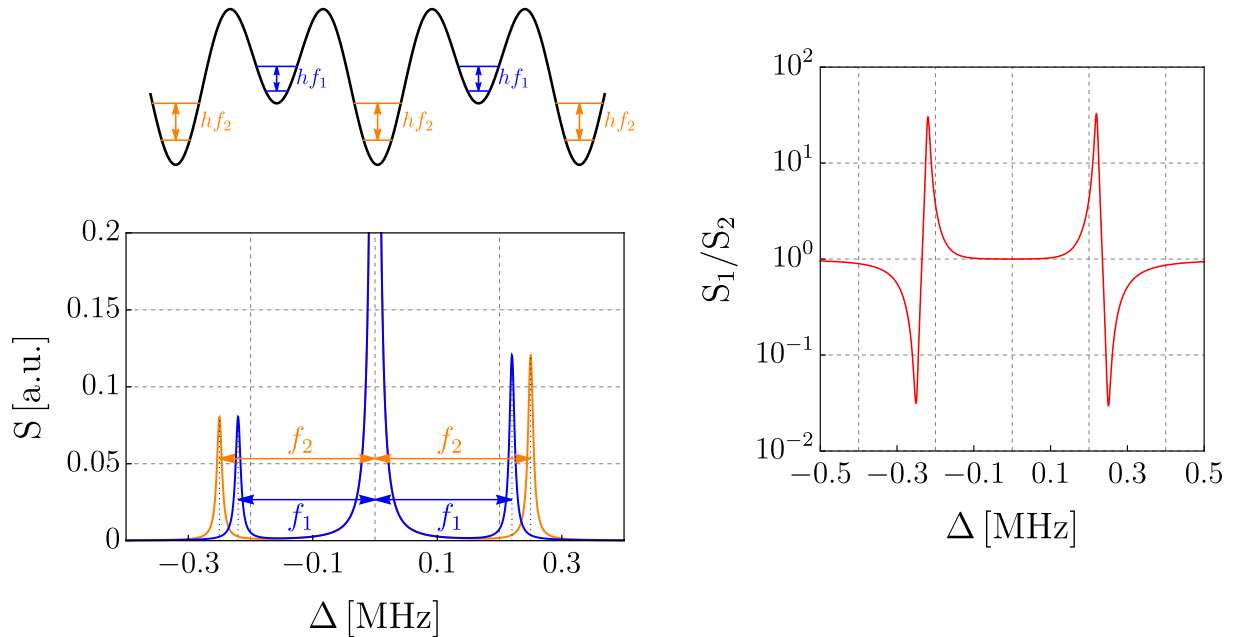


**Figure B.4** – Raman-selective Imaging. In a commensurate superlattice such as the kagome lattice, it is possible to change the curvature of a subset of short lattice sites with a long lattice. As the long lattice depth is increased, the HO spacing of sites in the targeted sublattice is increasingly shifted away from other sites (left). This can be used to have selected sites fluoresce more strongly than sites that are not in the selected sublattice (right). Here,  $S$  is the Rabi frequency of the Raman transition and  $S_1/S_2$  is the ratio of Rabi frequencies between imaged and unimaged sites. We assume parameters of  $\Gamma = 10$  kHz,  $f_1 = 220$  kHz,  $f_2 = 250$  kHz,  $\eta = 0.2$  (Lamb-Dicke parameter) and  $n = 2$  (motional quantum number).

For Raman-selective imaging it is paramount to avoid targeting the carrier transition, as it is independent of the trap frequency and thus site-independent. We therefore need to find a way to keep the Raman cycle of imaged sites going without targeting the carrier transition. One way in which this can be done is to have two pairs of Raman beams, one targeting the red sideband, the other the blue sideband. A weak drive on the blue sideband (weak with respect to the red sideband drive) would ensure that targeted atoms are continually pumped into the ground state of the repump transition. The blue sideband is evidently trap-frequency dependent. Thus it is possible to have atoms on imaged sites continually fluoresce while suppressing fluorescence on unimaged sites.

## C Lattice curvature

One of the main advantages of using optical lattices for quantum simulation is that the Hamiltonian can be calculated a priori with a very high degree of accuracy. Like any real system, however, optical lattices suffer from unwanted inhomogeneities such as lattice curvature<sup>139</sup>. As we already saw in [section 3.1.2](#), lattice curvature can be regarded as an additional term in the Bose-Hubbard model,

$$H_{BH} = -t \sum_{\langle i,j \rangle} \hat{a}_i^\dagger \hat{a}_j + \frac{U}{2} \sum_i \hat{n}_i(\hat{n}_i - 1) + V_0 \sum_i \hat{n}_i^2, \quad (\text{C.1})$$

where the magnitude of  $V_0$  is determined by the curvature of the lattice. To create negative temperatures, it is vital to know the amount of lattice curvature we should expect and what means we have to counteract it.

### C.1 Square lattice

In a square lattice with lattice beams propagating along the  $x$  and  $y$  directions, the curvature along  $x$  ( $y$ ) is caused by the lattice beam propagating along  $y$  ( $x$ ). We can distinguish between lattice curvature due to an energy offset of the lattice sites and lattice curvature caused by the inhomogeneity of the on-site, zero-point energy [40]. Both can be approximated as being harmonic and the magnitude of the third term in the Hubbard model is thus given by the sum of the two contributions. However, as we will derive further on, the magnitude of the two curvatures (quantified by their harmonic trap frequency) scale differently with lattice beam power.

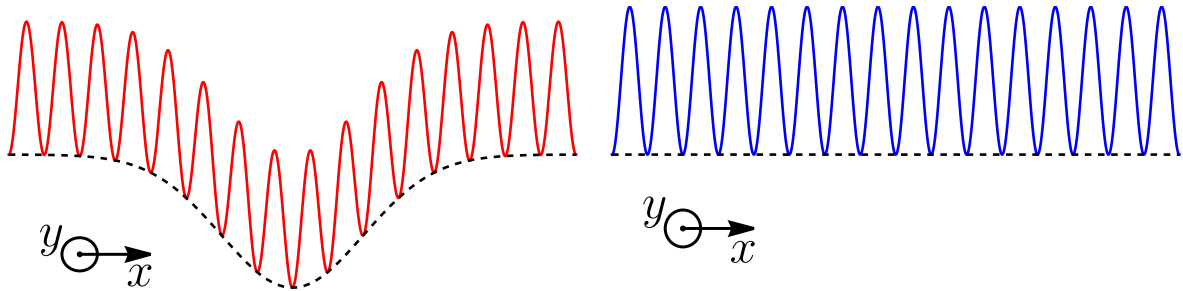


**Figure C.1** – Left: potential of a red-detuned square lattice. The lattice curvature along  $x$  is caused by the lattice beam propagating along  $y$ . The dashed line is a Gaussian envelope. The lattice curvature is exaggerated for illustrative purposes. Right: potential of a blue-detuned square lattice. Since the potential minima are the points of zero intensity, a blue-detuned lattice does not suffer from lattice curvature due to inhomogeneous energy offsets of the lattice sites

**Lattice curvature due to energy offsets** A schematic of how the lattice site offset energy changes when the lattice beams are Gaussian is shown in [Fig. C.1](#). Blue-detuned lattices do not suffer from lattice curvature caused by energy offsets. We will thus derive

<sup>139</sup>As mentioned previously, we use the term ‘lattice curvature’ exclusively to describe large-scale variations of the lattice potential, not curvature on the length-scales of individual lattice sites.

lattice curvature only for red-detuned lattices. The potential of a red-detuned square lattice can be written as

$$V(x, y) = -V_0 \left( \cos(kx)^2 e^{-\frac{2y^2}{w^2}} + \cos(ky)^2 e^{-\frac{2x^2}{w^2}} \right), \quad (\text{C.2})$$

where  $k$  is the magnitude of the lattice beam wavevector and  $w$  is the lattice beam waist. As can be seen in Fig. C.1, the energy offset of lattice sites is given by the Gaussian envelope of the lattice beams, i.e.

$$E_{\text{off}}(x, y) = -V_0 \left( e^{-\frac{2y^2}{w^2}} + e^{-\frac{2x^2}{w^2}} \right). \quad (\text{C.3})$$

For small  $x, y$ , this expression can be approximated as a harmonic potential:

$$\begin{aligned} E_{\text{off}}(x, y) &\approx -V_0 \left( 1 - \frac{2y^2}{w^2} + 1 - \frac{2x^2}{w^2} \right) \stackrel{!}{=} c + \frac{1}{2} m \omega_{\text{off}}^2 (x^2 + y^2) \\ &\Rightarrow \omega_{\text{off}} = \frac{1}{w} \sqrt{\frac{4V_0}{m}} \propto V_0^{\frac{1}{2}}. \end{aligned} \quad (\text{C.4})$$

Lattice curvature caused by lattice site offset energy is thus confining<sup>140</sup> and the associated trap frequency scales as  $V_0^{\frac{1}{2}}$ .

**Lattice curvature due to on-site energy** The second contribution to lattice curvature arises due to the reduction of on-site energy with decreasing lattice depth. Starting from the optical lattice potential,

$$V(x, y) = -V_0 \left( \cos^2(kx) e^{-\frac{2y^2}{w^2}} + \cos^2(ky) e^{-\frac{2x^2}{w^2}} \right), \quad (\text{C.5})$$

the on-site trap frequencies can be found by expanding the  $\cos^2$  terms,

$$\begin{aligned} -V_0 e^{-\frac{2y^2}{w^2}} \cos^2(kx) &\stackrel{kx \ll 1}{\approx} -V_0 e^{-\frac{2y^2}{w^2}} (1 - k^2 x^2) \stackrel{!}{=} c + \frac{1}{2} m \omega_{\text{on-site},x}^2 x^2 \\ &\Rightarrow \omega_{\text{on-site},x} = \sqrt{\frac{2V_0 k^2}{m}} e^{-\frac{y^2}{w^2}}, \end{aligned} \quad (\text{C.6})$$

and correspondingly for  $\omega_{\text{on-site},y}$ . The total on-site energy is

$$E_{\text{on-site}} = \frac{\hbar}{2} (\omega_{\text{on-site},x} + \omega_{\text{on-site},y}) = \frac{\hbar}{2} \sqrt{\frac{2V_0 k^2}{m}} \left( e^{-\frac{x^2}{w^2}} + e^{-\frac{y^2}{w^2}} \right). \quad (\text{C.7})$$

It is apparent that the on-site HO ground-state energy drops off as the distance from the centre is increased. This second contribution to lattice curvature thus creates an anti-confining potential, regardless of whether the lattice is blue or red detuned. To quantify the magnitude of curvature, we can again expand the function in Eq. C.7 into powers of  $x$  and  $y$  and extract a harmonic trap frequency which we will call  $\omega_{\text{on-site}}$ ,

<sup>140</sup>since the energy increases with distance from the centre.

$$\begin{aligned}
E_{\text{on-site}} &= \frac{\hbar}{2} \sqrt{\frac{2V_0 k^2}{m}} \left( e^{-\frac{x^2}{w^2}} + e^{-\frac{y^2}{w^2}} \right) \approx \frac{\hbar}{2} \sqrt{\frac{2V_0 k^2}{m}} \left( 1 - \frac{x^2}{w^2} + 1 - \frac{y^2}{w^2} \right) \\
&\stackrel{!}{=} c - \frac{1}{2} m \omega_{\text{on-site}}^2 (x^2 + y^2) \\
\Rightarrow \omega_{\text{on-site}} &= \frac{1}{w} \left( \frac{2V_0 \hbar^2 k^2}{m^3} \right)^{\frac{1}{4}}.
\end{aligned} \tag{C.8}$$

We can see that the trap frequency associated with the on-site energy scales as  $V_0^{\frac{1}{4}}$ . It is generally much smaller than confinement due to offset energy.

Having determined how different lattice curvature contributions scale with the lattice potential depth (and thus power), we can move on to look at the triangular, honeycomb, and kagome lattices. Before calculating the curvatures for the kagome lattice, we will calculate them for the short-wavelength lattice (triangular) and long-wavelength lattice (honeycomb) separately. For the entirety of this chapter, we will assume beam waists of  $w_h \times w_v = 100 \mu\text{m} \times 50 \mu\text{m}$ , where  $w_h$  and  $w_v$  are the horizontal and vertical beam waists, respectively. All results are for  $^{39}\text{K}$ .

## C.2 Triangular lattice

The blue-detuned triangular lattice is created using three interfering 532 nm beams and the potential is given by

$$V_{\text{tri}}(\mathbf{r}) = V_S \left| \sum_{j=1}^3 \mathbf{p}_j e^{i\mathbf{k}_j \cdot \mathbf{r}} e^{-\frac{(\mathbf{p}_j \cdot \mathbf{r})^2}{w_h^2}} \right|^2, \tag{C.9}$$

where  $\mathbf{p}$  and  $\mathbf{k}$  are as in [section 2.1](#) and  $w_h$  is the horizontal lattice beam waist (assumed to be equal for all three lattice beams). We then express the lattice depth in terms of power  $P_{532}$ ,  $V_S = 2U_{532}P_{532}/(\pi w_h w_v) > 0$ .

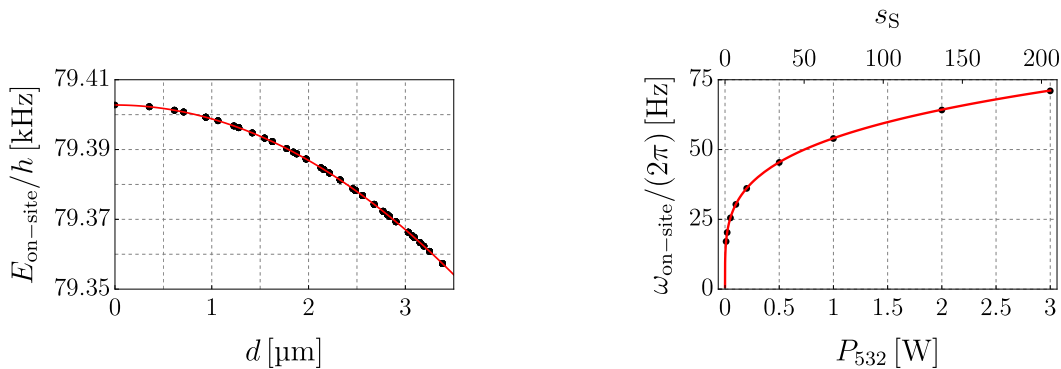


**Figure C.2** – Left: on-site energy as a function of distance from the centre of the lattice, for a lattice beam power of 0.5 W. The red line shows a harmonic fit used to extract an anti-confinement frequency. Right: anti-confinement frequency as a function of 532 nm lattice beam power. The red line is a guide to the eye which is proportional to  $P_{532}^{\frac{1}{4}}$ .

The offset and on-site energies are determined numerically by calculating the values and curvatures of Eq. C.9 at the lattice sites (see Fig. C.2). We extract the on-site trap frequency by finding the eigenvalues of the Hessian of the potential at the lattice sites and use Eq. C.7 to calculate the on-site energies [177]. The lattice curvature behaves exactly as expected from the blue-detuned square lattice. The offset energy is constant since the lattice sites are located where the intensity is zero. The anti-confining potential due to inhomogeneous on-site energies is still present however.

Fig. C.2 shows that the on-site anti-confinement is nearly perfectly harmonic over small distances from the trap centre. For larger distances, the harmonic approximation starts to increasingly deviate from the exact result (see Fig. C.3) due to higher-order terms in the Gaussian lattice beam intensities.

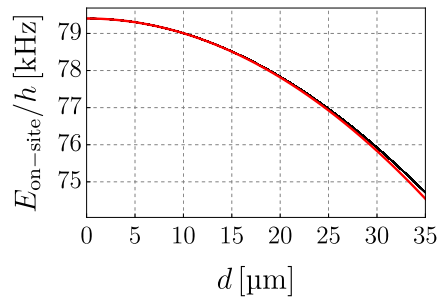


**Figure C.3** – On-site anti-confinement in the triangular lattice for a lattice beam power of 0.5 W over a large distance. The black line shows the numerically calculated on-site trap frequency for  $\sim 30,000$  sites in the centre of the lattice. The red line is a harmonic fit to the on-site energies of all sites within a radius of 5  $\mu\text{m}$  from the centre of the lattice.

Even for distances up to 35  $\mu\text{m}$ , corresponding to several tens of thousands of sites, the harmonic approximation is very accurate.

### C.3 Honeycomb lattice

The long-wavelength honeycomb lattice is formed by three interfering red-detuned lattice beams. The potential can be written as

$$V_{\text{hon}}(\mathbf{r}) = V_L \left| \sum_{j=1}^3 \mathbf{p}_j e^{i\mathbf{k}_j \cdot \mathbf{r}} e^{-\frac{(\mathbf{p}_j \cdot \mathbf{r})^2}{w_h^2}} \right|^2, \quad (\text{C.10})$$

where  $V_L = 2U_{1064}P_{1064}/(\pi w_h w_v) < 0$  and  $P_{1064}$  is the power of each lattice beam. The numerical results are shown in Fig. C.4. We determine the on-site and offset energies analogously to the triangular lattice case.

As expected from our treatment of the square lattice, the red-detuned honeycomb lattice shows a harmonic increase of offset energy and a harmonic decrease of on-site energy for small distances from the centre of the lattice. The magnitudes of both curvature components (expressed in HO frequencies) also show the same scaling with power as seen in the square lattice. As shown in Fig. C.5, the harmonic approximation is very accurate at large distance for both on-site energies as well as the offset energies.

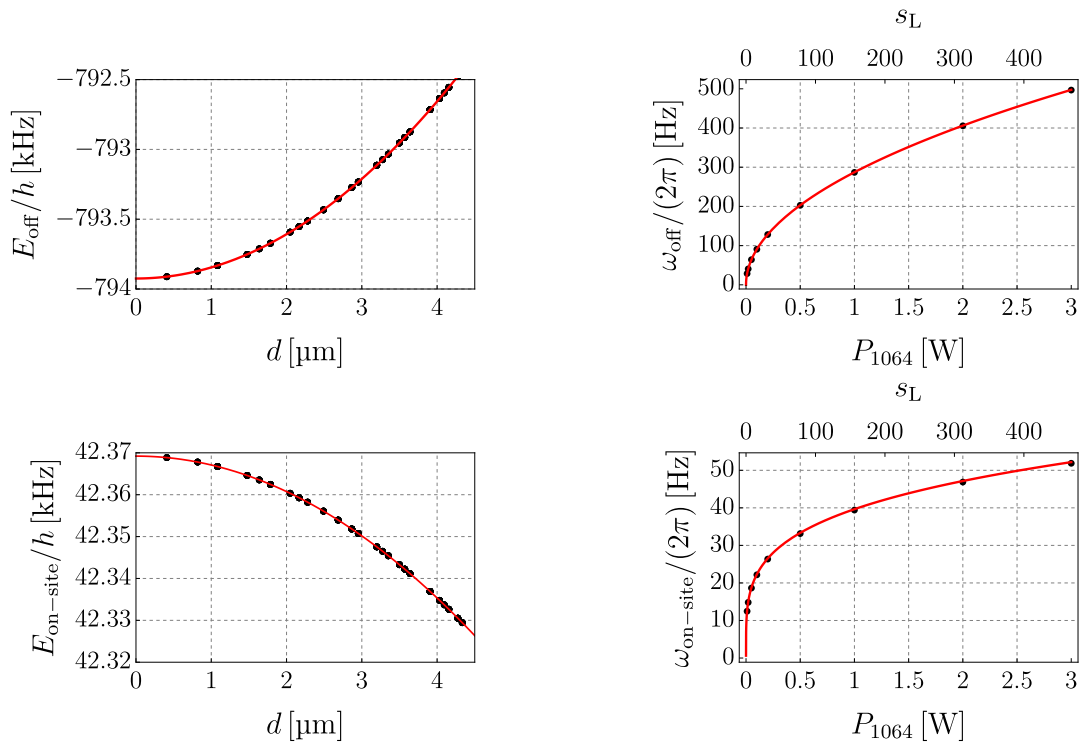


**Figure C.4** – Top (bottom) left: offset (on-site) energy as a function of distance in the honeycomb lattice, for a lattice beam power of 0.5 W. The red line is a harmonic fit used to extract  $\omega_{\text{off}}$  ( $\omega_{\text{on-site}}$ ). Top (bottom) right:  $\omega_{\text{off}}$  ( $\omega_{\text{on-site}}$ ) as a function of lattice beam power  $P$ . The red line is a guide to the eye with a  $P^{\frac{1}{2}}$  ( $P^{\frac{1}{4}}$ ) dependence.

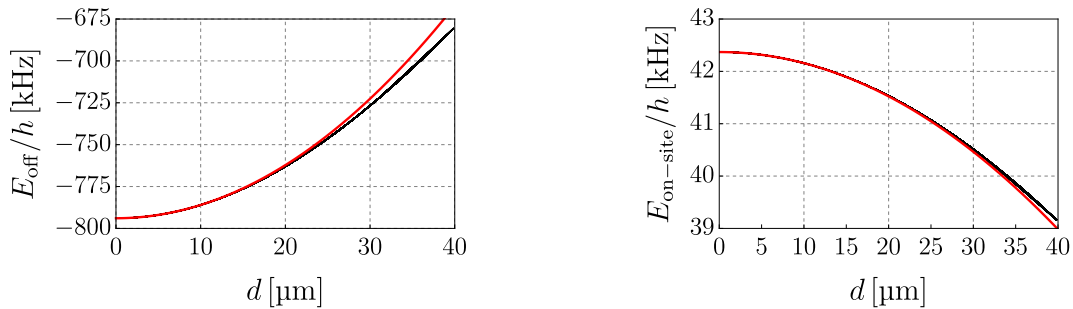


**Figure C.5** – Left (right): offset (on-site) energy over large distances from the centre of the honeycomb lattice for lattice beam powers of 0.5 W. Black lines show the numerically calculated values of the central  $\sim 17,000$  sites. Red lines are a harmonic fit to points within a distance of 5  $\mu\text{m}$  of the centre.

## C.4 Kagome lattice

Now that we have discussed the (red-detuned) honeycomb and (blue-detuned) triangular lattices, we can move on to the combination of the two, i.e. the kagome lattice. The potential is given by

$$V_{\text{kag}}(\mathbf{r}) = V_S \left| \sum_{j=1}^3 \mathbf{p}_j e^{2i\mathbf{k}_j \cdot \mathbf{r}} e^{-\frac{(\mathbf{p}_j \cdot \mathbf{r})^2}{w_h^2}} \right|^2 + V_L \left| \sum_{j=1}^3 \mathbf{p}_j e^{i\mathbf{k}_j \cdot \mathbf{r}} e^{-\frac{(\mathbf{p}_j \cdot \mathbf{r})^2}{w_h^2}} \right|^2, \quad (\text{C.11})$$

where  $\mathbf{k}$  is the wavevector of the long-wavelength lattice. As seen in Fig. C.6, the kagome lattice exhibits both types of lattice curvature.

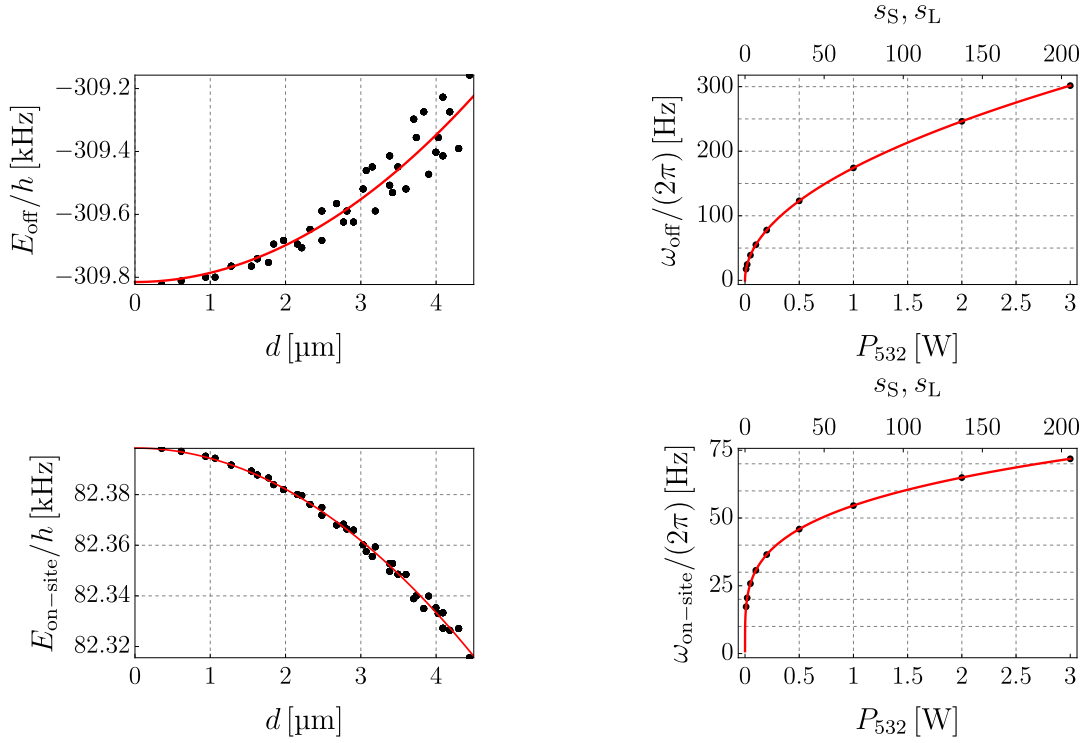


**Figure C.6** – Top (bottom) left: offset (on-site) energy as a function of distance in the kagome lattice, for lattice beam powers of  $P_{532}=0.5$  W and  $P_{1064}=0.22$  W. The red line is a harmonic fit and is used to extract a trap frequency, expressed as  $\omega_{\text{off}}$  ( $\omega_{\text{on-site}}$ ). Top (bottom) right:  $\omega_{\text{off}}$  ( $\omega_{\text{on-site}}$ ) as a function of lattice beam power  $P_{532}$ . The red line is a guide to the eye with a  $P^{\frac{1}{2}}$  ( $P^{\frac{1}{4}}$ ) dependence. The lattice depths are chosen to be equal for the 532 nm and 1064 nm beams. Therefore  $P_{1064} \approx 0.44P_{532}$

We see the typical  $P^{\frac{1}{2}}$  ( $P^{\frac{1}{4}}$ ) dependence of trap frequencies caused by inhomogeneous offset energy (on-site energy). It is apparent in Fig. C.6 that the spread of both the offset energy and on-site energy is non-zero, whereas there is no spread in the pure triangular and pure honeycomb case. This means that compensation cannot be done perfectly and that the lattice will always suffer from small inhomogeneities. Fig. C.7 shows how the on-site and offset energies evolve with distance. The offset energy has a severe spread for large distances from the centre of the lattice.

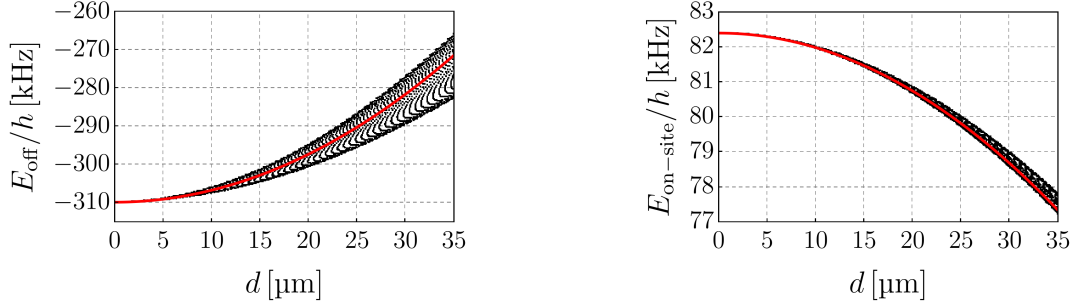


**Figure C.7** – Left (right): offset (on-site) energies for the central  $\sim 33,000$  sites in the optical kagome lattice (black points). The red lines are harmonic fits to sites within  $5 \mu\text{m}$  of the lattice centre.

**Compensating lattice curvature** We found that in the honeycomb and kagome lattices, the confining potential due to offset energy is roughly an order of magnitude larger than that due to the on-site energies. To create a negative temperature state we also need a vertical lattice, which for our machine has a wavelength of  $1064 \text{ nm}$ . The vertical lattice thus creates additional confinement. For a  $30E_R$  deep vertical lattice, the horizontal confinement is  $\sim 60 \text{ Hz}$ <sup>141</sup>. Additionally, the dipole trap creates a confinement of  $\sim 35 \text{ Hz}$  at  $0.5 \text{ W}$  (see [section 6.4](#)). Thus, in our machine, confinement is generally much stronger than anti-confinement. To create anti-confining potentials for negative temperatures, we use the blue-detuned vertical dipole beam. We can write the total confinement as

$$V_0 = \frac{1}{2}m \sum_i \omega_i^2, \quad (\text{C.12})$$

with

$$\begin{aligned} \omega_{\text{tot}}^2(P) &= \sum_i \omega_i^2 = \omega_{\text{kag,off}}^2 - \omega_{\text{kag,os}}^2 + \omega_{\text{vert}}^2 + \omega_{\text{dip}}^2 - \omega_{\text{vd}}^2(P) \\ &= \omega_0^2 - \omega_{\text{vd}}^2(P). \end{aligned} \quad (\text{C.13})$$

Using

$$\omega_{\text{vd}}^2(P) = \alpha P \quad (\text{C.14})$$

we can write the cumulative confinement (expressed as a trap frequency) as

$$\omega_{\text{tot}}(P) = \omega_0 \sqrt{1 - \frac{P}{P_0}}, \quad (\text{C.15})$$

where  $P_0 = \omega_0^2/\alpha$  is the power needed in the vertical dipole beam to fully compensate the confining potentials. [Fig. C.8](#) shows how the total trap frequency evolves as a function of the vertical dipole beam power.

<sup>141</sup>The vertical lattice has a design waist of  $100 \mu\text{m}$ .

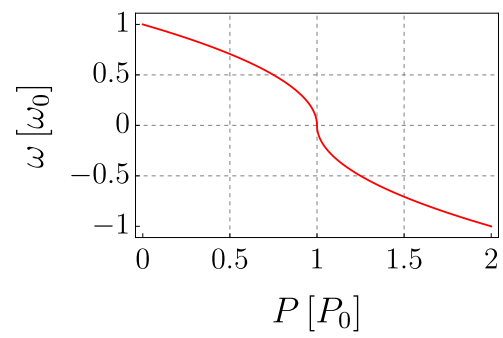


**Figure C.8** – Total confinement as a function of vertical dipole beam power. Positive (negative) values of  $\omega$  indicate a cumulative confining (anti-confining) potential

## D Wilson lines in the kagome lattice

In this chapter we will discuss Wilson lines in the kagome lattice and how the results compare with the honeycomb lattice. We will first cover the honeycomb lattice Wilson lines to recover the results obtained in [175] and then move on to calculate the Wilson lines in the kagome lattice. Wilson lines can be measured in cold-atom experiments via fast transport in momentum space. For sufficiently fast ramps from one momentum to another, the dynamical contribution to wave function evolution is negligible compared to the geometric contribution [175]. Thus, Wilson lines encode information about the geometric properties of a Bloch band.

In a lattice model in the tight-binding limit, the Wilson line can be written as an overlap between two Bloch states [175, 242],

$$W_{\mathbf{q}_0 \rightarrow \mathbf{q}_1}^{mn} = \langle u_{\mathbf{q}_1}^n | u_{\mathbf{q}_0}^m \rangle, \quad (\text{D.1})$$

where  $|u_{\mathbf{q}_0}^m\rangle$  is the Bloch state with momentum  $\mathbf{q}_0$  in the  $m^{\text{th}}$  band. Thus,  $|W_{\mathbf{q}_0 \rightarrow \mathbf{q}_1}^{mn}|^2$  is equal to one minus the squared quantum distance between the two Bloch states (see section 3.3.1). For this chapter we will only be interested in Wilson lines that connect to the  $\Gamma$  point<sup>142</sup>,

$$W_{mn}(\mathbf{q}) := W_{\Gamma \rightarrow \mathbf{q}}^{mn}. \quad (\text{D.2})$$

We will only show tight-binding results. In the limit of deep optical lattices, the tight-binding result is recovered in both the honeycomb [175] and kagome<sup>143</sup> lattices.

### D.1 Honeycomb lattice

The eigenstates of the honeycomb lattice can be written as [160]

$$u_{\mathbf{q}}^{\pm} = \frac{1}{\sqrt{2}} \begin{pmatrix} \mp 1 \\ e^{i\Theta_{\mathbf{q}}} \end{pmatrix}. \quad (\text{D.3})$$

Fig. D.1 shows  $|W_{11}(\mathbf{q})|^2$  for the honeycomb lattice. Since we are dealing with a two-band model we can write

$$|W_{12}|^2 = 1 - |W_{11}|^2, \quad (\text{D.4})$$

i.e. whatever population is not in the ground (first) band is necessarily in the second band.

<sup>142</sup>Since we start from a BEC at  $\Gamma$ , we generally only care about the overlap between the BEC and other states.

<sup>143</sup>based on unpublished numerical results.

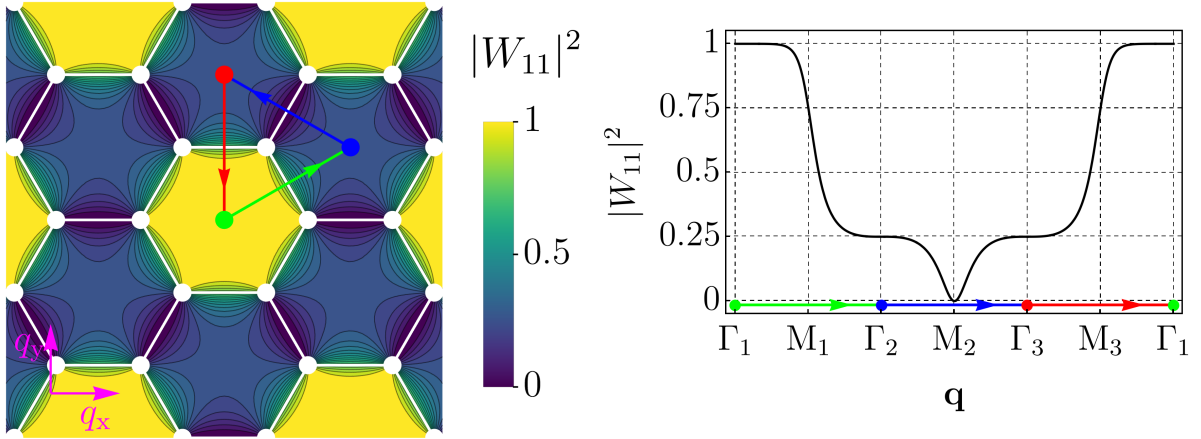


**Figure D.1** – Left:  $|W_{11}(\mathbf{q})|^2 = |W_{11}(q_x, q_y)|^2$  as a function of momentum. Reciprocal unit cells are drawn in white. The path in reciprocal space along which  $|W_{11}|^2$  is plotted on the right is indicated with arrows. Right:  $|W_{11}|^2$  plotted along the path indicated on the left plot. Note that this is the same result obtained in [175] and that the same behaviour would be obtained if the path were straight instead of triangular.

## D.2 Kagome lattice

The kagome lattice has three bands instead of two, which makes the maths somewhat more complicated. To make the calculation feasible it is important to find a convenient expression for the eigenstates of the kagome lattice, after which calculating the Wilson lines is straightforward using Eq. D.1. The eigenvalues and eigenvectors of the three tight-binding kagome bands are given by

$$\begin{aligned}
 E_1 &= -t(1 + |\gamma(\mathbf{q})|), & u_{\mathbf{q}}^1 &= N_1 \begin{pmatrix} \cos\left(\frac{1}{2}(\mathbf{q} \cdot \mathbf{n}_1 - \theta_{\mathbf{q}})\right) \\ \cos\left(\frac{1}{2}(\mathbf{q} \cdot \mathbf{n}_2 - \theta_{\mathbf{q}})\right) \\ \cos\left(\frac{1}{2}(\mathbf{q} \cdot \mathbf{n}_3 - \theta_{\mathbf{q}})\right) \end{pmatrix}, \\
 E_2 &= -t(1 - |\gamma(\mathbf{q})|), & u_{\mathbf{q}}^2 &= N_2 \begin{pmatrix} \sin\left(\frac{1}{2}(\mathbf{q} \cdot \mathbf{n}_1 - \theta_{\mathbf{q}})\right) \\ \sin\left(\frac{1}{2}(\mathbf{q} \cdot \mathbf{n}_2 - \theta_{\mathbf{q}})\right) \\ \sin\left(\frac{1}{2}(\mathbf{q} \cdot \mathbf{n}_3 - \theta_{\mathbf{q}})\right) \end{pmatrix}, \\
 E_3 &= 2t, & u_{\mathbf{q}}^3 &= N_3 \begin{pmatrix} \sin\left(\frac{1}{2}(\mathbf{q} \cdot (\mathbf{n}_2 - \mathbf{n}_3))\right) \\ \sin\left(\frac{1}{2}(\mathbf{q} \cdot (\mathbf{n}_3 - \mathbf{n}_1))\right) \\ \sin\left(\frac{1}{2}(\mathbf{q} \cdot (\mathbf{n}_1 - \mathbf{n}_2))\right) \end{pmatrix},
 \end{aligned} \tag{D.5}$$

where  $N_1, N_2, N_3$  are normalization factors,  $t$  is the tunnelling rate and  $\theta_{\mathbf{q}} = \arg(\gamma(\mathbf{q}))$ . The variables  $\{\mathbf{n}_i\}$ ,  $\gamma(\mathbf{q})$  are defined as in [243]. Note that we use a different convention for expressing the kagome Bloch states than in section 3.4. This is because we were only concerned with the flat band eigenstates which, on their own, can be expressed in a more compact way.

Using these expressions for the kagome lattice eigenstates, we obtain Wilson lines as shown in Fig. D.2 and Fig. D.3.

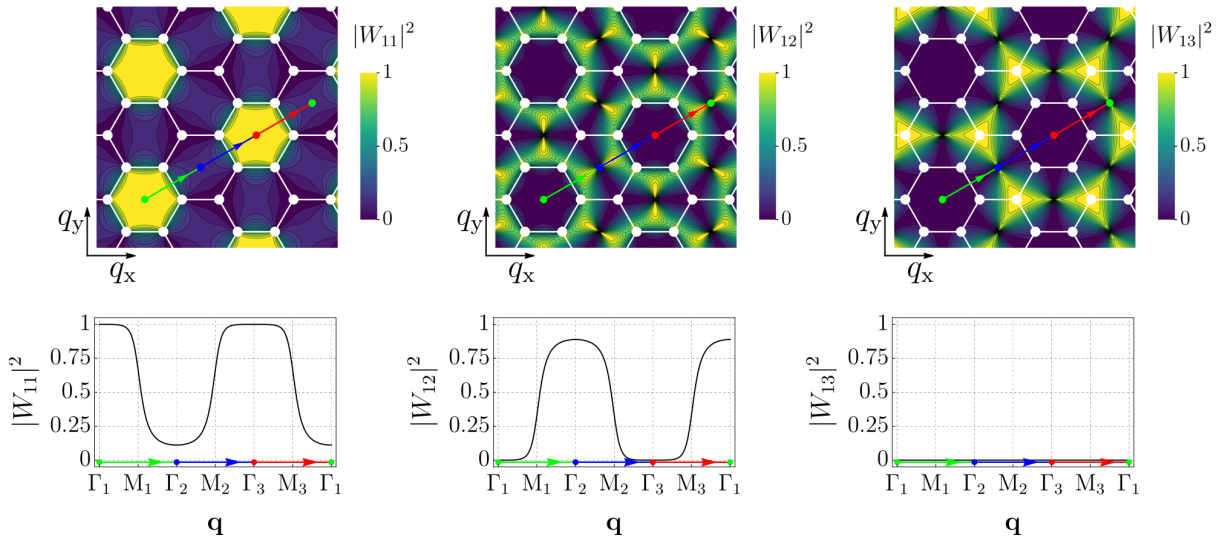


**Figure D.2** – Kagome Wilson lines  $|W_{1i}|^2$  in momentum space. Images on top show Wilson lines in 2D. Plots on the bottom show Wilson lines along straight path indicated in the 2D plots. In the honeycomb lattice this path is equivalent to the triangle path.

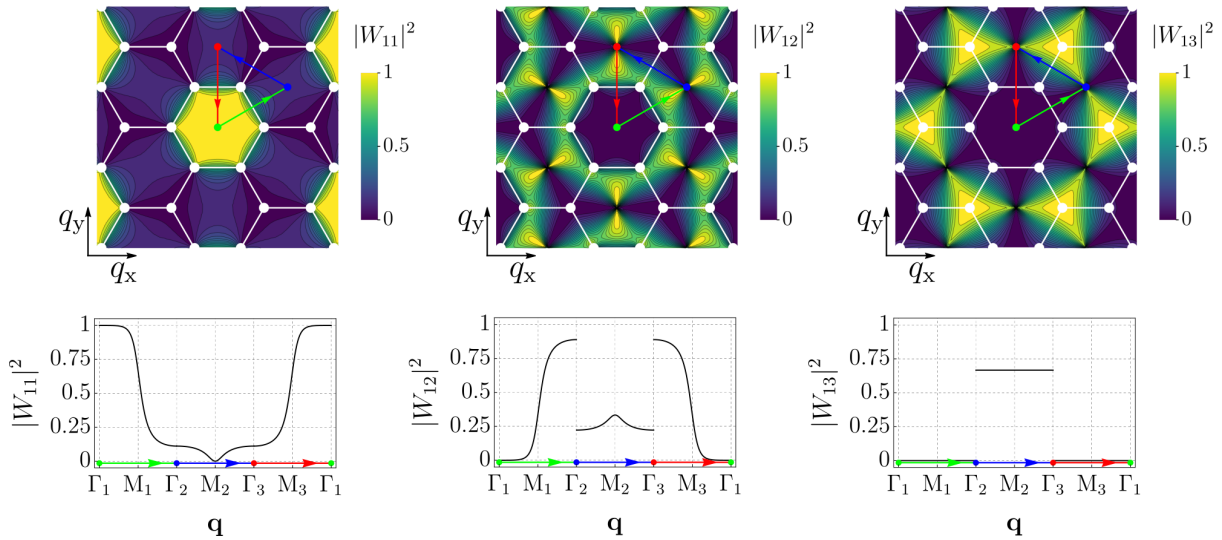


**Figure D.3** – Kagome Wilson lines  $|W_{1i}|^2$  in momentum space. Images on top show Wilson lines in 2D. Plots on the bottom show Wilson lines along triangle path indicated in the 2D plots. Note that, in contrast to the honeycomb lattice, the evolution is different compared to the straight path.

It is apparent that the Wilson lines in the kagome lattice obey a different symmetry than in the honeycomb lattice. The Wilson line in the kagome lattice is 2-BZ periodic, not 3-BZ periodic as with the honeycomb lattice. This also means that the state after traversing a triangle path is not the same as the state after traversing a straight path of 3 BZs (see Fig. D.2 and Fig. D.3). Note that there are now three bands involved instead of two, meaning that the relation  $|W_{12}|^2 = 1 - |W_{11}|^2$  no longer holds. This relation is superseded by

$$\sum_i |W_{1i}|^2 = 1. \quad (\text{D.6})$$

One interesting question that arises when considering the kagome lattice Wilson lines is if there is a path that connects the ground state to the flat band (especially while not crossing any degeneracies). A suitable path is shown in Fig. D.4

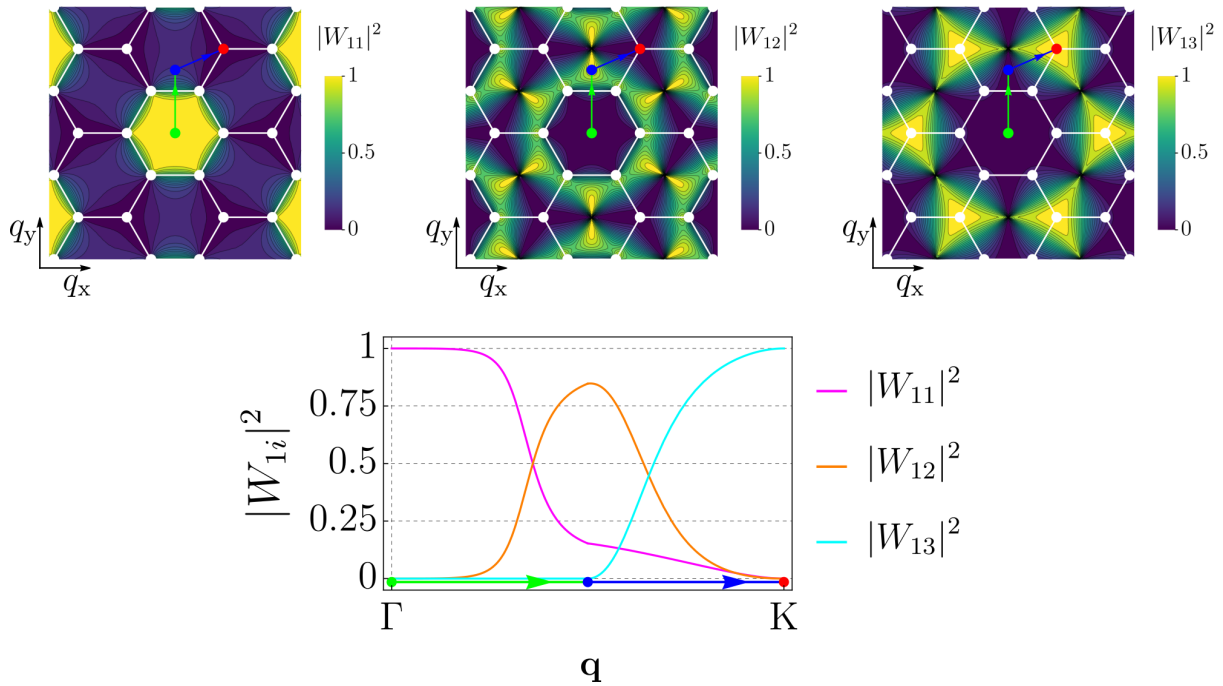


**Figure D.4** – Top: Wilson lines  $|W_{1i}|^2$  in momentum space. The drawn path connects the Bloch state at  $\Gamma$  in the lowest band to the Bloch state at K in the flat band. Transporting atoms along this path should allow for perfect transfer of atoms from the ground state to the flat band.

This path connects the ground state with the flat band without crossing any degeneracies<sup>144</sup>. It should therefore be possible to prepare a cloud in the flat band of the kagome lattice via this carefully chosen non-adiabatic path in reciprocal space. For non-interacting clouds this should be exact. For interacting clouds the spread in the momentum distribution will lead to fidelities less than one [158].

<sup>144</sup>The degeneracies are at  $\Gamma$  for the second and third band & K, K' for first and second band (Dirac points).

## References

- [1] H.-S. Zhong, H. Wang, Y.-H. Deng, M.-C. Chen, L.-C. Peng, Y.-H. Luo, J. Qin, D. Wu, X. Ding, Y. Hu, P. Hu, X.-Y. Yang, W.-J. Zhang, H. Li, Y. Li, X. Jiang, L. Gan, G. Yang, L. You, Z. Wang, L. Li, N.-L. Liu, C.-Y. Lu, and J.-W. Pan, “Quantum computational advantage using photons”, *Science* **370**, 1460–1463 (2020) (cited on page 1).
- [2] F. Arute, K. Arya, R. Babbush, D. Bacon, J. C. Bardin, R. Barends, R. Biswas, S. Boixo, F. G. S. L. Brandao, D. A. Buell, B. Burkett, Y. Chen, Z. Chen, B. Chiaro, R. Collins, W. Courtney, A. Dunsworth, E. Farhi, B. Foxen, A. Fowler, C. Gidney, M. Giustina, R. Graff, K. Guerin, S. Habegger, M. P. Harrigan, M. J. Hartmann, A. Ho, M. Hoffmann, T. Huang, T. S. Humble, S. V. Isakov, E. Jeffrey, Z. Jiang, D. Kafri, K. Kechedzhi, J. Kelly, P. V. Klimov, S. Knysh, A. Korotkov, F. Kostritsa, D. Landhuis, M. Lindmark, E. Lucero, D. Lyakh, S. Mandrà, J. R. McClean, M. McEwen, A. Megrant, X. Mi, K. Michielsen, M. Mohseni, J. Mutus, O. Naaman, M. Neeley, C. Neill, M. Y. Niu, E. Ostby, A. Petukhov, J. C. Platt, C. Quintana, E. G. Rieffel, P. Roushan, N. C. Rubin, D. Sank, K. J. Satzinger, V. Smelyanskiy, K. J. Sung, M. D. Trevithick, A. Vainsencher, B. Villalonga, T. White, Z. J. Yao, P. Yeh, A. Zalcman, H. Neven, and J. M. Martinis, “Quantum supremacy using a programmable superconducting processor”, *Nature* **574**, 505–510 (2019) (cited on page 1).
- [3] Google AI Quantum and Collaborators, “Hartree-Fock on a superconducting qubit quantum computer”, *Science* **369**, 1084–1089 (2020) (cited on page 1).
- [4] A. Robert, P. K. Barkoutsos, S. Woerner, and I. Tavernelli, “Resource-efficient quantum algorithm for protein folding”, *npj Quantum Information* **7**, 38 (2021) (cited on page 1).
- [5] Y. Cao, J. Romero, J. P. Olson, M. Degroote, P. D. Johnson, M. Kieferová, I. D. Kivlichan, T. Menke, B. Peropadre, N. P. Sawaya, S. Sim, L. Veis, and A. Aspuru-Guzik, “Quantum Chemistry in the Age of Quantum Computing”, *Chemical Reviews* **119**, 10856–10915 (2019) (cited on page 1).
- [6] R. Babbush, N. Wiebe, J. McClean, J. McClain, H. Neven, and G. K. L. Chan, “Low-Depth Quantum Simulation of Materials”, *Physical Review X* **8**, 11044 (2018) (cited on page 1).
- [7] C. Cade, L. Mineh, A. Montanaro, and S. Stanisic, “Strategies for solving the Fermi-Hubbard model on near-term quantum computers”, *Physical Review B* **102**, 235122 (2020) (cited on page 1).
- [8] A. Lucas, “Ising formulations of many NP problems”, *Frontiers in Physics* **2**, 1–14 (2014) (cited on page 1).
- [9] P. Scholl, M. Schuler, H. J. Williams, A. A. Eberharter, D. Barredo, K.-N. Schymik, V. Lienhard, L.-P. Henry, T. C. Lang, T. Lahaye, A. M. Läuchli, and A. Browaeys, “Programmable quantum simulation of 2D antiferromagnets with hundreds of Rydberg atoms”, *Nature* **595**, 233–238 (2020) (cited on page 1).

- [10] S. Ebadi, T. T. Wang, H. Levine, A. Keesling, G. Semeghini, A. Omran, D. Bluvstein, R. Samajdar, H. Pichler, W. W. Ho, S. Choi, S. Sachdev, M. Greiner, V. Vuletić, and M. D. Lukin, “Quantum phases of matter on a 256-atom programmable quantum simulator”, *Nature* **595**, 227–232 (2021) (cited on page 1).
- [11] G. Semeghini, H. Levine, A. Keesling, S. Ebadi, T. T. Wang, D. Bluvstein, R. Verresen, H. Pichler, M. Kalinowski, R. Samajdar, A. Omran, S. Sachdev, A. Vishwanath, M. Greiner, V. Vuletić, and M. D. Lukin, “Probing topological spin liquids on a programmable quantum simulator”, *Science* **374**, 1242–1247 (2021) (cited on pages 1, 12).
- [12] J. Koepsell, D. Bourgund, P. Sompet, S. Hirthe, A. Bohrdt, Y. Wang, F. Grusdt, E. Demler, G. Salomon, C. Gross, and I. Bloch, “Microscopic evolution of doped Mott insulators from polaronic metal to Fermi liquid”, *Science* **374**, 82–86 (2021) (cited on pages 1, 165).
- [13] J. P. Ronzheimer, M Schreiber, S Braun, S. S. Hodgman, S Langer, I. P. McCulloch, F Heidrich-Meisner, I Bloch, and U Schneider, “Expansion Dynamics of Interacting Bosons in Homogeneous Lattices in One and Two Dimensions”, *Physical Review Letters* **110**, 205301 (2013) (cited on page 1).
- [14] P. T. Brown, D. Mitra, E. Guardado-Sanchez, R. Nourafkan, A. Reymbaut, C.-D. Hébert, S. Bergeron, A.-M. S. Tremblay, J. Kokalj, D. A. Huse, P. Schauß, and W. S. Bakr, “Bad metallic transport in a cold atom Fermi-Hubbard system”, *Science* **363**, 379–382 (2019) (cited on page 1).
- [15] C. Gross and W. S. Bakr, “Quantum gas microscopy for single atom and spin detection”, *Nature Physics* **17**, 1316–1323 (2020) (cited on pages 1, 148).
- [16] E. Altman, K. R. Brown, G. Carleo, L. D. Carr, E. Demler, C. Chin, B. DeMarco, S. E. Economou, M. A. Eriksson, K.-M. C. Fu, M. Greiner, K. R. Hazzard, R. G. Hulet, A. J. Kollár, B. L. Lev, M. D. Lukin, R. Ma, X. Mi, S. Misra, C. Monroe, K. Murch, Z. Nazario, K.-K. Ni, A. C. Potter, P. Roushan, M. Saffman, M. Schleier-Smith, I. Siddiqi, R. Simmonds, M. Singh, I. Spielman, K. Temme, D. S. Weiss, J. Vučković, V. Vuletić, J. Ye, and M. Zwierlein, “Quantum Simulators: Architectures and Opportunities”, *PRX Quantum* **2**, 017003 (2021) (cited on page 1).
- [17] B.-B. Chen, C. Chen, Z. Chen, J. Cui, Y. Zhai, A. Weichselbaum, J. von Delft, Z. Y. Meng, and W. Li, “Quantum many-body simulations of the two-dimensional Fermi-Hubbard model in ultracold optical lattices”, *Physical Review B* **103**, L041107 (2021) (cited on page 1).
- [18] M. Atala, M. Aidelsburger, J. T. Barreiro, D. Abanin, T. Kitagawa, E. Demler, and I. Bloch, “Direct measurement of the Zak phase in topological Bloch bands”, *Nature Physics* **9**, 795–800 (2013) (cited on pages 1–2).
- [19] G. Jotzu, M. Messer, R. Desbuquois, M. Lebrat, T. Uehlinger, D. Greif, and T. Esslinger, “Experimental realization of the topological Haldane model with ultracold fermions”, *Nature* **515**, 237–240 (2014) (cited on pages 1–2, 8, 32, 39, 165).

- [20] A. Mazurenko, C. S. Chiu, G. Ji, M. F. Parsons, M. Kanász-Nagy, R. Schmidt, F. Grusdt, E. Demler, D. Greif, and M. Greiner, “A cold-atom Fermi-Hubbard antiferromagnet”, *Nature* **545**, 462–466 (2017) (cited on pages 1, 9–11, 44, 165).
- [21] M. Aidelsburger, M. Atala, M. Lohse, J. T. Barreiro, B. Paredes, and I. Bloch, “Realization of the Hofstadter Hamiltonian with Ultracold Atoms in Optical Lattices”, *Physical Review Letters* **111**, 185301 (2013) (cited on page 1).
- [22] E. T. Campbell, B. M. Terhal, and C. Vuillot, “Roads towards fault-tolerant universal quantum computation”, *Nature* **549**, 172–179 (2017) (cited on page 1).
- [23] K. B. Davis, M. O. Mewes, M. R. Andrews, N. J. Van Druten, D. S. Durfee, D. M. Kurn, and W. Ketterle, “Bose-Einstein condensation in a gas of sodium atoms”, *Physical Review Letters* **75**, 3969–3973 (1995) (cited on page 1).
- [24] M. H. Anderson, J. R. Ensher, M. R. Matthews, C. E. Wieman, and E. A. Cornell, “Observation of Bose-Einstein Condensation in a Dilute Atomic Vapor”, *Science* **269**, 198–201 (1995) (cited on page 1).
- [25] B. DeMarco and D. S. Jin, “Exploring a quantum degenerate gas of fermionic atoms”, *Physical Review A* **58**, R4267–R4270 (1998) (cited on page 1).
- [26] S. Inouye, M. R. Andrews, J. Stenger, H. J. Miesner, D. M. Stamper-Kurn, and W. Ketterle, “Observation of Feshbach resonances in a Bose-Einstein condensate”, *Nature* **392**, 151–154 (1998) (cited on page 2).
- [27] P. Courteille, R. S. Freeland, D. J. Heinzen, F. A. van Abeelen, and B. J. Verhaar, “Observation of a Feshbach Resonance in Cold Atom Scattering”, *Physical Review Letters* **81**, 69–72 (1998) (cited on page 2).
- [28] L. De Marco, G. Valtolina, K. Matsuda, W. G. Tobias, J. P. Covey, and J. Ye, “A degenerate Fermi gas of polar molecules”, *Science* **363**, 853–856 (2019) (cited on page 2).
- [29] M. Lu, N. Q. Burdick, S. H. Youn, and B. L. Lev, “Strongly Dipolar Bose-Einstein Condensate of Dysprosium”, *Physical Review Letters* **107**, 190401 (2011) (cited on page 2).
- [30] K. Aikawa, A. Frisch, M. Mark, S. Baier, A. Rietzler, R. Grimm, and F. Ferlaino, “Bose-Einstein Condensation of Erbium”, *Physical Review Letters* **108**, 210401 (2012) (cited on page 2).
- [31] N. Hinkley, J. A. Sherman, N. B. Phillips, M. Schioppo, N. D. Lemke, K. Beloy, M. Pizzocaro, C. W. Oates, and A. D. Ludlow, “An Atomic Clock with 10-18 Instability”, *Science* **341**, 1215–1218 (2013) (cited on page 2).
- [32] B. J. Bloom, T. L. Nicholson, J. R. Williams, S. L. Campbell, M. Bishof, X. Zhang, W. Zhang, S. L. Bromley, and J. Ye, “An optical lattice clock with accuracy and stability at the 10-18 level”, *Nature* **506**, 71–75 (2014) (cited on page 2).
- [33] R. Scheunemann, F. S. Cataliotti, T. W. Hänsch, and M. Weitz, “Resolving and addressing atoms in individual sites of a CO<sub>2</sub>-laser optical lattice”, *Physical Review A* **62**, 051801 (2000) (cited on page 2).

- [34] C. Becker, P. Soltan-Panahi, J. Kronjäger, S. Dörscher, K. Bongs, and K. Sengstock, “Ultracold quantum gases in triangular optical lattices”, *New Journal of Physics* **12**, 065025 (2010) (cited on pages 2, 124).
- [35] L. Tarruell, D. Greif, T. Uehlinger, G. Jotzu, and T. Esslinger, “Creating, moving and merging Dirac points with a Fermi gas in a tunable honeycomb lattice”, *Nature* **483**, 302–305 (2012) (cited on page 2).
- [36] G.-B. Jo, J. Guzman, C. K. Thomas, P. Hosur, A. Vishwanath, and D. M. Stamper-Kurn, “Ultracold Atoms in a Tunable Optical Kagome Lattice”, *Physical Review Letters* **108**, 045305 (2012) (cited on pages 2, 12, 94–95, 124, 127, 143).
- [37] S. Taie, H. Ozawa, T. Ichinose, T. Nishio, S. Nakajima, and Y. Takahashi, “Coherent driving and freezing of bosonic matter wave in an optical Lieb lattice”, *Science Advances* **1** (2015) (cited on page 2).
- [38] G. Roati, C. D’Errico, L. Fallani, M. Fattori, C. Fort, M. Zaccanti, G. Modugno, M. Modugno, and M. Inguscio, “Anderson localization of a non-interacting Bose-Einstein condensate”, *Nature* **453**, 895–898 (2008) (cited on page 2).
- [39] K. Viebahn, M. Sbroscia, E. Carter, J. C. Yu, and U. Schneider, “Matter-Wave Diffraction from a Quasicrystalline Optical Lattice”, *Physical Review Letters* **122**, 110404 (2019) (cited on page 2).
- [40] U. Schneider, “Interacting Fermionic Atoms in Optical Lattices - A Quantum Simulator for Condensed Matter Physics”, PhD thesis (Johannes Gutenberg-Universität Mainz, 2010) (cited on pages 2, 173).
- [41] M. Greiner, O. Mandel, T. Esslinger, T. W. Hansch, and I. Bloch, “Quantum phase transition from a superfluid to a Mott insulator in a gas of ultracold atoms”, *Nature* **415**, 39–44 (2002) (cited on pages 2, 44, 134–135).
- [42] I. Bloch, J. Dalibard, and W. Zwerger, “Many-body physics with ultracold gases”, *Reviews of Modern Physics* **80**, 885–964 (2008) (cited on page 2).
- [43] C. Gross and I. Bloch, “Quantum simulations with ultracold atoms in optical lattices”, *Science* **357**, 995–1001 (2017) (cited on pages 2, 148).
- [44] S. Trotzky, P. Cheinet, S. Fölling, M. Feld, U. Schnorrberger, A. M. Rey, A. Polkovnikov, E. A. Demler, M. D. Lukin, and I. Bloch, “Time-resolved observation and control of superexchange interactions with ultracold atoms in optical lattices”, *Science* **319**, 295–299 (2008) (cited on page 2).
- [45] M. Aidelsburger, M. Lohse, C. Schweizer, M. Atala, J. T. Barreiro, S. Nascimbène, N. R. Cooper, I. Bloch, and N. Goldman, “Measuring the Chern number of Hofstadter bands with ultracold bosonic atoms”, *Nature Physics* **11**, 162–166 (2015) (cited on page 2).
- [46] H. Lignier, C. Sias, D. Ciampini, Y. Singh, A. Zenesini, O. Morsch, and E. Arimondo, “Dynamical Control of Matter-Wave Tunneling in Periodic Potentials”, *Physical Review Letters* **99**, 220403 (2007) (cited on pages 2, 7).
- [47] J. Struck, C. Ölschläger, R. Le Targat, P. Soltan-Panahi, A. Eckardt, M. Lewenstein, P. Windpassinger, and K. Sengstock, “Quantum simulation of frustrated classical magnetism in triangular optical lattices”, *Science* **333**, 996–999 (2011) (cited on pages 2, 7, 69, 138, 163).

- [48] S Braun, J. P. Ronzheimer, M Schreiber, S. S. Hodgman, T Rom, I Bloch, and U Schneider, “Negative Absolute Temperature for Motional Degrees of Freedom”, *Science* **339**, 52–55 (2013) (cited on pages 2, 7, 138).
- [49] W. S. Bakr, J. I. Gillen, A. Peng, S. Folling, and M. Greiner, “A quantum gas microscope for detecting single atoms in a Hubbard-regime optical lattice”, *Nature* **462**, 74–77 (2009) (cited on pages 2, 149).
- [50] J. F. Sherson, C. Weitenberg, M. Endres, M. Cheneau, I. Bloch, and S. Kuhr, “Single-atom-resolved fluorescence imaging of an atomic Mott insulator”, *Nature* **467**, 68–72 (2010) (cited on pages 2, 147, 156).
- [51] M. Miranda, R. Inoue, Y. Okuyama, A. Nakamoto, and M. Kozuma, “Site-resolved imaging of ytterbium atoms in a two-dimensional optical lattice”, *Physical Review A* **91**, 063414 (2015) (cited on pages 2, 149).
- [52] R. Yamamoto, J. Kobayashi, T. Kuno, K. Kato, and Y. Takahashi, “An ytterbium quantum gas microscope with narrow-line laser cooling”, *New Journal of Physics* **18**, 023016 (2016) (cited on pages 2, 30).
- [53] R. Yamamoto, H. Ozawa, D. C. Nak, I. Nakamura, and T. Fukuhara, “Single-site-resolved imaging of ultracold atoms in a triangular optical lattice”, *New Journal of Physics* **22**, 123028 (2020) (cited on page 2).
- [54] K. Kwon, K. Kim, J. Hur, S. Huh, and J.-y. Choi, “Site-Resolved Imaging of Bosonic Mott Insulator of 7Li atoms”, *arXiv:2111.15188* (2021) (cited on page 2).
- [55] A. Omran, M. Boll, T. A. Hilker, K. Kleinlein, G. Salomon, I. Bloch, and C. Gross, “Microscopic Observation of Pauli Blocking in Degenerate Fermionic Lattice Gases”, *Physical Review Letters* **115**, 263001 (2015) (cited on pages 2, 147).
- [56] E. Haller, J. Hudson, A. Kelly, D. A. Cotta, B. Peaudecerf, G. D. Bruce, and S. Kuhr, “Single-atom imaging of fermions in a quantum-gas microscope”, *Nature Physics* **11**, 738–742 (2015) (cited on pages 2, 30, 147, 149–150, 156).
- [57] L. W. Cheuk, M. A. Nichols, M. Okan, T. Gersdorf, V. V. Ramasesh, W. S. Bakr, T. Lompe, and M. W. Zwierlein, “Quantum-Gas Microscope for Fermionic Atoms”, *Physical Review Letters* **114**, 193001 (2015) (cited on pages 2, 30, 147, 149–150, 156).
- [58] M. F. Parsons, F. Huber, A. Mazurenko, C. S. Chiu, W. Setiawan, K. Wooley-Brown, S. Blatt, and M. Greiner, “Site-Resolved Imaging of Fermionic 6Li an Optical Lattice”, *Physical Review Letters* **114**, 213002 (2015) (cited on pages 2, 147, 149, 156).
- [59] G. J. A. Edge, R. Anderson, D. Jervis, D. C. McKay, R. Day, S. Trotzky, and J. H. Thywissen, “Imaging and addressing of individual fermionic atoms in an optical lattice”, *Physical Review A* **92**, 063406 (2015) (cited on pages 2, 30, 147, 149, 156).
- [60] J. Yang, L. Liu, J. Mongkolkiattichai, and P. Schauss, “Site-Resolved Imaging of Ultracold Fermions in a Triangular-Lattice Quantum Gas Microscope”, *PRX Quantum* **2**, 020344 (2021) (cited on pages 2, 147).

- [61] I. Geisel, K. Cordes, J. Mahnke, S. Jöllenbeck, J. Ostermann, J. Arlt, W. Ertmer, and C. Klempt, “Evolutionary optimization of an experimental apparatus”, *Applied Physics Letters* **102**, 214105 (2013) (cited on page 2).
- [62] P. B. Wigley, P. J. Everitt, A. van den Hengel, J. W. Bastian, M. A. Sooriyabandara, G. D. McDonald, K. S. Hardman, C. D. Quinlivan, P. Manju, C. C. N. Kuhn, I. R. Petersen, A. N. Luiten, J. J. Hope, N. P. Robins, and M. R. Hush, “Fast machine-learning online optimization of ultra-cold-atom experiments”, *Scientific Reports* **6**, 25890 (2016) (cited on page 2).
- [63] J. Carrasquilla and R. G. Melko, “Machine learning phases of matter”, *Nature Physics* **13**, 431–434 (2017) (cited on page 2).
- [64] B. S. Rem, N. Käming, M. Tarnowski, L. Asteria, N. Fläschner, C. Becker, K. Senstock, and C. Weitenberg, “Identifying quantum phase transitions using artificial neural networks on experimental data”, *Nature Physics* **15**, 917–920 (2019) (cited on pages 2, 8).
- [65] K. Kim, S. Huh, K. Kwon, and J.-y. Choi, “Rapid production of large  $7\text{Li}$  Bose-Einstein condensates using D1 gray molasses”, *Physical Review A* **99**, 053604 (2019) (cited on page 2).
- [66] A. Urvoy, Z. Vendeiro, J. Ramette, A. Adiyatullin, and V. Vuletić, “Direct Laser Cooling to Bose-Einstein Condensation in a Dipole Trap”, *Physical Review Letters* **122**, 203202 (2019) (cited on page 2).
- [67] G. A. Phelps, A. Hébert, A. Krahn, S. Dickerson, F. Öztürk, S. Ebadi, L. Su, and M. Greiner, “Sub-second production of a quantum degenerate gas”, *arXiv:2007.10807* (2020) (cited on page 2).
- [68] J. Léonard, M. Lee, A. Morales, T. M. Karg, T. Esslinger, and T. Donner, “Optical transport and manipulation of an ultracold atomic cloud using focus-tunable lenses”, *New Journal of Physics* **16**, 093028 (2014) (cited on pages 2, 89, 113).
- [69] G. Unnikrishnan, C. Beulenkamp, D. Zhang, K. P. Zamariski, M. Landini, and H.-C. Nägerl, “Long distance optical transport of ultracold atoms: A compact setup using a Moiré lens”, *Review of Scientific Instruments* **92**, 063205 (2021) (cited on pages 2, 89).
- [70] T. Klostermann, C. R. Cabrera, H. von Raven, J. F. Wienand, C. Schweizer, I. Bloch, and M. Aidelsburger, “Fast long-distance transport of cold cesium atoms”, *arXiv:2109.03804* (2021) (cited on page 2).
- [71] I. M. Georgescu, S. Ashhab, and F. Nori, “Quantum simulation”, *Reviews of Modern Physics* **86**, 153–185 (2014) (cited on page 3).
- [72] D. C. Tsui, H. L. Stormer, and A. C. Gossard, “Two-dimensional magnetotransport in the extreme quantum limit”, *Physical Review Letters* **48**, 1559–1562 (1982) (cited on page 3).
- [73] M. Köhl, H. Moritz, T. Stöferle, K. Günter, and T. Esslinger, “Fermionic Atoms in a Three Dimensional Optical Lattice: Observing Fermi Surfaces, Dynamics, and Interactions”, *Physical Review Letters* **94**, 080403 (2005) (cited on page 3).

- [74] B. R. Ortiz, L. C. Gomes, J. R. Morey, M. Winiarski, M. Bordelon, J. S. Mangum, I. W. H. Oswald, J. A. Rodriguez-Rivera, J. R. Neilson, S. D. Wilson, E. Ertekin, T. M. McQueen, and E. S. Toberer, “New kagome prototype materials: discovery of  $\text{KV}_3\text{Sb}_5$ ,  $\text{RbV}_3\text{Sb}_5$ ,  $\text{CsV}_3\text{Sb}_5$ ”, *Physical Review Materials* **3**, 094407 (2019) (cited on page 3).
- [75] J.-H. Yang, J.-S. Park, J. Kang, W. Metzger, T. Barnes, and S.-H. Wei, “Tuning the Fermi level beyond the equilibrium doping limit through quenching: The case of  $\text{CdTe}$ ”, *Physical Review B* **90**, 245202 (2014) (cited on page 3).
- [76] Y. Cao, V. Fatemi, S. Fang, K. Watanabe, T. Taniguchi, E. Kaxiras, and P. Jarillo-Herrero, “Unconventional superconductivity in magic-angle graphene superlattices”, *Nature* **556**, 43–50 (2018) (cited on pages 3, 8).
- [77] Y. Margalit, Y.-K. Lu, F. Ç. Top, and W. Ketterle, “Pauli blocking of light scattering in degenerate fermions”, *Science* **374**, 976–979 (2021) (cited on page 3).
- [78] A. B. Deb and N. Kjærgaard, “Observation of Pauli blocking in light scattering from quantum degenerate fermions”, *Science* **374**, 972–975 (2021) (cited on page 3).
- [79] C. Sanner, L. Sonderhouse, R. B. Hutson, L. Yan, W. R. Milner, and J. Ye, “Pauli blocking of atom-light scattering”, *Science* **374**, 979–983 (2021) (cited on page 3).
- [80] T.-H. Han, J. S. Helton, S. Chu, D. G. Nocera, J. A. Rodriguez-Rivera, C. Broholm, and Y. S. Lee, “Fractionalized excitations in the spin-liquid state of a kagome-lattice antiferromagnet”, *Nature* **492**, 406–410 (2012) (cited on page 3).
- [81] J. A. M. Paddison, H. S. Ong, J. O. Hamp, P. Mukherjee, X. Bai, M. G. Tucker, N. P. Butch, C. Castelnovo, M. Mourigal, and S. E. Dutton, “Emergent order in the kagome Ising magnet  $\text{Dy}_3\text{Mg}_2\text{Sb}_3\text{O}_{14}$ ”, *Nature Communications* **7**, 13842 (2016) (cited on page 3).
- [82] M. Kang, S. Fang, J.-K. Kim, B. R. Ortiz, S. H. Ryu, J. Kim, J. Yoo, G. Sangiovanni, D. Di Sante, B.-G. Park, C. Jozwiak, A. Bostwick, E. Rotenberg, E. Kaxiras, S. D. Wilson, J.-H. Park, and R. Comin, “Twofold van Hove singularity and origin of charge order in topological kagome superconductor  $\text{CsV}_3\text{Sb}_5$ ”, *Nature Physics* **18**, 301–308 (2022) (cited on page 3).
- [83] D. L. Bergman, C. Wu, and L. Balents, “Band touching from real-space topology in frustrated hopping models”, *Physical Review B* **78**, 125104 (2008) (cited on pages 4, 7, 67).
- [84] S. D. Huber and E. Altman, “Bose condensation in flat bands”, *Physical Review B* **82**, 184502 (2010) (cited on pages 4, 7, 45, 67–69, 164).
- [85] O. Derzhko, J. Schnack, D. V. Dmitriev, V. Y. Krivnov, and J. Richter, “Flat-band physics in the spin-1/2 sawtooth chain”, *The European Physical Journal B* **93**, 161 (2020) (cited on page 4).
- [86] F. Steglich, J. Aarts, C. D. Bredl, W. Lieke, D. Meschede, W. Franz, and H. Schäfer, “Superconductivity in the presence of strong pauli paramagnetism:  $\text{CeCu}_2\text{Si}_2$ ”, *Physical Review Letters* **43**, 1892–1896 (1979) (cited on page 5).

- [87] H. Liu, Y. Cao, Y. Xu, D. J. Gawryluk, E. Pomjakushina, S.-Y. Gao, P. Dudin, M. Shi, L. Yan, Y.-f. Yang, and H. Ding, “Observation of flat bands due to band hybridization in the 3d-electron heavy-fermion compound  $\text{CaCu}_3\text{Ru}_4\text{O}_{12}$ ”, *Physical Review B* **102**, 035111 (2020) (cited on page 5).
- [88] Y.-Z. You, Z. Chen, X.-Q. Sun, and H. Zhai, “Superfluidity of Bosons in Kagome Lattices with Frustration”, *Physical Review Letters* **109**, 265302 (2012) (cited on pages 6, 45, 58, 62, 64, 69, 164).
- [89] A. Julku, G. M. Bruun, and P. Törmä, “Excitations of a Bose-Einstein condensate and the quantum geometry of a flat band”, *Physical Review B* **104**, 144507 (2021) (cited on pages 6, 61–64).
- [90] J. Struck, “Artificial Gauge Fields in Driven Optical Lattices - From Frustrated XY Models to Ising Ferromagnetism”, PhD thesis (Universität Hamburg, 2013) (cited on pages 6, 124, 138).
- [91] D. A. Huse and A. D. Rutenberg, “Classical antiferromagnets on the Kagomé lattice”, *Physical Review B* **45**, 7536–7539 (1992) (cited on pages 6, 60–61, 64).
- [92] A. Eckardt, C. Weiss, and M. Holthaus, “Superfluid-Insulator Transition in a Periodically Driven Optical Lattice”, *Physical Review Letters* **95**, 260404 (2005) (cited on page 7).
- [93] D. Yamamoto, T. Fukuhara, and I. Danshita, “Frustrated quantum magnetism with Bose gases in triangular optical lattices at negative absolute temperatures”, *Communications Physics* **3**, 56 (2020) (cited on page 7).
- [94] J. Léonard, A. Morales, P. Zupancic, T. Esslinger, and T. Donner, “Supersolid formation in a quantum gas breaking a continuous translational symmetry”, *Nature* **543**, 87–90 (2017) (cited on page 7).
- [95] J. R. Li, J. Lee, W. Huang, S. Burchesky, B. Shteynas, F. Ç. Topi, A. O. Jamison, and W. Ketterle, “A stripe phase with supersolid properties in spin-orbit-coupled Bose-Einstein condensates”, *Nature* **543**, 91–94 (2017) (cited on page 7).
- [96] M. A. Norcia, C. Politi, L. Klaus, E. Poli, M. Sohmen, M. J. Mark, R. N. Bisset, L. Santos, and F. Ferlino, “Two-dimensional supersolidity in a dipolar quantum gas”, *Nature* **596**, 357–361 (2021) (cited on page 7).
- [97] C. Wu, D. Bergman, L. Balents, and S. Das Sarma, “Flat Bands and Wigner Crystallization in the Honeycomb Optical Lattice”, *Physical Review Letters* **99**, 070401 (2007) (cited on pages 7, 67).
- [98] G. E. Volovik, “Graphite, Graphene, and the Flat Band Superconductivity”, *JETP Letters* **107**, 516–517 (2018) (cited on page 7).
- [99] E. J. Bergholtz and Z. Liu, “Topological Flat Band Models and Fractional Chern Insulators”, *International Journal of Modern Physics B* **27**, 1330017 (2013) (cited on pages 7, 9).
- [100] L. W. Clark, N. Schine, C. Baum, N. Jia, and J. Simon, “Observation of Laughlin states made of light”, *Nature* **582**, 41–45 (2020) (cited on pages 7–8).

- [101] C. L. Cleveland and R. Medina A., “Obtaining a Heisenberg Hamiltonian from the Hubbard model”, *American Journal of Physics* **44**, 44–46 (1975) (cited on pages 7, 9–10).
- [102] S. Yan, D. A. Huse, and S. R. White, “Spin-Liquid Ground State of the  $S = 1/2$  Kagome Heisenberg Antiferromagnet”, *Science* **332**, 1173–1176 (2011) (cited on pages 7, 11).
- [103] S. Depenbrock, I. P. McCulloch, and U. Schollwöck, “Nature of the Spin-Liquid Ground State of the  $S=1/2$  Heisenberg Model on the Kagome Lattice”, *Physical Review Letters* **109**, 067201 (2012) (cited on page 7).
- [104] S. Miyahara, S. Kusuta, and N. Furukawa, “BCS theory on a flat band lattice”, *Physica C: Superconductivity and its Applications* **460-462 II**, 1145–1146 (2007) (cited on page 8).
- [105] V. J. Kauppila, F. Aikebaier, and T. T. Heikkilä, “Flat-band superconductivity in strained Dirac materials”, *Physical Review B* **93**, 214505 (2016) (cited on page 8).
- [106] T. Löthman and A. M. Black-Schaffer, “Universal phase diagrams with superconducting domes for electronic flat bands”, *Physical Review B* **96**, 064505 (2017) (cited on page 8).
- [107] V. I. Iglovikov, F. Hébert, B. Grémaud, G. G. Batrouni, and R. T. Scalettar, “Superconducting transitions in flat-band systems”, *Physical Review B* **90**, 094506 (2014) (cited on page 8).
- [108] L. Balents, C. R. Dean, D. K. Efetov, and A. F. Young, “Superconductivity and strong correlations in moiré flat bands”, *Nature Physics* **16**, 725–733 (2020) (cited on page 8).
- [109] I. Mahyaeh, T. Köhler, A. M. Black-Schaffer, and A. Kantian, “Superconducting pairing from repulsive interactions of fermions in a flat-band system”, [arXiv:2111.03321](https://arxiv.org/abs/2111.03321) (2021) (cited on page 8).
- [110] E. Tang, J.-W. Mei, and X.-G. Wen, “High-Temperature Fractional Quantum Hall States”, *Physical Review Letters* **106**, 236802 (2011) (cited on pages 8, 32, 39, 165).
- [111] N. Regnault and B. A. Bernevig, “Fractional Chern Insulator”, *Physical Review X* **1**, 021014 (2011) (cited on pages 8, 165).
- [112] R. O. Umucallar, M. Wouters, and I. Carusotto, “Probing few-particle Laughlin states of photons via correlation measurements”, *Physical Review A* **89**, 023803 (2014) (cited on page 8).
- [113] B. Andrade, V. Kasper, M. Lewenstein, C. Weitenberg, and T. Graß, “Preparation of the  $1/2$  Laughlin state with atoms in a rotating trap”, *Physical Review A* **103**, 063325 (2021) (cited on page 8).
- [114] A. Wójs, K.-S. Yi, and J. J. Quinn, “Fractional quantum Hall states of clustered composite fermions”, *Physical Review B* **69**, 205322 (2004) (cited on page 8).
- [115] J. P. Eisenstein and H. L. Stormer, “The Fractional Quantum Hall Effect”, *Science* **248**, 1510–1516 (1990) (cited on page 8).

- [116] B. Jaworowski, A. Manolescu, and P. Potasz, “Fractional Chern insulator phase at the transition between checkerboard and Lieb lattices”, *Physical Review B* **92**, 245119 (2015) (cited on page 8).
- [117] F. D. M. Haldane, “Model for a Quantum Hall Effect without Landau Levels: Condensed-Matter Realization of the ”Parity Anomaly””, *Physical Review Letters* **61**, 2015–2018 (1988) (cited on pages 8–9, 165).
- [118] A. G. Grushin, Á. Gómez-León, and T. Neupert, “Floquet Fractional Chern Insulators”, *Physical Review Letters* **112**, 156801 (2014) (cited on page 8).
- [119] U. Schneider, L. Hackermüller, S. Will, T. Best, I. Bloch, T. A. Costi, R. W. Helmes, D. Rasch, and A. Rosch, “Metallic and Insulating Phases of Repulsively Interacting Fermions in a 3D Optical Lattice”, *Science* **322**, 1520–1525 (2008) (cited on page 9).
- [120] M. Boll, T. A. Hilker, G. Salomon, A. Omran, J. Nespolo, L. Pollet, I. Bloch, and C. Gross, “Spin- and density-resolved microscopy of antiferromagnetic correlations in Fermi-Hubbard chains”, *Science* **353**, 1257–1260 (2016) (cited on page 9).
- [121] P.-E. Melchy, “Geometric frustration: the case of triangular antiferromagnets”, PhD thesis (Université Grenoble-Alpes, 2010) (cited on page 10).
- [122] J. N. Reimers and A. J. Berlinsky, “Order by disorder in the classical Heisenberg kagomé antiferromagnet”, *Physical Review B* **48**, 9539–9554 (1993) (cited on pages 10, 62).
- [123] S. Sachdev, “Kagome- and triangular-lattice Heisenberg antiferromagnets: Ordering from quantum fluctuations and quantum-disordered ground states with unconfined bosonic spinons”, *Physical Review B* **45**, 12377–12396 (1992) (cited on pages 10–11, 60).
- [124] P. W. Anderson, “Resonating valence bonds: A new kind of insulator?”, *Materials Research Bulletin* **8**, 153–160 (1973) (cited on page 11).
- [125] A. W. Sandvik, “Finite-size scaling of the ground-state parameters of the two-dimensional Heisenberg model”, *Physical Review B - Condensed Matter and Materials Physics* **56**, 11678–11690 (1997) (cited on page 11).
- [126] U. Schollwöck, J. Richter, D. Farnell, and R. Bishop, *Quantum Magnetism* (Springer, Berlin, Heidelberg, 2004) (cited on page 11).
- [127] L. Capriotti, A. E. Trumper, and S. Sorella, “Long-Range Néel Order in the Triangular Heisenberg Model”, *Physical Review Letters* **82**, 3899–3902 (1999) (cited on page 11).
- [128] L. Balents, “Spin liquids in frustrated magnets”, *Nature* **464**, 199–208 (2010) (cited on page 11).
- [129] A. M. Läuchli, J. Sudan, and R. Moessner, “S=1/2 kagome Heisenberg antiferromagnet revisited”, *Physical Review B* **100**, 155142 (2019) (cited on pages 11, 165).
- [130] M Mambrini and F Mila, “RVB description of the low-energy singlets of the spin 1/2 kagomé antiferromagnet”, *The European Physical Journal B* **17**, 651–659 (2000) (cited on page 11).

- [131] J. Schnack, J. Schulenburg, and J. Richter, “Magnetism of the  $N=42$  kagome lattice antiferromagnet”, *Physical Review B* **98**, 094423 (2018) (cited on page 11).
- [132] S. A. Kivelson, D. S. Rokhsar, and J. P. Sethna, “Topology of the resonating valence-bond state: Solitons and high- $T_c$  superconductivity”, *Physical Review B* **35**, 8865–8868 (1987) (cited on page 12).
- [133] X. G. Wen, “Mean-field theory of spin-liquid states with finite energy gap and topological orders”, *Physical Review B* **44**, 2664–2672 (1991) (cited on page 12).
- [134] G. Misguich, D. Serban, and V. Pasquier, “Quantum Dimer Model on the Kagome Lattice: Solvable Dimer-Liquid and Ising Gauge Theory”, *Physical Review Letters* **89**, 137202 (2002) (cited on page 12).
- [135] L. Santos, M. Baranov, J. Cirac, H.-U. Everts, H. Fehrmann, and M. Lewenstein, “Atomic Quantum Gases in Kagomé Lattices”, *Physical Review Letters* **93**, 030601 (2004) (cited on page 12).
- [136] J Ruostekoski, “Optical Kagome Lattice for Ultracold Atoms with Nearest Neighbor Interactions”, *Phys. Rev. Lett.* **103**, 80406 (2009) (cited on page 12).
- [137] C. K. Thomas, T. H. Barter, T.-H. Leung, M. Okano, G.-B. Jo, J. Guzman, I. Kimchi, A. Vishwanath, and D. M. Stamper-Kurn, “Mean-Field Scaling of the Superfluid to Mott Insulator Transition in a 2D Optical Superlattice”, *Physical Review Letters* **119**, 100402 (2017) (cited on pages 12, 44, 145).
- [138] T. H. Barter, T.-H. Leung, M. Okano, M. Block, N. Y. Yao, and D. M. Stamper-Kurn, “Spatial coherence of a strongly interacting Bose gas in the trimerized kagome lattice”, *Physical Review A* **101**, 011601 (2020) (cited on pages 12, 165).
- [139] T.-H. Leung, M. N. Schwarz, S.-W. Chang, C. D. Brown, G. Unnikrishnan, and D. Stamper-Kurn, “Interaction-Enhanced Group Velocity of Bosons in the Flat Band of an Optical Kagome Lattice”, *Physical Review Letters* **125**, 133001 (2020) (cited on page 12).
- [140] D. Reed, “Phase Stabilised Superlattices for Quantum Simulation”, PhD thesis (University of Cambridge, 2022) (cited on pages 13, 72, 80–81, 89, 95, 97, 101, 118–119, 143–144, 160).
- [141] R. Grimm, M. Weidemüller, and Y. B. Ovchinnikov, “Optical Dipole Traps for Neutral Atoms”, in *Advances in atomic, molecular, and optical physics*, Vol. 42 (Academic Press, 2000), pages 95–170 (cited on pages 15, 20).
- [142] C. K. Thomas, T. H. Barter, T.-H. Leung, S. Daiss, and D. M. Stamper-Kurn, “Signatures of spatial inversion asymmetry of an optical lattice observed in matter-wave diffraction”, *Physical Review A* **93**, 063613 (2016) (cited on page 23).
- [143] N. Marzari and D. Vanderbilt, “Maximally localized generalized Wannier functions for composite energy bands”, *Physical Review B - Condensed Matter and Materials Physics* **56**, 12847–12865 (1997) (cited on page 32).
- [144] R. Walters, “Ultra-cold Atoms in Optical Lattices: Simulating Quantum Spin Systems”, PhD thesis (University of Oxford, 2012) (cited on page 32).

- [145] R. Walters, G. Cotugno, T. H. Johnson, S. R. Clark, and D. Jaksch, “Ab initio derivation of Hubbard models for cold atoms in optical lattices”, *Physical Review A* **87**, 043613 (2013) (cited on pages 32, 44).
- [146] S. Flannigan, L. Madail, R. G. Dias, and A. J. Daley, “Hubbard models and state preparation in an optical Lieb lattice”, *New Journal of Physics* **23**, 083014 (2021) (cited on page 32).
- [147] S. Kivelson, “Wannier functions in one-dimensional disordered systems: Application to fractionally charged solitons”, *Physical Review B* **26**, 4269–4277 (1982) (cited on page 32).
- [148] U. Bissbort, “Dynamical Effects and Disorder in Ultracold Bosonic Matter”, PhD thesis (Johann Wolfgang Goethe-Universität Frankfurt am Main, 2012) (cited on pages 32, 42, 44).
- [149] T. Uehlinger, G. Jotzu, M. Messer, D. Greif, W. Hofstetter, U. Bissbort, and T. Esslinger, “Artificial Graphene with Tunable Interactions”, *Physical Review Letters* **111**, 185307 (2013) (cited on page 32).
- [150] T. Neupert, L. Santos, C. Chamon, and C. Mudry, “Fractional Quantum Hall States at Zero Magnetic Field”, *Physical Review Letters* **106**, 236804 (2011) (cited on page 39).
- [151] C. Thomas, “Quantum Simulation of Triangular, Honeycomb and Kagome Crystal Structures using Ultracold Atoms in Lattices of Laser Light”, PhD thesis (University of California, Berkeley, 2017) (cited on pages 44, 53, 97, 122, 124, 127).
- [152] A. Julku, G. M. Bruun, and P. Törmä, “Quantum Geometry and Flat Band Bose-Einstein Condensation”, *Physical Review Letters* **127**, 170404 (2021) (cited on pages 45, 58, 62–63, 69, 163–164).
- [153] N. F. Ramsey, “Thermodynamics and statistical mechanics at negative absolute temperatures”, *Physical Review* **103**, 20–28 (1956) (cited on page 45).
- [154] K. Winkler, G. Thalhammer, F. Lang, R. Grimm, J. Hecker Denschlag, A. J. Daley, A. Kantian, H. P. Büchler, and P. Zoller, “Repulsively bound atom pairs in an optical lattice”, *Nature* **441**, 853–856 (2006) (cited on page 47).
- [155] E. M. Purcell and R. V. Pound, “A Nuclear Spin System at Negative Temperature”, *Physical Review* **81**, 279–280 (1951) (cited on page 47).
- [156] A. Rapp, S. Mandt, and A. Rosch, “Equilibration Rates and Negative Absolute Temperatures for Ultracold Atoms in Optical Lattices”, *Physical Review Letters* **105**, 220405 (2010) (cited on page 51).
- [157] A. S. Sørensen, E. Altman, M. Gullans, J. V. Porto, M. D. Lukin, and E. Demler, “Adiabatic preparation of many-body states in optical lattices”, *Physical Review A* **81**, 061603 (2010) (cited on page 51).
- [158] T. Li, “Probing Bloch band geometry with ultracold atoms in optical lattices”, PhD thesis (Ludwig-Maximilians-Universität München, 2016) (cited on pages 53, 184).

- [159] M. Hachmann, Y. Kiefer, J. Riebesehl, R. Eichberger, and A. Hemmerich, “Quantum Degenerate Fermi Gas in an Orbital Optical Lattice”, *Physical Review Letters* **127**, 033201 (2021) (cited on page 53).
- [160] L. Duca, “Probing topological properties of Bloch bands with ultracold atoms in a honeycomb optical lattice”, PhD thesis (Ludwig-Maximilians-Universität München, 2015) (cited on pages 53, 72, 75, 181).
- [161] A. H. Castro Neto, F. Guinea, N. M. R. Peres, K. S. Novoselov, and A. K. Geim, “The electronic properties of graphene”, *Reviews of Modern Physics* **81**, 109–162 (2009) (cited on page 55).
- [162] W. J. Mullin, “Bose-Einstein condensation in a harmonic potential”, *Journal of Low Temperature Physics* **106**, 615–641 (1997) (cited on page 57).
- [163] S. Braun, “Negative Absolute Temperature and the Dynamics of Quantum Phase Transitions”, PhD thesis (Ludwig-Maximilians-Universität München, 2014) (cited on pages 57, 138, 140–141).
- [164] S. E. Korshunov, “Phase transitions in the antiferromagnetic XY model with a kagomé lattice”, *Physical Review B* **65**, 054416 (2002) (cited on pages 61–62).
- [165] A. Andreanov and M. V. Fistul, “Frustration-induced highly anisotropic magnetic patterns in the classical XY model on the kagome lattice”, *Physical Review B* **102**, 140405 (2020) (cited on page 61).
- [166] L. Pitaevskii and S. Stringari, *Bose-Einstein Condensation and Superfluidity* (Oxford University Press, 2016) (cited on pages 61–64, 142).
- [167] D. Bergman, J. Alicea, E. Gull, S. Trebst, and L. Balents, “Order-by-disorder and spiral spin-liquid in frustrated diamond-lattice antiferromagnets”, *Nature Physics* **3**, 487–491 (2007) (cited on page 62).
- [168] A. G. Green, G. Conduit, and F. Krüger, “Quantum Order-by-Disorder in Strongly Correlated Metals”, *Annual Review of Condensed Matter Physics* **9**, 59–77 (2018) (cited on page 62).
- [169] R. Resta, “The insulating state of matter: A geometrical theory”, *European Physical Journal B* **79**, 121–137 (2011) (cited on pages 62–63).
- [170] R. Cheng, “Quantum Geometric Tensor (Fubini-Study Metric) in Simple Quantum System: A pedagogical Introduction”, *arXiv:1012.1337* (2010) (cited on page 63).
- [171] L. Liang, T. I. Vanhala, S. Peotta, T. Siro, A. Harju, and P. Törmä, “Band geometry, Berry curvature, and superfluid weight”, *Physical Review B* **95**, 024515 (2017) (cited on page 63).
- [172] T. Smoleński, P. E. Dolgirev, C. Kuhlenkamp, A. Popert, Y. Shimazaki, P. Back, X. Lu, M. Kroner, K. Watanabe, T. Taniguchi, I. Esterlis, E. Demler, and A. Imamoglu, “Signatures of Wigner crystal of electrons in a monolayer semiconductor”, *Nature* **595**, 53–57 (2021) (cited on page 67).
- [173] H. Li, S. Li, E. C. Regan, D. Wang, W. Zhao, S. Kahn, K. Yumigeta, M. Blei, T. Taniguchi, K. Watanabe, S. Tongay, A. Zettl, M. F. Crommie, and F. Wang, “Imaging two-dimensional generalized Wigner crystals”, *Nature* **597**, 650–654 (2021) (cited on page 67).

- [174] S. Braun, M. Friesdorf, S. S. Hodgman, M. Schreiber, J. P. Ronzheimer, A. Riera, M. Del Rey, I. Bloch, J. Eisert, and U. Schneider, “Emergence of coherence and the dynamics of quantum phase transitions”, *Proceedings of the National Academy of Sciences of the United States of America* **112**, 3641–3646 (2015) (cited on page 69).
- [175] T. Li, L. Duca, M. Reitter, F. Grusdt, E. Demler, M. Endres, M. Schleier-Smith, I. Bloch, and U. Schneider, “Bloch state tomography using Wilson lines”, *Science* **352**, 1094–1097 (2016) (cited on pages 70, 181–182).
- [176] K. G. H. Viebahn, “Quasicrystalline Optical Lattices For Ultracold Atoms”, PhD thesis (University of Cambridge, 2018) (cited on pages 72, 86, 106, 122).
- [177] M. Sbroscia, “Between order and disorder”, PhD thesis (University of Cambridge, 2019) (cited on pages 72, 75, 81, 86, 88, 106, 176).
- [178] T. Li, “An Apparatus for Probing Fermions in a Quasi-Two-Dimensional Geometry”, Master’s thesis (Ludwig-Maximilians-Universität München, 2011) (cited on page 72).
- [179] C. Weitenberg, “Single-Atom resolved imaging and manipulation of an atomic Mott insulator”, PhD thesis (Ludwig-Maximilians-Universität München, 2011) (cited on pages 72, 157).
- [180] W. S. Bakr, “Microscopic Studies of Quantum Phase Transitions in Optical Lattices”, PhD thesis (Harvard University, 2011) (cited on page 72).
- [181] L. W. Cheuk, “Quantum Gas Microscopy of Strongly Correlated Fermions”, PhD thesis (Massachusetts Institute of Technology, 2015) (cited on page 72).
- [182] A. Omran, “A Microscope for Fermi Gases”, PhD thesis (Ludwig-Maximilians-Universität München, 2016) (cited on page 72).
- [183] M. F. Parsons, “Probing the Hubbard model with single-site resolution”, PhD thesis (Harvard University, 2016) (cited on page 72).
- [184] G. Edge, “Imaging Fermionic Atoms in a Quantum Gas Microscope”, PhD thesis (University of Toronto, 2017) (cited on pages 72, 147, 157).
- [185] D. A. Cotta, “A single-site resolution fermionic quantum-gas microscope”, PhD thesis (University of Strathclyde, 2018) (cited on pages 72, 147).
- [186] P. Wieburg, “A Novel Fermionic Quantum Gas Microscope: Concept, Design and Construction.”, PhD thesis (Universität Hamburg, 2019) (cited on page 72).
- [187] N. Lorenz, “A Rydberg Tweezer Platform with Potassium Atoms”, PhD thesis (Ludwig-Maximilians-Universität München, 2021) (cited on page 72).
- [188] Atlas Technologies, *Aluminum’s Extreme Vacuum Performance* (cited on page 73).
- [189] VACOM, *Outgassing Rates of Aluminum compared to Stainless Steel* (cited on page 73).
- [190] G. Modugno, C. Benkő, P. Hannaford, G. Roati, and M. Inguscio, “Sub-Doppler laser cooling of fermionic 40K atoms”, *Physical Review A - Atomic, Molecular, and Optical Physics* **60**, R3373–R3376 (1999) (cited on page 74).

- [191] B. DeMarco, H. Rohner, and D. S. Jin, “An enriched 40K source for fermionic atom studies”, *Review of Scientific Instruments* **70**, 1967–1969 (1999) (cited on page 74).
- [192] T. G. Tiecke, *Properties of Potassium*, 2011 (cited on page 74).
- [193] D. A. Steck, *Rubidium 87 D Line Data*, 2003 (cited on page 74).
- [194] K. Dieckmann, R. J. C. Spreeuw, M. Weidemüller, and J. T. M. Walraven, “Two-dimensional magneto-optical trap as a source of slow atoms”, *Physical Review A* **58**, 3891–3895 (1998) (cited on page 86).
- [195] J. Catani, P. Maioli, L. De Sarlo, F. Minardi, and M. Inguscio, “Intense slow beams of bosonic potassium isotopes”, *Physical Review A* **73**, 033415 (2006) (cited on page 86).
- [196] A. Ridinger, S. Chaudhuri, T. Salez, U. Eismann, D. R. Fernandes, K. Magalhães, D. Wilkowski, C. Salomon, and F. Chevy, “Large atom number dual-species magneto-optical trap for fermionic 6Li and 40K atoms”, *European Physical Journal D* **65**, 223–242 (2011) (cited on page 86).
- [197] N. Tammuz, “Thermodynamics of ultracold 39K atomic Bose gases with tuneable interactions”, PhD thesis (University of Cambridge, 2011) (cited on pages 88, 114).
- [198] T. L. Gustavson, A. P. Chikkatur, A. E. Leanhardt, A. Görlitz, S. Gupta, D. E. Pritchard, and W. Ketterle, “Transport of Bose-Einstein Condensates with Optical Tweezers”, *Physical Review Letters* **88**, 020401 (2001) (cited on page 89).
- [199] S. Schmid, “Long distance transport of ultracold atoms using a 1D optical lattice”, Diploma thesis (Leopold-Franzens-Universität Innsbruck, 2006) (cited on page 89).
- [200] M. Greiner, I. Bloch, T. W. Hänsch, and T. Esslinger, “Magnetic transport of trapped cold atoms over a large distance”, *Physical Review A* **63**, 031401 (2001) (cited on page 89).
- [201] H. J. Lewandowski, D. M. Harber, D. L. Whitaker, and E. A. Cornell, “Simplified system for creating a Bose-Einstein condensate”, *Journal of Low Temperature Physics* **132**, 309–367 (2003) (cited on page 89).
- [202] D. Bloch, “Optical transport of ultracold atoms”, Pre-doctoral research year report (École normale supérieure Paris-Saclay, 2020) (cited on page 89).
- [203] D. Greif, “Quantum Magnetism with Ultracold Fermions in an Optical Lattice”, PhD thesis (ETH Zurich, 2013) (cited on page 94).
- [204] J. L. Roberts, N. R. Claussen, S. L. Cornish, E. A. Donley, E. A. Cornell, and C. E. Wieman, “Controlled collapse of a Bose-Einstein condensate”, *Physical Review Letters* **86**, 4211–4214 (2001) (cited on page 105).
- [205] C. J. Foot, *Atomic Physics* (Oxford University Press, 2004) (cited on page 105).
- [206] M. Landini, S. Roy, L. Carcagní, D. Trypogeorgos, M. Fattori, M. Inguscio, and G. Modugno, “Sub-Doppler laser cooling of potassium atoms”, *Physical Review A* **84**, 043432 (2011) (cited on page 106).
- [207] J. Dalibard and C. Cohen-Tannoudji, “Laser cooling below the Doppler limit by polarization gradients: simple theoretical models”, *Journal of the Optical Society of America B* **6**, 2023 (1989) (cited on page 106).

- [208] Y.-J. Lin, A. R. Perry, R. L. Compton, I. B. Spielman, and J. V. Porto, “Rapid production of  $^{87}\text{Rb}$  Bose-Einstein condensates in a combined magnetic and optical potential”, *Physical Review A* **79**, 063631 (2009) (cited on page 109).
- [209] T. H. Bergeman, P. McNicholl, J. Kycia, H. Metcalf, and N. L. Balazs, “Quantized motion of atoms in a quadrupole magnetostatic trap”, *Journal of the Optical Society of America B* **6**, 2249 (1989) (cited on page 109).
- [210] X. Su, “Optical Transport of Ultracold Atoms for Atom Interferometry”, Master’s thesis (University of Cambridge, 2021) (cited on page 113).
- [211] A. Simoni, M. Zaccanti, C. D’Errico, M. Fattori, G. Roati, M. Inguscio, and G. Modugno, “Near-threshold model for ultracold KRb dimers from interisotope Feshbach spectroscopy”, *Physical Review A* **77**, 052705 (2008) (cited on page 114).
- [212] C. D’Errico, M. Zaccanti, M. Fattori, G. Roati, M. Inguscio, G. Modugno, and A. Simoni, “Feshbach resonances in ultracold  $^{39}\text{K}$ ”, *New Journal of Physics* **9** (2007) (cited on page 115).
- [213] B. Gadway, D. Pertot, R. Reimann, M. G. Cohen, and D. Schneble, “Analysis of Kapitza-Dirac diffraction patterns beyond the Raman-Nath regime”, *Opt. Express* **17**, 19173–19180 (2009) (cited on page 122).
- [214] D. L. Freimund, K. Aflatooni, and H. Batelaan, “Observation of the Kapitza-Dirac effect”, *Nature* **413**, 142–143 (2001) (cited on page 123).
- [215] F. Gerbier, A. Widera, S. Fölling, O. Mandel, T. Gericke, and I. Bloch, “Phase Coherence of an Atomic Mott Insulator”, *Physical Review Letters* **95**, 050404 (2005) (cited on page 134).
- [216] Z. Lin, J. Zhang, and Y. Jiang, “Quantum phase transitions of ultracold Bose systems in nonrectangular optical lattices”, *Physical Review A* **85**, 023619 (2012) (cited on pages 134–136, 145).
- [217] D. van Oosten, P. van der Straten, and H. T. C. Stoof, “Quantum phases in an optical lattice”, *Physical Review A* **63**, 053601 (2001) (cited on page 135).
- [218] N. Elstner and H. Monien, “A numerical exact solution of the Bose-Hubbard model”, [arXiv:cond-mat/9905367](https://arxiv.org/abs/cond-mat/9905367) (1999) (cited on page 135).
- [219] N. Teichmann, D. Hinrichs, and M. Holthaus, “Reference data for phase diagrams of triangular and hexagonal bosonic lattices”, *EPL (Europhysics Letters)* **91**, 10004 (2010) (cited on page 135).
- [220] S. E. Korshunov, “Phase transitions in two-dimensional systems with continuous degeneracy”, *Physics-Uspekhi* **49**, 225 (2006) (cited on page 138).
- [221] R. Barakat, “Application of Apodization to Increase Two-Point Resolution by the Sparrow Criterion I Coherent Illumination”, *Journal of the Optical Society of America* **52**, 276 (1962) (cited on page 147).
- [222] D. C. McKay, D. Jervis, D. J. Fine, J. W. Simpson-Porco, G. J. A. Edge, and J. H. Thywissen, “Low-temperature high-density magneto-optical trapping of potassium using the open  $4S \rightarrow 5P$  transition at 405 nm”, *Phys. Rev. A* **84**, 63420 (2011) (cited on page 148).

- [223] M. McDonald, J. Trisnadi, K.-X. Yao, and C. Chin, “Superresolution Microscopy of Cold Atoms in an Optical Lattice”, *Physical Review X* **9**, 021001 (2019) (cited on page 148).
- [224] G. Morigi, J. Eschner, and C. H. Keitel, “Ground State Laser Cooling Using Electromagnetically Induced Transparency”, *Phys. Rev. Lett.* **85**, 4458–4461 (2000) (cited on page 150).
- [225] J. Eschner, G. Morigi, F. Schmidt-Kaler, and R. Blatt, “Laser cooling of trapped ions”, *J. Opt. Soc. Am. B* **20**, 1003–1015 (2003) (cited on page 150).
- [226] Newport Corporation, *Super High Resolution USAF Test Targets* (cited on page 160).
- [227] F. Huber, “Site-Resolved Imaging with the Fermi Gas Microscope”, PhD thesis (Harvard University, 2015) (cited on page 160).
- [228] L. Donini, “Quantum Simulation with an Optical Kagome Lattice”, First year report (University of Cambridge, 2020) (cited on page 161).
- [229] J. Steinhauer, N. Katz, R. Ozeri, N. Davidson, C. Tozzo, and F. Dalfovo, “Bragg Spectroscopy of the Multibranch Bogoliubov Spectrum of Elongated Bose-Einstein Condensates”, *Physical Review Letters* **90**, 060404 (2003) (cited on page 163).
- [230] D. Petter, G. Natale, R. M. Van Bijnen, A. Patscheider, M. J. Mark, L. Chomaz, and F. Ferlaino, “Probing the Roton Excitation Spectrum of a Stable Dipolar Bose Gas”, *Physical Review Letters* **122**, 183401 (2019) (cited on page 163).
- [231] J. L. Ville, T. Bienaimé, R. Saint-Jalm, L. Corman, M. Aidelsburger, L. Chomaz, K. Kleinlein, D. Perconte, S. Nascimbène, J. Dalibard, and J. Beugnon, “Loading and compression of a single two-dimensional Bose gas in an optical accordion”, *Physical Review A* **95**, 013632 (2017) (cited on page 164).
- [232] S. Shanokprasith, “Quantum Simulation with an Optical Kagome Lattice”, First year report (University of Cambridge, 2021) (cited on page 164).
- [233] B. Lim, S. Son, H. Kim, S. Nah, and K. M. Lee, “Enhanced Deep Residual Networks for Single Image Super-Resolution”, in *2017 IEEE Conference on Computer Vision and Pattern Recognition Workshops (CVPRW)* (2017), pages 1132–1140 (cited on page 164).
- [234] W. Yang, X. Zhang, Y. Tian, W. Wang, J.-H. Xue, and Q. Liao, “Deep Learning for Single Image Super-Resolution: A Brief Review”, *IEEE Transactions on Multimedia* **21**, 3106–3121 (2019) (cited on page 164).
- [235] S. Giorgini, L. P. Pitaevskii, and S. Stringari, “Theory of ultracold atomic Fermi gases”, *Rev. Mod. Phys.* **80**, 1215–1274 (2008) (cited on page 164).
- [236] R. B. Laughlin, “Quantized motion of three two-dimensional electrons in a strong magnetic field”, *Physical Review B* **27**, 3383–3389 (1983) (cited on page 165).
- [237] R. E. Prange and S. M. Girvin, *The Quantum Hall Effect*, edited by R. E. Prange and S. M. Girvin, Graduate Texts in Contemporary Physics (Springer New York, New York, NY, 1990) (cited on page 165).

- 
- [238] N. Elstner, R. R. Singh, and A. P. Young, “Finite temperature properties of the spin-1/2 Heisenberg antiferromagnet on the triangular lattice”, *Physical Review Letters* **71**, 1629–1632 (1993) (cited on page 165).
- [239] P. Henelius and A. W. Sandvik, “Sign problem in Monte Carlo simulations of frustrated quantum spin systems”, *Physical Review B - Condensed Matter and Materials Physics* **62**, 1102–1113 (2000) (cited on page 165).
- [240] T. A. Hilker, G. Salomon, F. Grusdt, A. Omran, M. Boll, E. Demler, I. Bloch, and C. Gross, “Revealing hidden antiferromagnetic correlations in doped Hubbard chains via string correlators”, *Science* **357**, 484–487 (2017) (cited on page 165).
- [241] Q.-H. Chen, P. Li, and H. Su, “Fractional Mott insulator-to-superfluid transition of Bose-Hubbard model in a trimerized Kagomé optical lattice”, *Journal of Physics: Condensed Matter* **28**, 256001 (2016) (cited on page 165).
- [242] T. Li, L. Duca, M. Reitter, F. Grusdt, E. Demler, M. Endres, M. Schleier-Smith, I. Bloch, and U. Schneider, “Bloch state tomography using Wilson lines”, *Science* **352**, 1094–1097 (2016) (cited on page 181).
- [243] C. Barreateau, F. Ducastelle, and T. Mallah, “A bird’s eye view on the flat and conic band world of the honeycomb and Kagome lattices: towards an understanding of 2D metal-organic frameworks electronic structure”, *Journal of Physics: Condensed Matter* **29**, 465302 (2017) (cited on page 182).